Fluorescence properties of Rhodamine 101 and Yb^{3+} in condensed phase systems

Krishnakumar Chullipalliyalil

Department of Physics

National University of Ireland,
University College Cork,
Cork, Ireland.

Thesis submitted for the Degree of

Doctor of Philosophy

Supervisor: **Prof. A. A. Ruth**

Head of the Department: **Prof. J. J. McInerny**

Research supported by Science Foundation of Ireland.

Contents

Abstract

The fluorescence properties of two high quantum yield substances, Rhodamine 101 and Yb^{3+}, were studied in different molecular environments. The prompt emission properties of these compounds were spectroscopically characterized using custom-made high resolution fluorescence detection set-ups in the visible and near IR spectral region. The anti-Stokes emission from Rhodamine 101 in ethanol was studied as a function of temperature and concentration. The emission and absorption properties of Yb^{3+} were investigated in glassy and crystalline matrices. The photophysical properties of Yb^{3+} phosphate glass nanoparticles, prepared by liquid-phase pulsed laser ablation was compared with those of the bulk material. Emission properties of chemically synthesized nanocrystals of Yb^{3+} doped tungstate (Yb^{3+}:$KGd(WO_4)_2$) were also compared to their bulk counterpart. Nano-glasses and crystals exhibited spectroscopic modifications in comparison to the corresponding bulk materials. These modifications were due to the alterations of the phonon coupling between Yb^{3+} and the host matrix.

Declaration

I declare that the content of this thesis is all my own work and has not been submitted for another degree, either at University College Cork or elsewhere. The work of others that has been used to augment my thesis has been referenced accordingly.

.....

Krishnakumar Chullipalliyalil

“ .. There are three things in this world.....

atoms, space between atoms, and opinions.. !! ”

Acknowledgement

Though only my name appears on the cover of this thesis, a great many people have contributed to its production. I owe my gratitude to all those people who have made this thesis possible and because of whom my postgraduate experience has been one that I will cherish forever. Firstly, I would like to express my sincere gratitude to my advisor Prof. Albert Andreas Ruth for the continuous support of my Ph.D study and related research, for his patience, motivation, and immense knowledge. His guidance helped me in all the time of research and writing of this thesis. He had been extremely patient throughout, and helped me gradually develop my skill set. Besides my advisor, I would like to thank the rest of my thesis committee: Prof. Joan Carvajal, and Dr. Simon Lawrence, for their insightful comments and encouragement, but also for the hard question which incented me to widen my research from various perspectives. I thank my fellow lab mates - Dr. Hemanth Dinesan, Dr. Satheesh Chandran, Karen Acheson, Bryan Keary and previous members, Dr. Ranjini Deitche, Dr. Sophie Dixneuf, Dr. Grzegorz Glaczynski in for the stimulating discussions and for all the fun we have had in the last four and half years. I specially thank Dr. Marc Goulette, for his help in the preparation of the thesis. Also I thank my friends in Tyndall National Institute for their timely guidance.

I would like to thank the supermen in the workshop, Joe Sheehan and Christy Roche for their help during the development of various optical set-up. I am also indebted to the members of the Chemistry department, with whom I have interacted during the course of my graduate studies. Particularly, I would like to acknowledge the collaborators Dr. Colm O'Dwyer, Dr. Hugh Geany, Dr. Mick Morris, Dr. Atul Thorat, Dr. Colm Glynn, for the many valuable discussions that helped me understand my research area better. I would like to thank Dr. Sibu Padhmanabhan,

discussions with whom were always fruitful. The Department of Physics has provided the support and equipment I have needed to produce and complete my thesis and the SFI has funded my studies.
Many friends have helped me stay sane through these years. Their support and care helped me overcome setbacks and stay focused on my study. I greatly value their friendship and I deeply appreciate their belief in me. Especially, I would like to thank my besties in Cork - Anjali Pai for the four year Corkathon together, Lekha Menon & Vimal Kumar Velayudhan for being my acting family, Sreeram Udayan for the Perlenbachers, Nisha Saini for the motivational times, Deepam Bhandari for being my younger sister, Nayana Turmari for the numerous chai sessions. Ambili, I owe you a lot, special thanks for the numerous skype conversations. I thank the Cork Indian community that helped me adjust to a new place without missing home. Most importantly, none of this would have been possible without the love and patience of my family. Amma, Achan whose sweat and tears made me who I am now; I thank you for being a constant source of love, concern, support and strength all these years. I would like to express my heart-felt gratitude to chechi, aliyan, and our only Sayu for all the help and guidance during my initial days of Job search.

Chapter 1

Introduction

Materials with very high emission quantum yields are of considerable interest for optical technologies [1]–[9]. They are used for laser development [7], [10]–[12], cooling with laser light [13]–[22], detector technologies [3], [4], [23], [24], and general lighting applications [25], [26]. Two classes of high yield materials, that are rather distinct in their molecular composition and hence in their application areas are (1) organic laser dyes and (2) rare earth doped materials. Despite their distinct structural differences, their photo-physical properties enable very high emission quantum yields in excess of 95% in both of these systems [11], [27]. This thesis aims at the investigation of the photo-physical properties of Rhodamine dyes and Yb^{3+} doped solids, which were selected as representative species types.

1.1 Absorption and emission properties of Rhodamine dyes

Laser dyes are organic materials consisting of large aromatic molecules. For laser applications they are generally used in solutions [8], [11] like in this work, but other molecular environments have also been used for their investigation. The laser dye of interest in this study is Rhodamine 101, its structure is shown in Figure 1.1. As an aromatic molecule, its energy level structure can be schematically described in form of a Jablonski diagram (Figure 1.2). With an even number of electrons, Rhodamine possesses a singlet ground state (S_0). The absorption of a photon by a molecule in the ground state can lead to population of an excited singlet

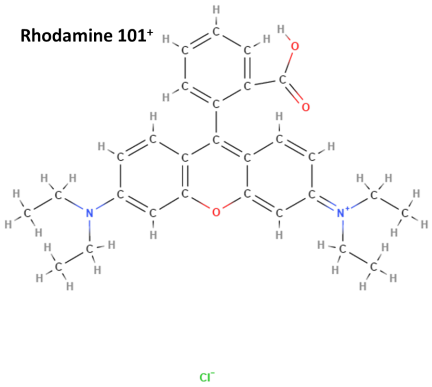

Figure 1.1: Chemical structure of Rhodamine 101. Cl^- is the counter anion.

state (S_n, n$\geq$ 1). In Rhodamines the first excited singlet state is located at ≈10,000-20,000 cm^{-1}. If the excitation energy is such that when the vibronic states are excited, then fast (non-radiative) vibrational relaxation ($\tau \sim 10^{-11}$ s [8], [11], [28]) rapidly leads to the population of S_1, and a prompt fluorescence with high yield ($>$ 97% [29]–[32]) can be observed. Typical fluorescence lifetimes are of the order of ns in solution (∼10 ns for Rhodamine 101 in ethanol [33]). This value can vary significantly depending on the molecular environment of the dye molecule. In solution the interaction with the dielectric continuum of the solvent molecules leads to the inhomogeneous broadening of the observed transition. The typical spectral line widths for rhodamines in organic solutions are ≈ 40-100 cm^{-1}at 300 K [36].

1.1.1 Anti-Stokes Fluorescence in Rhodamine 101

Anti-Stokes (AS) fluorescence in organic compounds in the condensed phase (e.g. in Rhodamine 101 in methanol) can potentially be observed, if the energy of the excitation photons is smaller than the gap between the origins of the ground state (S_0) and first excited electronic state (S_1) of the respective dye (see Figure 1.2). In this case only molecules that can be excited are "hot", i.e., vibrationally excited. The excited S_1 states contain mainly electronic but only very little vibrational energy. Therefore Franck-Condon-uninhibited transitions to the ground state will mainly occur at wavelengths that are shorter than the excitation wavelength and hence give rise to so-called anti-Stokes (blue-shifted) fluorescence. The

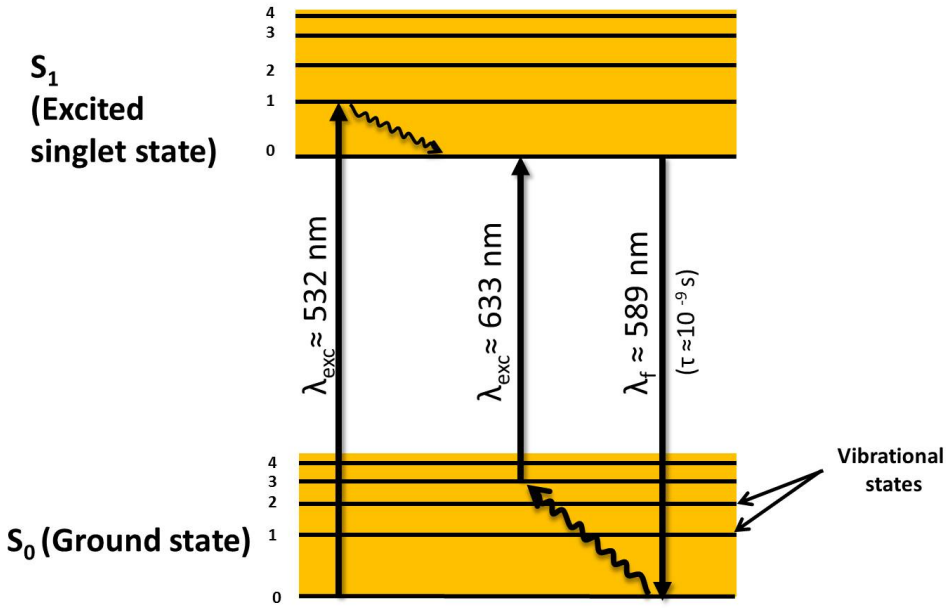

Figure 1.2: Jablonski energy diagram showing excitation of excited singlet electronic level of Rhodamine 101 dye molecule. The stack of horizontal lines represents vibronic state manifolds, in which the ground singlet state is S_0 and excited singlet states is S_1 and so on. The dotted box shows the anti-Stokes excitation scheme (section 1.1.1): The excitation at 633 nm would excite the "hot band" denotes and the relaxation to the vibrational origin of S_0 produces anti-Stokes fluorescence. The black curved arrows represents the interaction of the dye molecules to the phonons due to coupling with the host matrix.

energy for this higher energy emission is delivered by the molecular environment of the organic dye. Therefore anti-Stokes fluorescence strongly depends on the temperature of the host matrix and on the (phonon) coupling between the dye and the host material. These so-called "red edge effects" (because excitation on the far red edge of the absorption spectrum is required to observe it) are known and many studies tried to explain the physical nature of this peculiar phenomenon [19], [22], [37], [38].

1.2 Absorption and emission properties of Yb^{3+} doped systems

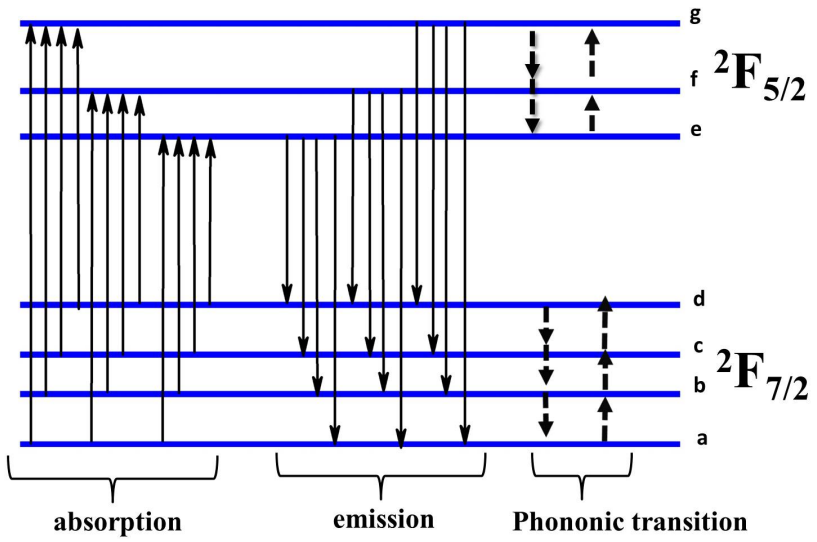

Figure 1.3: Level scheme of Yb^{3+} and possible transitions (optical absorption and emission, phononic transitions). The upper multiplet $^2F_{5/2}$ consists of three Stark levels, e, f and g; the ground state mutliplet $^2F_{7/2}$ consists of four Stark levels: a, b, c and d. Energy separation between the levels are arbitrary and not to scale.

Yb^{3+} (Ytterbium IV) is a lanthanide ion with the electronic structure [Xe] $4f^{13}$ [39], [40]. The term scheme of Yb^{3+} in di-electric solids such as crystals and glasses is simple compared to that of Rhodamines. The general schematic energy level structure of Yb^{3+} is shown in Figure 1.3 and can be explained as follows: In rare earth metals, spin-orbit interaction is of a magnitude that justifies the assumption of LS-coupling. Therefore the total orbital momentum $L = \sum_{i=1}^{N} l_i$ and the total spin momentum $S = \sum_{i=1}^{N} s_i$ are given by the sums of the individual orbital angular momenta l_i and spins s_i of all electrons i. The total angular momentum J is then defined as

$$J = L + S \tag{1.1}$$

with J = |L+S|,...,|L-S|.

The total angular momentum has 2J+1 eigenstates represented by the magnetic quantum number M = –J, ...+J. Since the 4f sub-shell in the Yb^{3+} ground state is filled with 13 electrons, this single hole configuration makes the ground state a ^2F doublet. A single 4f hole has a spin of s=1/2 and orbital angular momentum l = 3, producing a total orbital angular momentum of L = 3 and spin of S = 1/2 (hence the total angular momentum can take the values J = 5/2 and 7/2). LS-coupling splits this ^2F doublet into the two manifolds $^2F_{7/2}$ and $^2F_{5/2}$[1] (where $^2F_{7/2}$ is at lower energy due to the 4f shell being more than half-filled). The statistical weights of each of the multiplets are (2J+1) = 8 and 6 for $^2F_{7/2}$ and $^2F_{5/2}$ respectively. The magnitude of spin orbit coupling is defined as E_{LS}= ζ (l+1/2) where spin orbit coupling parameter ζ= 2, 918 cm^{-1} for free Yb^{3+} ions [41]. For l =3 this produces a $^2F_{7/2}$ - $^2F_{5/2}$ splitting of ≈10,200 cm^{-1}.

For a free ion, the J_z degeneracy is not lifted since the ion has spherically symmetric environment. But in dielectrics, such as crystals or glasses, the non-spherically symmetric arrangement of charges around the Yb^{3+} ion partially or completely lifts the (2J+1) fold degeneracy in J_z. Each of the $^{(2s+1)}L_J$ multiplet will be split into crystal field components. As the electric field induced by the charge distribution is invariant under time reversal, Kramer's degeneracy theorem is applicable [42], [43]. According to Kramer's theorem, every energy level of a time-reversal symmetric system with half integral total spin will be at least doubly degenerate. Hence each of the J_z levels for $^2F_{7/2}$ (2J+1= 8) and $^2F_{5/2}$(2J+1= 6) remain as doublets (known as Kramer's doublets) [28],[33]. Therefore, the $^2F_{7/2}$ and $^2F_{5/2}$ multiplets split into at most 4 and 3 Kramer doublets respectively. The upper state, $^2F_{5/2}$, is degenerated into three Stark doublets e, f, and g, the lower state, $^2F_{7/2}$, into four Stark doublets a, b, c, and d (Figure 1.3) . Each doublet can be spectroscopically resolved only in the presence of a magnetic field [43]. The splitting of the Stark levels depends on the host matrix and varies from ≈400 cm^{-1} to ≈1300 cm^{-1} for a whole multiplet [44]. A complete lifting of the (2J+1) fold degeneracy with respect to J_z is only possible under the influence of a

[1]Spectroscopic term symbol notation: $^{2S+1}L_J$ where (2S + 1) is the multiplicity and L is the term. The quantum number S is a total spin and is always an integer, J is the total angular momentum, which is either an integer or a half-integer and L is the total orbital angular momentum.

magnetic field which is not invariant under time reversal.
The $^2F_{5/2}$ level can be populated by excitation using photons of typical average energy of 10000 cm^{-1}. The transitions to $^2F_{7/2}$ will result in a resonance emission with a small Stokes shift. The individual transitions between each of the Stark levels get broadened both homogeneously and inhomogeneously like that for Rhodamine dyes in solutions. Mechanisms of broadening in Yb^{3+} doped solids are different from that of fluids. The spectral linewidths of Yb^{3+} observed at room temperature are mainly the result of homogeneous broadening by electron-phonon coupling and, in many hosts, of inhomogeneous broadening by a varying crystal field.

1.2.1 Line widths in Yb^{3+} doped systems

Homogeneous broadening (by electron-phonon coupling)
The 4f-4f electronic transitions in Yb^{3+} are coupled with the vibrations in the lattice. The shielding of the 4f electrons by the 5s and 5p orbitals reduces the strength of coupling in Lanthanides. The shielding of 4f orbitals is minimum for Yb^{3+} among the lanthanides and hence exhibit relatively strong coupling compared to other lanthanides. Therefore, Yb^{3+} as the last but one in the lanthanide series exhibits significant homogeneous line broadening, and in many hosts pronounced vibronic features are observed in absorption and emission spectra [44],[45],[46].
Homogeneous line broadening in Yb^{3+} is mostly based on two processes:
(i) one-phonon absorption and emission [48] : In one phonon absorption, a phonon is absorbed from or emitted into the lattice [47]. In this case, the energy of the absorbed or emitted photon lacks or includes the energy of the phonon.
(ii) Raman-scattering of phonons [48]: During Raman-scattering of phonons, a phonon is absorbed during an electronic transition and another phonon of different energy is emitted instantaneously. The energy of the absorbed or emitted photon is reduced or increased by the difference in energy of the phonon [47].
Homogeneously broadened transitions are described by Lorentzian line profiles [49]:

$$g_L(\nu) = \frac{\Delta\nu_H/2\pi}{(\nu-\nu_0)^2 + (\frac{\Delta\nu_H}{2})^2} \tag{1.2}$$

where ν_0 is the central frequency of the optical transition and $\Delta\nu_H$ is the transition spectral line full width at half maximum (FWHM). The Lorentzian function g_L is normalized by $\int_{+\infty}^{-\infty} g_L(\nu)\,d\nu = 1$.

Inhomogeneous broadening:

Interaction of the lanthanide ions with its di-electric surrounding leads to a variation of the potential energy of the ion and hence to a variation of energy levels from site to site. The different energetic conditions per site manifest in spectra by inhomogeneous broadening of the transitions. The crystal field experienced by Yb^{3+} in solids can vary for different reasons [50]–[52]: The active ions may be introduced at different sites[1] in the lattice, where they see different ion groups (ligands) in the matrix or where they are located at varying distances from these ion groups. Some hosts show structural disorder; an extreme example are glasses. Furthermore, local distortions of the crystal field by strain, defects, impurities, or other active ions in the vicinity cause smaller effects.

The line shape of inhomogeneously broadened optical transitions is described by the Gaussian line profile [49]:

$$g_G(\nu) = \frac{1}{\Delta\nu_{INH}}\sqrt{\frac{4\ln 2}{\pi}}\exp\left[-4\ln 2\left(\frac{\nu-\nu_0}{\Delta\nu_{INH}}\right)^2\right] \tag{1.3}$$

where $\Delta\nu_{INH}$ is the FWHM of the inhomogeneously broadened line. Determined by the optical center surrounding fields, the inhomogeneous line width is insensitive to the temperature of the host material.

Since the different transitions at room temperature between $^2F_{7/2}$ and $^2F_{5/2}$ are affected by both homogeneous and inhomogeneous broadening, the band shapes of these transitions are best described by Voigt profiles [49], [52], which are a convolution of Gaussian and Lorentzian functions. The description of Voigt profile is given in more in detail chapter 4.

[1] In this thesis, I will refer to certain prominent molecular environments in glasses and crystals as "sites", even though for glasses and other non-crystalline materials this terminology is not common.

Over view of host matrices for Yb^{3+}used in this study

One-photon transitions between the $^2F_{5/2}$ and $^2F_{7/2}$ manifolds of Yb^{3+} are electric-dipole-forbidden, since the states have the same parity. Therefore only magnetic dipole radiation should be observed, which is rather low in intensity; electric quadrupole transitions are negligible [53]. Hence the transition rates for Yb^{3+} are expected to be inherently small. However, transition rates found in Yb^{3+} are usually one to two orders larger than those based on magnetic dipole radiation alone [53]. This can be explained by interaction of the rare earth ions with the crystal field (which is dependent on the host matrix), which mixes energetically higher-lying states of opposite parity (5d, 5g, ...) into the 4f states and thus enables electric-dipole transitions. To understand the transition rates in Yb^{3+}, it is important to study the host matrix-ion interactions. The variation in Stark splitting of Yb^{3+} doped phosphate glasses serves as one of several appropriate new model system in this context.

Phosphate glass

The phosphate glass used in the study is a commercially available glass, YP1 [1]. Even though commercially available, the information on Stark energy separation of YP1 glass is sparse (see also section 2.1).
The main character of the structure of a phosphate glass is the absence of long range order. Phosphate glass is a typical "network glass", in which the nature of the bonding in the glass is the same as that in a crystal [54], [55]. The basic structural units however are connected in a random manner, and hence there is no periodic arrangement as in a crystal. Even though they do not show long range order, they show a degree of order in short ranges [58]. The basic building blocks of crystalline and amorphous phosphates are the phosphate tetrahedra [56].
Previous works on Raman spectroscopy of phosphate glasses reveal that the glass behaves like a phonon reservoir [55]. Most of the bands formed are from the bending and stretching of O-P-O bonds, and the alkali metals present in different phosphate glasses play no significant role in the observation of vibrational bands.

[1] YP1 is a commercially available Yb^{3+} doped phosphate glass. The exact composition of the YP1 glass was not revealed by the manufacturer.

KGW crystal

The monoclinic $KGd(WO_4)_2$ (called KGW in this thesis) crystal belongs to the family of $KLn(WO_4)_2$ crystals, in which the lanthanide Ln is Y, Gd or other lanthanides. Owing to the excellent general performance as laser material and Raman material, a large number of studies have been carried out on the KGW crystal growth techniques and its spectroscopic analysis [57]–[66]. Yb^{3+} doped KGW crystals show strong absorption and emission bands [46], [58], [67]–[69].

KGW crystals have a monoclinic lattice system with *C2/c* symmetry [67]. The monoclinic unit cell parameters at room temperature are a = 10.683(2) Å, b = 10.452(2) Å, c = 7.583(2) Å, β = 130.70(3)° [51] (a, b, c are the monoclinic Bravais lattice axial distances and β is the angle between c and b). Yb^{3+} ion replace the Gd^{3+}ions in the KGW matrix.

Emission properties of Yb:KGW crystals prepared using three different methods were studied and compared. The details of the preparation and the sample properties are provided in chapter 2, section 2.1.

1.2.2 Anti-Stokes fluorescence in Yb^{3+}

Like for Rhodamines, anti-Stokes fluorescence can be induced in Yb^{3+} doped systems as well. The excitation scheme for anti-Stokes fluorescence in Yb^{3+} doped systems are shown in Figure 1.4.

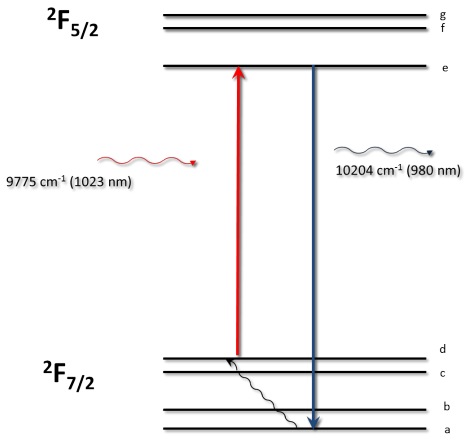

Figure 1.4: Excitation scheme for observing anti-Stokes fluorescence in Yb^{3+}: The red arrow denotes the absorption of photon (curved red arrow) and blue arrow denotes the relaxation due to anti-Stokes fluorescence (curved blue arrow). Black curved arrow represent the non-radiative transitions due to coupling with the host matrix.

States b, c and d of the $^2F_{7/2}$ manifold are thermally accessible at room temperature. Excitation of "hot" Yb^{3+} from one of these states can lead to a blue shifted emission from $^2F_{5/2}$ (as seen in Figure 1.4). This one photon up-conversion can lead to the cooling of the system since the energy difference between the excitation and emission energy is provided by the thermal phonon bath of the host crystal. The process depends on the interaction between the dopant and the host matrix. The cooling process is termed as "anti- Stokes fluorescence cooling" [13], [15], [19], [20]. It has been shown that the temperature can be reduced well beyond the cryogenic regime [14], [71], [72]. The research in this field is progressed to a stage where "an all solid-state cryogenic cooler" appears to be feasible , as a substitute for conventional peltier coolers [73].

1.3 Motivation

1.3.1 Anti-Stokes emission for laser cooling

Since anti-Stokes fluorescence requires the excitation of "hot" excitation centers (dye or rare-earth), thermal energy can be potentially removed from the host matrix and essentially lead to the cooling of the condensed phase system. Even though the principle of removing heat from a system by anti-Stokes fluorescence has been already proposed by Pringsheim in 1929 [48], the experimental realization of radiation cooling of condensed phase systems has only worked for bulk rare-earth (RE) doped solids and semiconductors so far [19], [20], [75]–[78]. For laser dyes as well as for bulk semiconductors or confined quantum well structures (which also exhibit Anti-Stokes fluorescence and have been suggested as potential coolants) successful demonstration of laser cooling has not been demonstrated yet.

Experimental aspects

The challenges involved in radiation cooling of solids can be understood on basis of a few basic considerations concerning the cooling efficiency, η_{cool}, by radiation. Assuming a quasi 3-level system (as seen in Figure 1.4), for a fluorescence emission with mean excitation energy $h\nu_a$ and mean fluorescence energy $h\nu_f$, the cooling efficiency is given by [20]:

$$\eta_{cool} = \eta_{ext}\eta_{abs}\frac{\nu_f}{\nu_a} - 1 \tag{1.4}$$

η_{abs} is the absorption efficiency which defines the number of transitions from the ground to the excited state producing fluorescence.

$$\eta_{abs} = \frac{\alpha}{(\alpha + \alpha_b)} \tag{1.5}$$

$$\eta_{ext} = \frac{\eta_e W_r}{(\eta_e W_r + W_{nr})} \tag{1.6}$$

α is the extinction coefficient of the atom/ ion and α_b is the extinction coefficient of the potential impurities in the host matrix. The probability for an excited state ion/ molecule having absorption efficiency η_{abs}, to produce a photon that will leave the matrix is represented by η_{ext} , the external quantum efficiency. The external fluorescence quantum

efficiency is determined by the non-radiative transition rate W_r, non-radiative transition rate W_{nr}, and the escape efficiency η_e.

Only for $\eta_{cool} > 0$ cooling of the system is possible. The experimental challenge in cooling of solids is to find an appropriate molecular system for which η_{ext}, η_{abs} and $\frac{\nu_f}{\nu_a}$ can be maximized. The main challenges to maximize η_{cool} are: (i) re-absorption, (ii) impurities, (iii) not high enough emission yields.

Aspects related to rhodamines: In laser dyes (such as Rhodamines) fluorescence quantum yields of 0.97-0.98 have been reported in solution upon excitation in the main $S_0 \rightarrow S_1$ absorption band [32], [33], [79]. Anti-stokes fluorescence quantum yields are not well documented in the literature yet. Undesirable effects such as internal reflection, re-absorption of anti-Stokes fluorescence, and photochemical degradation may lower η_{ext} to ca. 0.95 – 0.96. The sample purity determines the value for η_{abs}. The purities of dyes, solvents or other chemicals as specified by typical suppliers (Exalite, Lambda Physik GmbH, or Aldrich) are generally in excess of 99% and it is expected that $\eta_{abs} > 0.995$ can be achieved. Hence $\eta_{abs} \times \eta_{ext} \approx 0.95$ appears achievable for organic laser dyes. If an anti-Stokes shift of 6% can be found, i.e. $(\frac{\nu_f}{\nu_a})>1.06$, laser cooling of dye doped systems should become achievable. However, 6% anti-Stokes shifts are by no means trivial to achieve. Typical anti-Stokes shifts that have been observed for laser dyes (e.g. Rhodamine101) are in the region of >2% [22], [37], [77], [80]. A systematic study of the maximally achievable anti-Stokes shift will hence be one of the subjects of this project. The main parameters to be varied in search of an optimal AS shift will be: (i) the excitation wavelength, (ii) the temperature, (iii) the sample concentration and of course most importantly, (iv) the dye structure itself, and (v) its respective host matrix. Quantum yields of AS fluorescences as a function of the above parameters (i)-(v) are sparse in the literature [37]. Anti-Stokes fluorescence for laser cooling has triggered some interest in the past [37], [80], but there appears to be a lack of systematic studies that target laser dyes as potential molecular systems for radiation cooling. This project will address this deficit.

Aspects related to Yb^{3+} doped systems: Laser dyes have a drawback in comparison to Yb^{3+}doped materials, however, that their fluorescence quantum yield is highly variable with the molecular environment [32],

[33], [79], [81] and may vary with the excitation wavelength at the red edge of the absorption spectrum. Yb^{3+} doped systems are found to be efficient in bulk cooling [13], [20], [68], [82] compared to rhodamines, but the impurities present in the host matrix limit their performance. The usage of high purity host matrices (enabling a high value of α_b) for Yb^{3+} can lead to cryogenic cooling operation [14], [83]. KGW crystals are considered a good choice as a Yb^{3+} host matrix, since high Yb^{3+} doping concentrations can be achieved without concentration quenching[1] since it has a narrow ground state multiplet [18], [44], [84], [85]. Hence a study of anti-Stokes fluorescence from Yb:KGW crystals using novel methods can produce interesting results. A study of anti-Stokes emission from glasses is also relevant, since there is a limitation on the level of doping of Yb^{3+} in crystals due to concentration quenching [86]. Phosphate glasses becomes excellent choice here, since they allow doping concentrations as high as 14×10^{20} ions/cm^3[87], significantly higher than in crystals [45], [70], [88].

1.3.2 Emission from smaller structures doped with Yb^{3+} and Rhodamine

If smaller systems like nano or micron sized particles are used for anti-Stokes emission, many of the challenges in cooling can be met. Smaller structures exhibit lesser re-absorption, since their dimensions are much smaller compared to bulk material. Another advantage is that smaller areas can be cooled, for purposes that need local cooling. A nano to micron sized particle can potentially cool small junctions in complex integrated circuits. Also, the effect of impurities can be reduced. The drawback here is that the surface defects act as quenching sites potentially reducing the quantum yield. It is interesting to find out the parameters that determine the anti-Stokes fluorescence for cooling purposes as a function of size.

Even though rhodamine doped luminescent nanostructures like silica

[1] As more ions are added, their average separation is reduced leading to more and more ion-ion interactions. This can result in energy transfer between an excited active ion to a nearby active ion. The energy transfer between two similar ions happens with high degree of resonance. There is a possibility that the energy quantum migrates and will eventually reach a defect site where the energy is dissipated non-radiatively. This is called concentration quenching and sets an upper limit for the active ion concentration. It strongly depends on the level of purity of the host material.

nanoparticles, zeolites [89]–[91], and dentrites [92] in solvents are characterized for their emission properties, no reports have been made on their anti-Stokes fluorescence yields. Yb^{3+} doped nano-crystals have been studied before for their anti-Stokes efficiencies [86]. According to Ruan *et al.* [86], the calculated electronic transition rates for anti-Stokes emission in Yb:Y_2O_3 nanopowder is enhanced by a factor of 2-3 compared to the bulk material, due to the influence of the modification of the phonon density of states. Hence glasses and crystals in nano-dimensions are excellent choices for checking their anti-Stokes efficiency. In addition, no previous work on fluorescence from Yb: KGW crystals and YP1 glasses in nano dimensions exist.

Not much work has been done on emission from Yb^{3+} doped nanoparticles generated by pulsed laser ablation in liquid medium [93]–[96]. No previous reports are made on anti-Stokes fluorescence properties of Yb^{3+} doped nanoparticles generated by pulsed laser ablation. Since YP1 glass is a relatively new material, studies of YP1 structure synthesized by pulsed laser ablation have not been performed yet. A study on line widths in emission and absorption of nanoparticles generated by pulsed laser ablation can be interesting since the properties of the particle surface depend on the ablation conditions [93].

Normal fluorescence from smaller structures doped with rhodamine and Yb^{3+} are also of interest. Quantum confinement effects have been reported on luminescent molecules attached to nanostructures like zeolites [89]–[91], and dentrites [92] in solvents. No reports have been published yet on the modifications of Rhodamine 101 electronic energy levels attached to silica nanoparticle surfaces. Even without a modification in energy level, shifts (to higher and lower energy) can be expected in dye emissions when attached to particles of nano dimensions [91], [92] due to the interaction between the host matrix and the guest. Quantum Confinement would have effect on Yb^{3+}electronic energy levels only for extremely smaller particle sizes (less than 5 nm) since they are already confined in the 4f orbital by the screening effect of outer orbitals [84], [97]. But the reduction in size of the host matrix will bring about changes in its phonon distribution. In a bulk crystal, the distribution of lattice vibrational modes forms a quasi-continuum [61], [64], [97]. In nanocrystals the distribution becomes more quantised, and the low frequency lattice

excitations are absent due to the quantization of wavelengths [97]. When the phonon density of states is low, it would affect the electron-phonon and phonon-phonon interactions in the Yb^{3+} doped nano glass/crystal matrix. The confinement effect on the phonon density of states is expected to lead to changes in optical linewidths and lifetimes of electronic excitations [97].

In this context the work described here seeks to establish new knowledge on systems containing either Rhodmaine 101 or Yb^{3+} as potentially useful species in experimental approaches for radiation cooling. The role that Rhodamine 101 can play in the laser cooling through anti-Stokes fluorescence is to be elucidated and investigations in the literature are to be scrutinized [22], [37], [98]. Yb^{3+}doped systems that are most suitable concerning their anti-Stokes emission properties for laser cooling are to be identified, spectroscopically characterized and tested in appropriate solid state host systems. Thereby the size dependence and loss mechanism are to be studied and the photo-physical properties investigated. Starting from solution work, nano-composites and meso-structured thin films are to that be studied as potentially appropriate geometries for the Yb^{3+} systems. New synthesis methods of Yb^{3+} of nano- or micron-sized structures e.g. through laser ablation in liquids are also to be studied.

1.4 Objectives and thesis outline

Main objectives of this thesis are:

1. To design and implement a fluorescence detection set-up for liquid samples and films both in the visible and near-IR region. This includes: (i) Design and alignment of instrument's excitation and detection optics (ii) Optimization and characterization of the set-up through rigorous testing.

2. To study the emission properties of Rhodamine 101 and Yb^{3+} in the condensed phase.

    - Obtain fluorescence properties of Rhodamine 101 molecules in solutions and silica nanoparticle surfaces under varying conditions: (1) concentration, (2) excitation wavelength, and (3) host matrix.
    - Obtain an estimate of Stark level splitting in the YP1 glass and compare it with that of YP1 glass nanoparticles generated by pulsed laser ablation. Determine the difference in line widths in bulk and nanoparticles at different excitation wavelengths.
    - Comparison of the Yb:KGW nanoparticle emission, vibronic interaction and the broadening characteristics with the bulk at two different excitation wavelengths.

3. To obtain fluorescence from optically trapped nano to micron sized particles doped[1] with rhodamine 101 and Yb^{3+}.

The second chapter describes the samples analysed and the experimental techniques used for characterization. In the third chapter the fluorescence spectra of Rhodamine 101 are described. Fourth chapter comprises a photo-physical study work of Yb^{3+}doped glasses and crystals. A summary and outlook section concludes the thesis.

[1]This objective was not fully met, and the results are only mentioned in Appendix C.

Chapter 2

Experimental

The experimental techniques employed in the study are described in the context of the different samples used. A description of the samples is provided initially followed by the methods used to characterize and investigate them spectroscopically.

2.1 Sample overview

2.1.1 Samples with Rhodamine as fluorophore

2.1.1.1 Rhodamine solutions

Solutions of three Rhodamine dyes, Rhodamine 101 (Rh 101), Rhodamine B (Rh B) and Rhodamine 6G (Rh6G) with concentrations 10^{-6} to 10^{-2} M in ethanol were prepared. A 10^{-2} M solution of Rh 101, Rh B and Rh 6G was made and concentrations of the solutions were adjusted by appropriate dilution.

2.1.1.2 Silica nanoparticles with Rhodamine molecules attached to the surface

Micro porous silica nanoparticles doped (individually) with the three Rhodamine dyes (HTS Rh X in Table 2.1) were prepared by a modified Stöber process [23], [99]. Suspensions of the nanoparticle were made in ethanol. The concentrations of the rhodamines attached to the particles in suspension could not be determined accurately using the weight of the sample. Approximate values of concentrations of the Rh X were found

from the baseline subtracted extinction curves to be in the range 10^{-2} M to 10^{-6} M.

(Details on the modified Stöber process is given in Appendix A)

Fluorophore	Sample used in the study	Environment	Characterization method			Sample code
			FS[1]	AS[2]	Imaging[3]	
Rhodamine molecule	Rhodamine 101, Rhodamine B, and Rhodamine 6G in organic solvents (ethanol, DMSO) {Section 2.1.1}	Solvent	✓	✓		Rh X solution (X= 101, B or 6G)
	Rhodamine 101, Rhodamine B, and Rhodamine 6G attached to silicon nanoparticle (suspension in ethanol) {Section 2.1.1}	Silicon	✓	✓	✓	HTS Rh X (X= 101, B or 6G)
Yb^{3+} ion	Bulk crystal prepared by Top Seeded Solution Growth (TSSG) method (Yb^{3+}doping concentration = 5%) {Section 2.1.2.1}	Tungstate(KGW)	✓	✓		Yb:KGW bulk
	Nanocrystals prepared by ball milling bulk crystal prepared by Top Seeded Solution Growth (TSSG) method (Yb^{3+}doping concentration = 3%) {Section 2.1.2.2}		✓		✓	Yb:KGW HTSG
	Nanocrystals prepared by sol-gel method (modified Pechini method) (Yb^{3+}doping concentration = 5%) {Section 2.1.2.2}		✓		✓	Yb:KGW Pechini Method
	Bulk glass (Yb^{3+}doping concentration = 16%) {Section 2.1.2.3}	Phosphate glass	✓	✓		YP1 bulk
	Glass nanoparticle suspension in DMSO prepared by pulsed laser ablation (Yb^{3+}doping concentration = 16%) {Section 2.1.2.4}		✓	✓	✓	YP1 nanoparticles

Table 2.1: List of samples used in the study. ([1] Fluorescence spectroscopy, [2] Absorption spectroscopy, [3] SEM/TEM/AFM)

2.1.2 Samples with Yb^{3+} as fluorophore

Monoclinic double tungstate (potassium-gadolinium tungstate ($KGd(WO_4)_2$) doped with Yb^{3+}(referred to as Yb:KGW or Yb^{3+}:KGW, see Table 2.1) is the crystal characterized in the study. 16% Yb^{3+} doped phosphate glass is the glass studied (referred to as YP1 glass, see Table 2.1).

2.1.2.1 Bulk Yb:KGW

The Top-Seeded Solution Growth (TSSG) method (a high temperature solution growth (HTSG) technique) was employed to create bulk single crystals of Yb:KGW [95], [88]. In high temperature solution growth techniques, crystals are allowed to grow below their melting temperatures on a KGW crystal seed. Crystals of two different Yb^{3+} doping concentrations 5% and 0.5% were prepared. The crystals were neither cut nor polished before use.

2.1.2.2 Yb:KGW nanoparticle

Single crystals of Yb:KGW were prepared using two different synthesis methods:

(a) Ball milling

A bulk Yb:KGW crystal prepared using the TSSG technique was grinded using ball milling to produce nanopowders of 3% Yb:KGW.

(b) Sol-gel modified Pechini method

Nanoparticles of 5% Yb:KGW were also grown chemically by a sol-gel technique (modified Pechini method) [51], [95], [100], [57].
(Details of the two sample preparation methods for Yb:KGW samples are given in Appendix A)

Preparation of nanoparticle thick film of Yb:KGW

The emission from Yb:KGW nanoparticle was studied by depositing the nanoparticles on glass slides. There are many ways to deposit the

Glass properties	
Yb_2O_3 (wt)	16.1
Yb^{3+} conc. ($\times 10^{20}$ions/cm^3)	14.51
Fluorescence lifetime (μsec)	2200
Non-linear refractive index coeff. $n_2(10^{-13}$e.s.u.)	1.48
n (1053 nm)	1.52123

Table 2.2: YP1 glass optical properties relevant for the study (provided by Moltech GmBh)

sample material on to microscope glass slides, such as spin coating, chemical solution/vapour deposition and atomic layer deposition. Since the technical expertise required for is extensive, much simpler approach of solvent evaporation was adopted. A drop of the suspension containing particles is placed on the glass slide and was allowed to evaporate. The effective thickness of the layer is directly proportional to the concentration of the nanoparticle in the suspension. This approach (also known as drop casting) is very simple and has little waste of material. The limitations in the approach are poor control of the thickness of the coating, and poor sample uniformity. The suspensions were made in ethanol and dimethyl sulfoxide (DMSO).

2.1.2.3 Bulk YP1 glass

Two Yb^{3+}doped phosphate glasses (referred to as YP1 glass in Table 2.1) of dimension 10x10x5 mm^3 and absorption maximum at 976 nm were purchased from Moltech GmbH. One was used for liquid phase-pulsed laser ablation for the generation of nanoparticles. Important optical properties of YP1 relevant to the study are shown in Table 2.2.

2.1.2.4 YP1 glass nanoparticles

Preparation of Yb^{3+}doped glass nanoparticle suspension by pulsed laser ablation

Laser ablation in liquid (Liquid Phase - Pulsed Laser Ablation- LP-PLA) [93] is a method employed to create suspensions of nanoparticles. The purity of the nanoparticle suspension obtained using LP-PLA is high due to the physical nature of the approach. LP-PLA was carried out on YP1 glass with the aim of producing Yb^{3+} doped glass nanoparticles in

DMSO. In laser ablation, an intense light pulse is focussed onto a solid target immersed in an appropriate solvent, to remove small amounts of the material from the target sample (Figure 2.1). In LP-PLA, the laser ablates a target placed in a liquid (usually transparent to the laser) at the liquid-solid interface. In the Figure 2.1, laser induced plasma is generated on surface of the YP1 glass. For the ablation Nd:glass laser system (TWINKLE, Light Conversion Ltd.) was used. The laser had an active-passive mode-locked negative-feedback controlled master oscillator, a stretcher, a Nd:glass regenerative amplifier, and a compressor in order to generate pulses of duration of ≈216 fs [101]. On its fundamental at 1055 nm and the second harmonic at 527 nm it delivers pulses of ≈1.9 mJ at a repetition rate of 27 Hz [102]. Both the fundamental and the second harmonic were used for the ablation, they were not separated. The solvent used (DMSO) is transparent to the second harmonic of the laser (at 527 nm) and DMSO has minimal absorption in the near infrared in the wavelength range 950-1100 nm (compared to other solvents like ethanol and water), where the Yb^{3+} ion has maximum absorption.
The second harmonic of the laser (at 527 nm) was used for aligning the optics. The laser beam was guided with two dielectric mirrors (reflective at 1064 nm and 532 nm). A short focal length lens (CaF_2, f = 35 mm) was used mounted on a translational stage to adjust the position of the sample relative to the laser focus. The power was monitored using a power meter which used a photodiode as a detection head. The total ablation time was 390 minutes. Nanoparticles of sizes ranging from 350±50 nm were generated.
The absorption spectrum of the suspensions was measured immediately after ablation using a double beam absorption spectrometer, with the confining liquid as the reference. The suspension was well sonicated for 20 min in an ultrasonic bath before measuring the fluorescence spectra.

2.2 Size characterization of nanoparticles

Imaging of nanoparticles using SEM/TEM

The nanoparticles were imaged using SEM (Scanning Electron Microscope) and TEM (Transmission electron microscope). Silica nanoparticles (spherical in shape) prepared had average diameter around

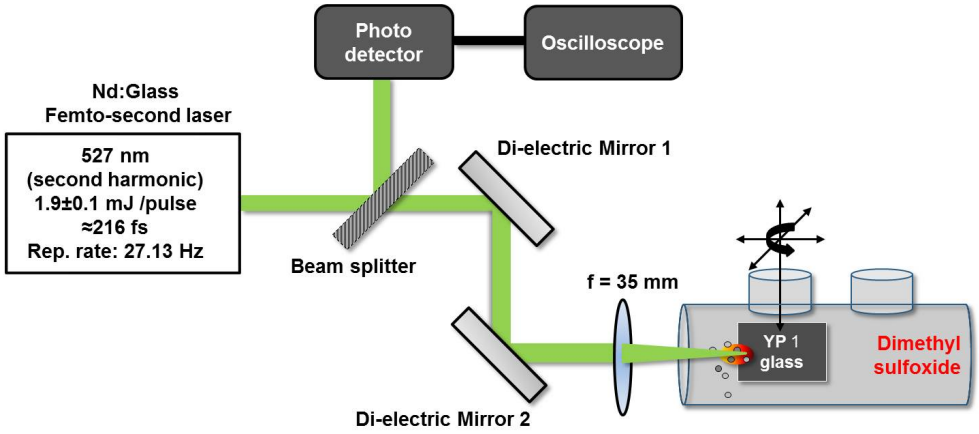

Figure 2.1: Schematic of pulsed laser ablation set-up. The target is immersed in a solvent (DMSO). The focal length of the CaF_2 lens used for focussing the beam is 35 mm. The target can be moved in x, y, z directions using a translational stage. The laser delivers 1.9 mJ/ pulse on its fundamental at 1055 nm and its harmonic at 527 nm.

100±20 nm (Figure 2.2).

An SEM image of 3% Yb:KGW crystal nanopowder prepared by HTSG method is shown in Figure 2.3. The particles appeared to have sharp edges and had no regular shape. The surfaces of the particles are uneven. Surface defects can lead to quenching of fluorescence through non-radiative processes. Therefore, small fluorescence yield are anticipated for these nanostructures. The particles had different sizes ranging from 10 μm to 50 nm.

An SEM image of a 5% Yb:KGW Pechini crystal nanoparticle sample is shown in Figure 2.4. Unlike the nanopowder prepared by ball-milling, the chemically prepared sample seem to be agglomerated. The agglomeration could not be removed even when the particles are agitated (as suspensions in organic solvents) using an ultrasonic bath for 40 minutes.
Size distribution of YP1 nanoparticles prepared by LP-PLA where characterized using TEM (Transmission Electron Microscopy). Particles of average size 200-300 nm were found (Figure 2.5).

Selection of Yb:KGW nanoparticles of specific size range using centrifugation

Yb:KGW nanoparticles (using both preparation methods) showed a

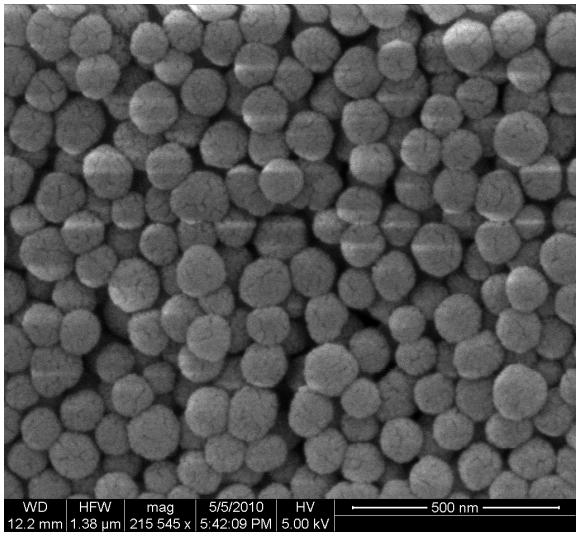

Figure 2.2: SEM image of Hydro Thermally prepared Silica nano particles. The average particle size was 100±20 nm.

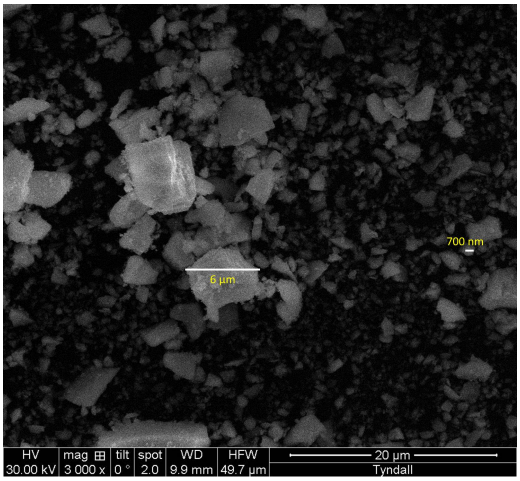

Figure 2.3: A large scale SEM image of Yb:KGW nanopowder prepared by HTSG method. The particle with sizes greater than 6μm and less than 700 nm can be seen. The heavier particles were removed later by centrifuging the suspension of the nanopowder (see section 2.2, selection of nanoparticles using centrifugation).

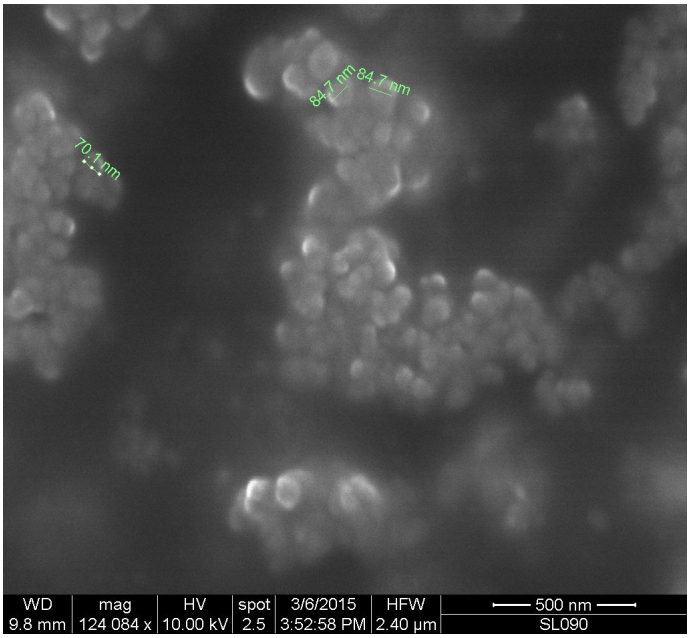

Figure 2.4: SEM image of Yb:KGW Pechini nanopowder sample in ethanol (before centrifugation). The size range of the particles was from 100-500 nm, and the particles were found agglomerated.

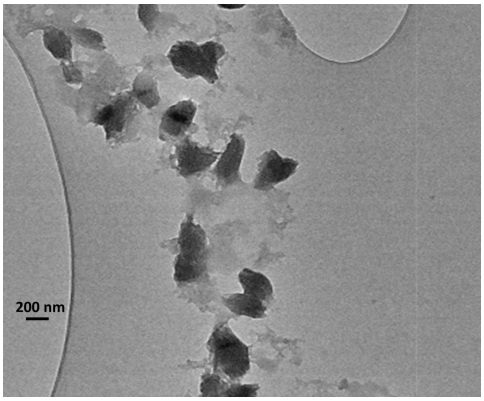

Figure 2.5: TEM image of YP1 glass nanoparticles. The average particle sizes of the particles were 350 nm.

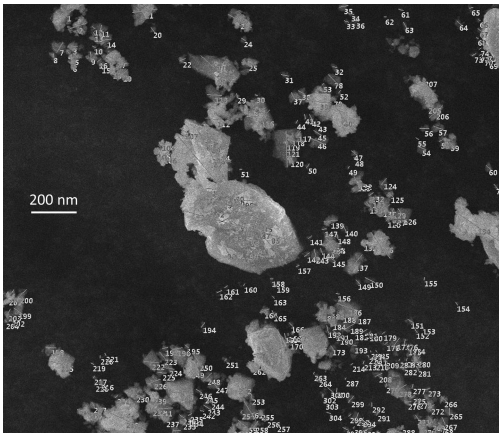

Figure 2.6: Manual analysis method used for determining the size of the particle: lines manually drawn across individual particles in the SEM image is considered as the approximate diameter of the particles. The SEM image is taken after centrifugation of Yb:KGW sample at 1000 r.p.m for 20 minutes.

wide size distribution of particles ranging from a few nanometres to micrometers. Centrifugation with small angular frequency (1000-5000 rpm[1]) were applied to separate the heavier from lighter particles in suspensions of Yb:KGW crystals. Six solvents of different densities (water, ethanol, propanol, DMSO, DCM and hexane) were used for preparing the suspensions. After centrifugation, the particles in suspensions were imaged using SEM. Centrifugation at 1000 rpm for 20 min gave skewed normal distribution of particle diameters with maximum particles diameters around 350 nm and a full width half maximum of 400 nm. Particles of same size range were used for the fluorescence measurements. For the nanopowder prepared by the Pechini method, the particles were found to agglomerate even after centrifugation.

Size analysis of Yb:KGW particles were done manually with the help the image analysis software "gwyddion". Using the software, lines were drawn across isolated features which were considered to be approximate diameters (Figure 2.6). The length of the lines was compiled and the average number of particles of a certain size ranges were plotted as a function of particle diameter (Figure 2.7). For the current study, particle diameters were around 350 nm (1000 rpm for 20 min).

Two additional methods were used to find the average particle size (Blobs method and circles method). The Blobs method uses the intensity vari-

[1]rotations per minute

Sample	Method	Peak diameter (nm)	Average diameter (nm)
3% Yb:KGW (HTSG)	Manual count	450	384±22
	Blobs method	175	362±38
	Circles method	325	284±56
5% Yb:KGW (Pechini)	Manual count	425	375±30
	Blobs method	190	381±44
	Circles method	375	275±64

Table 2.3: Summary of particle size distributions made by three different methods.

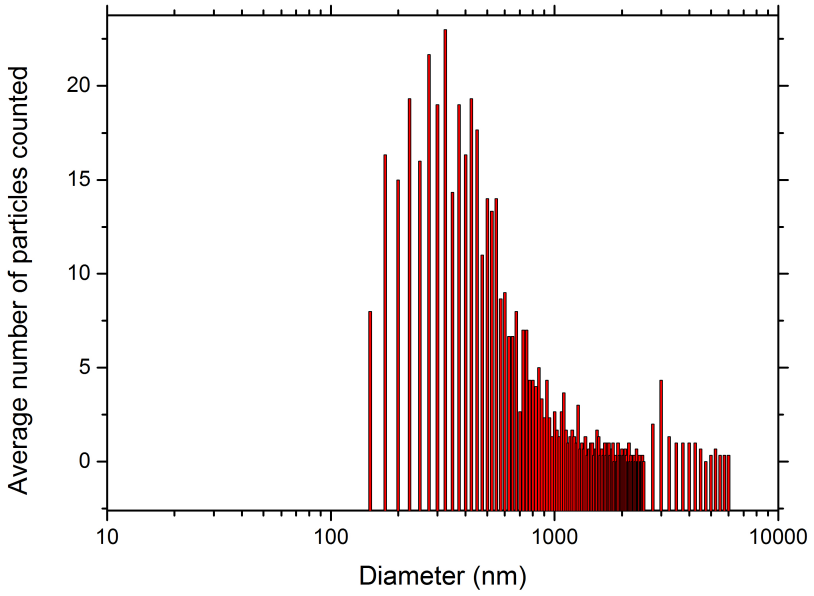

Figure 2.7: Yb:KGW HTSG particle size bin selected by centrifuging at 1000 rpm for 20 minutes : Average size distribution of the particles imaged.

ation in the image for an approximation of the particle size, and in circles method, the diameters of the circles drawn over particles were taken. The average of the three analysis methods is summarized in Figure 2.7 and is listed in detail in Table 2.3. The average particle size distribution was asymmetric to larger particle sizes and had a maximum diameter at 294 nm for Yb:KGW HTSG nanoparticles and 305 nm and 450 nm for Yb:KGW Pechini nanoparticles. The distribution of particles (in a logarithmic scale) was a normal distribution with FWHM of 546 nm and maximum particle size of 331 nm.

These size selected particles in DMSO were then drop cast on the glass slides (as mentioned in section 2.1.2.2). AFM (Atomic Force Microscopy) was used to find the thickness of the nanoparticle film (both for Yb:KGW

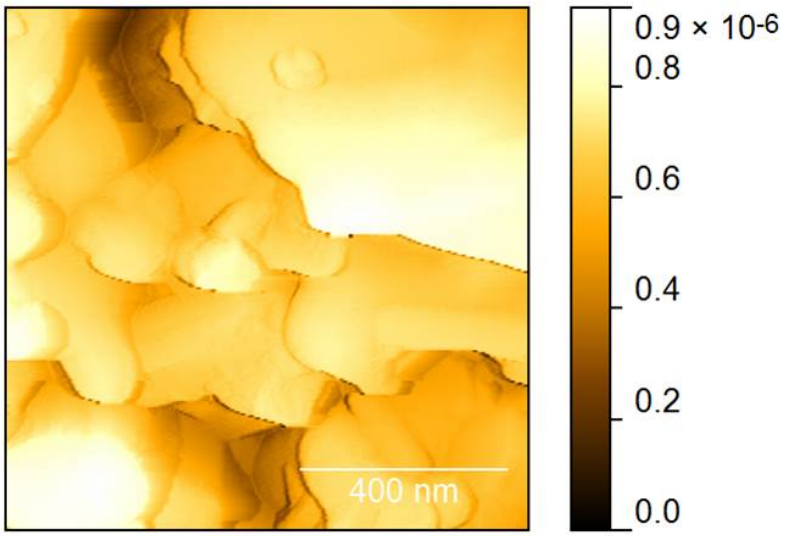

Figure 2.8: AFM image of a small area (ca. 1μm×1μm) of a sample suspension drop cast on a glass slide of Yb:KGW (HTSG). The scale on the right demonstrates the depth of the deposit in terms of the intensity gradient.

HTSG and Yb:KGW Pechini) on the glass slide (Figure 2.8). The average thickness of the nanoparticle deposit over the glass slide was 1-1.5 µm.

2.3 Methods used for spectroscopic characterization of samples

2.3.1 Fluorescence spectroscopy

The set-up developed for the measurement of fluorescence spectra is shown in Figure 2.9. Light from a continuous wave laser is collimated using a biconvex lens and focused into a cuvette placed in a sample holder. Excitation of the sample in the cuvette produces fluorescence which is collected by a mirror-lens combination. The light is optically filtered with a di-electric bandwidth filter and imaged into the entrance aperture of an optical fiber bundle light guide. The light guide guides the light to the slit of a spectrometer. Depending on the wavelength range of interest, 2 types of spectrometers were utilized: (a) a monochromator-CCD assembly (Oriel MS 125- Andor 401 BV) (b) a Fourier Transform Spectrometer (FTS) (Bruker Vertex 80). The data is then transferred to a computer for processing and analysis. The beam transmitted through

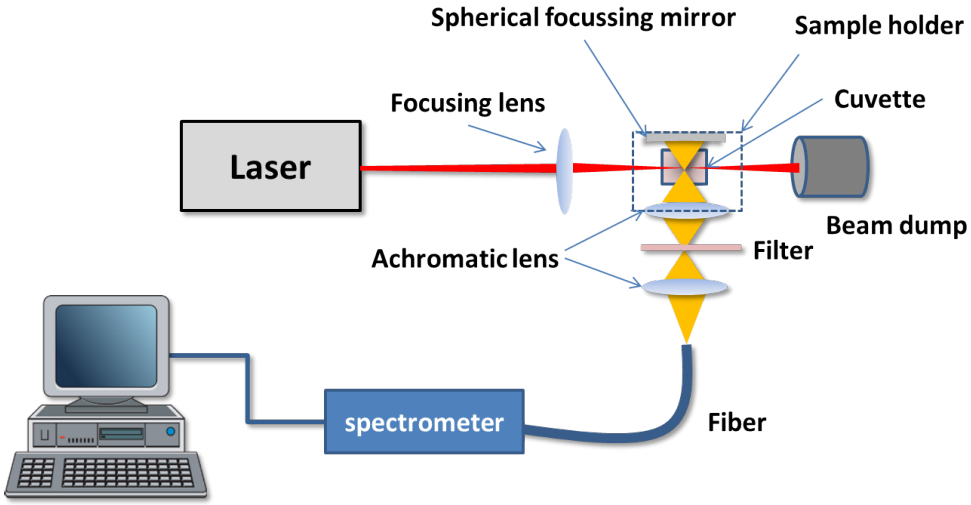

Figure 2.9: Schematic of the experimental set-up for fluorescence detection. Laser sample holder, imaging optics, filter and spectrometer were varied depending on the application.

the sample was terminated by a beam dump. For coated samples, the cuvette holder was replaced with a thick film holder. Details of the components used will be discussed in the following sections.

2.3.1.1 Lasers used for fluorescence spectroscopy

Table 2.4 shows different laser sources that were used for the development of fluorescence detection set up[1]. Since the supercontinuum source was modified to suit the purpose, a small description of it is included in this section.

[1]The specified parameters are approximated to the point of excitation on the sample.

Wavelength/ wavelength range (nm)	Source description	Target sample &purpose	Specification (operation mode, wavelength, power, pulse width, rep rate)
450 nm	Diode laser (Multi-mode)	Impurity luminescence excitation of Yb:KGW	TEM_{00}, CW, 450 ± 1 nm, 300 mW Spotsize: ≈1.5 mm
532 nm	Diode laser (Multi-mode)	Impurity luminescence excitation of Yb:KGW	TEM_{00}, CW, 532 ± 1 nm, 197 mW Spotsize: ≈1 mm
632.8 nm	He-Ne laser (Single mode)	Fluorescence excitation of Rhodamine dyes	TEM_{00}, CW, 632.8 nm, 1 mW Spotsize: ≈1 mm
980 nm	Diode laser (Multi-mode)	Fluorescence excitation of YP1 and Yb:KGW bulk and nano samples	TEM_{00}, CW, 980±1 nm, 200 mW Spotsize: ≈1 mm
1023 nm	Diode laser (Multi-mode)	Fluorescence excitation of YP1 and Yb:KGW bulk and nano samples	TEM_{00}, CW, 1024 ± 10 nm, ≥ 20mW Spotsize: ≈1 mm
450-1750 nm	Externally tuned super continuum source (Temporally incoherent)	Wavelength dependence of fluorescence from Rhodamines	Quasi CW, 450-1750 nm ≈5W, ≈ 5 ps pulse duration, rep rate - 50 MHz Spotsize: ≈1.5-2 mm

Table 2.4: List of lasers used in the fluorescence spectroscopy set-up

Supercontinuum source

The super continuum source used in this work is a Fianium femto-power 1060 SC 450. The SC 450 is a high power fibre continuum source generating directional emission from 450 nm to beyond 1750 nm and generating optical pulses with duration of ≈5 ps. The SC450 laser consists of three main components: (i) a master source (passively mode-locked low power fiber laser), (ii) an amplifier (high power cladding pumped fiber) and (iii) a highly nonlinear hollow core photonic crystal fibre. The master source is a passively mode locked fiber laser based on a core-pumped Yb-doped fiber seeded at 1060 nm. The laser operates at a fixed repetition rate, providing transform limited pulses of approximately 4.0

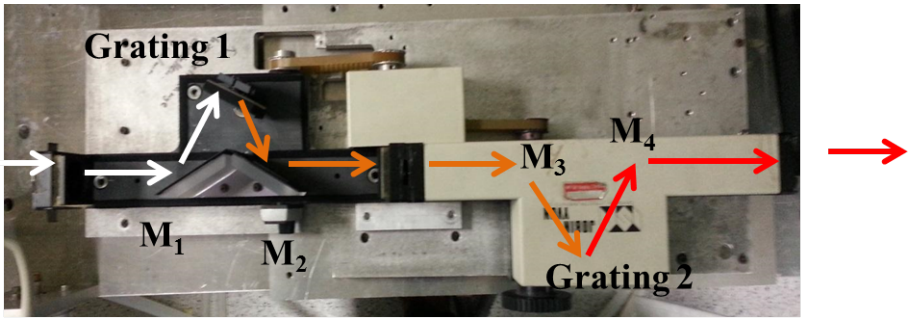

Figure 2.10: Wavelength tuning using Jobin-Vyon monochromator: The beam is guided through a rotatable double-mirror grating combination which selects the desired wavelength range.

ps. The high power fiber amplifier is based on a double-clad Yb-doped fiber, pumped by a high power, multi-emitter laser diode pump module (PUMA 976-20). The supercontinuum generator comprises a length of highly-nonlinear hollow core photonic crystal fiber, with dispersion and length tailored to the high power picosecond pump laser. Due to the high pulse peak powers and high nonlinearity within the fiber, the pulses experience large spectral broadening within the nonlinear fiber, covering the spectrum from 450 nm to 1750 nm.

Wavelength tuning of supercontinuum

A grating double monochromator (Jobin-Vyon) was used to select a specific wavelength range of ≈4 nm tunable between ≈400 and 750 nm (Figure 2.10). The monochromator was fixed on an aluminium base plate in front of the supercontinuum source. Simultaneous rotation of the two gratings by a rubber belt ensured that both gratings were tuned simultaneously. The super continuum and an example of a spectrally selected wavelength range are shown in Figure 2.11.

2.3.1.2 Optics

Achromatic lenses for collection

Achromatic doublets (Thorlabs, AC254-080-A (visible), AC254-100-C (Infrared)) were used for collection and imaging of the fluorescence. Depending on the wavelength range of interest different achromatic lenses were utilized; for the near IR AC 254-100C and for the visible AC 254-080-A was used.

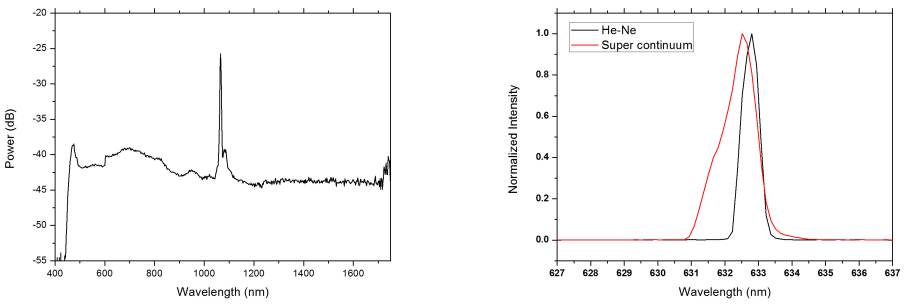

(a) (b)

Figure 2.11: (a) Supercontinuum spectrum produced by the source (taken from manufacturer's manual of SC 450) (b) Wavelength region selected by the double monochromator with center at 632.8 nm. The normalized emission line of a He-Ne laser as recorded by the same spectrometer is shown as a comparison. The resolution of the spectrometer corresponds to the FWHM of the laser line, i.e ≈1 nm.

Filters

A set of filters were used for removing stray (mostly laser light) from the detection beam. Transmission spectra of the filters used are shown in Figure 2.12 and their purposes are given in Table 2.5.

Optical Fibre

(a) In the near-Infrared, a fiber with large core diameter was used for collection (Leoni fiber optics, NA 0.22, 1.5 mm core diameter). (b) In the visible, a circular to rectangular fiber bundle was used (Newport fused silica bundle, 11 mm ferrule, 0.8×9.7 mm slit, NA 0.22). Transmission specifications of both fibers are shown in appendix A. The light from the excitation zone of the sample was imaged onto the entrance aperture of the fiber using achromatic lenses held inside a lens tube (see Figure 2.13). The lens tube was used to further reduce ambient stray light.

Sample holder

The sample holder is a modified cage cube from Thorlabs (Figure 2.13). The cage cube has 1" threads on all faces which is used to connect to lens tubes or adapters to hold lenses/mirrors and filters.
Samples in the form solutions or suspensions were carried in cuvettes for measurements. For solutions and suspensions square quartz cuvettes (UV- Quartz, 10 mm ×10 mm×40 mm) were used for fluorescence meas-

Filter name	Type	Application
FEL 1000 (Thorlabs)	Long pass filter, cut off wavelength 1000 nm	Fluorescence excitation using super continuum source for fluorescence detection of Yb:KGW/YP1 nanoparticles
FESH 1000 (Thorlabs)	Short pass filter, cut on wavelength 1000 nm	Stray light elimination for fluorescence detection of Yb:KGW/YP1 nanoparticles at λ_{exc}≈1023 nm
NF 980-41 (Thorlabs)	Notch filter, center wavelength 980 nm, FWHM ≈41 nm	Stray light elimination for fluorescence detection of Yb:KGW/YP1 nanoparticles at λ_{exc}≈980 nm
OD 6 Rugate 632.8 nm Notch filter (Semrock)	Notch filter, center wavelength 632.8 nm, FWHM ≈15 nm	Stray light elimination for fluorescence detection of rhodmine at λ_{exc}≈632.8 nm
LP02-488-RU-25 (Semrock)	Long pass filter, cut off wavelength 488 nm	Stray light elimination for luminescence detection from impurities in Yb:KGW nanoparticles
NF 533-17 (Semrock)	Notch filter, center wavelength 533 nm, FWHM ≈17 nm	Stray light elimination for fluorescence detection of Rhodamine at λ_{exc}≈533 nm and stray light elimination for luminescence detection from impurities in Yb:KGW nanoparticles

Table 2.5: List of filters used and their purpose in the study. Also see Fig. 2.12

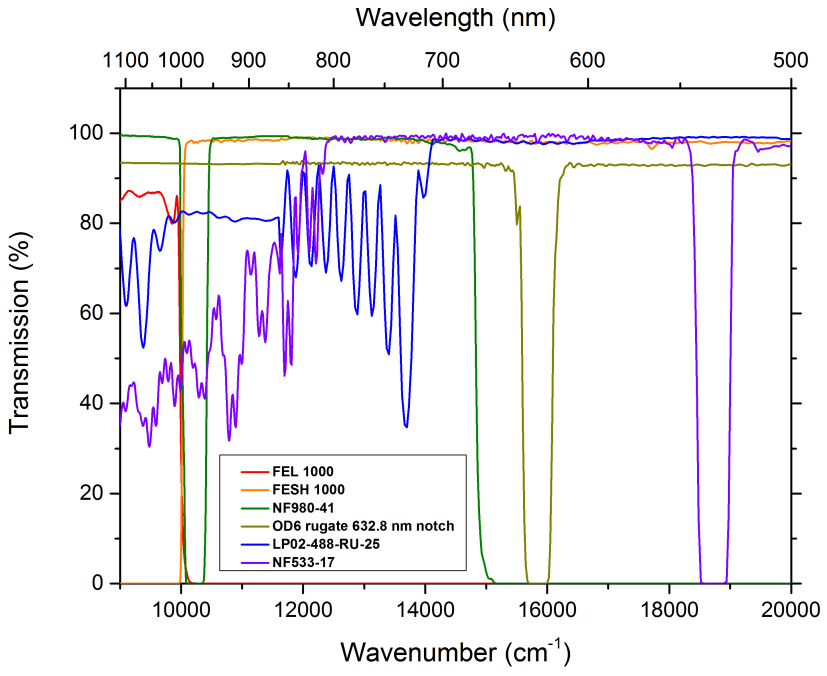

Figure 2.12: Transmission curves of the filters used plotted as against energy.

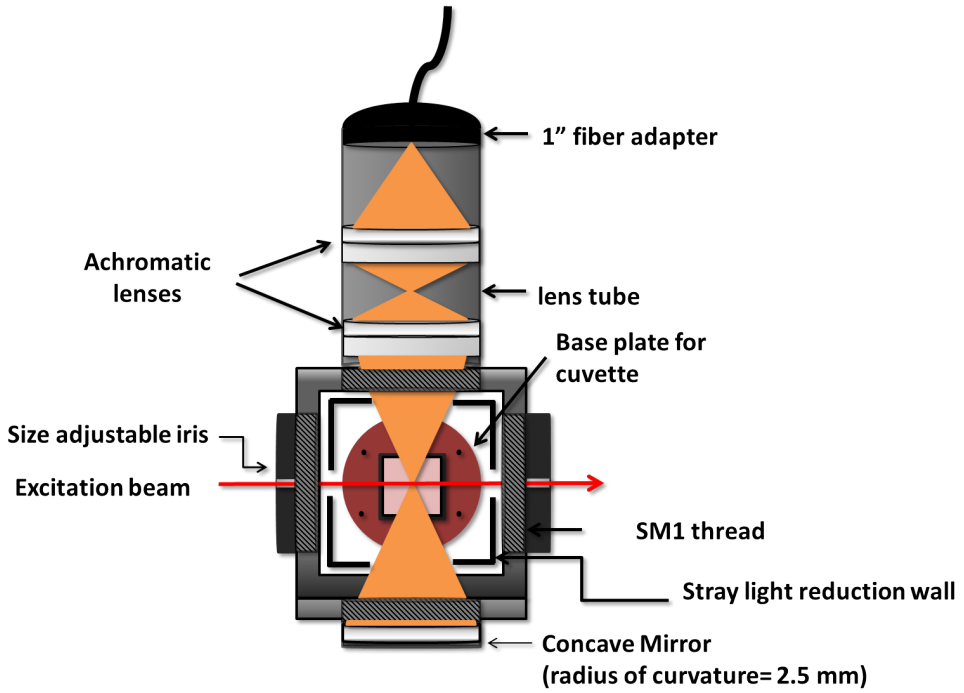

Figure 2.13: Top view of the sample holder used in the fluorescence detection set-up (See also Figure 2.9).

urements. The excitation beam entered parallel to one of the faces of the cuvette and the fluorescence was collected at right angles to the excitation beam (Figure 2.13). For solutions/suspensions with high concentration of fluorophore, the excitation beam does not penetrate deeply into the cuvette. Thus the fluorescence is confined to the volume close to the window. This results in smaller fluorescence collection efficiencies at 90°. Hence for high concentration samples the beam penetrated the cuvette off-center and the beam is maintained as close as possible to the walls of the cuvette to assure minimum re-absorption.

Rectangular cuvettes (45 mm × 12.5 mm × 12.5 mm) were used for holding the samples. The material of the cuvette was quartz which has minimal absorption in the visible region.

For temperature dependent measurements the sample in cuvette was placed in a cryostat (CCSR/202 cold head model from Janis). The sample is kept in vacuum on a metallic sample holder plated with gold. A temperature sensor (DT-670B-CU silicon diode) records the temperature. A copper head heater is used to regulate the temperature using a temperature controller (Lakeshore model 335).

2.3.1.3 Spectrometer

Spectrometer in visible wavelength range

A monochromator (Oriel MS125) in conjunction with CCD detector (Andor 401 BV) was used to record fluorescence spectra in the visible. The CCD is connected to a computer and is controlled with the manufacturer's software (Andor solis). The CCD has 1024×127 active pixels. The pixel size is 26 × 26 μm. It was cooled with a Peltier cooler to ≈-25 ° C to minimize dark noise. The CCD was used in a "full-vertical binnning mode" to collect the data. In that mode the charge from each column of pixels is combined on the chip, to give a single value per column.
The monochromator consists of two mirrors and a grating with entrance and exit slits arranged in crossed Czerny-Turner configuration. The output slit of the monochromator is replaced by the CCD chip. Each pixel covers a spectral range of approximately 0.16-0.18 nm depending on the wavelength region (see "calibration"). The wavelength range that can be covered by the detector-wavelength combination is ≈ 160-180 nm for one position of the grating. By tuning the grating the entire visible (≈ 400-800 nm) can be accessed.
The minimum integration time was 100 ms. For the dye samples, typical integration times of 1-3 seconds were used.
For measurements used in this thesis: typical exposure time per scan was 100 ms, with 10-20 averages resulting in total exposure times of 1-2 s per spectrum (will be stated otherwise in the emission spectrum).

Calibration

The spectrometer was calibrated using a Hg-Ar pen ray lamp, a diode laser at 532.8 nm, a He-Ne laser at 632.8 nm and a sodium vapour lamp. The emission spectrum of the lamp at a particular position of the grating was measured and the pixel numbers of peak positions in the spectrum were found using peak finder software in Origin. The known wavelengths of the lines were plotted against the pixel values and fitted with a 2^{nd} order polynomial. Figure 2.14 shows calibration curve of the line position wavelength versus pixel number. Calibration curves were measured for different dial positions of the monochromator. The resolution of the

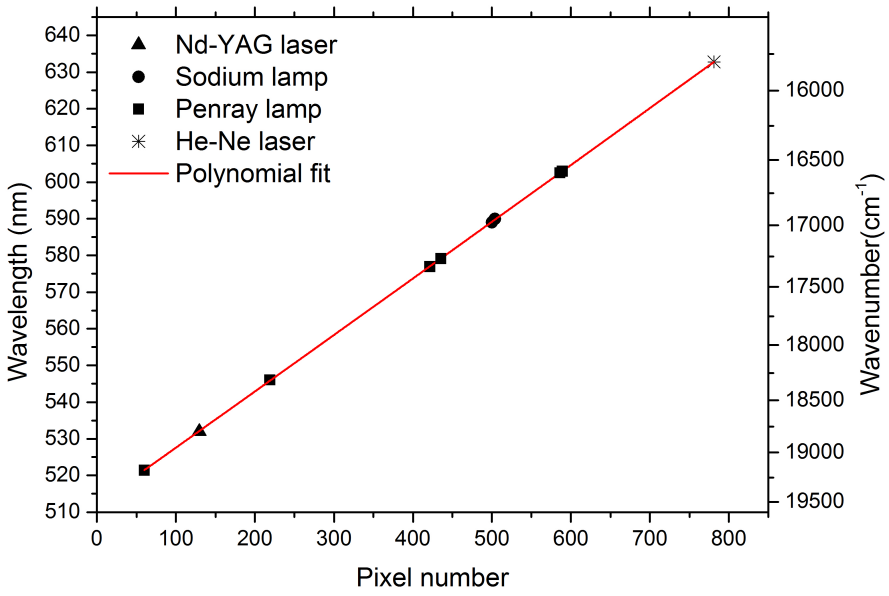

Figure 2.14: Calibration curve for monochromator CCD combination- wavelength versus pixel number. The data points represent the measured line positions of the calibration source used. The red curve is the 2nd order polynomial fit of the data.

monochromator CCD combination was 0.33 nm.

The corresponding fit parameters are given in the following equation (calculated for a centre wavelength adjusted at 590 nm) :

$$\lambda = (512.264 \pm 0.17515) + (0.15288 \pm 0.00094)P - (1.80017 \pm 1.14357) \times 10^{-6} P^2 \quad (2.1)$$

where λ(nm) is the wavelength and P is the pixel number.

Fourier transform near Infra-red spectrometer

A Fourier transform spectrometer (Vertex 80, Bruker optics) was used to record emissions in the near infrared (800-1100 nm). The heart of the spectrometer is a modified Michelson interferometer (Rocksolid TM interferometer, Bruker) with a moving mirror in one arm. The spectrometer is equipped with two detectors: InGaAs diode with a spectral range of 12800-5800 cm^{-1}(780-1724 nm) and a silicon diode with a spectral range of 25000-9000 cm^{-1} (400-1111 nm). The spectrometer uses a modified

CaF_2 beam splitter covering a range 50000 cm^{-1} to 4000 cm^{-1}(200-2500 nm). The highest possible spectral resolution of the spectrometer is 0.08 cm^{-1}. The fluorescence entered the spectrometer through an external fiber coupled port via the fiber (see section 2.3.1). The end of the fiber is placed in front of the external port on an XYZ stage. The fiber exit aperture was imaged onto the entrance aperture of the interferometer by means of two off-axis focussing mirrors. The diameter of this aperture was set at 1.5 mm. The interferogram measured is processed by custom designed software (Bruker Opus) and is Fourier transformed into the frequency domain to obtain the emission spectrum. The data measured is apodized (Norton-Beer apodization) before performing a Fourier transform.

For measurements used in this thesis: for the emissions from Yb:KGW coatings, the spectra recorded were measured for an integration time of 3-4 hours. The emissions from YP1 suspensions were recorded for a scan time of 3-3.5 hr. Typical scan time descriptions will be provided with the emission spectra in the results section. The resolution of each measurement is ≈10 cm^{-1} for an entrance aperture size of 1.5 mm.

2.3.2 Absorption spectroscopy

A commercial double beam absorption spectrometer, Lamda 1050 UV/ Vis/ NIR spectrometer from Perkin-Elmer was used for recording all absorption spectra. Lamda 1050 is a double beam, double monochromator, ratio recording UV/Vis/NIR spectrometer with microcomputer electronics controlled by a computer. The monochromators have a holographic gratings with 1440 lines/mm blazed at 240 nm in the UV-Vis and 360 lines/mm mounted at 1100 nm in the NIR. The main light beam is split into a sample beam and a reference beam using beam splitting optics, a chopper (46+ Hz) is used for that purpose. The two source lamps include a pre-aligned tungsten-halogen and a deuterium lamp.The instrument can scan between 175-3300 nm and has a resolution of $\leq$0.05 nm in the UV-Vis and $\leq$0.20 in the NIR. The measurements taken can be assumed accurate to within $\pm$0.080 nm in UV -Vis and $\pm$0.300 nm in the NIR. The double beam spectrometer comprises a sample beam and

a reference beam. The extinction "A" of the samples was obtained from the transmission curve of the sample using the relation:

$$A = ln\frac{I}{I_0} \tag{2.2}$$

where I is the sample transmission and I_0 is the reference transmission. For all the solutions/suspensions prepared, the solvent was used as the reference. For thick films, uncoated glass slides were used as the reference.

Chapter 3

Photophysics of Rhodamine doped materials

In this section, fluorescence from Rhodamines is analyzed by excitation in the lower energy part of the absorption spectrum. The schematic of the set-up used for the fluorescence studies is as in Figure 2.9. The fluorescence collected at right angles to the cuvette is recorded using the spectrometer with detection range in the visible part of the electromagnetic spectrum (see figure 2.9). The variation in the fluorescence spectrum of Rhodamine 101 in ethanol solution with changing concentration and temperature is analysed.

3.1 Rhodamine dye solutions

3.1.1 Absorption spectrum of Rhodamine 101 in solutions

The $S_0 \rightarrow S_1$ absorption and the corresponding prompt fluorescence ($S_1 \rightarrow S_0$) of Rhodamine dyes in solution at room temperature exhibit largely unstructured spectra in the visible. The absorption spectrum of Rh 101 is shown in Figure 3.1 together with spectra of Rhodamine B and Rhodamine 6G for comparison. The position of the band depends on the end alkyl groups of the xanthene chromophore (Figure 1.1) as explained in section 1.2. The $S_0 \rightarrow S_1$absorption band of Rhodamine 101 solution in

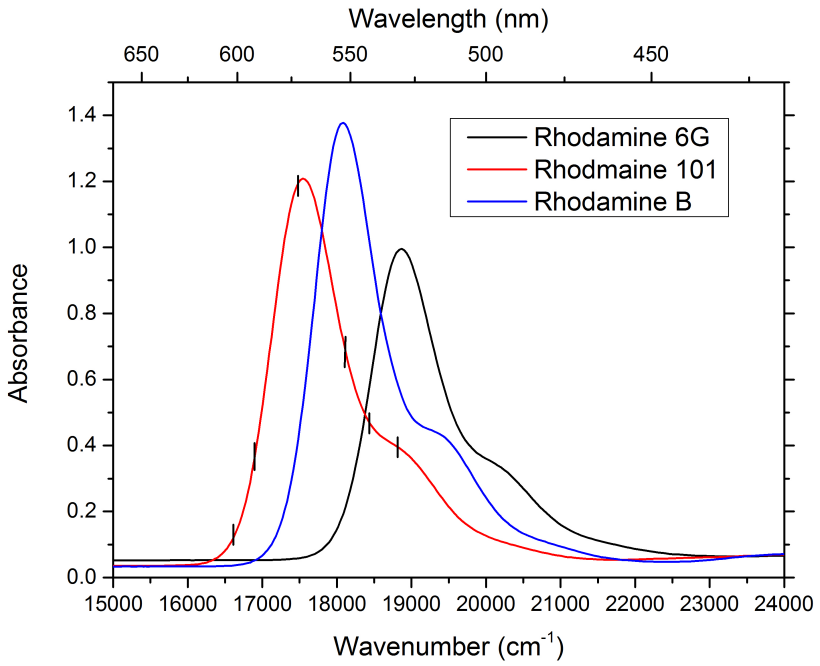

Figure 3.1: Extinction spectrum of (i) 1.16 $\times 10^{-5}$ M Rh 101 (ii) 1.29×10^{-5} M Rh B and (iii) 9.4 $\times 10^{-5}$ M Rh 6G solutions. The solvent used is ethanol. The black vertical lines in the red Rh 101 extinction curve denote the excitation wavelengths till 602 nm mentioned in Figure 3.3. Only the results on Rh 101 is mentioned further in this thesis since it provided the maximum anti-Stokes efficiency at 633 nm excitation.

ethanol has an absorption maximum at 17391 cm^{-1} (λ_{max}= 575 nm). The vibronic contour structure extends over ca. 4000 cm^{-1} with shoulders at 18800 cm^{-1} and 20300 cm^{-1}[19], [22]. The absorption maximum at 17391 cm^{-1} corresponds to the 0→0 vibronic band[1], and the shoulders at 18800 cm^{-1} and 20300 cm^{-1}correspond to 0→1 and 0→2 vibronic bands respectively [19], [22].

The absorption spectrum of Rhodamines shift with the polarity of the solvent used (Figure 3.2). Rhodamines react to pH variations in an interesting manner. As explained in section 1.2, it is the re-orientation of the π-elecron cloud that determines the excited energy levels of the Rhodamine 101 chromophore [103]. The carboxyl group present in Rhodamine 101 (Figure 1.1) is completely protonated in acidic solution, but dissociates in alkaline solution. The negative charge has an inductive effect (an experimentally observable effect of the transmission of charge through a chain of atoms in a molecule, resulting in a permanent dipole

[1]The vibrational states in S_0 and S_1 are numbered 0, 1, 2, 3.. See Figure 1.2.

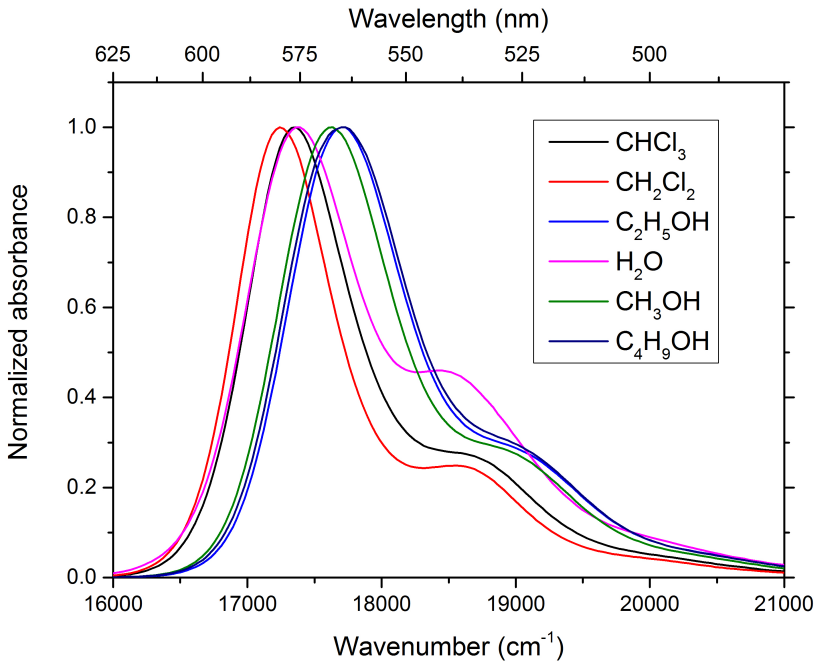

Figure 3.2: Variation of peak absorption with polarity for Rhodamine 101 in various solvents

in a bond) on the central carbon atom of the Rhodamine 101 chromophore. The maxima of the main absorption band and of the fluorescence are shifted to shorter wavelengths, and the extinction coefficient at the absorption maximum is slightly reduced. The wavelength shift amounts to about 10 nm in polar organic solvents (methanol, ethanol, etc.). The corresponding change is also observed in the fluorescence spectra.

3.1.2 Emission spectrum of Rhodamine 101 in ethanol

The emission spectrum resembles a mirror image of the absorption spectrum indicating that the spacing of the vibrational energy levels of the excited state is similar to that of the ground state. This also indicates that the nuclear geometry of ground and excited state species are similar. The Stokes shift is small, and the fluorescence band overlaps with the absorption band.

Stokes fluorescence

The emission spectrum of 4.5×10^{-5} M Rhodamine 101 at different ex-

citation energies is shown in Figure 3.3. The excitation wavelength was tuned between 532 nm to 632 nm (see section 2.3.1.1). As the excitation energy is gradually decreased from 18796 cm^{-1}(532 nm), the emission intensity increases till the excitation energy reaches 18115 cm^{-1} (552 nm). After that the fluorescence intensity is found to drop till the recorded emission intensity becomes zero at 15337 cm^{-1} (652 nm)[1].

This behaviour of emission intensity with change in excitation wavelength is the reflection of the change in extinction (absorption) of the dye (refer figure 3.1). As the excitation energy is gradually decreased from 18796 cm^{-1}(532 nm) to 18115 cm^{-1} (552 nm), the 0→1 vibronic absorption band is scanned. The excitation wavelength crosses the band maxima and as the excitation energy crosses 18115 cm^{-1}, the extinction coefficients drop and the emission intensities decrease, since the absorption drops. The shape of the emission spectrum is the same at all excitation wavelengths in accordance with the Vavilow's law as stated in section 1.2. The emission intensities in the higher energy part (or the net anti-Stokes intensity) increases as the excitation energy is tuned beyond the absorption maximum at 17391 cm^{-1}(575 nm).

The excitation energies are marked with vertical lines in the extinction spectrum of Rhodamine 101 dye (Figure 3.1). The increase in emission intensity happens when the excitation energy crosses the 0→0 vibronic absorption (band maximum at 18800 cm^{-1}) band of the $S_0 \rightarrow S_1$ electronic transition. As the excitation energy crosses 17482 cm^{-1} (572 nm) the extinction coefficients drop and the emission intensities decrease.

The shape of the emission spectrum is the same at all excitation wavelengths holding the Vavilow's law as stated in section 1.2. Even when the excitation energy is lowered to the red edge of the absorption spectrum (above 15822 cm^{-1}) an intense emission was recorded which indicated the high quantum efficiency of the solution despite the low absorption cross-sections. The number of emissions in the higher energy part (or the net anti-Stokes fluorescence) increases as the excitation energy is tuned further the absorption maximum at 17391 cm^{-1}(575 nm).

Figure 3.4 shows integrated intensities of the emission curves (absolute area under the emission curve) against their corresponding excitation en-

[1]The emission spectrum at 632 nm is not shown because of low signal to noise ratio. The integration time for recording the spectra are the same.

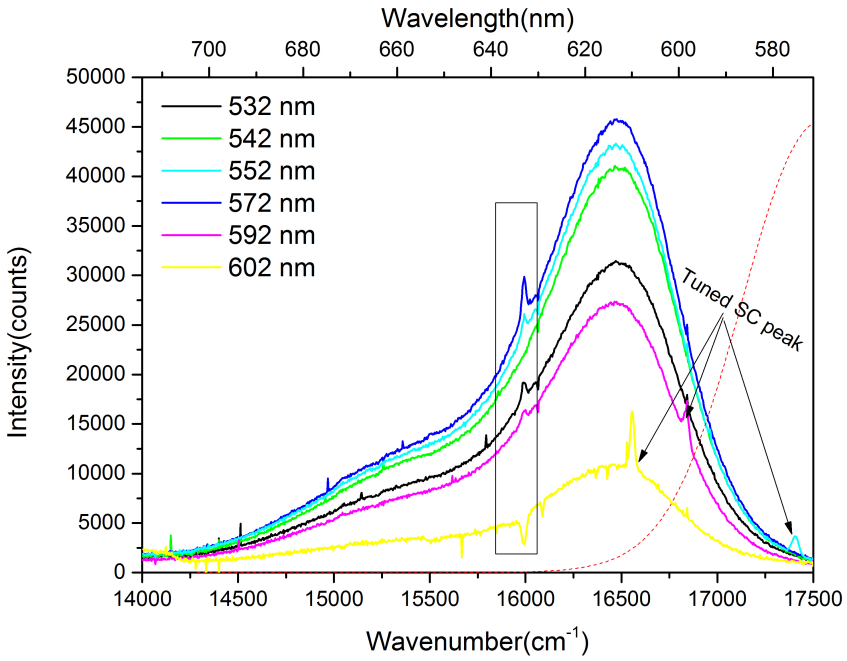

Figure 3.3: Emission spectrum of 5×10^{-4}M Rhodamine 101 in ethanol at different excitation wavelengths using a supercontinuum source. The features repeated in each spectra (shown in the rectangle) is the noise (mercury lines from the ceiling lights) at high integration times. Each spectrum was obtained with an integration time of 400 s. The arrows show localized intensity peaks due to elastic scattering from the excitation source, which were not suppressed with an optical filter. The red dotted curve is the absorption from Rh 101 normalized to the maximum fluorescence. (Refer Figure 3.1 for position of excitation energies which are marked as vertical lines in the dye absorption spectrum).

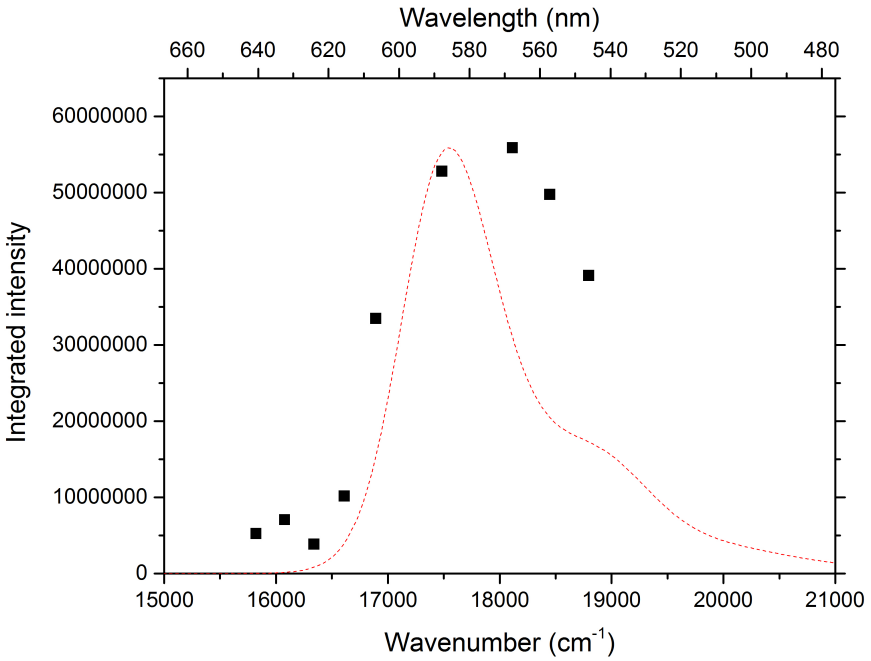

Figure 3.4: Area of entire fluorescence emission from 5×10^{-4}M Rh 101 in ethanol at different excitation wavelengths plotted against corresponding excitation wavelengths. The red dotted curve is the normalized absorption spectrum.

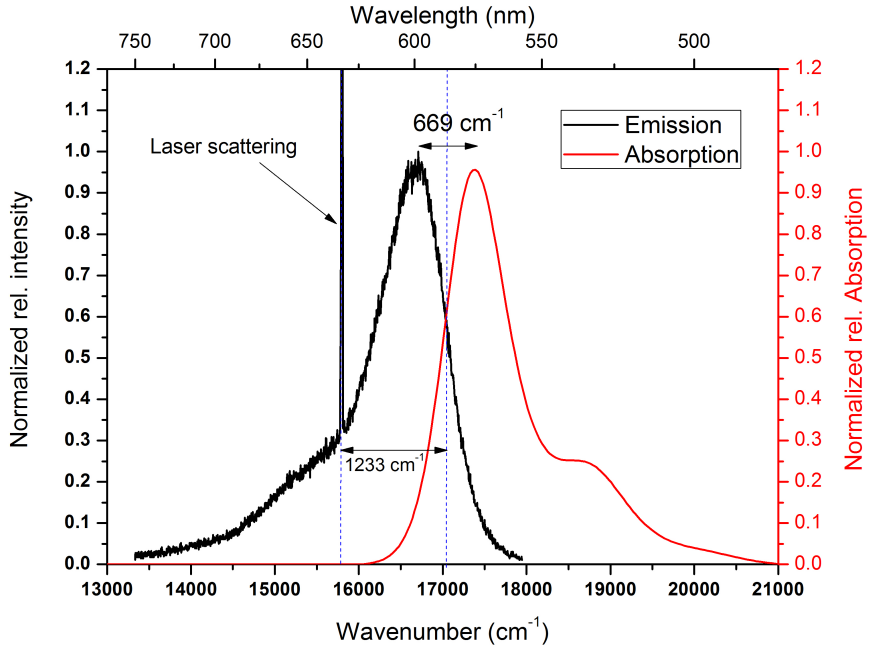

Figure 3.5: Absorption spectrum compared to emission spectrum at λ_{exc}= 632.8 nm for 10^{-4} M Rhodamine 101 ethanol solution.

ergies. It is observed that the emission intensities follow the trend in the absorption curve, which indicates that the quantum yield is wavelength independent. This can be best considered as an example for Kasha-Vavilow law.

Anti-Stokes fluorescence: Fluorescence spectrum of Rhodamine 101 in ethanol at 632.8 nm

The emission spectrum of 10^{-4} M Rhodamine 101 in ethanol when excited at 632.8 nm using a He-Ne laser is shown in Figure 3.5. The anti-Stokes luminescence is observed as a yellow fluorescence when excited with red light from the He-Ne laser. An estimate of the true isolated molecular 0→0 vibronic band origin (of the $S_0 \rightarrow S_1$ electronic transition) is often taken as the energy of the overlap point of the normalized absorption and emission spectra [19], [77]. 0→0 vibronic band thus obtained is 17035 cm^{-1}(587 nm) from Figure 3.5. Excitation at this wavelength (632.8 nm) occurs to the low-energy tail of Rhodamine 101 absorption spectrum and is 1233 cm^{-1} lower in energy than the 0→0 band origin at 587 nm and even 864 cm^{-1} lower than the emission maximum at 16686 cm^{-1}(599.3 nm). The average emission wavelength (calculated from the average emission intensity) was found to be approximately 628 nm[1].

3.1.2.1 Effect of concentration on Rh 101 fluorescence

Many dyes self-associate forming dimers or polymers in solutions owing to strong intermolecular interactions like van-der Waals forces [22]. This phenomenon is called "aggregation", and can affect the photo-physical properties of dyes [104]–[107]. In most of the dyes (including Rhodamines), a monomer-dimer equilibrium exists in the concentration range 10^{-2}-10^{-3} [107]. At higher concentrations the dimer concentration increases. The dimer has different absorption compared to the monomer, and hence the absorption spectrum of Rhodamine 101 solution will change its shape at higher concentrations [104]. Corresponding changes will also be reflected in the emission spectrum.

The effect of dye aggregation in the fluorescence emission properties of

[1]The scattering of the laser was avoided while calculating the weighted center of the band emission wavelength (The area made by a Gaussian fit made for the laser peak was subtracted from the whole area of the emission spectrum).

Rhodamine 101 solution (in ethanol) occurs when the solution concentration exceeds 5×10^{-3} M, when the dye aggregation starts [22], [108].The fluorescence spectra of Rhodamine 101 for concentrations in 10^{-3} M and below are shown in Figure 3.6. These spectra with varying concentration were recorded using the set-up in Figure 2.9. The emission spectrum of Rhodamine 101 in ethanol shifts to longer wavelengths with the increase in concentration (Figure 3.6) from 10^{-6} to 10^{-3}. This shift of the spectrum to longer wavelengths with increasing concentration is limited to the emission spectrum and no shift was recorded in the absorption spectrum. Since the concentration is below 5×10^{-3} M, this is not the effect of dye aggregation.

The shift in the emission spectrum can be explained as follows: As mentioned before, the Stokes shift between absorption and emission for Rhodamine 101 ($\simeq 669$ cm^{-1}) is small , which results in a major overlap between the emission and absorption spectrum. It is this overlap that is indirectly resulting in the concentration dependent red shift of the emission spectra. This concentration dependent red shift is also referred to as "inner filter effect" [77], [109]. This effect is due to the absorption of some of the incident light before it reaches the point in the sample from which luminescence is observed (known as primary inner filter effect) and re absorption of some of the emitted light before it leaves the cell and reaches the detector (known as secondary inner filter effect). The light absorbed by the molecules will be re-emitted, which will be red-shifted. The amount of red-shifted photons increases as the number of molecules (concentration) increases. The detector records the integrated intensity, and hence the spectrum will be red-shifted with increasing concentration. The shift of the emission spectrum with concentration (even at lower concentrations) puts a limitation on the maximum concentration that can be used for obtaining maximum anti-Stokes intensity. The ratio of anti-Stokes to Stokes intensity decreases as the concentration is increased. In the Figure 3.7 AS denotes integrated anti-Stokes intensity and S denotes integrated Stokes intensity. AS/S denotes the ratio of anti-Stokes to Stokes intensity. The variation in fluorescence maxima is listed in Table 3.1. When excited in the red the quantum efficiency of solution of Rhodamine 101 is independent of excitation wavelength but for concentrations greater than 10^{-3} M, the increase in dye aggregation will induce red shifts

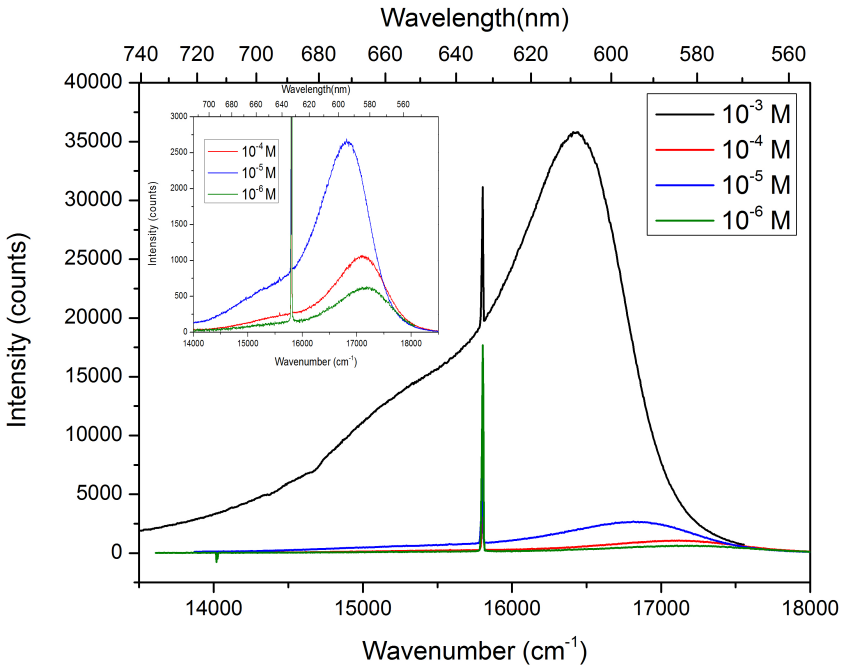

Figure 3.6: Variation of anti-stokes luminescence in Rhodamine 101 in ethanol from 1×10^{-6}M to 1×10^{-3}M. Plots at lower concentrations are zoomed in the inset. Integration time is 45 seconds.

Concentration [mol/l]	Fluorescence maxima
10^{-2}	15912 cm^{-1} (628.45 nm)
10^{-3}	16372 cm^{-1} (610.78 nm)
10^{-4}	16557 cm^{-1} (603.96 nm)
10^{-5}	16757 cm^{-1} (596.73 nm)
10^{-6}	16936 cm^{-1} (590.43 nm)

Table 3.1: Fluorescence maxima as a function of concentration.

in the emission spectrum. This results in quantum efficiency falling far from unity. Clark *et al.*[22] had modelled the change in emission intensity with increasing concentration of Rhodamine 101 concentration, and suggested the choice of an optimum concentration for fluorescence measurements. At concentrations greater than 10^{-3} M, the quantum efficiency of the solution has really decreased from unity or the extent of inner filter effect has become so large that the spectral distortions can no more be corrected.

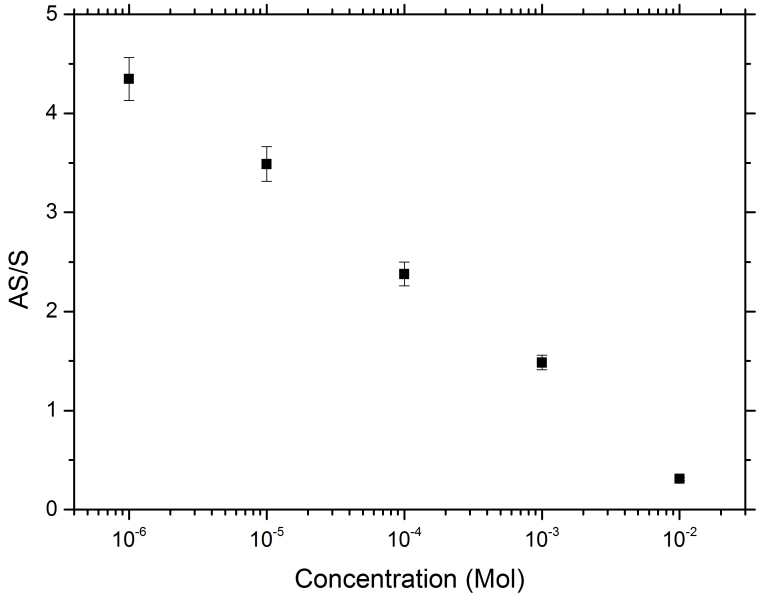

Figure 3.7: Ratio of Anti-Stokes to Stokes with increasing concentration at λ_{exc}=632.8 nm. S denotes the integrated Stokes intensity and AS denotes integrated anti-Stokes intensity.

3.1.2.2 Temperature dependence of anti-Stokes fluorescence

The absorbed quanta at 632.8 nm (15802 cm^{-1}) is far less than the energy difference of the 0-0 transition[1] in Rhodamine 101. Since the 0-0 vibronic band origin in S_0 is found to be 17035 cm^{-1}, the levels of S_0 involved in absorbing the light from the laser have to be $\geq$1233 cm^{-1} above the S_0 vibrational ground state for the excitation at 632.8 nm. Since there is a measurable fluorescence observed, there is enough population among these "hot bands". The weak but small absorption is due to small but finite population of energy states which is about $\approx$1200-1300 cm^{-1} above the lowest vibrational level of the electronic ground state (there will also be contribution from inhomogeneous broadening [28], [110]). An estimate of the energy difference between the lowest and the highest occupied vibrational level of the S_0 can be estimated from the Arrhenius plot of the fluorescence with varying temperature [19].

As the temperature is decreased, the population of these higher excited

[1] 0-0 transition: 0 vibrational state in S_0 to 0 vibrational state in S_1

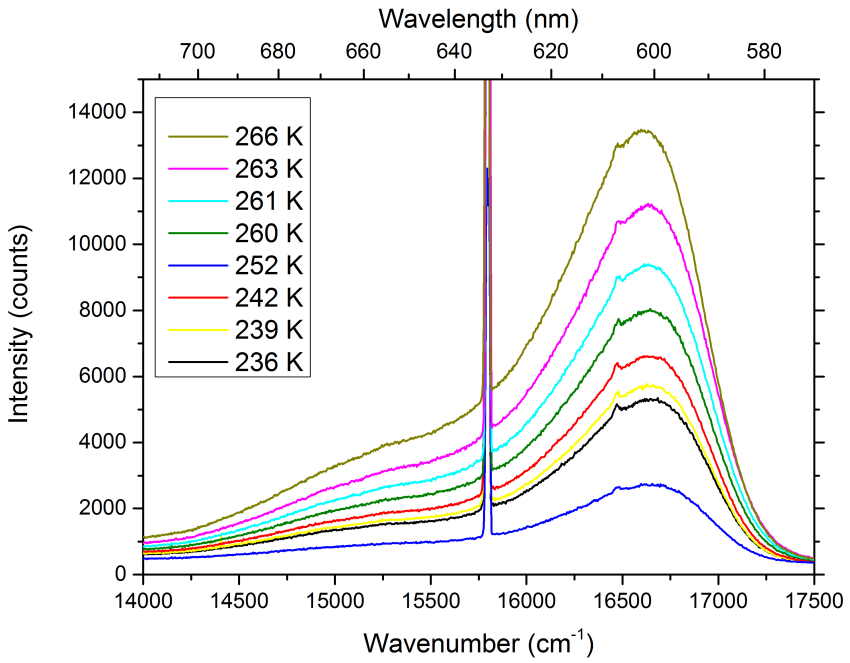

Figure 3.8: Emission spectra of 10^{-3}M Rhodamine 101 in ethanol (λ_{exc}=632.8 nm) between temperatures 236 K and 266 K.

vibrational states decreases, and consequently the emission intensities will decrease. The temperature of a 10^{-3} M of Rh 101 in ethanol enclosed in a cuvette inside a cryostat was decreased gradually and the emission spectra were recorded upon excitation at λ_{exc}= 632.8 nm. The temperature was dropped till 236 K which is higher than the freezing point of ethanol at 159.2 K. The temperature dependent spectra are shown in Figure 3.8.

The emission intensity was found to decrease with temperature. The average wavelength of the anti-Stokes emission dropped from 628 nm at 294 K to 626.56 at 236.8 K. The temperature dependence of fluorescence intensity at 610 nm plotted against inverse of temperature can be described according to the Boltzmann distribution as

$$\mathrm{I} = \mathrm{A}\exp^{\left(-\frac{\triangle \mathrm{E}}{\mathrm{K_b T}}\right)} \tag{3.1}$$

$$\ln \mathrm{I} = \ln \mathrm{A} - (\frac{\triangle \mathrm{E}}{\mathrm{K_b}})\frac{1}{\mathrm{T}} \tag{3.2}$$

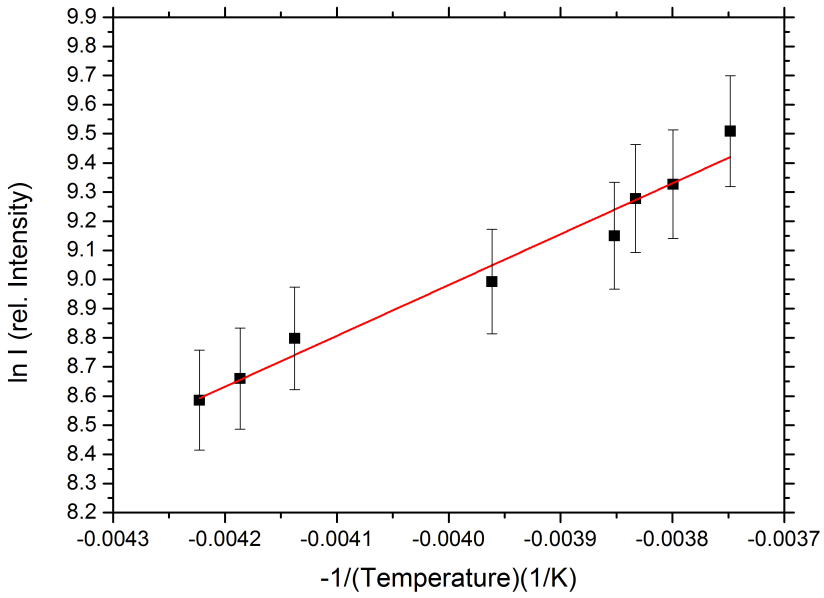

Figure 3.9: Fluorescence intensities at 610 nm plotted against inverse of temperature along with the straight line fit.

Where ΔE is the energy difference corresponding to the finite population and the lowest vibrational level, T is the temperature at which the spectra is recorded, and K_b the Boltzmann constant. Equation (3.1.2.2) is the Arrhenius equation and ΔE can be called as the activation energy for obtaining an anti-Stokes emission. The straight line fit (Figure 3.9) provided for plotting $(-\frac{1}{T})$ versus logarithm of intensity at 610 nm was obtained as $\ln I = (15.95 \pm 0.48) - (1744.491 \pm 122.14)\frac{1}{T}$. This gives $(\Delta E/k_b)$ a value of $\approx$ 1744.491 and thus $\Delta E = 2.402\times10^{-20}$ J which is $\approx$1212 cm^{-1}. An agreement of the value of ΔE from the fit with the expected energy difference of 1233 cm^{-1} proves the existence of hot band absorption involved in the process.

3.2 Hydrothermally prepared silica nano particles attached with Rhodamine

Sol-gel synthesized porous silica is an ideal host matrix to confine photo-luminescent molecules [111]–[113]. Its range of optical transparency is compatible with the emission of Rhodamine dye molecules [23], [114], [115]. Rhodamine doped silica nanoparticle (abbreviated as HTS Rh101, HTS Rh B and HTS Rh 6G) suspensions were prepared in ethanol. A silica nanoparticle should encapsulate thousands or more of Rhodamine 101 molecules in its pores and also take up Rh 101 in its surface. The silica (SiO_2) used is colloidal amorphous silica.
The surface of the silica nanoparticle will be usually covered with Si-OH (Silanol) groups. Si-O-Si (Siloxane) bonds can also be formed by Si-OH groups reacting with adjacent Si-OH groups on the same particle. Si-OH groups that are close to the silica surface can also form hydrogen bonds with each other. The stability of the colloidal suspension depends on the electrostatic repulsion and van-der Waals attraction between the nanoparticles. Hydrogen bonds can also exist between Si-OH groups on the silica surface and the solvent. Colloidal amorphous silica tends to arrange itself into spherical particles when using the synthesis method (by Stöber [116]) as evident from the image of the particles (shown in Figure 2.2). A silica nanoparticle created by modified Stöber process is expected to trap the Rhodamine dye molecules inside the porous silica matrix by covalent bonding. The particles formed as per the Stöber process are expected to be mono-dispersed.

3.2.1 Extinction spectrum of HTS Rh 101

The extinction spectrum (black line) of HTS Rh 101 shown in Figure 3.10 has contributions from: (i) the original absorption of Rh 101 dye (red line) and (ii) the scattering of the HTS particles (blue line). The black line is the measured extinction and is a combination of the original absorption from the Rhodamine 101 molecules and the scattering from

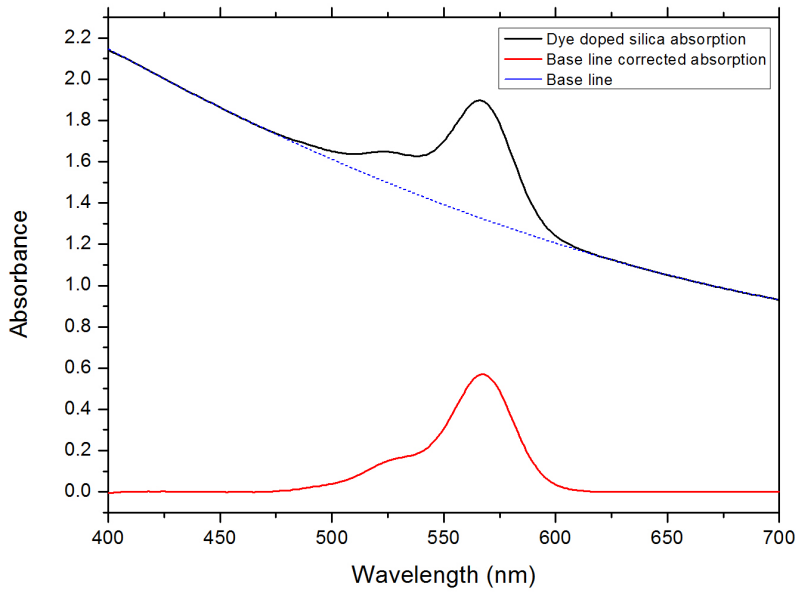

Figure 3.10: Base line corrected absorption curve for HTS Rh101suspended in ethanol

the silica nanoparticles. The scattering contribution to the extinction spectrum can be best described by a third order polynomial as shown in the Figure 3.10. Based on the polynomial behaviour of the scattering the absorption of of Rh 101 can be found.

The extinction spectrum was found to change over time. The suspension of HTS Rh101 was left to sediment over time, and the extinction spectrum was taken at regular intervals (Figure 3.11a). A scattering baseline was created for each spectrum of the sample, and then a ratio was taken between the scattering base lines and the absorption at 552 nm. It was found that the ratio kept decreasing as a function of time. The existence of dye absorption even after the particles were completely settled after ca. 8 hr shows that the interaction between dye molecules and the silica nanoparticles are minimized. The ratio of scattering to dye absorption versus the dye absorption (at 570 nm) is shown in Figure 3.11b. As evident from the figure, the ratio clearly drops, indicating the sedimenting silica nanoparticles, while the dye absorption remains constant, indicating the dye molecules dissolved in the solvent. The molecules present in the solvent should be those which got detatched from the silica nanoparticle surface.

The forces of attraction between the dye molecules and the silica nano particles were not strong enough to prevent the dye getting dissolved into the solution. Hence these particles could not be considered to be a good sample to work with for achieving reliable fluorescence data, since over time there will be a difference in the average number of fluorophores producing luminescence. Such a system can't be considered stable (or isotropic). Also, the concentration values obtained from the extinction spectra would not be a good measure of the concentration.

3.2.2 Emission spectrum of HTS Rh 101

The emission spectrum of HTS Rh 101 suspended in ethanol (at $\lambda_{exc} =$ 632.8 nm) compared to its extinction is shown in Figure 3.12. The difference between the excitation energy and the ground of the electronic state is increased to 1449 cm^{-1}, indicating a red shift in the emission spectrum compared to the same for Rh 101 in ethanol (Figure 3.5). The concentration that can be obtained from the extinction spectrum indicated a concentration of 2×10^{-4} M. The red shift of the emission spectrum can be attributed to the increase in concentration. It has to be noted here that the extinction is changing over time, due to the detachment of the dye molecules from the silica nanoparticle surface. As from Figure 3.11a the extinction drops from 1.2 to 0.2 within 3 hours. This rate would not be significant over the integration time of the recorded emission spectra (1 sec). Concentration and temperature dependence of these nano particles suspended in organic solvents are similar to dye molecules in solutions. The other three dyes attached to the silica nano particles gave spectrum similar to free molecules in solutions. All the similar spectra are included in Appendix B.

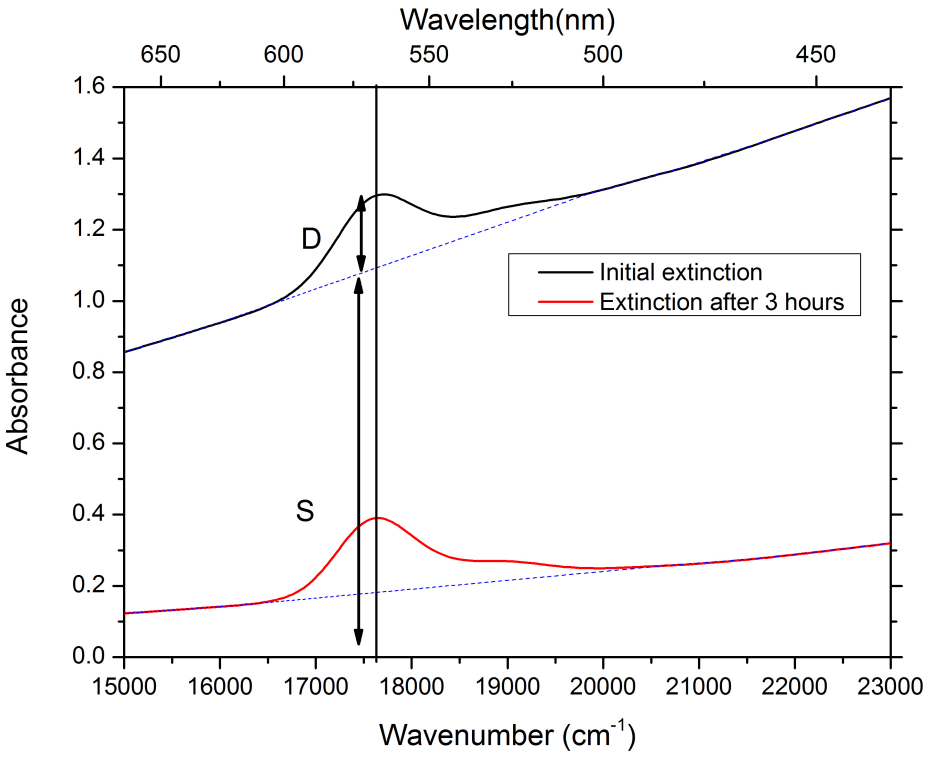

(a) Extinction spectra of HTS Rh 101 suspended in ethanol at different times. The ratio S/D (scattering of the silica/ dye absorption) changes over time as exemplified at 570 nm (vertical dashed line).

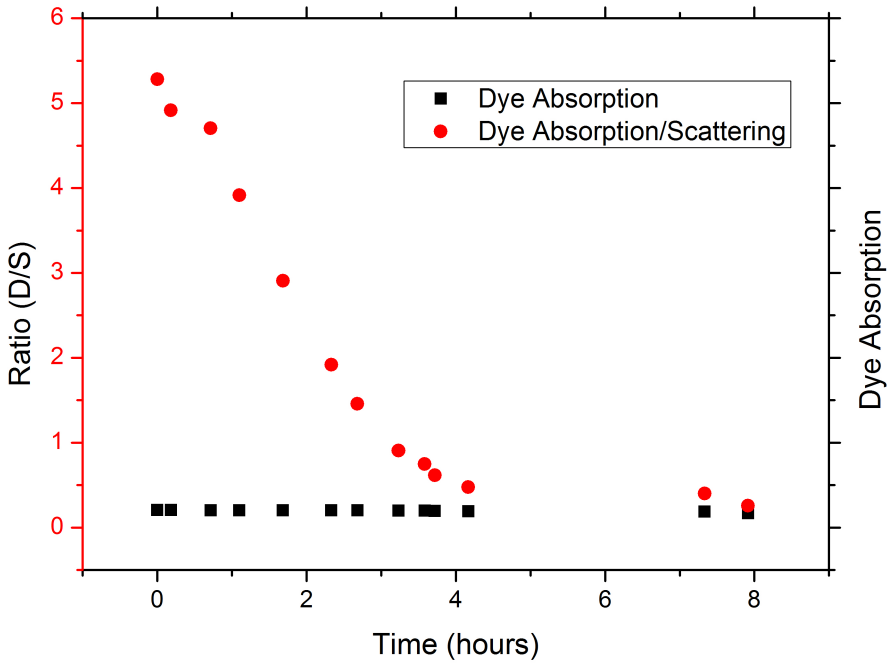

(b) Scattering/dye absorption (S/D) at 570 nm as a function of time.

Figure 3.11

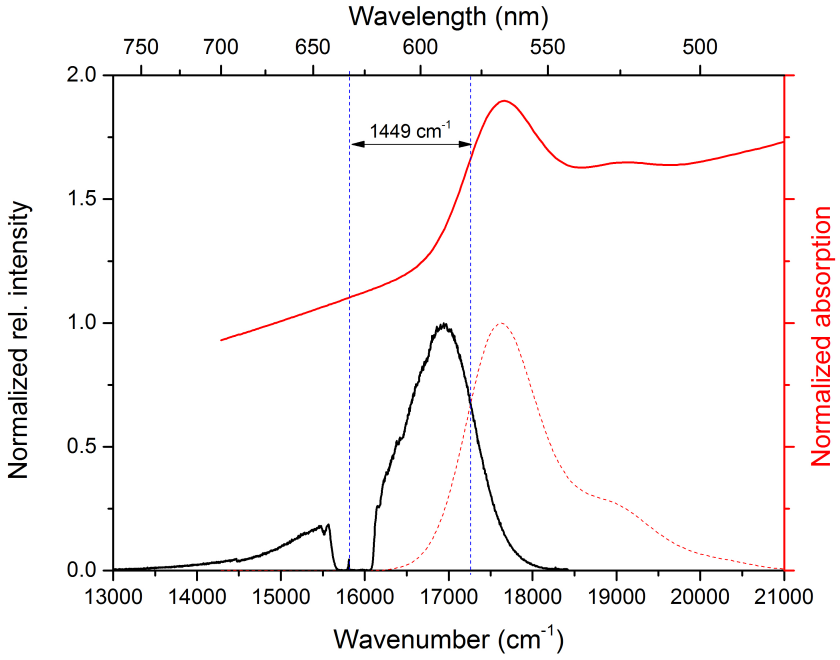

Figure 3.12: Anti-Stokes fluorescence (black line) in comparison to absorption (red line) from HTS-Rh101 suspended in ethanol. The fluorescence curve is normalized to the peak emission intensity. The red dotted curve is the base line corrected, normalized curve obtained from the absorption curve for HTS Rh101. The concentration as obtained from the base line corrected absorption spectrum is 2×10^{-4} M. The 1449 cm^{-1} shown is the energy of separation between the excitation energy and the origin of the vibrational ground state.

Chapter 4

Photophysics of Yb^{3+} doped materials

Transitions between $^2F_{5/2}$ and $^2F_{7/2}$ Stark levels (refer section 1.2) of Yb^{3+} in a glass and crystal environment were recorded and analysed. All fluorescence and absorption measurements were recorded at room temperature. The absorption spectra were recorded using a Perkin-Elmer 1050 UV-Vis spectrometer with a resolution of 10 cm^{-1} (refer section 2.3.2). All the emission spectra were recorded with high resolution ($\approx$1 cm^{-1}) using a Bruker Vertex 80 FTIR spectrometer (refer section 2.3.1).

4.1 Yb^{3+} doped phosphate glass (YP1)

The 16 wt% Yb_2O_3 doped phosphate glass with 1.44×10^{21} ions/cm^3 was purchased from Moltech GmbH. Figure 4.1 shows the most probable transitions of Yb^{3+} in a phosphate glass matrix [117].

Reported absorption and emission bands in bulk Yb^{3+} doped phosphate glasses

As stated in the introduction, Yb^{3+} has a simple $4f^{13}$ electronic structure. It consists of $^2F_{7/2}$ ground state and $F_{5/2}$ excited state separated by $\sim$10,000 cm^{-1}. Both states are connected by moderately strong electric-

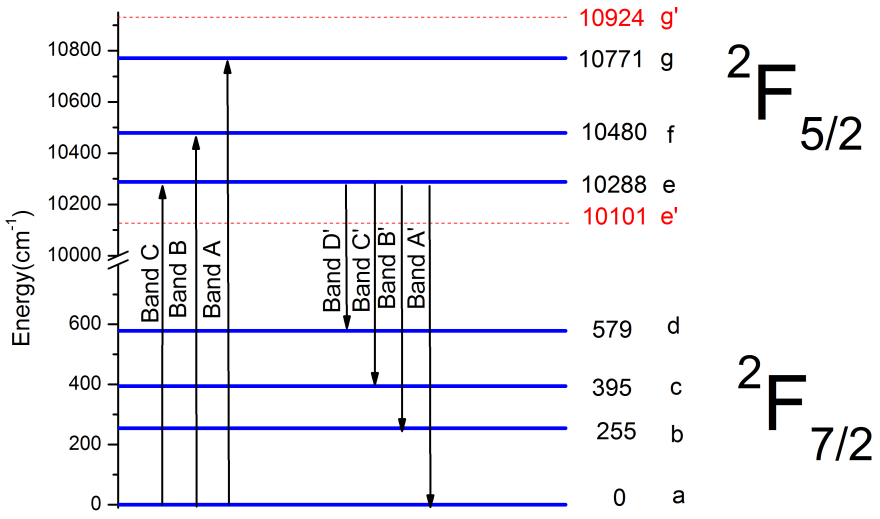

Figure 4.1: Energy level diagram of Yb^{3+} ion in phosphate glasses showing the Stark splitting and the major transitions. (Compare Figure 1.3 for level scheme and nomenclature of levels). The energy values of the Stark levels shown (as blue horizontal lines) are for Yb^{3+} commercially available Kigres Qx/Yb glass used in Dai *et al.* [117]). The black arrows represent the transitions corresponding to the reported band maxima in the absorption and emission spectrum. The red dotted lines show the energy levels corresponding to Yb^{3+} ions occupying slightly different sites from other Yb^{3+} ions.

dipole transitions. In a phosphate glass, Yb^{3+} occupies a site[1] which is usually co-ordinated by PO_4 tetrahedron (see section 1.2). Even though these sites are of low symmetry, it is enough to completely lift the Stark degeneracy except for the Kramers degeneracy [50]. The upper manifold splits into three levels and the lower manifold splits into four levels. The observed widths and asymmetries of the spectral lines of Yb^{3+} in phosphate glass are attributed to systematic site-to-site variations in the crystal field at the rare earth. The (typical) energy level scheme of Yb^{3+} in phosphate glasses from the band maxima mentioned in different publications is shown in Figure 4.1 [50], [87], [117]–[120].

[1] In this thesis, I will refer to certain prominent molecular environments as "sites", even though for glasses and other non-crystalline materials this terminology is not common.

Absorption:

The studies on Ytterbium doped phosphate glasses at low temperatures report five bands in the absorption spectrum [117], [118]. The (reported) principal absorption bands for ytterbium in phosphate glass at low temperature (50 K) are located at 10288 cm^{-1} (972 nm) (here after called "band A"), 10480 cm^{-1}(954 nm) ("band B"), and 10771 cm^{-1}(928 nm) ("band C"). Two another bands, "band E" and "band C" are also reported near 10924 cm^{-1}(915 nm) and 10101 cm^{-1}(990 nm) respectively. The peak energies (wavelengths) of the bands at 10288 cm^{-1} (972 nm), 10480 cm^{-1}(954 nm), and 10771 cm^{-1}(928 nm) correspond to the transitions a→e, a→f and a→g, respectively (see Fig 4.1). Although the spectral positions of the maxima of these bands vary slightly with the doping concentration and the composition of the phosphate glass, the main transitions assigned to these bands are the same in literature [117]-[120]. Depending on the composition of the YP1 glass, the addition of different metal oxides in the glass can add to the asymmetry of the Yb^{3+}environment. This will lead to a situation where a fraction of the Yb^{3+} ions occupy a slightly different site from those Yb^{3+} ions which cause the main absorption bands. The bands at 10924 cm^{-1}(915 nm) and 10101 cm^{-1}(990 nm) are defined as a→e' and a→g' transitions of Yb^{3+} ions at different site respectively. The peak position of the bands shift to shorter wavelengths with increasing temperature, as previously reported in [117].

All bands depend on temperature. The intensity variation with temperature is different for different bands (variations are also found for different glass compositions [118]). The peak intensity of band A increases with increasing temperature while that of B and C are reported to decrease. The maxima of the bands will shift to lower energies with increasing temperature. The maximum of band A shifts to 10271 cm^{-1} (973.6 nm), band B shifts to 10470 cm^{-1}(955.1 nm), and band C shifts to 10761 cm^{-1}(929.2 nm) as temperature increases from 50 K to 240 K [117].

Emission:

The maxima of the principal emission bands (at low temperature) in phosphate glass (50 K) appear at around 10266 cm^{-1} (974.3 nm) (band

A'), 10033 cm^{-1}(996.7 nm) (band B'), 9893 cm^{-1} (1010.8 nm) (band C'), and 9709 cm^{-1} (1030.0 nm) (band D'). These band maxima are assigned to the primary $^2F_{5/2} \rightarrow {}^2F_{7/2}$ transitions e→a, e→b, e→c, and e→d (see fig 4.1). A weak band at about 9474 cm^{-1} (1055.2 nm) and a shoulder at 10112 cm^{-1} (988.80 nm) are also reported [117]. The band at 10112 cm^{-1} (988.80 nm) is resulting from the e→a transition of Yb^{3+} ions at different sites in comparison with those which generates the principal bands [119], [120]. The band at 9474 cm^{-1} is identified as a vibronic band. This band is not attributed to any Stark level transitions of Yb^{3+} till now.
The red lines shown in Figure 4.1 are the energy levels of Yb^{3+} ions at different sites obtained from absorption band maxima E and F. (The energy levels a', b' c' and d' corresponding to Yb^{3+}at different sites are not shown because any band maxima corresponding to transitions involving them are not reported).
It should be noted that most of the bands reported are distinctly visible in the absorption/emission spectrum only when the temperature is low (below 50 K) and the electron-phonon coupling is reduced. At room temperature (300 K), only the bands C and A are distinctly visible in the absorption spectrum. Similarly at room temperature only the bands A' and B' are observed in the emission spectrum.

Line widths for transitions in absorption and emission

The spectral shape of the optical transitions of Yb^{3+} in glasses is determined mostly by the following factors:

1. Magnitude of the Stark splitting of the $^2F_{5/2}$ and $^2F_{7/2}$ energy levels of the free ion, which is determined by the host material.

2. Relevant line broadening mechanisms, such as homogeneous and inhomogeneous broadening.

The overall full width at half maximum (FWHM) width of the emission and absorption lines in the glassy host matrix is due to two effects, homogeneous and inhomogeneous broadening [50]. As described in the introduction, homogeneous broadening originates from dynamic perturbations on energy levels and affects each ion equally. Inhomogeneous broadening originates from the site to site variation produced by a random distribution of local crystal fields. Typical spectral line width of a

lanthanide in a glass is approximately a few hundred wavenumbers. The determination whether the transition line shape is dominated by homogeneous or inhomogeneous broadening is based on whether the majority of lines are originating from the same type of ion centers or from different types. These two broadening mechanisms contribute almost equally to the resultant spectral line width, with an individual contribution of up to several hundred wavenumbers at 300 K. The typical measured homogeneous[1] and inhomogeneous FWHM at 300 K for Yb^{3+} in phosphate glasses were reported to be ≈80 $cm^{-1}$and 66 cm^{-1} respectively [12], [50]. (These values vary in different glass hosts).
The quantum efficiency of fluorescence for Yb^{3+} doped glasses never reach to 100 %, hence the total decay rate k should have contributions from both the radiative and non-radiative decay rates k_{rad} and k_{nrad} (same as for the inverse of the fluorescence life time).

$$k = k_{rad} + k_{nrad} = \frac{1}{\tau_{rad}} + \frac{1}{\tau_{nrad}} = \frac{1}{\tau} \tag{4.1}$$

The fluorescence life time of the $^2F_{5/2}$ state will be influenced by the radiative and non-radiative life times of the levels e, f and g. The reported fluorescence life times for Yb^{3+} in glasses are of the order of 1.2-2 ms [117]. A high uncertainty in life time would indicate that the uncertainty in energy is minimal for these Stark levels (typically of the order of 1-10 GHz). But large inhomogeneous line widths (FWHM) of 88 cm^{-1} have

[1]It has to be noted that the homogeneous widths in phosphate glasses also depend on temperature. Homogeneous widths are linear at low temperature (<40 K) and show a T^2 dependence at higher temperatures. According to fluorescence line narrowing (FLN) studies of the e→a transitions in Yb^{3+} phosphate glasses by Brundage *et al.* [128], the homogeneous line widths were found to vary with temperature. The homogeneous line width varied as $(15 \times T^{1.3})$ MHz for $6.5K < T < 40K$ and $4 \times T^{1.8}$ MHz for $40 < T < 70K$ where T is the temperature. Another work done on Yb^{3+} doped ZBLANP (fluorozirconite) glasses using deconvolution methods by Voigt profiles (described in the next section) show that the temperature dependency for line widths using absorption spectra (a→e) $(12 \times T^{1.9\pm0.1})$ MHz for $10K < T < 300K$ and $(10 \times T^{1.9\pm0.1})$ MHz for $10K < T < 300K$ using emission spectra (e→a) data [49]. The T^2 dependence at higher temperature is attributed to two-phonon processes, as in crystalline host matrices. The inhomogeneous widths are reported to be independent of temperature [49].

been reported for these glasses which is contradictory to the fluorescence life time reported.

The reported homogeneous line widths of the order of 80 cm^{-1} in combination with the life time of 1.2-2 ms for the Yb^{3+} doped glasses has to follow the energy level scheme shown in Figure 4.2 [121]. The large homogeneous widths reported indicate the large non-radiative relaxation rates of the states other than the lowest Stark levels in $^2F_{7/2}$ and $^2F_{5/2}$. The lowest levels in $^2F_{7/2}$ and $^2F_{5/2}$ ('a' and 'e' respectively) are long lived (meta-stable) in comparison to the other Stark levels of both multiplets. Since they are metastable, the homogeneous widths for these levels will be negligibly small. The other levels are extremely short lived; hence the widths will be the sum of Full Width Half Maxima (FWHM) of the Lorentzian profiles representing the homogeneous broadening and the FWHM of the Gaussian profiles representing inhomogeneous broadening. The lowest long lived levels in the Stark multiplets contributes for the longer life time of the fluorescence. Also, the Lorentzian width of a band associated with the transition from the lower $^2F_{7/2}$ to upper $^2F_{5/2}$ will have the approximate summation of the widths of both states. For example, let us assume that the FWHM of the Lorentzian for the higher Stark levels at 300 K is $\approx$80 cm^{-1}. A band originated by the transition from 'a' to 'e' would result in an approximate minimum width of 0 cm^{-1}, and a transition from 'b' to 'e' will be 80 cm^{-1}, and 'b' to 'f' will be 160 cm^{-1} and so on.

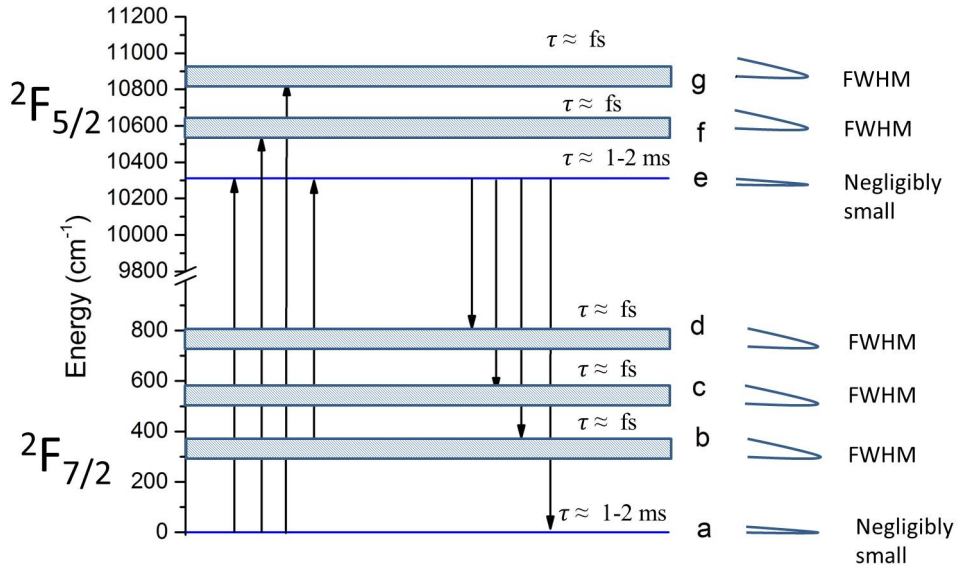

Figure 4.2: Energy level scheme from Figure 4.1 where the life time of the Stark levels and the corresponding homogeneous half widths are schematically indicated. Levels 'a' and 'e' are long lived (≈1-2 ms) and other levels are short lived (≈ 50-100 fs). The homogeneous widths of the levels 'a' and 'e' are negligibly small compared to the other levels. If the FWHM of all the levels (other than 'a' and 'e') are ≈ 80 cm^{-1}, band A which originates from the transition a→e hence would have negligibly small homogeneous width, band B which originates from the transition a→f would have an approximate width 80 $cm^{-1}$and so on. Similarly in the emission, band A' which originates from the transition e→a would have a negligibly small width, band B' which originates from the transition e→b would have an approximate width 80 $cm^{-1}$and so on. At room temperature, transitions from Stark level 'b' also comes into play, hence a band originating from the transition b→e would have a minimum width of 80 cm^{-1}, and b→f would have a minimum width of 160 $cm^{-1}$and so on [121].

Deconvolution of the spectroscopic data using Voigt profiles: The spectral line widths and the band positions (in thermal equilibrium) can be extracted by fitting Voigt profiles to the emission and absorption spectra [49]. Since the bands originating from the different transitions between $^2F_{7/2}$ and $^2F_{5/2}$ have contributions from both homogeneous and inhomogeneous broadening, the band shapes are best described by Voigt profiles. Fitting Voigt profiles to the absorption and emission spectra enables the retrieval of band center and Lorentzian as well as Gaussian contributions to the FWHM. Voigt fits are the best choice for the estimation of band positions. Voigt fits are convolution of a Gaussian function (W_G for FWHM) and a Lorentzian function. A Voigt profile can be given as:

$$y = A\frac{2\ln 2}{\pi^{3/2}}\frac{W_L}{W_G}\int_{-\infty}^{+\infty}\frac{\exp(t^2)}{(\sqrt{\ln 2}\frac{W_L}{W_G})^2 + (\sqrt{4\ln 2}\frac{x-x_0}{W_G} - t)^2}dt \tag{4.2}$$

The convolution formula is:

$$y(x) = (f_1 \times f_2)(x) \tag{4.3}$$

where f_1 is the Lorentzian

$$f_1(x) = \frac{2A}{\pi}\frac{W_L}{4(x-x_0)^2 + W_L^2} \tag{4.4}$$

and f_2 is the Lorentzian

$$f_2(x) = \sqrt{\frac{4\ln 2}{\pi}}\frac{e^{\frac{-4\ln 2}{W_G^2}\times x}}{W_G^2} \tag{4.5}$$

where y = I (emission intensity) or A (extinction), x_0 = center frequency of an emission or absorption band, A = area of emission or absorption band, W_G = Gaussian FWHM, W_L = Lorentzian FWHM.

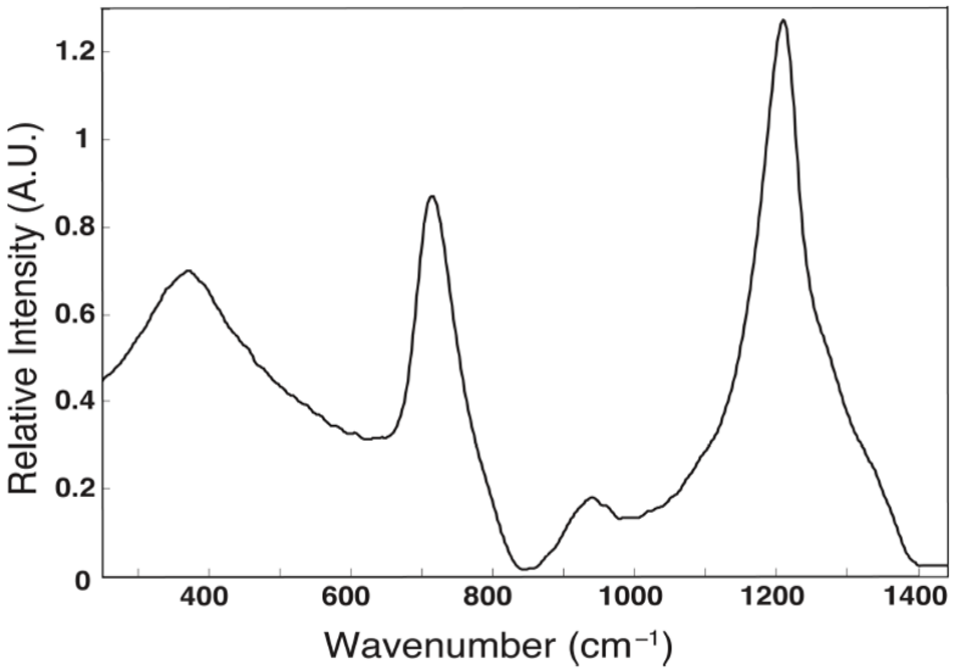

Figure 4.3: Raman spectrum of a commercial phosphate glass (MM-2a60 from Kigre Inc.) obtained from Fletcher *et al.* [123]

The integral in eq. 4.2 is computed numerically, and the non-linear least square fits to the data were carried out using the data analysing software Origin 8.

Deriving the widths from numerical fits has the advantage that it is capable of spanning a wide range of temperature and measure both homogeneous and inhomogeneous widths at the same time. Experimental techniques may feature different time scales and measure different physical quantities, which leads to different temperature limitations. For example, in fluorescence line narrowing (FLN) doesn't work perfectly at low temperature when the measured linewidth is smaller than the laser bandwidth [129].

Vibrational bands in Phosphate glasses:

Figure 4.3 shows the Raman spectrum of commercially available phosphate glass (MM-2a60 from Kigre Inc.) obtained from Fletcher *et al.* [123]. The broad Raman band between 200 cm^{-1} and 600 cm^{-1} is due to internal deformation bending modes of phosphate chains; both in-chain PO_2 and O-P-O bending (refer Figure 4.3). The large band around 710 cm^{-1} is due to the symmetric stretching mode of bridging oxygen between

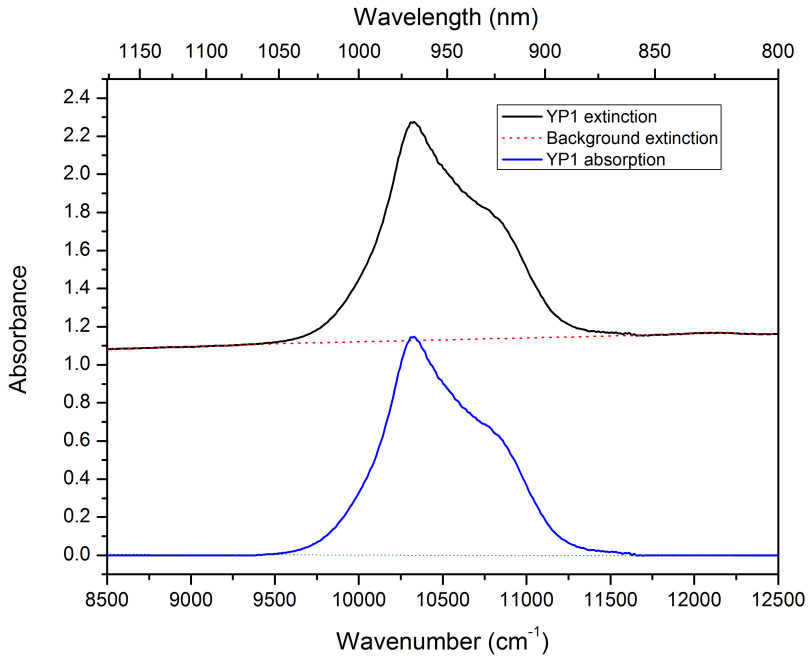

Figure 4.4: The measured extinction spectrum of Yb^{3+} in YP1 glass at room temperature (black) as well as the subtracted scattering background (red dotted line). The curve obtained after subtracting the scattering background is shown in blue.

two Q_2 tetrahedra, $(POP)_{sym}$. The small band at 940 cm^{-1} is assigned to the asymmetric stretching mode, $(POP)_{asym}$. The large band at 1209 cm^{-1} is due to the symmetric stretching of the P–O non-bridging oxygens on Q_2 phosphate tetrahedra, $(PO_2)_{sym}$. The 1300 cm^{-1} peak, a shoulder of the 1209 cm^{-1} peak, is the asymmetric stretching of P–O non-bridging oxygen atoms, $(PO_2)_{asym}$.

4.1.1 Absorption spectrum of YP1 glass

At room temperature, only one main band and a shoulder are visible in the extinction spectrum of YP1 glass (Figure 4.4). The peak extinction was recorded at 10319 cm^{-1} (969 nm), unlike the usually reported absorption maxima of Ytterbium doped phosphate glasses (at 10265 cm^{-1} (975 nm) corresponding to band A) [117]. A shoulder at higher energies appear at $\approx$ 10844 cm^{-1}(922 nm), a position matching the energies reported for the band C. Band B will be visible only at lower temperatures.
Figure 4.5 shows the room temperature extinction spectrum compared

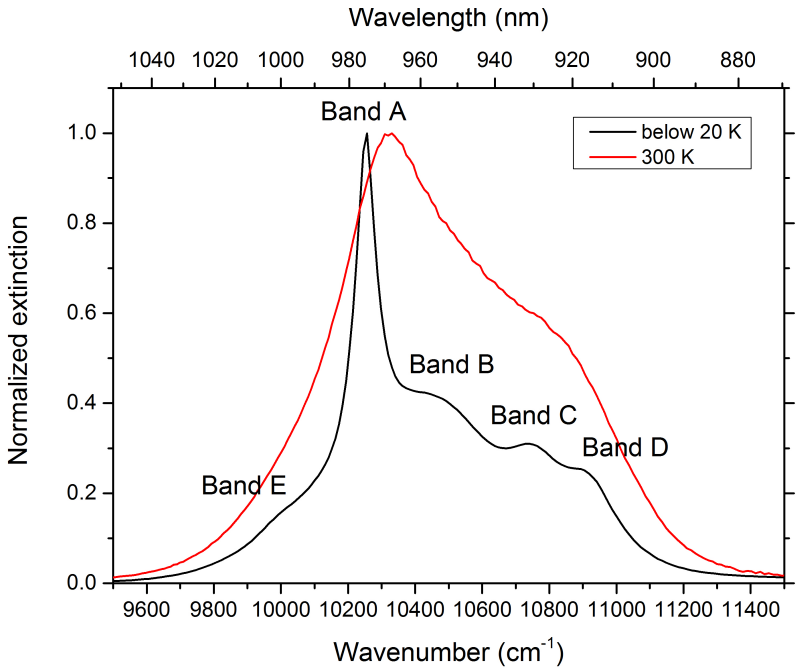

Figure 4.5: Normalized extinction spectrum of YP1 glass at 300 K and below 20 K. The extinction spectrum for the glass below 20 K was provided by the manufacturer.

to a low temperature extinction spectrum ($<$ 20 K) of another sample of YP1 glass. The low temperature spectrum was obtained from the manufacturer. The low temperature absorption spectrum shows bands A, B, C, D, and E as previously assigned in ref. [117]. The maxima of the extinction shifts to 10256 cm^{-1} below 20 K from 10316 cm^{-1} at 300 K. Since all the Stark levels in $^2F_{7/2}$ are well accessible in a 'phonon bath' at 300 K, the hot bands from Stark level 'b' should be also present, in the red trace in Fig. 4.5. The additional bands are not apparent in comparison to the low temperature spectrum; they carry less than ca. 25% of the intensity of the bands.

Estimation of band position and widths

YP1 extinction at low temperature ($<$ 20 K):

At low temperature, the Stark levels 'b', 'c', 'd', 'f' and 'g' have very low populations and hence transitions from Stark level 'a' will be dominant. The widths of these bands will have contributions from inhomogeneous and homogeneous broadening, hence the best Voigt fits were made when Lorentzian widths were near to zero (Figure 4.6). The parameters ob-

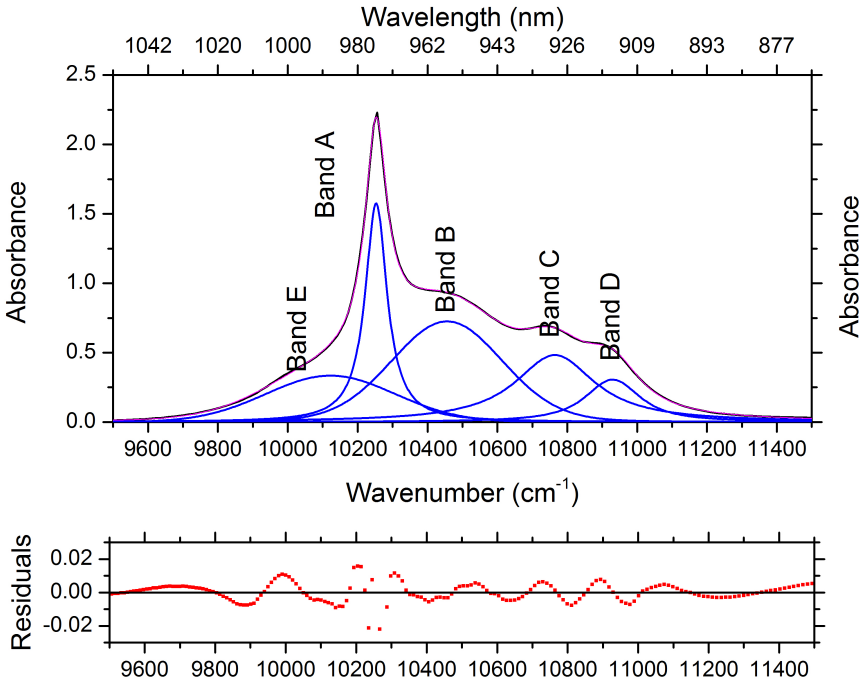

Figure 4.6: The sum of 5 Voigt profiles fitted to the extinction spectrum of YP1 glass (T < 20 K). The black curve is the baseline corrected extinction curve. Blue traces represent the individual Voigt profiles fitted to the spectrum and the magenta line is the sum of all fits. These band maxima are assigned to the primary $^2F_{7/2} \rightarrow {}^2F_{5/2}$ transitions. Band A represents the transition a→e, band B represents a→f, band C represents a→g, band D represents a→e', and band E represents a→g'. Bottom plot shows the residuals (Residuals = observed value of extinction - predicted value of extinction).

tained for the Voigt fits are listed in Table 4.1.

YP1 extinction at room temperature:

Since the extinction spectrum at room temperature does not exhibit significant structure, a decomposition of the spectrum is needed to find the Stark level positions. (The measurement is also limited by the resolution of the spectrometer). At room temperature, the homogeneous widths will be higher than those at low temperature. Eight Voigt profiles can be fit to the extinction spectrum (Figure 4.7). Voigt profiles (equation 4.2) corresponding to the transitions a→e (band A), a→f (band B) and a→g (band C) were fitted to the extinction spectrum. Voit profiles corresponding to transitions b→e (band F),b→f (band G) and ,b→g (band H), were also considered since at room temperature (300 K) the Stark level "b" will be populated up to ≈ 23% of Stark level "a". Bands D and E originate as a result of transitions from Yb^{3+} in different sites. The

Band name	Assignment	Band center (x_0) cm^{-1} (nm)	Lorentzian width (W_L) (cm^{-1})	Gaussian width (W_G) (cm^{-1})	Area a.u
A	a→e	10253 cm^{-1}(975.3 nm)	≈0	435±18	187
B	a→f	10455 cm^{-1}(956.5 nm)	5±6	365± 25	300
C	a→g	10764 cm^{-1}(929.02 nm)	1 ± 3	276± 94	209
D	a→e'	10929 cm^{-1}(914.99 nm)	3± 28	185±24	86
E	a→g'	10122 cm^{-1}(987.87 nm)	≈0	435±18	154

Table 4.1: Major bands in low temperature YP1 extinction spectrum and assignment of transitions. The parameters given in the table are obtained from Voigt fits.

Voigt bands obtained will give an approximate spectral position of the transitions and the corresponding FWHM will be having contributions from homogeneous and inhomogeneous broadening.

The peak positions and the widths of the fitted Voigt profiles are summarized in the Table 4.2. The band maxima at 10316 cm^{-1}(969.36 nm), 10444 cm^{-1}(957.48), 10844 cm^{-1}(957.48 nm) and 10769 cm^{-1}(929.02 nm) are transitions a→e(band A), a→f (band B) and a→g (band C). Bands F (10067 cm^{-1}), G (10207 cm^{-1}), band H (10562 cm^{-1}) represent the transitions from the second Stark level 'b' to $^2F_{5/2}$. Lorentzian widths for the bands A, and E which corresponds to transitions a→e and a→e' are negligibly small as explained in the section 3.2.1. Bands B and C have similar Lorentzian widths. Maximum Lorentzian width are observed for transitions b→f (band G) and b→g (and H) respectively. The errors on the Lorentzian and Gaussian fits are taken from the fit. The errors on band centers were small and are not included.

Band name	Assignment	Band center (x_0) cm^{-1} (nm)	Gaussian width (W_G) cm^{-1}	Lorentzian width (W_L) cm^{-1}	Area a.u
A	a→e	10316 cm^{-1}(969 nm)	191±35	4.37±2	127
B	a→f	10444 cm^{-1}(957.48 nm)	365± 25	75±11	115
C	a→g	10769 cm^{-1}(929.02 nm)	310±45	74± 15	151
D	a→g'	10921 cm^{-1}(915.66 nm)	358±56	94± 27	138
E	a→e'	10082 cm^{-1}(991.86 nm)	435±18	≈0	81
F	b→e	10067 cm^{-1}(993.34 nm)	539±108	76±5	56
G	b→f	10207 cm^{-1}(979.71 nm)	152 ±8	156±4	89
H	b→g	10562 cm^{-1}(946.46 nm)	120 ±19	160±76	116

Table 4.2: Major bands in YP1 extinction spectrum and assignment of transitions.The parameters given in the table are obtained from Voigt fits shown in Figure 4.7.

It is observed that band A in the absorption spectrum at low temperatures 10253 cm^{-1}(975 nm) is shifted by 63 cm^{-1} to 10316 cm^{-1} (969 nm) at 300 K and band B recorded at 10455 cm^{-1} (956.5 nm) is shifted to blue by 11 cm^{-1} to 10444 cm^{-1} (947.48 nm) at 300 K. Band C recorded at 10764 cm^{-1}(929.02 nm) at low temperature remains almost unchanged

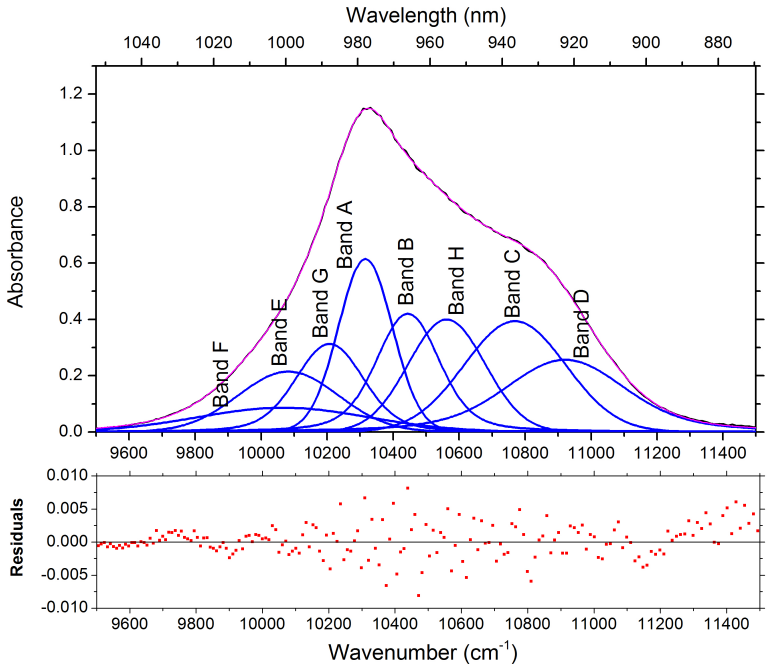

Figure 4.7: Voigt fits obtained for extinction spectrum of YP1 glass (T = 300 K). The black curve is the baseline-corrected extinction curve. Blue traces represent the individual Voigt profiles fitted to the spectrum and the magenta line is the sum of all fits. These band maxima are assigned to the primary $^2F_{7/2} \rightarrow {}^2F_{5/2}$ transitions. Band A represents the transition a→e, band B represents a→f, band C represents a→g, and band D represents a→g', band E represents a→e' , band F represents b→e band, G represents b→f, band H represents b→g. The lower panel shows the residuals (Residuals = observed value of extinction - calculated value of extinction as per fit function).

at 10769 cm^{-1} (928.59 nm). The change in the shift in each band is not consistent. The inconsistent shift of these bands with temperature has been previously reported [117] but there is no explanation given as to why the bands shift to both higher and lower energies.
The considerable shift in band A can be due to the error in obtaining the absorption of YP1 glass from YP1 extinction spectrum at room temperature. Phosphate glasses always react with water vapour in the surrounding medium forming chain terminating hydroxyl groups. YP1 extinction spectrum recorded is a sum of YP1 absorption and the absorption from OH^- ions. The second overtone of the OH^- stretching band (3ν), produces an absorption band near 10310 cm^{-1} (970 nm) [124]. Since this OH^- band was not distinguishable from YP1 absorption on basis of the present measurement (see also next section), it can influence the peak extinction of the glass measured.

4.1.2 Emission spectrum of YP1 glass

(Stokes) Fluorescence upon excitation at 982 nm

The room temperature emission spectrum obtained from the bulk glass is shown in Figure 4.8. The YP1 glass is excited at room temperature by a laser at wavelength 981.8 nm (refer table 2.4). The spectrum was recorded with an integration time of 5 min using the FTIR. The input aperture diameter of the spectrometer is set as the same as the internal diameter of the fiber (1.5 mm). Fourier transformation was performed with Norton-Beer apodization (refer section 2.3). Narrow laser excitation selects a particular sub-group of sites that have identical excitation energies, which are a measure of the strength of the crystal field surrounding the ytterbium ion.
In Figure 4.8, the intensity spike at 981.8 nm in the emission spectrum is caused by the scattered light from the laser. A dip is observed in the luminescence spectrum at 10256 cm^{-1}. This arises due to the absorption from the rotational-vibrational band of OH^- groups present in the YP1 glass [125]. The dip was removed by interpolating the spectrum between 10208 cm^{-1} and 10301 cm^{-1}.
For the description of the emission spectrum by Voigt profiles, the laser spike was removed from the emission spectrum. This adds uncertainty

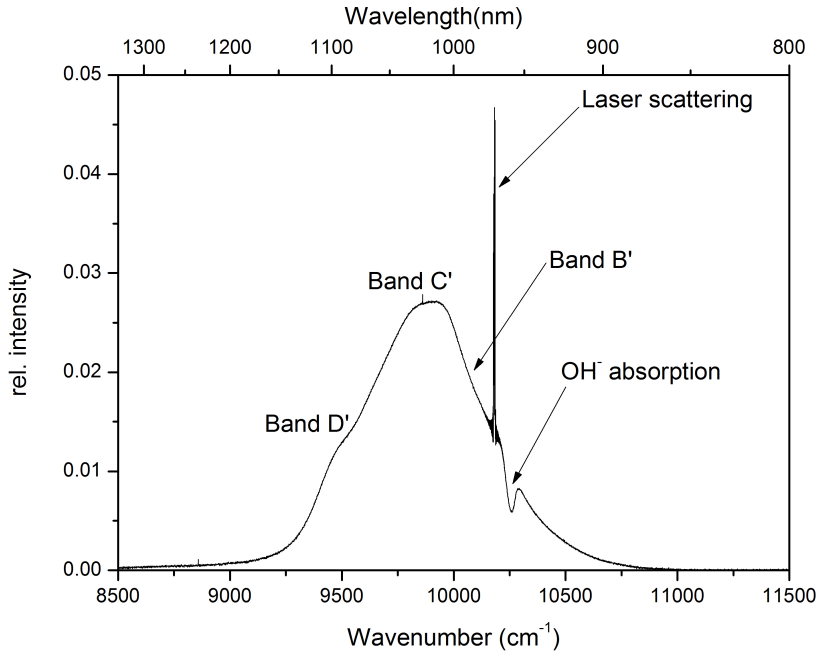

Figure 4.8: Luminescence spectrum of YP1 glass (excitation wavelength = 981.8 nm). The narrow peak is caused by the scattered light from the laser source, and the dip observed is the transmission loss produced by OH^- ions. The different bands observed are also shown. Band A, as seen in the spectrum, is over-shadowed by the laser scattering peak.

to the peak position of the band A', however with the laser peak present fitting profiles to the data proved impossible.

A spectrum without laser scattering and OH^- absorption is shown in Figure 4.9. The four major transitions from Stark level 'e' of $^2F_{5/2}$ to $^2F_{7/2}$, i.e e→a, e→b, e→c, and e→d are considered (see Figure 4.9). The band centers and FWHM obtained from the best fits are summarized in Table 4.3.

An additional band E' at 1052 nm is added, without which the fits were not in good agreement in terms of widths and band positions. The low center frequency of the band at 9482 cm^{-1} arises a possibility of a multi-phonon transition in a glass matrix with phonon energies as high as 1200 cm^{-1}. This band at 1052 nm is indicated in few works before [117], [119], [120], in which this band is identified as a vibronic band. Since Raman scattering studies in the same work on undoped phosphate glass does not show any evidence of a phonon band at 1052 nm, the band at 9482 cm^{-1} would have originated by shifting of the electronic line e→b (at 10172

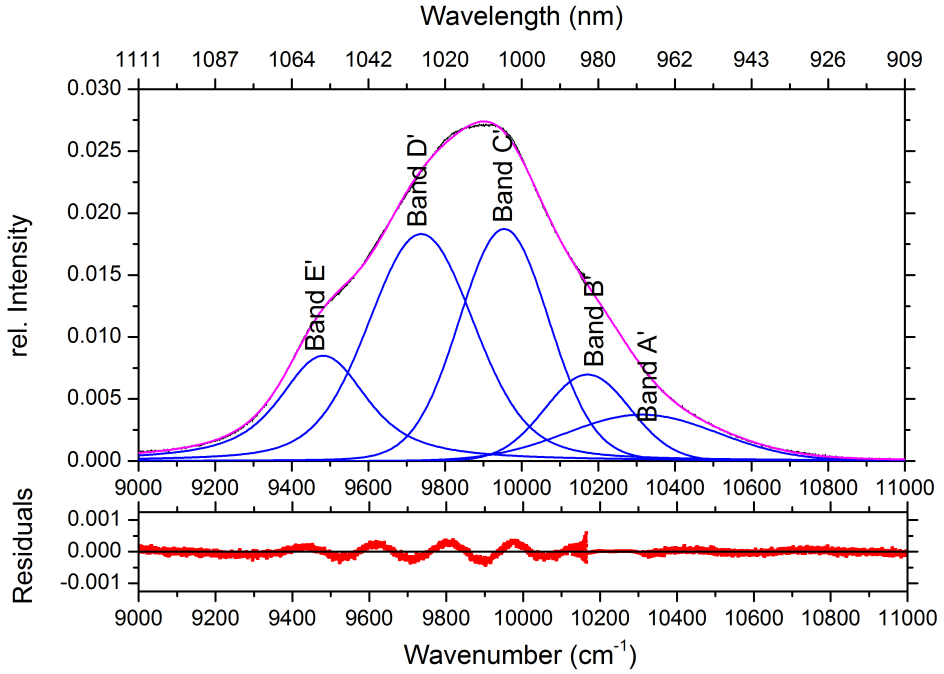

Figure 4.9: Emission spectrum of YP1 glass upon excitation at 981.8 nm. Laser scattering and OH^- absorption has been removed from the spectrum. The best Voigt fits obtained for the main transitions listed in table 4.3 are also shown. These band maxima are assigned to the primary $^2F_{5/2} \rightarrow {}^2F_{7/2}$ transitions. Band A' represents the transition e→a, band B' represents e→b, band C' represents e→c, band D' represents e→d, and band E' is unassigned. Lower plot shows the residuals (difference between calculated and measured value) obtained for the fits.

cm^{-1}) by the phonon energy $\hbar\omega \approx 700$ cm^{-1}. The reported Raman band at 710 cm^{-1} (check Figure 4.3) for pure phosphate glasses justifies the assumption.

Band name	Assignment	Band center (x_0) cm^{-1} (nm)	Lorentzian width (W_L) (cm^{-1})	Gaussian width (W_G) (cm^{-1})	Area a.u
A'	e→a	10314 cm^{-1}(969.55 nm)	≈ 0	465±65	1.84
B'	e→b	10172 cm^{-1}(983.09 nm)	45±6	209± 32	1.95
C'	e→c	9954 cm^{-1}(1004.6 nm)	58 ± 1	226± 94	5.66
D'	e→d	9737 cm^{-1}(1027.01 nm)	79± 27	280.627±24.45	7.01
E'	un-assigned	9482 cm^{-1}(1054.62 nm)	136 ± 4.9	198.39±10.58	3.27

Table 4.3: Voigt parameters obtained for different bands obtained from YP1 emission spectrum ($\lambda_{exc} = 981.8$ nm) and their assignment to different transitions.

The band maxima obtained from the Voigt fits are different from the ones reported in the literature for similar phosphate glasses [117]. The bands A' (transition e→a), B'(e→b), D'(e→d) (Figure 4.9 and 4.1) which are centered at 969.55 nm (10175 cm^{-1}), 983 nm (10172 cm^{-1}), 929 nm (9954 cm^{-1}) and 1027 nm (9737 cm^{-1}) are blue shifted, and band C' centered

at 9954 cm^{-1} is red shifted compared to the values reported in Dai *et al.* [117]. The determination of band positions is affected by:

1. The subtraction of the laser peak and OH^- transmission: The excitation wavelength at 981.8 nm coincide with the zero phonon band at 975 nm. While subtracting the laser peak at 981 nm, the band at 975 nm is affected. The position of the band B' corresponding to the e→b transition shifted by 10 nm apart in comparison with the band B (transition b→e) in the extinction spectrum (which should essentially have the same energy).

2. No bands were included for the emission bands generated by Yb^{3+} in different sites.

The width of the emission bands should also be influenced by the presence of OH^- ions. The vibrational frequency of OH^- ions fall in the range of 2700 to 3500 cm^{-1}. This is much larger than the typical phonon energies of the glass host matrix (Typical phonon energies for phosphate glasses (at room temperature) are around 1200 cm^{-1}). The energy gap between $^2F_{5/2}$ and $^2F_{7/2}$ corresponds to 3 vibrational quanta of OH^- ions. Hence a decay route via OH^- overtone is more probable than multi-phonon decay by the glass host matrix which needs around 8-10 phonons. The non-radiative decay via the OH^- overtone can shorten the excited state life times and leads to homogeneous broadening. This essentially affects the fluorescence life time.

(Anti-Stokes) fluorescence upon excitation at 1023 nm

Figure 4.10 shows the emission spectrum of YP1 glass upon excitation at 1023 nm (anti-Stokes spectrum). The bands A', B', and D' are present in the emission spectrum. The scattered light from the excitation beam covers the band C'. In the Stokes spectrum (λ_{exc} =981.8 nm) the absorption maxima of the OH^- stretching band ($3\nu_{1,3}$) (dip in the fluorescence spectrum) is at 10256 cm^{-1}(975 nm). This does not indicate a shift of the OH^- stretching band (3ν) , but instead a change in shape of the emission spectrum. The OH^- band shape solely depends on the shape of the emission spectrum. The shape of the emission spectrum is dependent on the way it is probed (excitation wavelength) and hence the change in the

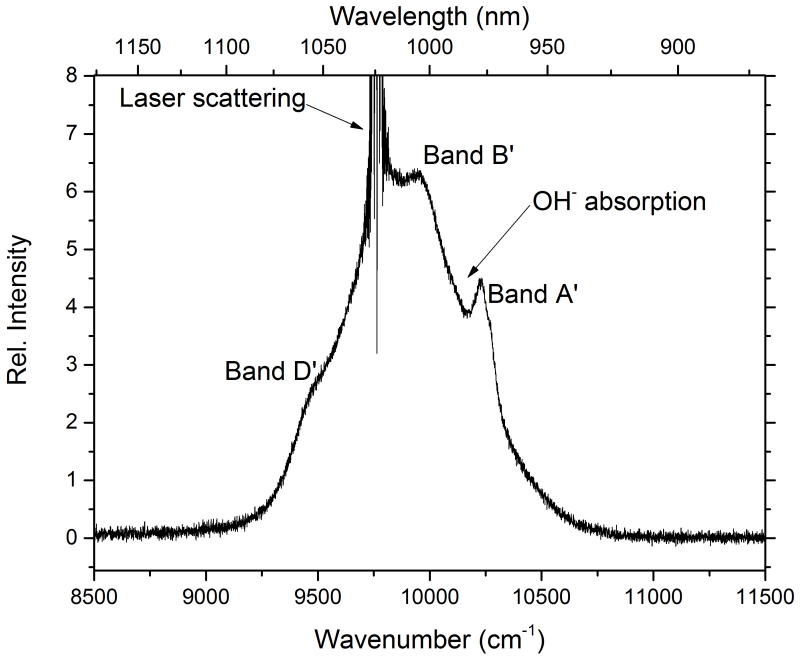

Figure 4.10: YP1 emission spectrum upon excitation at 1023 nm. Different band positions are also shown. Band C' is over shadowed by the scattering from the excitation laser. The spectrum is obtained with an integration time of 30 min.

Band name	Assignment	Band center (x_0)	Lorentzian width (W_L) (cm^{-1})	Gaussian width (W_G) (cm^{-1})	Area
A'	e→a	10324 cm^{-1}(970.55 nm)	≈ 0	401±33	0.036
B'	e→b	10234 cm^{-1}(977.1 nm)	38 ± 5.35	100± 10	1.955
C'	e→c	9970 cm^{-1}(1003 nm)	57 ± 70	263± 13	0.167
D'	e→d	9728 cm^{-1}(1027.9 nm)	79± 27	201±6	0.166
E'	un-assigned	9481 cm^{-1}(1054.74 nm)	85 ± 10	201±10	0.054

Table 4.4: Voigt fit parameters for different bands obtained from the YP1 emission spectrum (λ_{exc}=1023 nm) and their assignments to different transitions.

absorption maximum of the OH^- stretching band (3ν) in the anti-Stokes emission spectrum.

Figure 4.11 shows the Lorentzian fits for the bands in the emission spectrum of YP1 glass when excited at 1023 nm.

The error in estimation of the band position of C' and the corresponding Lorentzian FWHM is large since the excitation laser scattering over shadows the emission.

Comparison of YP1 glass fluorescence spectra upon excitation at 982 nm and 1023 nm

The Lorentzian widths of the bands A', B', C' and D' are comparable

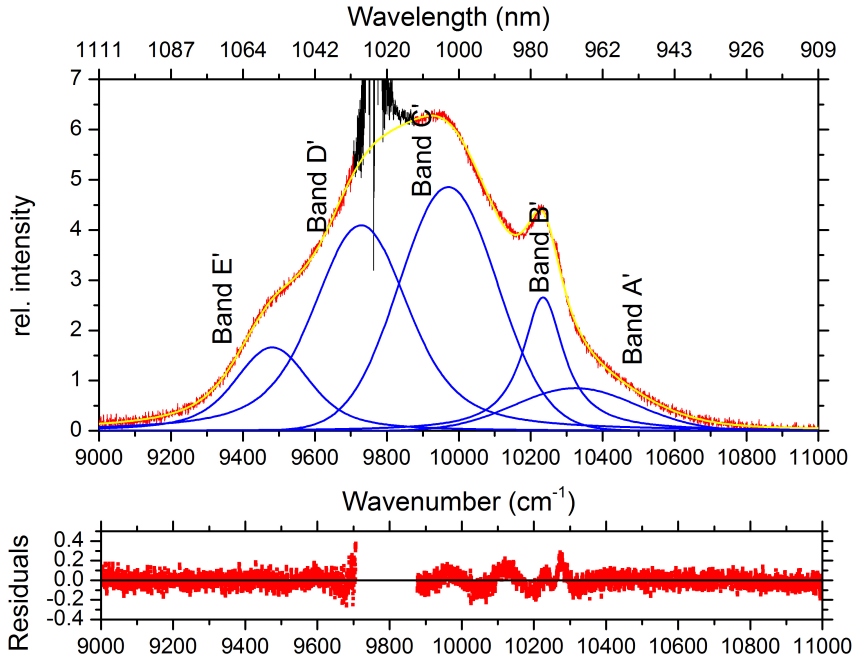

Figure 4.11: Emission spectrum of YP1 glass upon excitation at $\lambda_{exc} = 1023$ nm (black trace). The magenta line is the cumulative fit obtained for all the Voigt fits for the corresponding data in red. Individual profiles from the fit are shown in blue (listed in table 4.4). Lower panel shows the corresponding residuals obtained for the fits.

within error limits, for both excitation wavelengths. For excitation at 981.8 nm, the width of band A' is influenced by the laser peak. Hence the width appears to be larger than for the same when excited at 1023 nm (158.28 cm^{-1}). The same is the case for band D' when excited at 1023 nm.

The relative intensity difference between the bands maxima are also the same for both excitation wavelengths. For both excitation wavelengths, the band C' and D' have approximately the same area (and height). When YP1 is excited at a wavelength near band B' (at 981.8 nm) then band D' is the strongest and vice versa. The Lorentzian width for band E' is larger for Stokes excitation when compared to anti-Stokes excitation. The Gaussian widths differ slightly for all the transitions.

All band positions are unaltered confirming the validity of Kasha's rule in the present case [126].

Discussion on homogeneous and inhomogeneous line widths

Previous works on homogeneous widths report ≈ 0.16 cm^{-1}(< 20 K)

and 36.02 cm^{-1}(300 K) respectively for transition e→a [122]. The widths obtained from YP1 glass extinction spectra is ≈ 0 cm^{-1} at < 20 K and 4 cm^{-1}at 300 K for a→e transitions. There are limitations in the accuracy of these widths. The retrieval of the fit parameters depends on the initial values chosen for the fit. This is also applicable for the W_L (Lorentzian width). Results in this study show that the homogeneous line widths for YP1 glasses are quite large, proving the high electron phonon coupling for phosphate glasses. The higher homogeneous widths also indicate higher density of states of low energy phonons in YP1 glasses.

According to previous reports, the inhomogeneous widths will vary for absorption and emission transitions. Differences for inhomogeneous line widths as high as 33 cm^{-1} are reported for Yb^{3+} in glasses [129]. The reasons for differences in inhomogeneous widths in absorption and emission are still unclear.

The inhomogeneous widths are found to vary according to the excitation wavelengths 981.8 nm and 1023 nm for all transitions. A variation in inhomogeneous widths has been reported before to be excitation dependent [50], [51], [127].

Determination of energy levels

The crystal field splitting in the YP1 glass are affected due to the strong interaction between Yb^{3+} ions and the lattice vibrations. This interaction can give rise to strong phononic side bands and deformation of electronic bands. The phononic bands were not included in the Voigt fits made for the extinction and emission spectrum.

The energy level diagram derived from the principal emission and absorption bands is shown in Figure 4.12. The most prominent excitation transition at room temperature is a→e. The electrons relax from level e to any of the levels a, b, c, or d.

The three levels e, f, g correspond to band centers of A, B, C from table 4.2 and levels a, c, d are obtained by comparing the band centers of B', C' and D' to the lower energy level e (table 4.3). For obtaining the Stark energy level 'b' the band B from the extinction spectrum was considered, since the emission band B' was influenced by the laser peak at 981.8 nm. The extent of Stark splitting in YP1 can be estimated and compared with data from other glasses and crystals using a barycenter plot [128].

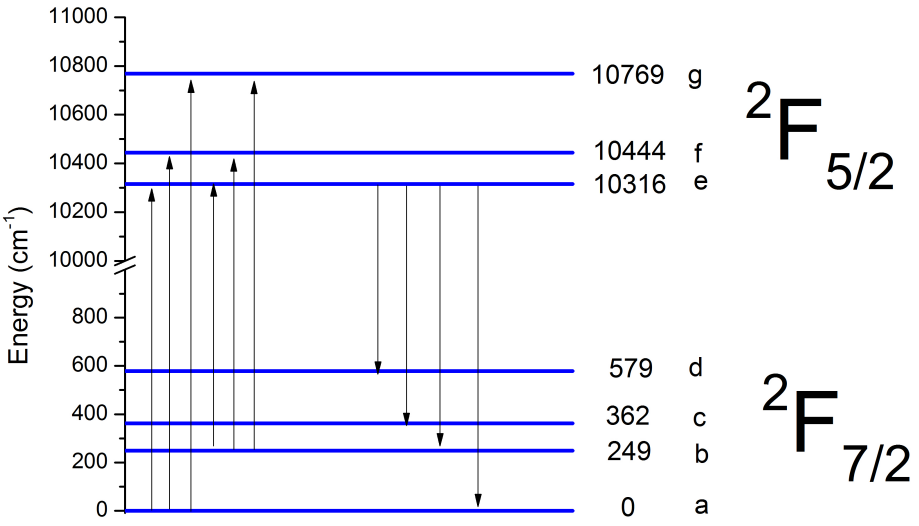

Figure 4.12: Energy levels of YP1 glass obtained from the absorption and emission spectrum at 300 K in the present study.

The emission from different ion positions (bands D, E, and E') were not considered in the determination of the energy levels.

Barycenter plot

There are many tools used to determine the accuracy of energy level diagrams obtained from the spectroscopic data [128]. A 'Barycenter plot' is one such tool [129]. The separation between the $^2F_{7/2}$ and $^2F_{5/2}$ manifolds results from spin–orbit interaction. The magnitude of the splitting is given by $\Delta E_{LS} = \zeta(l+\frac{1}{2})$ with spin-orbit coupling parameter $\zeta = 2918$ cm^{-1} for Yb^{3+}[121]. This produces a $^2F_{7/2}$ - $^2F_{5/2}$ splitting of ≈ 10200 cm^{-1} for Yb^{3+} ion (see Figure 4.1). For an ytterbium ion embedded in a host lattice, two distinct effects could alter this energy separation. The first one is a modification of the spin–orbit coupling constant ζ. Theoretically predicted, this variation is very weak for lanthanide ions [130]. The second possible effect is J-J coupling, which is caused by the interaction of the crystal field of states belonging to the $^2F_{7/2}$ and $^2F_{5/2}$ levels. In the case of ytterbium, the energy difference between $^2F_{7/2}$ and $^2F_{5/2}$ (about 10200 cm^{-1}) is large enough for J-J mixing to be neglected in good approximation. Hence the separation between $^2F_{7/2}$ and $^2F_{5/2}$ can be considered constant in any host matrix, and will be comparable to the spin orbit coupling observed for the free ion. When we take the lowest Stark level as the origin of energies (ground electronic state) and plot the $^2F_{5/2}$ manifold energy barycenter versus the $^2F_{7/2}$ barycenter for different host matrices, the representative points should align in a straight line whose slope is equal to one [128]. Barycenter plot for several host matrices obtained from the energy levels values of Yb^{3+} energy levels obtained from literature is shown in Figure 4.13. The barycenters of each configuration were calculated as the degeneracy weighted mean of the energy levels of the Stark configuration. Barycenters '$E_{^2F_{5/2}}$' and '$E_{^2F_{7/2}}$' are calculated using

$$E_{^2F_{7/2}} = \frac{(g_a \times E_a + g_b \times E_b + g_c \times E_c + g_d \times E_d)}{(g_a + g_b + g_c + g_d)} \tag{4.6}$$

$$E_{^2F_{5/2}} = \frac{(g_e \times E_e + g_f \times E_f + g_g \times E_g)}{(g_e + g_f + g_g)} \tag{4.7}$$

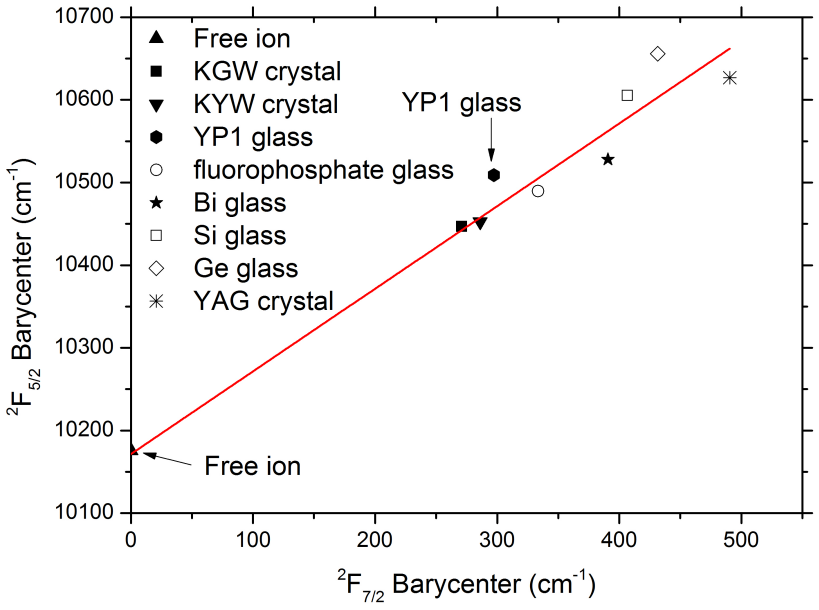

Figure 4.13: Barycenter of the $^2F_{7/2}$ versus $^2F_{5/2}$ levels in various host matrices (see table 4.5). The red line (straight line with slope = 1) represents the Barycenter plot where there is no dependence of the splitting between $^2F_{7/2}$ and $^2F_{5/2}$ as a function of the host matrix. The energy values were obtained from the absorption and emission data of the bulk YP1 glass.

where E_a, E_b, E_c, E_d and E_e, E_f, E_g are energies of Stark levels (in cm^{-1}) in $^2F_{7/2}$ and $^2F_{5/2}$ respectively. g_i (i = a..g) are degeneracies of each Stark level (in Yb^{3+} g_i= 2, i = a..g). The band center positions of bands A, B, and C (from the extinction spectrum) were used for determining energy values of E_e, E_f, E_g and band center positions of band A', B', and C' and D' (from the emission spectrum) were used to determine E_a,..., E_d.

The barycenters obtained for YP1 glass as obtained from the absorption and emission spectra are shown in Figure 4.13. The barycenters of $^2F_{7/2}$ and $^2F_{5/2}$ were obtained as 297.3 cm^{-1} and 10509.6 cm^{-1}respectively.

The position of YP1 in the barycenter plot (in Figure 4.13) is somewhat higher than the theoretical prediction. This is likely to be due to the estimation of the spectral position of the absorption band A which is influenced by OH^- absorption and the emission band A' which is affected by laser scattering spectrum and water band.

Host	$^2F_{7/2}(cm^{-1})$				$^2F_{5/2}(cm^{-1})$			Reference
	a	b	c	d	e	f	g	
YP1	0	249	362	579	10316	10444	10769	This work
Ge glass	0	316	509	901	10246	10684	11038	[119]
Silica glass	0	265	488	874	10246	10593	10977	[119]
Fluorophosphate glass	0	277	511	734	10267	10504	10834	[119]
KGW	0	163	385	535	10188	10471	10682	[131]
KYW	0	169	407	568	10187	10476	10695	[131]
YAG	0	565	612	785	10327	10624	10929	[132]

Table 4.5: Energy levels of Yb^{3+} in various host matrices.

Emission cross-section calculation

The emission cross-sections of the YP1 glass can be determined using the reciprocity method described by McCumber [133]. The emission cross-section, σ_{emi} of Yb^{3+} in a strongly phonon coupled system can be calculated from the measured absorption cross-section, σ_{abs}, i.e,

$$\sigma_{emi} = \sigma_{abs}(\lambda)\frac{Z_l}{Z_u}exp\left[\frac{E_{zl} - hc\lambda^{-1}}{kT}\right] \tag{4.8}$$

where Z_l and Z_u represent the partition functions of the lower and upper states, k is the Boltzmann's constant, and E_{zl} is the zero line energy which is defined as the separation between the lowest components of upper and lower states. The ratio of the partition function can be obtained from the energy levels (Figure 4.12, see table 4.5). In the high temperature limit, the ratio of Z_l/Z_u simply becomes the degeneracy weighting of the two states. Parameter E_{zl} can be determined by matching the magnitude of actual emission spectrum of the glass to its absorption spectrum. The wavenumber where the normalized emission and absorption spectrum intercept is considered to approximately correspond to the zero line energy in the present case ($\approx$10147 cm^{-1}, see Figure 4.14). Alternatively, the zero line energy can also be taken as the lowest Stark level of the $^2F_{5/2}$ energy levels. The absorption cross-section for the $^2F_{7/2}$ - $^2F_{5/2}$ transition ($\sigma_{abs}[cm^2]$) of $Yb^{3+}$is given by:

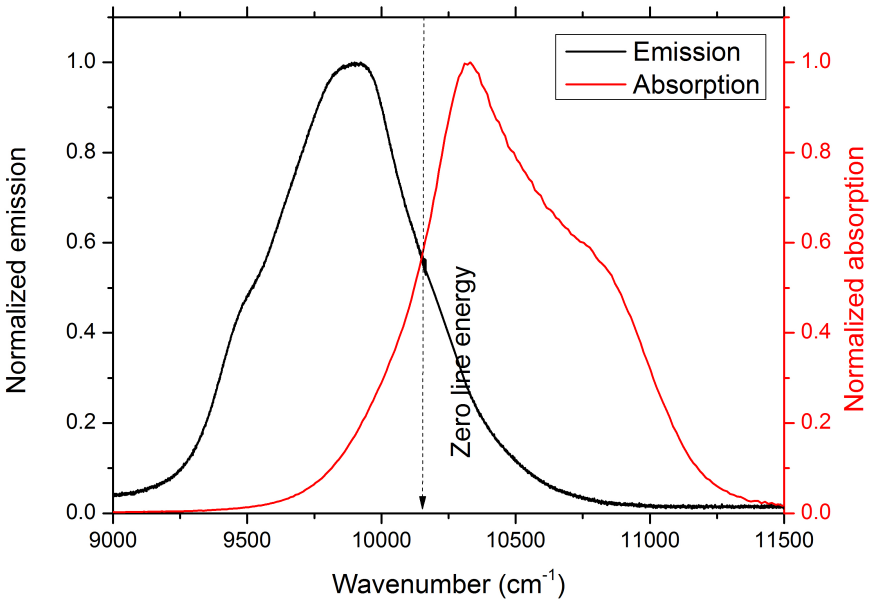

Figure 4.14: Determination of the zero line energy (10147 cm^{-1}) by comparison of the normalized emission and absorption spectrum.

$$\sigma_{\text{abs}} = \left(\frac{2.303\text{OD}}{\text{cl}}\right) \tag{4.9}$$

Where OD is the optical density, c [cm^{-3}] is the ion concentration and l [cm] is the length of the sample. The emission cross-section spectrum thus obtained from Equation (4.9) for the low temperature ($<$ 20 K) absorption cross-sections are shown in Figure 4.15. The shape of the emission cross-sections agree with the ones previously reported for Yb^{3+} doped glasses [134].

The same can be applied for the emission cross-sections at room temperature (Figure 4.16). The shape of the emission cross-section spectrum varies with the baseline of the extinction spectrum. But the behaviour of the cross-sections is similar to the emission spectrum (Figure 4.17), below the zero line energy. In general, reciprocity equation forces the absorption cross-section to behave according to an exponentially decaying function (with energy) which is decided by the zero line energy. A small change in the polynomial baseline of the absorption spectrum strongly increases the uncertainty of the emission cross-section calculation. Emis-

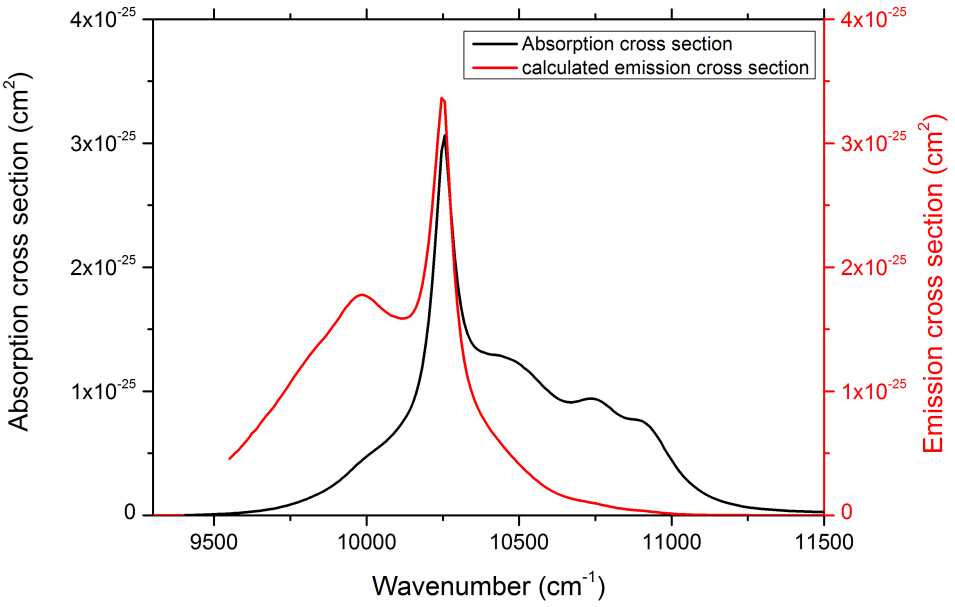

Figure 4.15: Experimentally obtained absorption cross-section and calculated emission cross-sections for YP1 glass at low temperature ($<$ 20 K)

sion cross-sections obtained through this method are used for estimating the shape of the emission spectrum of YP1 nanoparticles.

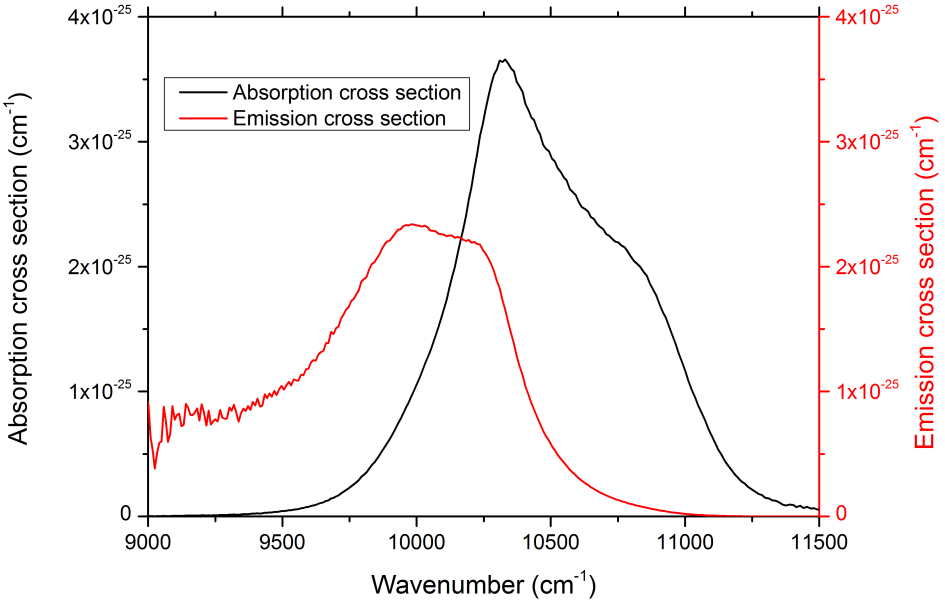

Figure 4.16: Calculated emission cross-section from room temperature absorption cross-sections (equation 4.9).

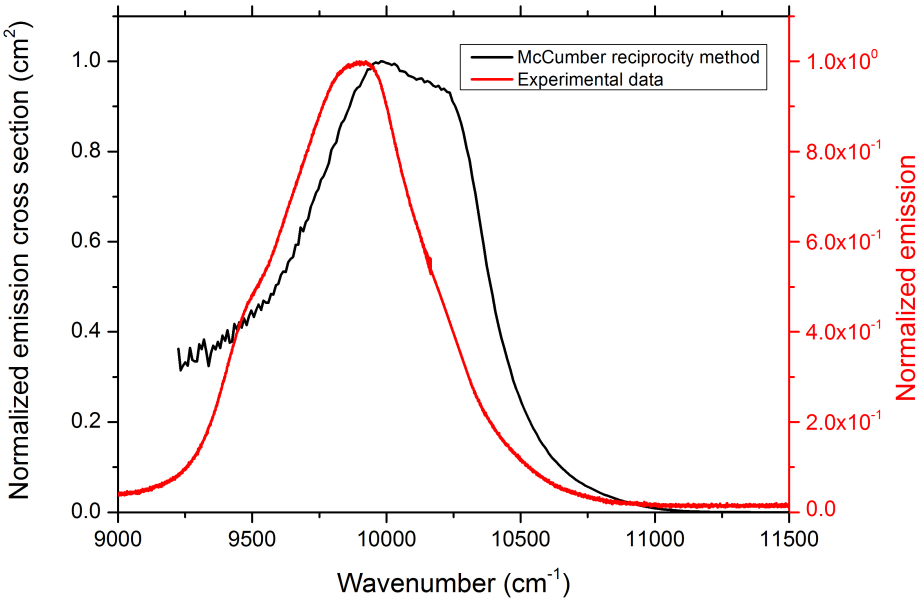

Figure 4.17: Normalized calculated emission cross-section compared with normalized (measured) emission spectrum (λ_{exc}= 981.8 nm).

4.2 YP1 glass nanoparticle

Lanthanide ions in nanoscale materials are reported to exhibit spectroscopic properties which differ from their bulk counterparts, due to modifications of the phonon density of states of the material[1] [135]. Increased structural defects and increased disorder in the nanoparticles result in significant changes in inhomogeneous broadening compared to bulk [136]. Particle size may also affect emission life time, luminescence quantum efficiency, and concentration quenching [137]. The following section investigate the variation (if any) present in the spectroscopic data obtained for YP1 glass nanoparticles in comparison with its bulk glass counterpart. YP1 glass colloidal solution was prepared by ablating YP1 bulk glass [96] in DMSO for 6 hrs using a pulsed laser as described in the experimental chapter (Figure 2.1). Nano particles of YP1 were generated with sizes ranging from 200-300 nm. Photographs of the particles are shown in Figure 2.5.
Several aspects are to be considered in the analysis of the spectroscopic data of YP1 nanoparticles are:

- In bulk glass systems the phonon states form a continuous band, however, in nano-glass materials the density of states is modified due to the finite particle size. For an isolated nanoparticle site the phonon spectrum can become discrete [138].

- No quantum confinement effects are expected in the electronic states for these particles (average diameter of 350 nm, check Figure 2.5). Therefore non-radiative relaxations to the vibrational ground state is expected to be faster than in the bulk material.

- The particles will have surface defects as evident from the TEM image (Figure 2.5), indicating the increased non-radiative relaxations to the vibrational ground state.

[1] In lanthanides, there will be little modification of electronic energy levels due to quantum confinement as stated in section 1.3.2. In solids, electrons in $4f^n$ orbitals of lanthanides are localized, therefore lanthanides do not exhibit significant quantum confinement even in nano materials. Confinement effects have only been found for lanthanides doped in semiconductors e.g. for Eu^{3+} doped ZnO with sizes below 5 nm [135].

- Absorption and emission spectra are measured at room temperature. Absorption and emission bands thus obtained will be broadened homogeneously as well as inhomogeneously.
- The OH^- ions in the bulk glass matrix are not homogeneously distributed [125]. Hence the influence of OH^- ions on the spectroscopic properties of the bulk glass and nanoparticles of glass can be assumed to be necessarily the same.

4.2.1 Extinction spectrum of YP1 nanoparticle

The extinction spectrum of YP1 nanoparticle suspension in DMSO was measured between 9400 cm^{-1} and 11150 cm^{-1}. The absorption spectrum of the nanoparticles was normalized to compare it with the absorption of the bulk glass (Figure 4.18). Scattering by the particles was accounted for by a polynomial ($A = (-4.7 \times 10^{-4}) + 0.001\bar{\nu} - (3.03 \times 10^{-7})\bar{\nu}^2 + (2.74 \times 10^{-11})\bar{\nu}^3 + (8.28 \times 10^{-16})\bar{\nu}^4$)[1] and was subtracted from the extinction spectrum. (The extinction spectrum of the nanoparticle suspension including the scattering contribution is shown in Figure B.4 in Appendix A).

The maximum of the extinction spectrum was shifted by 198 cm^{-1} ($\sim$19 nm) to lower energies for the nanoparticle suspension when compared to the bulk (from 10319 cm^{-1} for bulk to 10121 cm^{-1} for nanoparticle). For the bulk YP1 glass, the spectrum extended $\sim$1400 nm (from 892.8 nm to 1020.4 nm). For the nanoparticles, the width of the spectrum increased to $\sim$1700 nm (from 896.9 nm to 1063.8 nm).

Bands in the extinction spectrum

As for the bulk glass, Voigt profiles were fitted to the nanoparticle extinction spectrum. Eight Voigt profiles were fitted corresponding to different transitions from Stark levels 'a' and 'b' to $^2F_{5/2}$ (Figure 4.19). Fitting was run by assigning initial values for the band centres to be the same as those for the bulk[2] (Table 4.3) with the parameter values unfixed. Voigt profiles (equation 4.1) corresponding to the transitions

[1] $\bar{\upsilon}$ is the energy in wavenumber (cm^{-1})

[2] Fits were run using fit analyser in Origin 8.1 which allows to initialize parameters x_0, W_G, W_L and area. None of the parameters were fixed. The end fit parameters will be influenced slightly by the initial values.

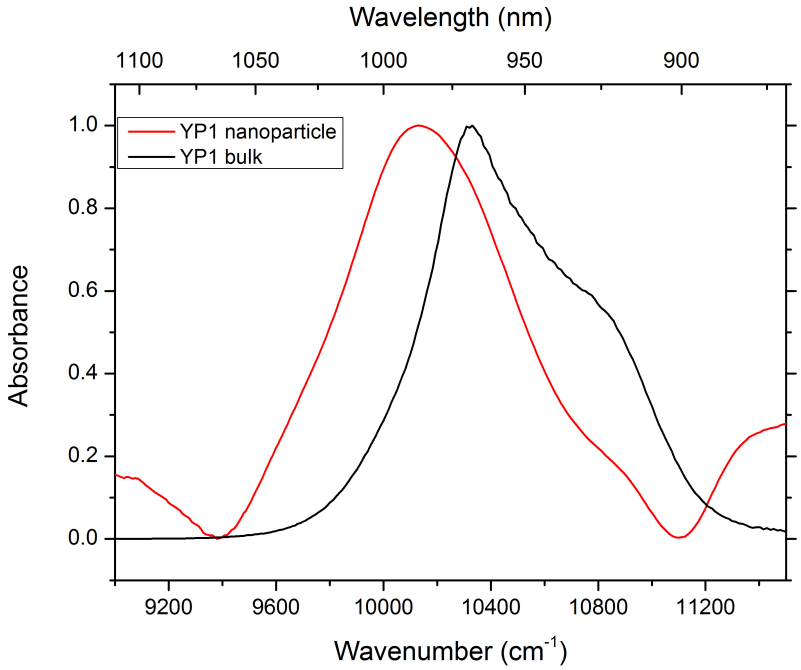

Figure 4.18: Normalized extinction spectra of YP1 nanoparticle suspension (red) and the bulk YP1 glass. The local maximum at 969 nm for the bulk YP1 glass is shifted to 988 nm (red-shifted compared to that of YP1 bulk by 19 nm). A polynomial baseline was subtracted from the extinction spectrum of the YP1 nanoparticle suspension to compare it with that of the bulk glass.

a→e (band A), a→f (band B) and a→g (band C), b→e (band F), b→f (band G) and b→g (band H) were fit to the extinction spectrum. Bands D (a→e') and I (a→e') originate as a result of transitions from Yb^{3+} in different sites[1].

The bands corresponding to transitions from the Stark level 'a' (band A, B and C) have center frequencies similar to bulk. The transitions from the Stark level 'b' however are shifted in comparison to those observed in the bulk. Band F, which was at 10067 cm^{-1} in the bulk red-shifted to 9982 cm^{-1}, band G red shifted from 10207 cm^{-1} to 10153 cm^{-1}, while band H shifted to higher energies from 10562 cm^{-1} to 10584 cm^{-1}.

The bands in the extinction spectrum with maximum areas (considering the areas listed in Table 4.2) are for the transitions that originate from

[1]Instead of the band E present in the extinction spectrum of the bulk (which corresponds to the transition a→e' at 991 nm) (Table 4.2) there is another band which appears at 1024 nm for the nanoparticles. This band can be originated from a different Yb^{3+} site than the one assigned to band E specified in Table 4.2, hence the band is named 'I' in the case of nanoparticles.

Band name	Assignment	Band center (x_0) cm^{-1} (nm)	Gaussian width (W_G) cm^{-1}	Lorentzian width (W_L) (cm^{-1}) cm^{-1}	Area a. u
A	a→e	10314 cm^{-1}(969 nm)	256±35	6±28	12.64
B	a→f	10444 cm^{-1}(957.48 nm)	174± 66	76±27	8.27
C	a→g	10769 cm^{-1}(929.02 nm)	225±107	74± 15	3.59
D	a→g'	10921 cm^{-1}(915.66 nm)	168±95	95± 27	1.28
I	a→e'	9763 cm^{-1}(1024.27 nm)	354±18	≈0.00[1]	12.66
F	b→e	9982 cm^{-1}(1001.80 nm)	99±190	163±4	13.19
G	b→f	10153 cm^{-1}(984.93 nm)	148 ±185	115±105	17.05
H	b→g	10584 cm^{-1}(946.46 nm)	211 ±42	35±76	6.09

Table 4.6: Major bands in YP1 nanoparticle extinction spectrum and assignment of transitions corresponding to Figure 4.19. The parameters in given in the table are obtained from Lorentzian fits.

the lowest Stark level 'a' (bands A, B and C). In the extinction spectrum of the nanoparticles, the bands F, G and H which correspond to the transitions originating from the Stark level 'b' have larger areas than those from the lowest Stark level 'a'.

Band G, corresponding to transition b→f, has the largest area in the YP1 nanoparticle extinction spectrum, as opposed to the situation in the bulk extinction spectrum where the band C, corresponding to transition a→g, had the maximum area. The area of band F (transition b→e) is slightly larger compared to band A (transition a→e) for nanoparticles. In the bulk YP1 extinction spectrum, the area of band F was less than 50% compared to the band A.

The homogeneous widths obtained for the fits (W_L) agree within 90 % for the nanoparticles and the bulk (within error limits) except for band H. For band H, the homogeneous width decreases from 160 $cm^{-1}$to 35 cm^{-1}. The removal of the scattering baseline would have influenced the width of the band H which is close to the edge of the spectrum. Band D at the higher energy end of the extinction spectrum had a dramatic reduction from 358 cm^{-1} to 168 cm^{-1} in Gaussian width (W_G). There is a 10-20% increase in W_G for band A and H for the nanoparticles compared to the bulk, while for bands D, F, B, and C, W_G decreases slightly.

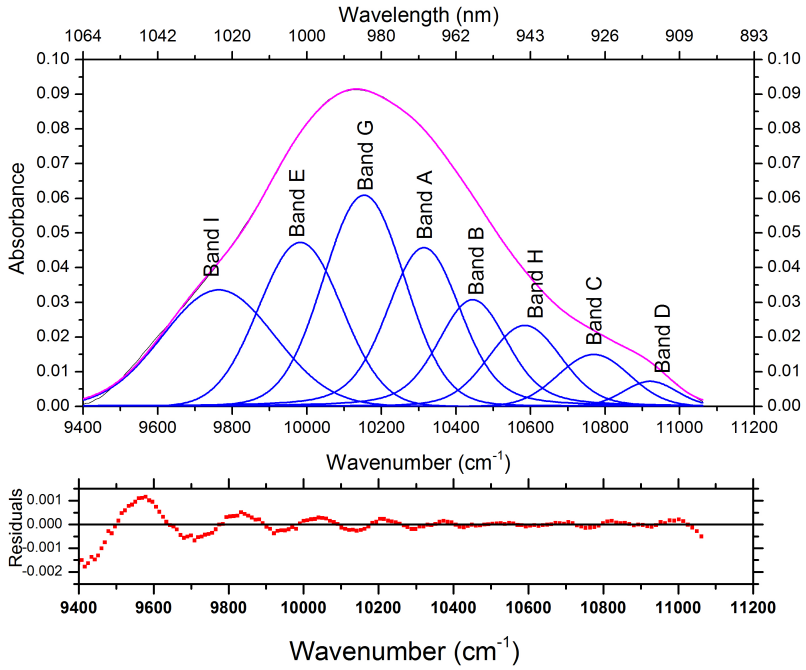

Figure 4.19: Voigt fits obtained for absorption spectrum of YP1 glass nanoparticles (T = 300 K). The black curve is the baseline corrected extinction spectrum. Blue traces represent the individual Voigt profiles fitted to the spectrum and the magenta line is the sum of all fits. These band maxima are assigned to the primary $^2F_{7/2} \rightarrow {}^2F_{5/2}$ transitions. Band A represents the transition a→e, band B represents a→f, band C represents a→g, band D represents a→g', band I represents a→e', band F represents b→e, band G represents b→f, and band H represents b→g. Bottom plot shows the residuals (Residuals = difference between calculated and measured value).

4.2.2 Emission spectrum of YP1 nanoparticles

Fluorescence upon excitation at 981.8 nm

The emission spectrum of the YP1 glass nanoparticles upon excitation at λ_{exc}= 981.8 nm is shown in Figure 4.20. Site selective excitation of YP1 nanoparticles gave an emission spectrum similar to that of the bulk YP1 glass. A Notch filter (NF 980-41, refer table 2.5) had to be used to reduce elastically scattered light at the excitation wavelength.
Since the Notch filter was used to avoid the scattering from the source, a part of the emission spectrum (band B') was eliminated from the spectrum. Also, band A' was partially removed due to the filter extinction.

Estimation of band positions and widths

Voigt profiles were fit to the emission spectrum using the same method as for the bulk YP1 glass (Figure 4.21). The portion of the emission spec-

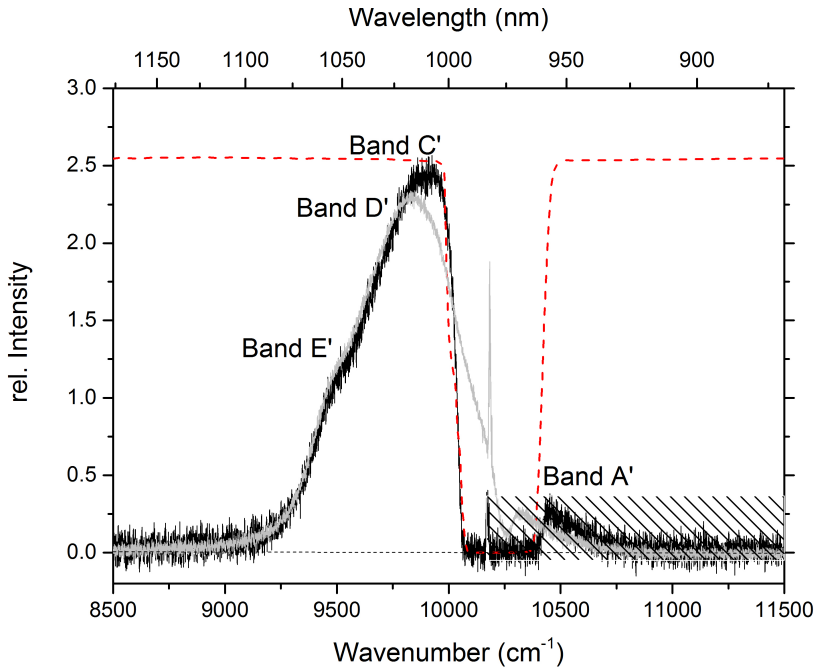

Figure 4.20: Black curve represents the emission spectrum of YP1 nanoparticle suspension atλ_{exc} = 981.8 nm (laser power ≈100 mW). The integration time is 3 hr. The input aperture size of the Fourier-Transform spectrometer was matched to the internal diameter of the fiber (1.5 mm). The Beer-Lambert apodization function was employed to avoid side bands of the interferrogram. The red dotted curve is the NF 980-41 filter transmission normalized to the maximum fluorescence intensity. The light grey curve is the bulk YP1 emission curve excited at λ_{exc} = 981.8 nm and rescaled to the emission of the nanoparticles. The shaded region denotes the anti-Stokes part of the spectrum.

trum cut by the Notch filter was not included in the fits. The parameters obtained for the Voigt fits for the bands are shown in table 4.7. The center frequency of band C' appear to be shifted to longer wavelength by 3 nm compared to the bulk. The center frequency of band D' and E' appear to be in the same position when compared to the bulk.
The Lorentzian (W_L) and and Gaussian (W_G) widths of the three bands are similar (within error limits) when compared to the bulk.

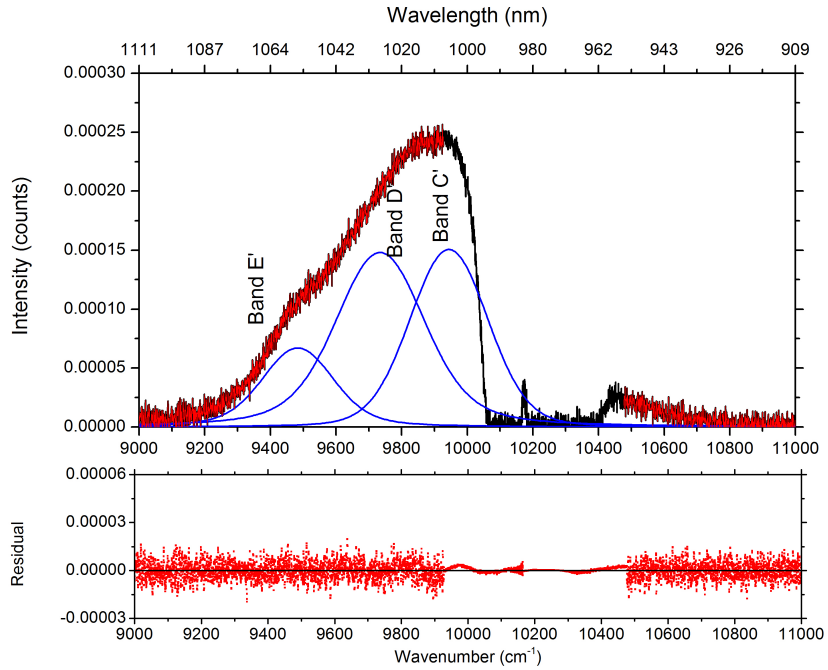

Figure 4.21: Emission spectrum of YP1 glass nanoparticles upon excitation at 981.8 nm. The best Voigt fits (for the data shown in red) obtained for the main transitions listed in table 4.3 are also shown. These band maxima are assigned to the primary $^2F_{5/2} \rightarrow {}^2F_{7/2}$ transitions. Band A' is not observed due to the optical filter blocking the light in that region. Band C' represents e→c, band D' represents e→d, and band E' is unassigned. The bottom plot shows the residuals (difference between calculated and measured value) obtained for the fits.

Fluorescence upon excitation at 1023 nm

Figure 4.22 shows the emission from YP1 glass upon excitation at 1023 nm (anti-Stokes spectrum). To avoid the scattering from the source a cut-off filter at 1000 nm had to be used. The filter blocked more than half of the fluorescence. Only band A and the OH^- absorption band are visible in the anti-Stokes emission spectrum after an integration time of 3 hrs. Hence the deconvolution of the spectrum using curve fitting was not possible.

Band name	Assignment	Band center (x_0)	Lorentzian width (W_L) (cm^{-1})	Gaussian width (W_G) (cm^{-1})	Area a.u
C'	e→c	9944 cm^{-1}(1005.6 nm)	38 ± 110	260± 41	0.05
D'	e→d	9734 cm^{-1}(1027.01 nm)	115± 61	255±27	0.06
E'	un-assigned	9483 cm^{-1}(1054.62 nm)	83 ± 27	210±12	0.02

Table 4.7: Voigt fit parameters obtained for different bands obtained from YP1 nanoparticle emission spectrum (λ_{exc} = 981.8 nm) and their assignment to different transitions of Figure 4.21.

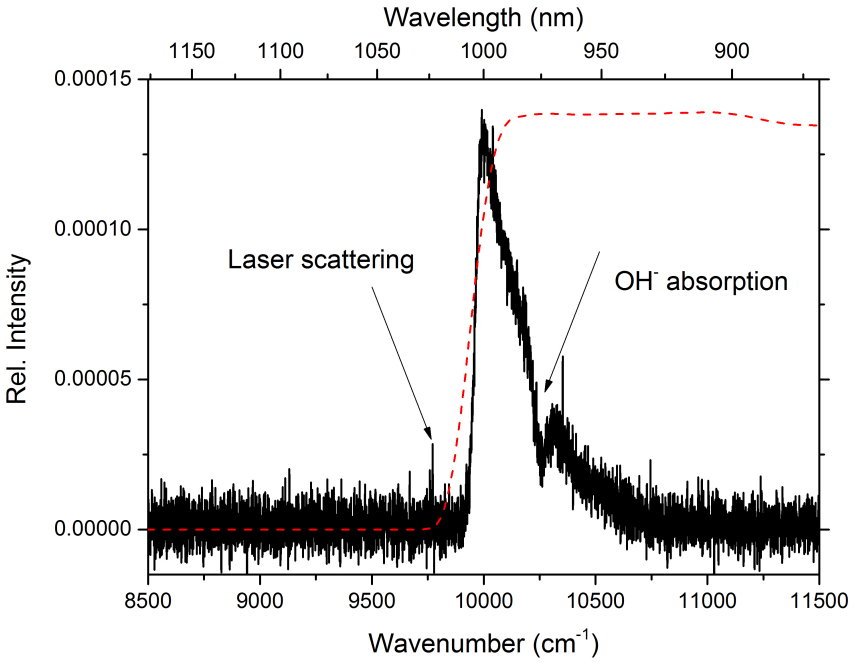

Figure 4.22: Emission spectrum of YP1 nanoparticle suspension upon excitation at λ_{exc} = 1023 nm. The red dotted curve is the filter transmission normalized to the maximum fluorescence intensity. The integration time is 3 hr.

Estimation of energy levels

The electronic energy level diagram of the nanoparticle derived from the principal emission and absorption bands is shown in Figure 4.23. The most prominent excitation transition at room temperature is b→f.
The three levels e, f, g correspond to band centers of A, B, C from table 4.6 and levels a, c, d are obtained by comparing the band centers of B', C' and D' to the lower energy level e (table 4.7). For obtaining the Stark energy level 'b' the band G from the extinction spectrum was considered since the emission band B' was not observed due to the Notch filter. The emission from different sites of Yb^{3+} (bands D, E, and E') were not considered in the determination of the energy levels. The electronic energy levels resemble that of the bulk except for the slight difference in Stark level 'b'. The energy level value for 'b' was obtained by subtracting the center frequency of band G from band B in the extinction spectrum. The center frequency of band G had shifted to lower energies compared to bulk, which gave a higher value for stark level 'b' compared to the bulk.

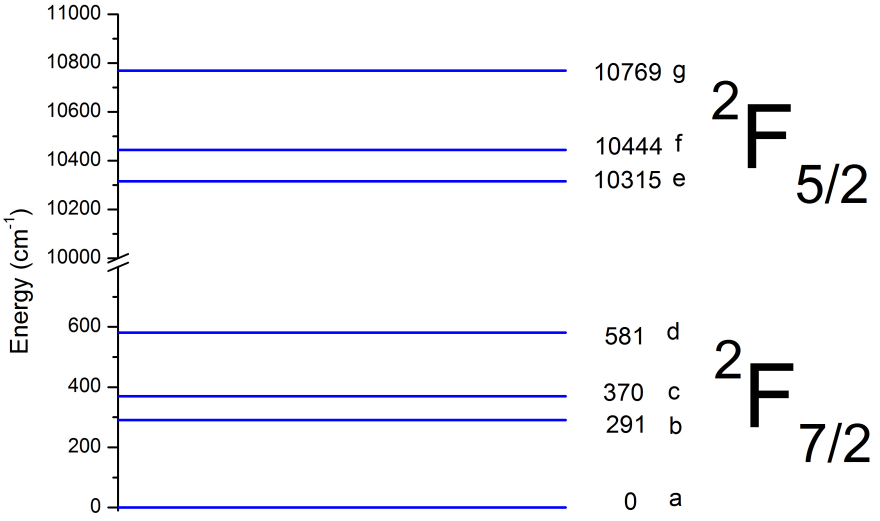

Figure 4.23: Energy levels of YP1 glass nanoparticles obtained from the absorption and emission spectrum at 300 K.

The estimation of the Stark splitting can be compared with the known data using the barycenter plot [128]. The barycenters of each configuration were calculated as the degeneracy weighted mean of the energy levels of the Stark configuration. The energy barycenters $E_{^2F_{5/2}}$ and $E_{^2F_{7/2}}$ are calculated using equation 4.7 and 4.8. The barycenter plot thus obtained is shown in Figure 4.24.

The barycenters for $E_{^2F_{5/2}}$ and $E_{^2F_{7/2}}$ obtained for bulk YP1 from the absorption and emission spectrum were 10509.6 cm^{-1} and 297.3 cm^{-1}respectively. For YP1 glass nanoparticles, this becomes 10510 cm^{-1} and 305 cm^{-1} respectively.

The position of YP1 in the barycenter plot (in Figure 4.13) is somewhat higher than the theoretical prediction. Usually Stark splitting for the ground levels are obtained from the emission spectrum. The Notch filter remove the band B' in the emission spectrum, which allows calculating the energy of the Stark level 'b' only from the extinction spectrum. This would definitely influence the barycenter $E_{^2F_{7/2}}$. Also the estimation of the spectral position of the absorption band A is influenced by the OH^-

absorption[1].

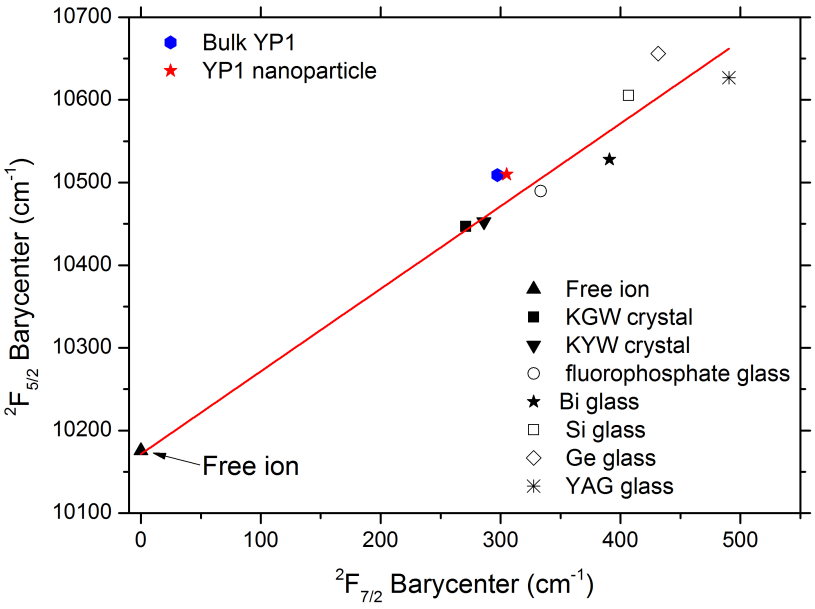

Figure 4.24: Barycenter of the $^2F_{7/2}$ versus $^2F_{5/2}$ levels in various host matrices for YP1 nanoparticle. The red line (straight line with slope = 1) represents the Barycenter plot where there is no dependence of the splitting between $^2F_{7/2}$ and $^2F_{5/2}$ as a function of the host matrix. The barycenters were calculated based on the equation 4.7 and 4.8. The energy values were obtained from the absorption and emission data of the YP1 glass nanoparticle. The points denoted by coloured symbols denote the measurements in this work and those which are black denote those from literature.

Reciprocity method for emission cross-section calculation

The reciprocity method (equation 4.9) was used to calculate the emission cross-sections of the nanoparticles from their absorption cross-sections (Figure 4.25). The absorption cross-section of the nanoparticles was calculated from the extinction spectrum using the equation 4.10.

The ratio of the partition functions of the lower to the upper Stark manifolds Z_l/Z_u was found to be 1.0139 for the nanoparticles. E_{zl} was determined by matching the magnitude of the emission spectrum of the nanoparticle to its absorption spectrum. The wavenumber where the normalized emission and absorption spectrum intercept is considered to

[1]The second overtone of the OH^- stretching band (3ν), produces an absorption band near 10310 cm^{-1} (970 nm), around the same region near band A [124].

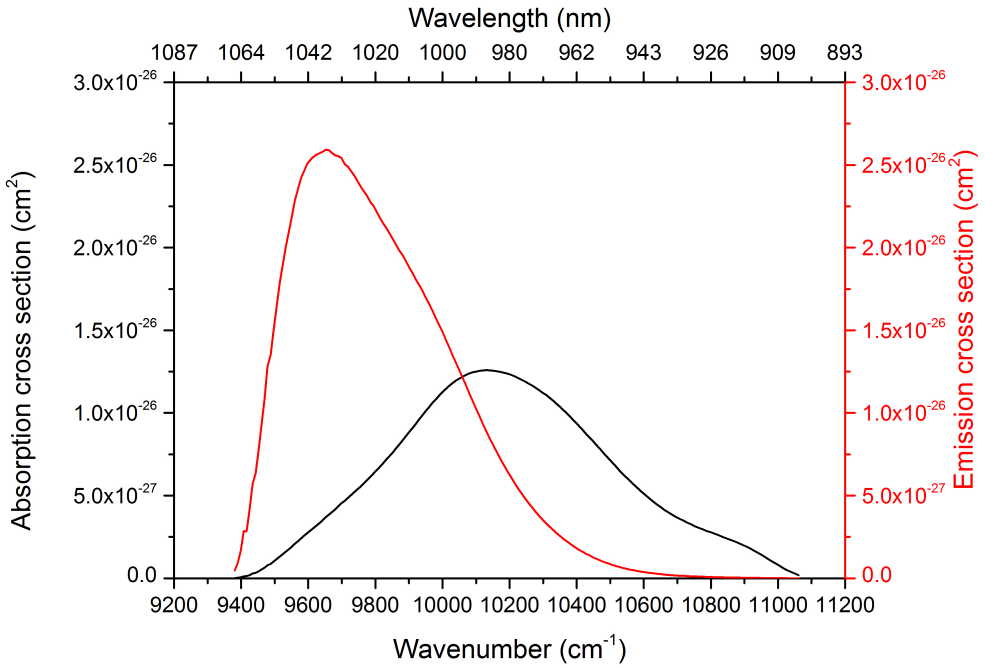

Figure 4.25: Experimentally obtained absorption cross-section (black trace) and calculated emission cross-sections for YP1 glass nanoparticles (red trace).

approximately correspond to the zero line energy in the present case (≈10010 cm^{-1}, see Figure 4.14 for the method used for bulk glass).
As for the bulk, the behaviour of the emission cross-section spectrum depends on the baseline of the extinction spectrum. The behaviour of the cross-sections is similar to the emission spectrum (Figure 4.26), below the zero line energy.

Comparison of anti-Stokes and Stokes emission intensities for YP1 nanoparticle

A comparison between the emission intensities for both excitation wavelengths can be made for the YP1 nanoparticles. Both spectra were recorded with same integration times. The normalized absorbance (scattering subtracted extinction) at 980 nm is 0.09. This value is more than a factor of 2 larger than upon excitation at 1023 nm (A=0.04). The laser at 980 nm was 5 times more powerful (100 mW) than at 1023 nm (20 mW) (see table 2.4). This made the excitation at 980 nm ca. 10 times more efficient than at 1023 nm. The anti-Stokes spectrum (excited at 1023 nm) however, when multiplied by a factor of 1.64 (Figure 4.27), gave ap-

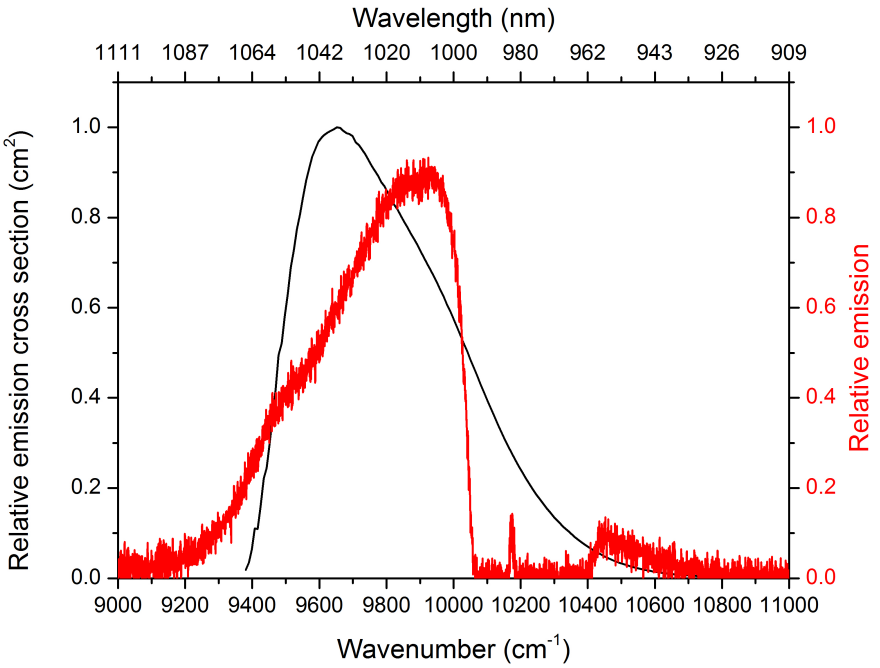

Figure 4.26: Calculated emission cross section (black trace) compared to measured emission spectrum (red trace) for YP1 nanoparticles.

proximately the same intensities as the Stokes emission spectrum. Hence the anti-Stokes emission is approximately $(10/1.64) \approx 6$ times stronger than Stokes emission (excited at 980 nm). For this comparison the following manipulations were performed on the data. The main errors in the measurements can be summarised as follows (a) Detector base line error for absorption (ΔE_1): The base line of the detector had to be subtracted from the emission curves (b) Filter transmission (ΔE_2): The filter transmission will reduce the overall emission recorded by 2-4 %. (c) Error in the subtraction of a base line (ΔE_3) to determine the particle absorption in the suspension: the base line polynomial subtracted from the particle absorption in the suspension adds to the error. The uncertainties in the correction lead to an overall systematic uncertainty , $\Delta \mathrm{E} = \sqrt{[(\Delta E_1)^2 + (\Delta E_2)^2 + (\Delta E_3)^2]} = \sqrt{[(.110)^2 + (.025)^2 + (0.100)^2]}$ $\approx 0.15 (\approx 15\%)$. ΔE_1 is obtained by studying the variation of the baseline over different measurements, ΔE_2 is obtained from the filter transmission spectrum, and ΔE_3 is obtained from the polynomial baseline fit for the nanoparticle extinction spectrum.

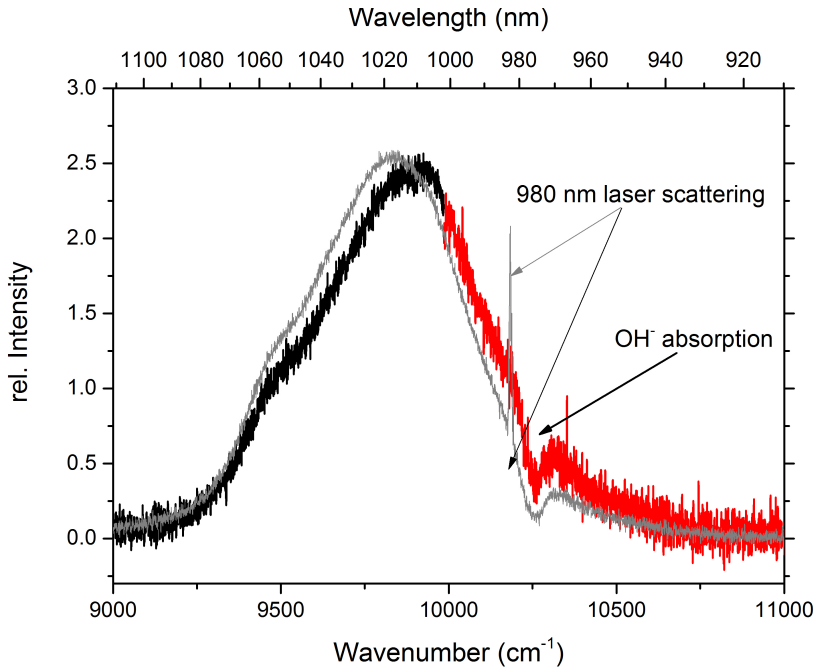

Figure 4.27: Emission spectra upon excitation at λ_{exc} =1023 nm (red, multiplied by a factor of 1.64) and λ_{exc} = 980 nm (black). Grey: fluorescence spectrum from the bulk (λ_{exc} = 980 nm).

Conclusion: A comparison of spectroscopic data of the YP1 nanoparticles to that of bulk YP1

Little modifications are observed in the electronic energy levels of Yb^{3+} when the ion is embedded in YP1 nanoparticle. This is as expected since quantum confinement is not prominent among lanthanide ions. But size reduction will quantize the phonon bands of the di-electric phosphate glass matrix in which Yb^{3+} is incorporated in. Since the electronic energy levels of Yb^{3+} and phononic energy levels of the glass are strongly coupled, the transitions involved during absorption and emission can be influenced through size reduction.

In the comparison between the spectroscopic data of bulk YP1 glass and nanoparticles of YP1 glass, changes in the extinction spectrum were observed whereas the emission spectrum remained the same. The extinction spectrum appeared to be broader for the nanoparticles. The maximum of the extinction spectrum was shifted by 198 cm^{-1} (∼19 nm) to lower energies for the nanoparticle suspension when compared to the bulk. There are no reports on shift of absorption maximum with particle

size for glasses, but similar red-shift in the absorbed frequencies with change in size is reported for Eu^{3+} doped Y_2O_3 nanocrystals [135]. A work on comparison of measurements in micron sized crystals and nano crystals of monoclinic Eu^{3+}: Eu_2O_3 by Yang *et al.* [135] showed that, for the excitation spectra of $^7F_0 \rightarrow {}^5D_1$ transition at site A[1] of Eu^{3+} ions in Y_2O_3 nanocrystals, the peak at 578 nm red shifts by 1 nm when the size of the particle decreases from 12 nm to 5 nm [135]. The shift is not that small considering that the change in size is from 12 nm to 5 nm. The excitation spectra of nanoparticles were found to be broadened significantly compared to the micron sized particles. Also, the time-resolved emission from the upper levels of the $^5D_1$ manifold in the Eu^{3+} nano crystalline material was observed to be qualitatively different from that observed in the micron sized crystals. The significant inhomogeneous broadening relative to the micron sized crystals appeared to be due to the presence of defects in the nanoparticles and activated surface sites or potentially adsorbed constituents on the surface. The surface defects on the YP1 nanoparticle can be the reason behind the red shift in YP1 nanoparticle extinction spectrum.

Considering the bands in the extinction spectrum of the bulk, the bands A, B and C had larger areas and heights. These three bands originate from the lowest Stark level 'a'. For the nanoparticles, the bands F, G and H corresponding to the transitions from Stark level 'b' appear to dominate in the extinction spectrum.

The inhomogeneous widths (W_G) of the bands F, G and H which correspond to transitions from Stark level 'b' decrease considerably for a nanoparticle when compared to bulk. W_G increases for band A which originates from the Stark level 'a'.

For the nanoparticle, either the transitions originating from the Stark level 'a' is suppressed or the transitions from the Stark level 'b' is enhanced during the absorption process.

In the emission spectrum, all the bands included are corresponding to the transitions originating from the Stark level 'e', which is the ground level of $^2F_{5/2}$. No modifications are found in the emission spectrum of the nanoparticle compared to the bulk.

[1]monoclinic phase of Eu^{3+}: Y_2O_3 possesses three crystallographically distinct cation sites denoted as A, B, and C.

4.3 Yb^{3+} doped tungstate crystal

The Stark energy levels of Yb^{3+} doped in laser crystals form a three level lasing system. Potassium gadolinium tungstate $KGd(WO_4)_2$ or in short, KGW allows high doping concentrations of Yb^{3+} with minimum concentration quenching [61]. In Yb^{3+} doped KGW, Yb^{3+} replaces the Gd^{3+} ions in the KGW matrix. Yb^{3+} in Yb:KGW crystal matrix experiences crystal field (section 1.2 in first chapter) produced by the monoclinic structure of K^+ and $(WO_4)^{2-}$ surrounding it. The crystal field effect in Yb:KGW is stronger compared to YP1 glasses and hence Stark levels are well defined in Yb:KGW crystals. The degenerate $^2F_{7/2}$ (ground) and $^2F_{5/2}$ (excited state) are also split into four and three levels respectively like that for Yb^{3+} in YP1 glass. The absorption and emission spectra of Yb^{3+} in KGW consist of parity forbidden transitions between these $4f^n$ levels with oscillator strengths of the order of 10^{-6}. The corresponding spectra are a measure of the modifications in the energy levels of Yb^{3+} by the crystal field. The reported electronic energy levels for Yb^{3+} in the KGW crystal matrix are shown in Figure 4.28 [58].

The spectroscopic properties of Yb:KGW crystals vary according to the crystallographic axes [131]. The Yb:KGW crystal shows anisotropic properties with respect to its three axes “a”, “b”, and “c”, resulting in polarization dependent absorption and emission spectra. The largest absorption and emission cross sections are observed for the light polarized along the “a” axis. The absorption and emission cross sections over three crystallographic axes obtained from Eksma optics [140] are shown in Figure 4.29. Yb:KGW crystals have absorption cross-sections of the order of $\approx 10^{-20}$ cm^2 at 981 nm and fluorescence life time of 0.3 ms.

In thermal equilibrium at 300 K, the relative population of Stark levels b, c and d are 45 %, 15 % and 7 % respectively of that of Stark level ’a’ (Figure 4.28). The levels e, f and g are separated from the ground $^2F_{7/2}$ by $\approx$10000 cm^{-1}, and hence are not populated at room temperature. There is strong coupling between the electronic energy levels of Yb^{3+} and phonon levels of KGW. The phonon energies in KGW matrix are high enough to enhance phonon assisted transitions between the Stark levels ’a’, ’b’, ’c’, and ’d’ of $^2F_{7/2}$ [18].

The emission and absorption spectra of Yb^{3+} in Yb:KGW are overlapping

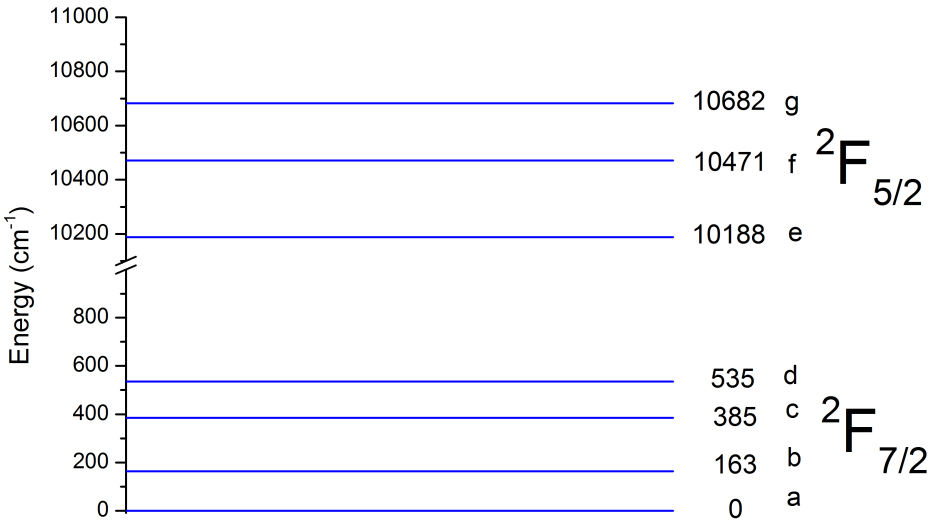

Figure 4.28: Energy levels of Yb:KGW. Energies of the Stark levels in cm^{-1} are obtained from [131], [141], [58]

(Figure 4.29) [58]. Yb^{3+} has broad band absorption from 900 nm to 1050 nm. Excitation of Yb^{3+} by means of $^2F_{7/2} \rightarrow {}^2F_{5/2}$ transition leads to reversed $^2F_{5/2} \rightarrow {}^2F_{7/2}$ transitions giving rise to intense and broad Yb^{3+} emission lines in the range of 970–1130 nm. The transition between the Stark levels 'a' and 'e' form the zero phonon band. The inhomogeneously broadened FWHM of the bands for Yb^{3+} in crystals are smaller than in glasses. Hence the emission bands due to $^2F_{5/2} \rightarrow {}^2F_{7/2}$ transitions in the spectrum are generally better resolved than the glasses. The strongest transition is the zero phonon transition e→a having an energy 10187 cm^{-1} (981.6 nm). There are three other major transitions from Stark level 'e' to $^2F_{7/2}$: e→b at 10024 cm^{-1} (997.6 nm), e→c at 9803 cm^{-1} (1020.1 nm) and e→d at 9653 cm^{-1} (1035.9 nm) [58]. Emission line widths as high as 4 nm are reported for Yb:KGW crystals [58].

This section of the thesis investigates the variation in the emission spectra of Yb:KGW nanocrystals compared to the uncut, unpolished bulk counterpart (refer Table 2.1). A 5% Yb^{3+} doped KGW bulk crystal (Yb:KGW bulk) was prepared by top-seeded solution growth method. A 3% Yb^{3+} doped KGW bulk crystal, prepared using the same method

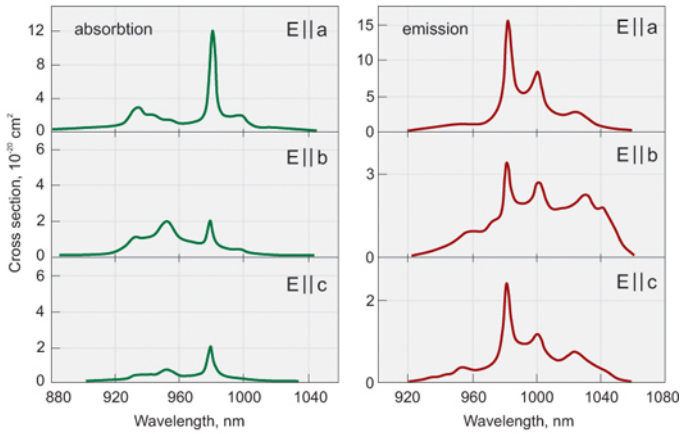

Figure 4.29: Relative absorption and emission cross section over a, b, and c axis for Yb:KGW (figure obtained from [140]). E||a implies electric field of the light is aligned parallel to the a-axis; the same nomenclature holds for the b and c axes. The light aligned parallel to the a-axis produces the maximum absorption and emission cross sections for the zero phonon transition a→e at 980 nm.

was ball milled to obtain nanocrystals (Yb:KGW HTSG). 5% Yb:KGW nanocrystals (Yb:KGW Pechini) were also prepared chemically by a sol-gel process known as Pechini method (refer Appendix Figure A.6). The crystal structure of the nanoparticles and bulk were identified by XRD measurements (Figure A.7 in appendix) and it could be observed that the diffracted intensities of all three samples (for all planes) are well matched, detecting less impurity phases. The crystalline nature of the samples was confirmed by the strongest features in the XRD spectrum. The nanocrystals were then drop cast on the surface of glass slides, forming thin layers of several μm thicknesses.

The variation of spectroscopic properties according to the crystallographic axes for nanocrystals deposited on a glass surface is hard to characterize since the orientation of the nanocrystals will not be uniform. Hence the variation of the emission with the change in crystal axes was not characterized for the three samples. The emission from the uncut, unpolished 5% Yb:KGW bulk crystal, 3% Yb:KGW HTSG nanocrystal, and 5% Yb:KGW Pechini nanocrystal are described in the next sections.

4.3.1 Emission spectrum of Yb:KGW bulk crystal

The emission spectrum of the uncut, unpolished 5% Yb:KGW was measured at two different excitation wavelengths, λ_{exc}= 981.8 nm and λ_{exc}= 1023 nm. The set-up for fluorescence is as described in the experimental section with the crystal replacing the cuvette (refer Figure 2.9) and the fluorescence perpendicular to the crystal was recorded using the Bruker FTIR spectrometer for an integration time of 5 min. The bulk crystal used was uncut and unpolished; hence the excitation beam is in an unknown direction with respect to the crystallographic plane. All the conditions during excitation and detection were kept the same for both the excitation wavelengths.

Emission spectrum of 5% Yb:KGW bulk crystal at λ_{exc}= 981.8 nm

According to the thermal population of the $^2F_{7/2}$ ground state, the Stark levels "a" , " b" , "c" and "d" can be excited at the excitation wavelength 981.8 nm (10185 cm^{-1}) can excite electrons present in any of the Stark levels in $^2F_{7/2}$ to the levels "e" , "f" , "g" in the excited state $^2F_{5/2}$. The corresponding $^2F_{5/2}\rightarrow$ $^2F_{7/2}$ transitions would lead to an emission spectrum shown in Figure 4.30.

The spectrum was recorded at 300 K using the FTIR spectrometer for an integration time of 5 min. Five emission bands are observed between 9000 cm^{-1} to 11000 cm^{-1}. The maxima of the emission bands are well resolved, indicating the reduced inhomogeneous broadening in Yb:KGW crystal compared to YP1 glass. The bands are labelled A', B', C', D' and E' (see Figure 4.30).

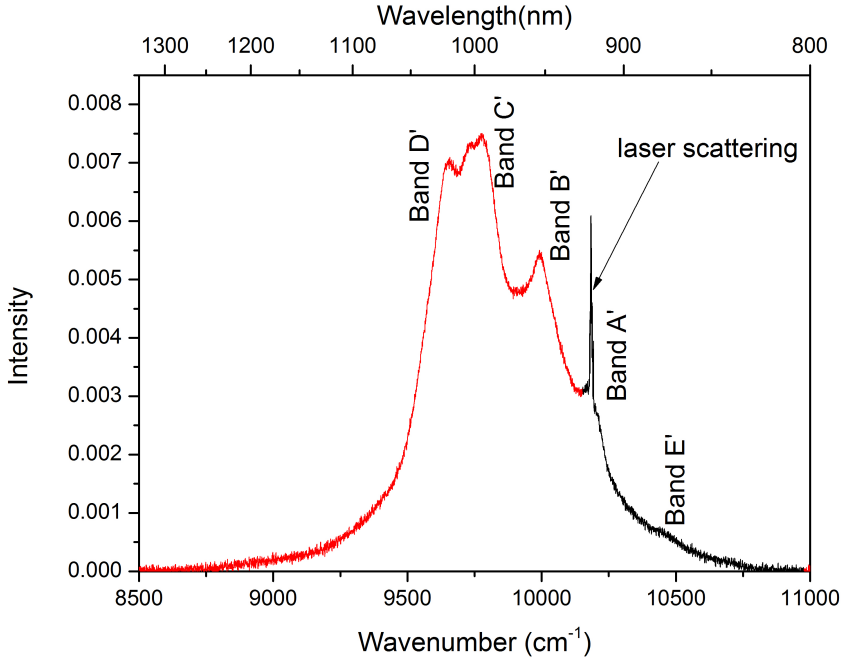

Figure 4.30: Emission spectrum of 5% Yb:KGW (λ_{exc}= 981.8 nm). The spectrum recorded is for an integration time of 5 minutes. A band name is assigned for each local emission maximum. The region in red denotes the Stokes part of the spectrum, and region in black denotes the anti-Stokes part of the spectrum.

The deconvolution of the spectra using Voigt profiles (refer to section 4.1) is used for obtaining the Lorentzian and Gaussian FWHM and the individual intensities of the bands.

Deconvolution of emission spectra at 981.8 nm using Voigt fits

A set of Voigt fits can be made for each of the bands A', B', C', D' and E' (Figure 4.31). The band centers and the linewidths are summarised in table 4.8. The band center values were initialized for the energy values in the literature [44], [61], [142]. The widths and area were unfixed.
Band A' (partially masked by laser scattering) at 10164 cm^{-1}(983.86 nm) in Figure 4.30 corresponds to the transition e→a, band B' at 9993 cm^{-1}(1000.71 nm) is the transition e→b, band C' at 9779 cm^{-1}(1022.59 nm) corresponds to the transition e→c and band D' at 9637 cm^{-1}(1037.66 nm) corresponds to the transition e→d. Only one band (band E') is observed in the anti- Stokes part of the emission spectrum. Band E' has a local maximum at 10468 cm^{-1}(955.20 nm) with an energy similar to the transition f→a (see discussion below). Finally, band A' is reported to be

the 'zero-phonon' band [58].

Band C', the maxima of which corresponds to the e→c transition has the highest emission intensity compared to the other bands (from Figure 4.30). The energetically lower most band D' has nearly the same emission intensity (96 %) as band C'. The emission intensity of band B' is only 73% of C'. The maximum of band A' (e→a) at 982.6 nm is only ≈ 2 nm separated from the excitation wavelength. Therefore the FWHM and the center position is least certain among all values shown in Table 4.8. The emission intensity of band E' is only 9 % of band C'.

The band center of E' in the anti-Stokes emission region (at 10468 cm^{-1}) is close to the expected energy of f→a transition at 10471 cm^{-1}. All the other emission bands have energies matching transitions from the Stark level 'e'. Since level 'f' is short lived (check analysis on YP1 glass, section 1.2) an emission from that level is highly unlikely to happen. Hence there is a possibility that band E' is a vibronic band. KGW crystals have several vibrational modes (phonon quanta) of WO_6, WOOW and WOW groups (known as the internal vibrational modes) and Gd–O, K–O bonds (known as external vibrational modes). The Raman studies on KGW crystals reveal several peaks ranging from 210 to 905 cm^{-1}[64]–[66], [143], [144]. The several vibrational modes of KGW single crystal obtained using Raman spectroscopy are listed in Table 4.9 [145]. The Raman set-up with excitation wavelength at 533 nm could not produce the Raman spectra due to very strong impurity luminescence at 533 nm (described in the last section 4.3.3). Hence Raman data from the literature had to be used for a comparison.

Given that the electronic and phonon energy levels in Yb:KGW are coupled, it is possible that the band E' is the resultant of an electronic transition involving an association with phonons. If the electronic line e→c (9673 cm^{-1}) absorb energy from a phonon of energy 760 cm^{-1}, it can result in the vibronic band E' at 10459 cm^{-1}. Raman studies on KGW single crystals describe a very intense vibrational band originating from a stretch vibration ν(W–O) vibration in WO_6 at 760 cm^{-1}(see table 4.9). Also the two stretch bands ν(WOOW) and ν(WOW) at 770 cm^{-1} and 810 cm^{-1} respectively will also generate the same band. The peak located at 810 cm^{-1} is assigned to the antisymmetric stretching vibration of WOW oxygen bridge bonds. The Raman peak at 770 cm^{-1} is assigned to the

coupling of stretching vibrations of WOOW. The association of a phonon with an electronic line e→c is quite possible and is studied for anti-Stokes efficiency measurements by Ruan *et al.* [86]. There is no explanation to why the association is restricted only to the e→c electronic line. An association with phonons to form vibronic bands having energies lower than the electronic band are reported for Yb^{3+} doped $Ca_{1-X}Yb_XF_{2+X}$ crystals [45]. The e→d emission at 10199 cm^{-1}(980.5 nm) in the Yb^{3+} doped $Ca_{1-X}Yb_XF_{2+X}$ crystal was shifted to 9879 cm^{-1}(1012.24 nm) due to the association with the phonon of vibrational energy 321 cm^{-1}.

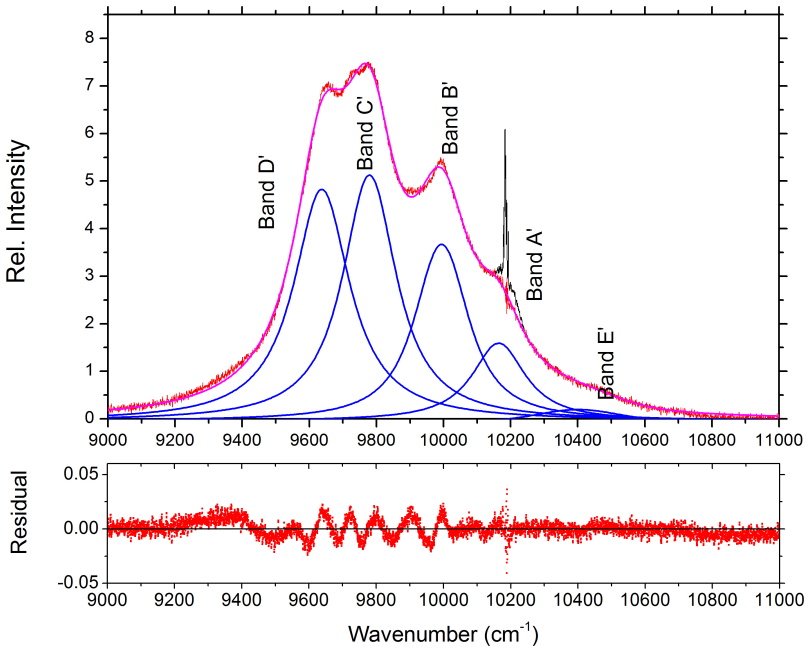

Figure 4.31: Voigt fits for 5% Yb:KGW bulk crystal emission features (λ_{exc}= 981.8 nm). The blue lines represent the Voigt fits of the corresponding data in red. Magenta line represents the sum of all fits. Black line denotes the laser peak in the emission spectrum which is not included for fitting. Bottom plot shows the residuals obtained for the Voigt fits.

Band name	Assignment	Band center (x_0) cm^{-1} (nm)	Lorentzian width (W_L) (cm^{-1})	Gaussian width (W_G) (cm^{-1})	Area a. u
A'	e→a	10164 cm^{-1}(983.86 nm)	≃ 0	202±30	0.49±0.05
B'	e→b	9993 cm^{-1}(1000.7 nm)	36±7	186± 6	1.06±0.08
C'	e→c	9779 cm^{-1}(1022.5 nm)	68 ± 12	164± 16	1.55±0.06
D'	e→d	9637 cm^{-1}(1037.66 nm)	26± 19	187±13	1.55±0.03
E'	f→a or vibronic band	10459 cm^{-1}(956.92 nm)	120± 5	276±17	0.07±0.01

Table 4.8: Fit parameters obtained for Voigt fits of Yb:KGW bulk emission (λ_{exc}= 981.8 nm).

Raman shift (cm^{-1})	Assignment
905	ν(W–O) in WO_6
810	ν(WOW)
770	ν(WOOW)
760	ν(W–O) in WO_6
689	ν(W–O) in WO_6
531	ν(WOOW)
441	δ(WOW)
404	ν(W–O) in WO_6
375	δ(W–O) in WO_6
351	γ(WOOW)
210	T´(Gd^{3+})

Table 4.9: Raman shift and assignment for the phonon bands in KGW crystal at 300 K obtained from Zhang *et al.* [145]. Abbrevations: ν - stretching in-plane modes, δ - bending in-plane modes, γ - out of plane bending modes , T´ is the translatory mode.

The Gaussian FWHM are considerably smaller for Yb:KGW crystals (≈190 cm^{-1}) when compared to YP1 glasses, where the average FWHM was found to be 275 cm^{-1}. In Yb:KGW emission spectrum, the bands B', C' and D' have similar Gaussian widths (Table 4.8) and those of bands A' and E' are larger. The FWHM of band A' is only an estimate since the fit is affected by the feature due to strong stray light.
Average Lorentzian FWHM for Yb:KGW crystals (≈40 cm^{-1}) are smaller when compared to YP1 glasses (≈65 cm^{-1}). The Lorentzian FWHM of the band E' is larger compared to the other three bands. If the band represents the electronic transition f→a, this is in accordance with the concept of homogeneous widths described in section 4.1 (Figure 4.2). This is in agreement with the interpretation of band E' to be based on a vibronic transition. The vibronic band E' in the emission spectrum of the YP1 glass also exhibited a larger Lorentzian FWHM compared to the other emission bands.
The main transitions involved in the emission spectrum in Yb:KGW are schematically shown in Figure 4.32.

Emission spectrum of 5% Yb:KGW bulk crystal at λ_{exc}= 1023 nm

The 5% Yb:KGW bulk crystal was excited at 1023 nm (laser characteristics described in table 2.4, Figure A.3 in appendix). The emission

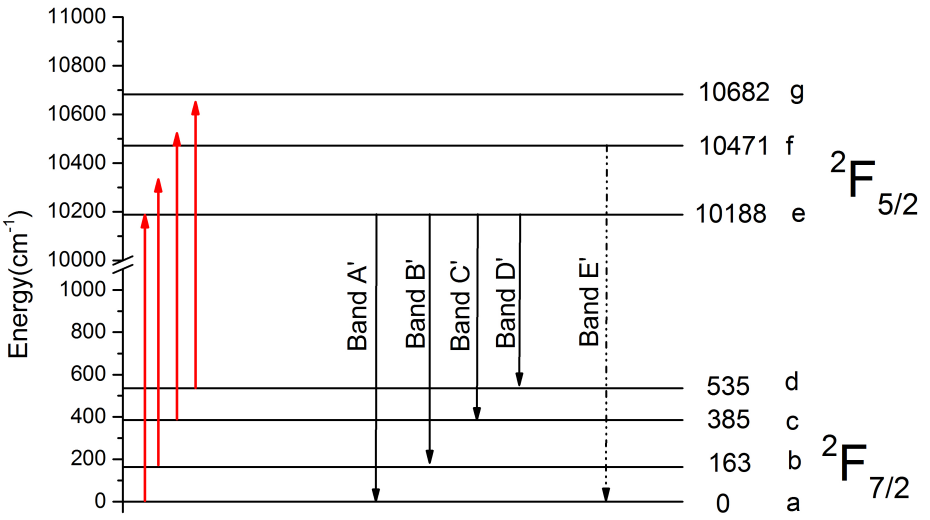

Figure 4.32: Emission transitions in Yb:KGW (λ_{exc}= 981.8 nm) for 5% Yb:KGW. The red lines show the laser excitations from the ground (length of the arrow is roughly the excitation energy in cm^{-1} according to the energy axis scale), and the black lines show transitions corresponding to the maxima of the bands A', B', C', D' and E' in the emission spectrum. The dotted black line for band E' denote the possibility of a phonon association.

Band name	Assignment	Band center (x_0) cm^{-1} (nm)	Lorentzian width (W_L) (cm^{-1})	Gaussian width (W_G) (cm^{-1})	Area a. u
A'	e→a	10183 cm^{-1}(982.00 nm)	≃0	153±6	0.08±0.01
B'	e→b	10003 cm^{-1}(999.7 nm)	32±7	175± 6	0.39±0.07
D'	e→d	9664 cm^{-1}(1034.76 nm)	36± 19	207±13	0.5±0.01
E'	f→a or vibronic band	10468 cm^{-1}(955.29 nm)	100± 5	270±17	0.07±0.01

Table 4.10: Fit parameters of Voigt fits of 5% Yb:KGW bulk emission (λ_{exc}= 1023 nm).

spectrum obtained is shown in Figure 4.33. The emission spectrum extended from 9000 cm^{-1} to 10900 cm^{-1}. Bands B', A' and E' are present in the emission spectrum, while band C' is swamped by the laser scattering. Band D' is also slightly influenced by the laser scattering. A deconvolution of the emission spectrum using Voigt fits is also shown in Figure 4.33. The fit parameters thus obtained for the Voigts are given in table 4.10. Fit conditions are as previously explained for YP1 glasses (section 4.2).

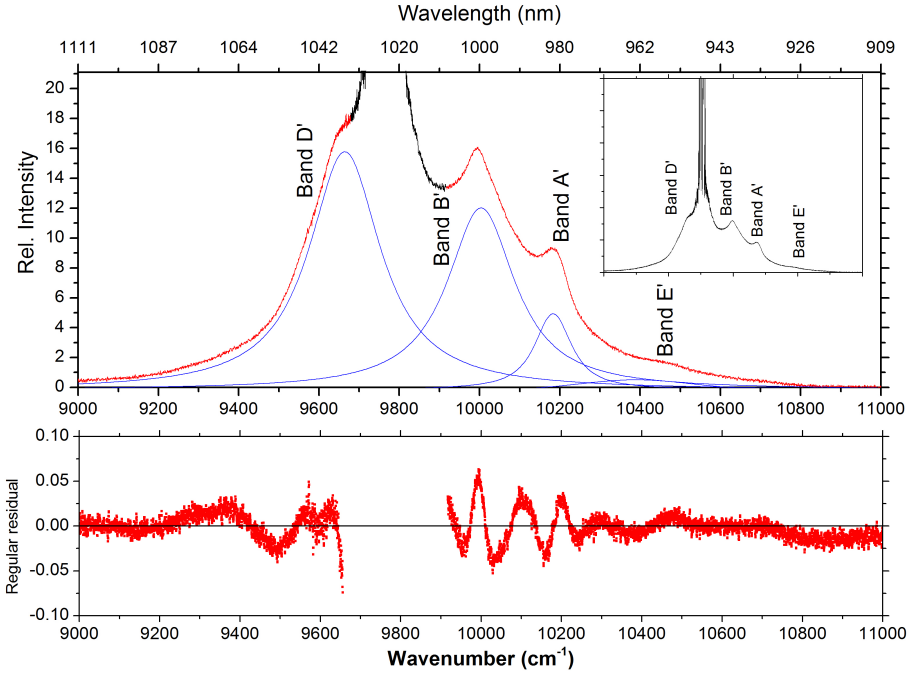

Figure 4.33: Emission spectrum of 5% Yb:KGW bulk crystal at λ_{exc}=1023 nm (anti-Stokes emission) including Voigt fits (blue line) of the corresponding data in red. Inset shows the overall emission spectrum. Lower panel shows the residuals obtained for the Voigt fits.

FWHM of bands

The Lorentzian FWHM of bands in the anti-Stokes emission are similar to the Stokes emission spectrum for the bulk crystal (within $\approx$ 20 %). e$\rightarrow$a transitions have extremely smaller Lorentzian FWHM compared to other transitions for both excitation wavelengths.

The larger Gaussian FWHM for band A' upon excitation at 981.8 nm is due to the presence of the laser scattering peak. Band C' is not included in the fits since it was influenced by the presence of the laser scattering. Gaussian width decrease by 25% for band A', 5% for band B' , and increase by 10% for band D' and 2% for band E'.

4.3.2 Emission spectra of Yb:KGW nanoparticles

Emission spectra of 3% Yb:KGW HTSG nanoparticles[1] and 5% Yb:KGW Pechini nanoparticles upon excitation at $\lambda_{exc} = 981.8$ nm were recorded and compared. Suspensions of these nanoparticles in various solvents (ethanol, propanol, DMSO, water, hexane) did not emit due to efficient quenching (possibly solvent quenching), hence suspensions were not used for nanoparticle emission studies. The nanoparticles were instead deposited on a glass surface. The excitation beam was propagating collinear to the thin side of the glass slide. The fluorescence was recorded right angle to the excitation beam using the FTIR spectrometer (set-up described in Figure 2.9). The spin coating procedures for both the samples were the same; only different sample concentrations were used. The nanoparticles deposited on the glass surface have an average diameter of $\approx$ 250 nm, well above the quantum confinement regime for rare-earth ions [146], [147] (refer Figures 2.3, 2.4). Both sample types were excited in the same way and the acquisition times used for recording the spectra were 3 hrs.

Emission spectrum of 3% Yb:KGW HTSG nanoparticles upon excitation at $\lambda_{exc} = 981.8$ nm

Figure 4.34 shows the emission spectrum of 3% Yb:KGW HTSG nanoparticles. The only pronounced difference between the bulk and the HTSG nanoparticle emission spectra is the change in emission intensity due to change in concentration.
Laser scattering at the excitation wavelength was so large that a Notch filter (NF 980-41 in Figure 2.12) was used to prevent it from dominating the fluorescence. The transmission loss through the filter changes the

[1] The emission spectra of the nanoparticles at $\lambda_{exc} = 1023$ nm were dominated by laser scattering. A necessary short pass filter at 1000 nm cut out most of the spectrum except bands A' and E'. Thus not much information can be gathered from the emission spectra. Hence the corresponding measurements are not described in this section. The parts of the emission spectra that were measurable did not show any difference other than the change in intensity due to the difference in concentration between the two samples. The emission spectra obtained when excited at $\lambda_{exc} = 1023$ nm for both the 3% Yb:KGW HTSG and 5% Yb:KGW Pechini samples are nevertheless included in Appendix B, Figure B.6.

relative height between the bands D' and C' (as recorded by the detector) when compared to the bulk crystal (Figure 4.31, no filter was used for bulk emission spectrum). Band B' is partially and band A' is fully cut out by the filter. Also the intensity of band E' is relatively higher than that for the bulk in Figure 4.31. The increase in height of band B' (when compared to the bulk crystal) is due to the filter transmission (shown in inset of Figure 4.34).

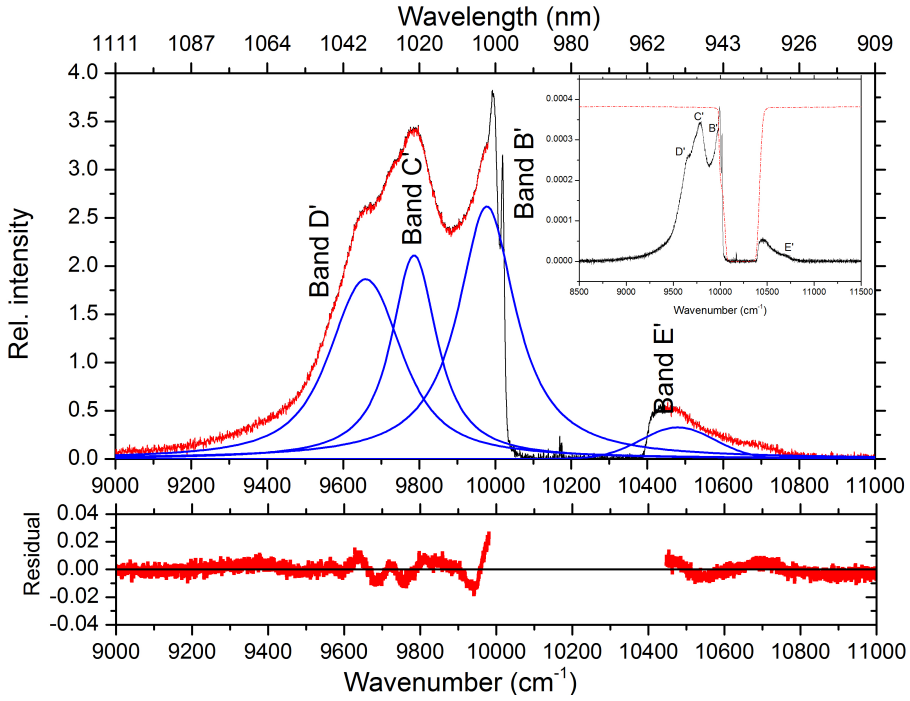

Figure 4.34: Emission spectrum of 3% Yb:KGW HTSG (λ_{exc}= 981.8 nm) nanoparticle deposited on glass (thickness of the coating ≃0.6 to 0.9 μm, particle average diameter ≃ 250 nm) at room temperature. The integration time of the recorded spectrum is 3 hrs. Voigt fits for the data corresponding in red of Yb:KGW HTSG emission features are shown in blue. Lower panel plot shows residuals obtained for the fits. Inset: The black line is the emission spectrum and the red dotted line is the transmission of NF 980-41 normalized to the maximum emission intensity.

Band name	Assignment	Band center (x_0) (cm^{-1})	Lorentzian width (W_L) (cm^{-1})	Gaussian width (W_G) (cm^{-1})	Area a. u
Band B'	e→b	9989±0.68 cm^{-1}(1001.10 nm)	43±20	221±30	70±5
Band C'	e→c	9786±0.15 cm^{-1}(1022.07 nm)	78±30	201±45	40±2
Band D'	e→d	9657±0.30 cm^{-1}(1035.51 nm)	33±24	184±22	50±4
Band E'	f→b or vibronic band	10465±1.05 cm^{-1}(955.41 nm)	130±23	286±33	7±1

Table 4.11: Band assignments and Voigt fit parameters of 3% Yb:KGW HTSG emission (λ_{exc}= 981.8 nm).

Band B' has the maximum intensity and area (Table 4.11). Band A'

which is in the filter cut off range is not included in the fits. Bands C' and D' have similar intensities.
Deconvolution of the spectrum using Voigt profiles gives an estimate of the Lorentzian and Gaussian FWHM and areas of the bands. Only the spectral parts where the transmission of the filter was larger than 99% were included in the fits. The fits were made for the data in red in Figure 4.30. Table 4.11 shows the Voigt fit parameters. The Lorentzian FWHM (W_L) shows an average increase of 16% when compared to the bulk. The surface defects and active sites present on the nanoparticle leads to higher non-radiative processes, which resulted in the increase of W_L. The error of FWHM is relatively higher compared to the bulk due to the filter cut off region.
There is an average increase of 20% in Gaussian FWHM (W_G) compared to the bulk crystal. The maximum increase in W_G is observed for the band C'. The increase in W_G for the emission bands should have contributions from the increased surface defects on the nanoparticle surface. The irregularities in the surface (check Figure 2.3, SEM of 3% Yb:KGW HTSG nanoparticle) are consistent with this interpretation.

Emission spectrum of 5% Yb:KGW nanoparticles prepared by Pechini method $\lambda_{exc} = 981.8$ nm

The emission spectrum of 5% Yb:KGW nanoparticles prepared by the Pechini method is shown in Figure 4.35. There is a definitive change in the emission features in the Stokes part of the emission spectrum. The emission band maxima which show the bands C' and D' were clearly resolved in the 3% Yb:KGW HTSG emission spectrum. A pronounced difference from the emission spectrum of 5% Yb:KGW Pechini nanoparticles is that the band D' is not clearly resolved. The intensity at 9637 cm^{-1} where the origin of the band D' is placed is considerably decreased.
The Voigt fits made to the emission features in the 5% Yb:KGW emission spectrum is also shown in Figure 4.35. The fit procedure followed is the same as for 3% Yb:KGW HTSG nanoparticles. The portion of the spectrum cut off by the filter was avoided from the fits. The parameters thus

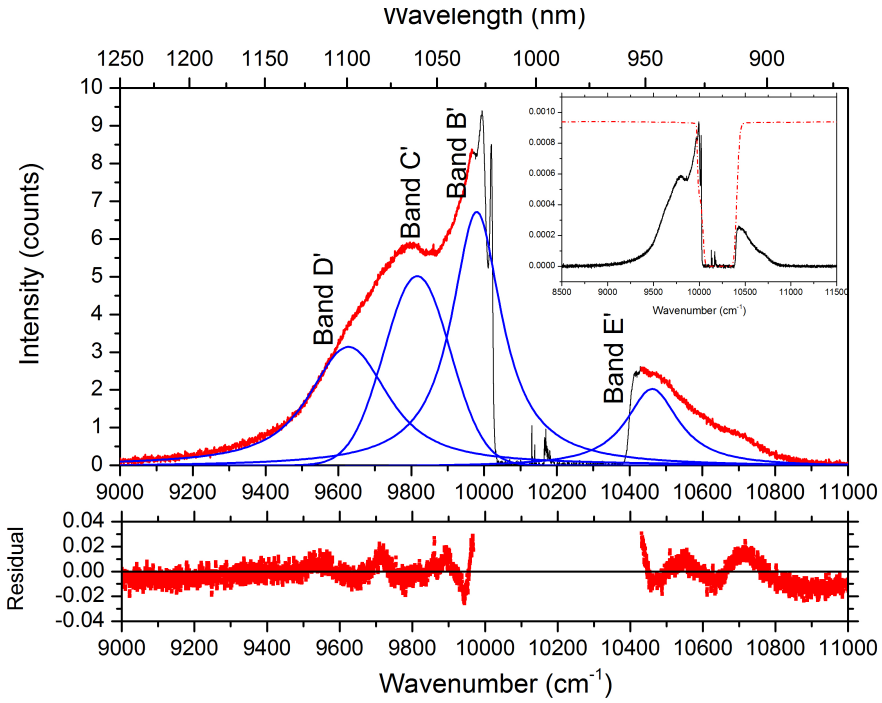

Figure 4.35: Emission spectrum of 5% Yb:KGW Pechini (λ_{exc}= 981.8 nm) nanoparticle deposited on glass (thickness of the coating≃0.6 to 0.9 μm, particle average diameter ≃250 nm) at room temperature. The integration time of the recorded spectrum is 3 hours. Blue lines represent Voigt fits for the corresponding data in red. Bottom plot shows residuals obtained for the Lorentzian fits. Inset: The black line is the emission spectrum and the red dotted line is the transmission of NF 980-41 normalized to the maximum emission intensity.

obtained are summarized in table 4.12. For the HTSG nanoparticles, the maximum intensity of the band D' was 96% of band C', while for Pechini nanoparticles, this decreased to 46%. The reduction in intensity of band D' would imply quenching of the transition e→d for the nanoparticles prepared by Pechini method. No reasoning can be provided for now as to why only the transition e→d is selectively quenched.

The Gaussian FWHM (W_G) have considerably increased compared to the 3% Yb:KGW Pechini nanoparticles. For band D', W_G has increased from 184 cm^{-1} in 3% Yb:KGW HTSG to 253 cm^{-1} in 5% Yb:KGW Pechini. The increase in the Gaussian FWHM results in both bands C' and D' having the same area despite the decrease in relative intensities.

Band name	Assignment	Band center (x_0) (cm^{-1})	Lorentzian width (W_L) (cm^{-1})	Gaussian width (W_G) (cm^{-1})	Area a.u
Band B'	e→b	9979±0.95 cm^{-1}(1001.10 nm)	46±15	167±34	110
Band C'	e→c	9786±0.44 cm^{-1}(1022.07 nm)	73±23	220±33	110
Band D'	e→d	9635±0.97 cm^{-1}(1036.91 nm)	63±25	253±12	65
Band E'	f→b	10462±1.55 cm^{-1}(955.01 nm)	150±11	290±37	56

Table 4.12: Peak position and widths of Voigt fits of 5% Yb:KGW Pechini emission (λ_{exc}= 981.8 nm).

4.3.3 Impurity emission in Yb:KGW

Rare earths are regularly found together in nature [146] and are hard to separate them chemically. It is not easy to estimate their purity. Probably the most sensitive methods for detecting small amounts of impurities are fluorescence spectroscopy and paramagnetic resonance methods [147], but it is hard to estimate it quantitatively and accurately.
In the experiments presented here, a strong green impurity luminescence was visible at the surface of the bulk Yb:KGW crystal when excited at 981.8 nm. This section describes the processes leading to impurity luminescence from the 5% Yb:KGW bulk crystal.

Up-conversion in Yb^{3+}-Er^{3+} co-doped systems

The spectrum of the green glow in Yb:KGW bulk crystal upon excitation at 980 nm is shown in Figure 4.36. The spectrum was recorded using the set-up described in Figure 2.9 with the Andor spectrometer on the detector side. The spectrum was obtained with an integration time of 3 sec. The green luminescence emission bands resembled $^2H_{11/2}\rightarrow{}^4I_{15/2}$ transition from Er^{3+} through energy transfer from Yb^{3+} [130], [148], [149]. Er^{3+} occur as a natural impurity in the Yb:KGW crystal.
The energy transfer process from Yb^{3+} to Er^{3+} can be described with the help of an energy level diagram sketched in Figure 4.37. The energy overlap between the $^2F_{5/2}$ level in Yb^{3+} and the $^4I_{11/2}$ level in Er^{3+} allows the efficient resonant energy transfer between both the ions [148], [150]. After the excitation in $Yb^{3+}$to $^2F_{5/2}$energy transfer to Er^{3+} ions can occur and lead to the excitation of the $^4I_{11/2}$ level in Er^{3+} (process 'a' in Figure 4.37) [151].

$$^2F_{5/2}(Yb^{3+}) +^4 I_{15/2}(Er^{3+})\rightarrow{}^2F_{7/2}(Yb^{3+}) +^4 I_{11/2}(Er^{3+}) \qquad (4.10)$$

From the $^4F_{11/2}$ (Er^{3+}) level the energy can be either transferred back to Yb^{3+} or the Er^{3+} ions relaxes to the ground state. This relaxation produces luminescence around 10000 cm^{-1}(1000 nm) (associated with the $^4I_{11/2} \rightarrow {}^4I_{15/2}$ transition). The metastable state $^4I_{13/2}$ can also be populated via non-radiative relaxation from $^4I_{11/2}$. Relaxation from $^4I_{13/2}$ to the electronic ground ($^4I_{13/2} \rightarrow {}^4I_{15/2}$ transition) creates an emission band around 6666.67 cm^{-1} (1500 nm). Both these emissions are much weaker than the Yb^{3+} emission and hence could not be recorded. Er^{3+} in state $^4I_{13/2}$ can also absorb energy from another Yb^{3+} ion. Energy transfer from $^2F_{5/2}$ (Yb^{3+}) can lead to the population of $^2H_{11/2}$ (Er^{3+}) state.

$$^2F_{5/2}(Yb^{3+}) + {}^4I_{13/2}(Er^{3+}) \rightarrow {}^2F_{7/2}(Yb^{3+}) + {}^2H_{11/2}(Er^{3+}) \qquad (4.11)$$

(shown as process b in figure 4.37)
$^2H_{11/2} \rightarrow {}^4I_{15/2}$ transitions in Er^{3+} generate the emission at 530 nm. Some Er^{3+} ions excited to $^2H_{11/2}$ will also relax non-radiatively to $^4S_{3/2}$ and relax to the ground $^4I_{15/2}$ giving green emission around 552 nm.
Some Er^{3+} ions excited to $^2H_{11/2}$ will also relax non-radiatively to another long lived state,$^4F_{9/2}$. Er^{3+} in $^4F_{9/2}$ can also absorb energy from adjacent Yb^{3+} and be excited to $^4H_{9/2}$ according to the energy transfer mechanism,

$$^2F_{5/2}(Yb^{3+}) + {}^4F_{9/2}(Er^{3+}) \rightarrow {}^2F_{7/2}(Yb^{3+}) + {}^2H_{9/2}(Er^{3+}) \qquad (4.12)$$

(shown as process c in figure 4.37)
Er^{3+} ions in $^2H_{9/2}$ level relax to the ground $^4I_{15/2}$ producing violet emission at 407 nm.
The Yb^{3+} ion acts as a donor of energy to the Er^{3+} acceptor ion. The quantum yield of this "resonance energy transfer" (better known as "Förster resonance energy transfer") is based on dipole-dipole coupling mechanism and scales with $(r_{da})^{-6}$, r_{da} is the donor-acceptor separation.
This energy transfer process will diminish the population of $^2F_{5/2}$ hence affecting the quantum efficiency and lifetime of $^2F_{5/2}$ to $^2F_{7/2}$transition.

Other impurities present in 5% Yb:KGW bulk crystal

Figure 4.38 shows the emission spectrum of Yb:KGW bulk crystal when excited at 450 nm. The set-up in Figure 2.9 was used. The laser power

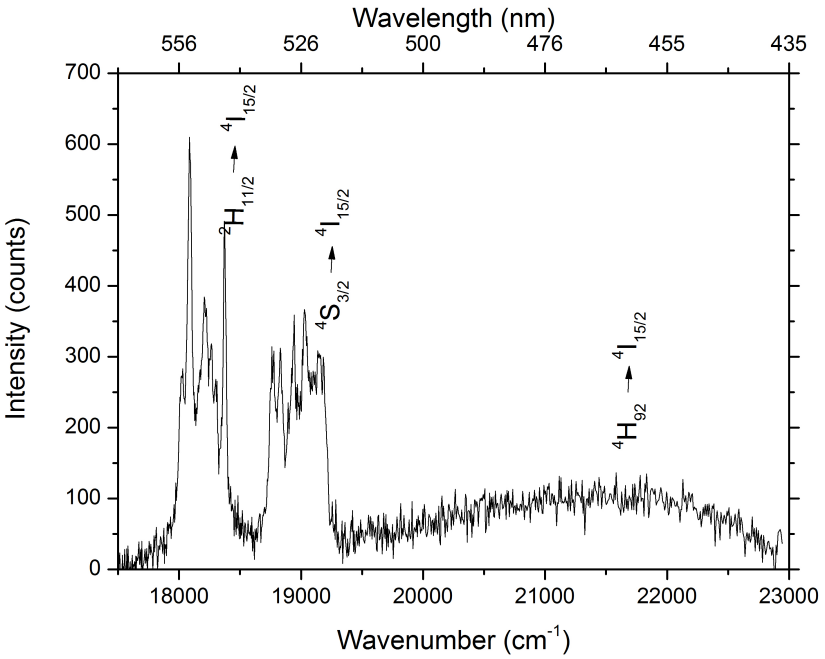

Figure 4.36: Up-converted emission from 5% Yb^{3+}:KGW bulk crystal due to resonance energy transfer between Yb^{3+} and an impurity Er^{3+} . Excitation wavelength is 980 nm. Integration time of the spectrum is 3 s.

was 300 mW. The luminescence was recorded using the Andor spectrometer. Five bands were recorded in the range 640-500 nm. Each of these bands can be assigned to an impurity rare earth present in the KGW matrix as shown in table 4.13. The emission bands were identified as originating from three impurity ions, namely Er^{3+}, Dy^{3+} and Sm^{3+} [153]–[161].

The excitation and emission process in Sm^{3+} and Dy^{3+} can be sketched as different processes as shown in figure 4.39. The excitation at 22222 cm^{-1} (450 nm) populates the $^4F_{7/2}$ level of Sm^{3+}. $^4F_{7/2}$ is a short-lived state and non-radiative relaxation processes from that state will populate $^4G_{5/2}$ [152]. $^4G_{5/2}\rightarrow{}^6H_{7/2}$ gives rise to the band 5 at 16658 cm^{-1} (599 nm) in Figure 4.38. Electronic transitions $^4G_{5/2}\rightarrow{}^6H_{5/2}$ can also occur which produces band 3 at 17825 cm^{-1} (561 nm) in Figure 4.38.

The excitation at 22222 cm^{-1}(450 nm) also populates the $^4I_{15/2}$ level of Dy^{3+}. Non-radiative transitions from $^4I_{15/2}$ will populate the level $^4F_{9/2}$. $^4F_{9/2}\rightarrow{}^6H_{11/2}$luminescence will give rise to band 4 at 17523 cm^{-1} (570 nm). $^4F_{9/2}\rightarrow{}^6H_{13/2}$ luminescence at 20833 cm^{-1} (481 nm) can in principle also be observed [151], [159], [161] but was not covered by the

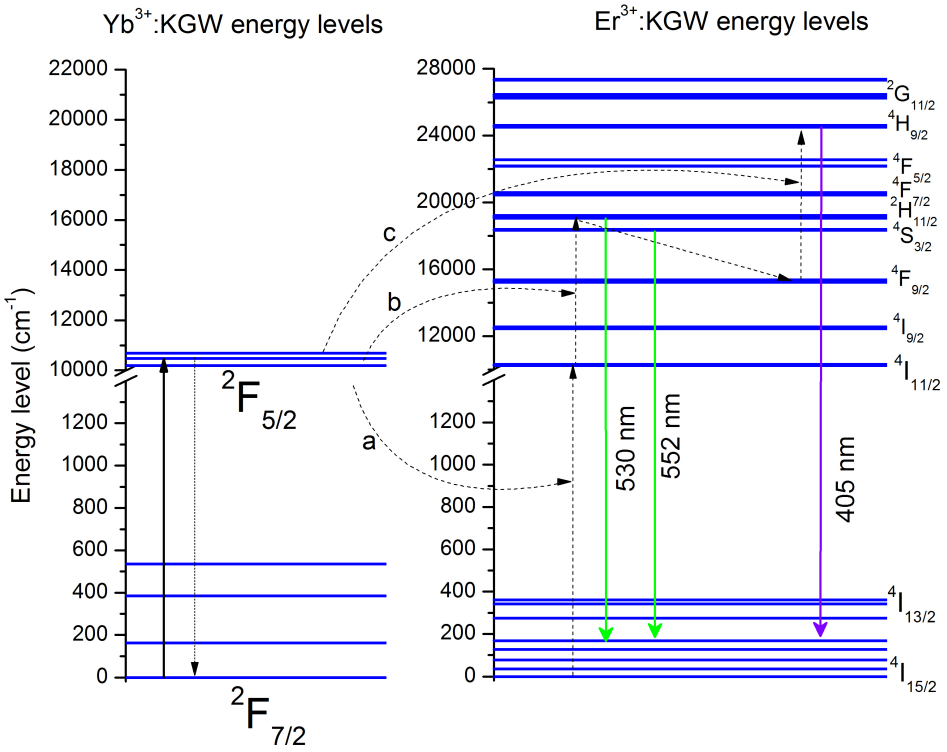

Figure 4.37: Excitation scheme of up-conversion luminescence at 300 K. Energy transfer between Yb^{3+} and Er^{3+} populates $^4I_{11/2}$ in Er^{3+}(process 'a'). $^4I_{11/2}$ is meta-stable, and can again receive energy from another Yb^{3+} ion at $^2F_{5/2}$, populating the level $^2H_{11/2}$ of Er^{3+} (process 'b'). $^2H_{11/2} \rightarrow {}^4I_{15/2}$ transitions in Er^{3+} generates green light having center wavelength 530 nm. Parts of Er^{3+} ions getting excited to $^4H_{11/2}$ will also relax non-radiatively to $^4S_{3/2}$ and relax to ground $^4I_{15/2}$ giving green emission around 552 nm. Radiative relaxation from $^4H_{11/2}$will also populate $^4F_{9/2}$, which is also meta-stable. Er^{3+} at $^4F_{9/2}$ can also absorb energy from adjacent Yb^{3+} and be excited to $^4H_{9/2}$(process 'c'). Er^{3+} ions in $^2H_{9/2}$ relax to the ground $^4I_{15/2}$ producing violet emission at 405 nm. The energy values are obtained from Pujol *et al.* [152].

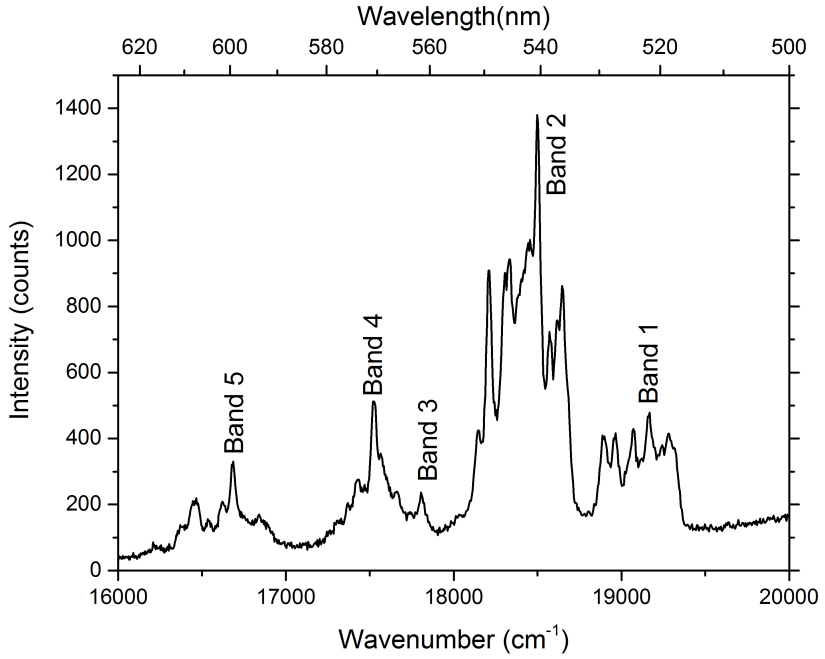

Figure 4.38: Impurity emission from 5% Yb:KGW bulk when excited at 450 nm. The edge at the higher energy side is due to the presence of the cut off filter at 488 nm. Bands 1 and 2 represent the emission from Er^{3+} ions, bands 3 and 5 are emissions from Sm^{3+} and band 4 is emission from Dy^{3+}. The shaded region is the short pass filter cut off region, which cuts off the 481 nm emissions from Dy^{3+}. The spectrum is obtained for an integration time of 3 sec.

measurement shown in Figure 4.38.

Band 1 and band 2 originate from Er^{3+} ions. The excitation energy at 22222 cm^{-1}(450 nm) populates the $^4F_{5/2}$ level in Er^{3+} (Figure 4.37). Non-radiative relaxation from $^4F_{5/2}$ level populates the Stark level $^2H_{11/2}$. Band 1 at 18867 cm^{-1} (530 nm) is the resultant of the transitions $^2H_{11/2} \rightarrow {}^4I_{15/2}$. Er^{3+} can again non-radiatively relax from $^2H_{11/2}$ to $^4S_{3/2}$. $^4S_{3/2} \rightarrow {}^4I_{15/2}$ transitions gives rise to the band 2 at 18115 cm^{-1} (552 nm) (Figure 4.38). Band 2 appears stronger than band 1 since $^2H_{11/2} \rightarrow {}^4I_{15/2}$ is spin forbidden. Band 1 extends from 19284 cm^{-1} to 18886 cm^{-1} and band 2 extends from 18646 cm^{-1} to 18208 cm^{-1}.

Band 3 at 17804 cm^{-1} (561 nm) results from $^4G_{5/2} \rightarrow {}^6H_{5/2}$transition and band 5 results from $^4G_{5/2} \rightarrow {}^6H_{7/2}$ in Sm^{3+} ions. Band 4 results from $^4F_{9/2} \rightarrow {}^6H_{11/2}$ transition in Dy^{3+} ion. This processes are schematically shown in Figure 4.39.

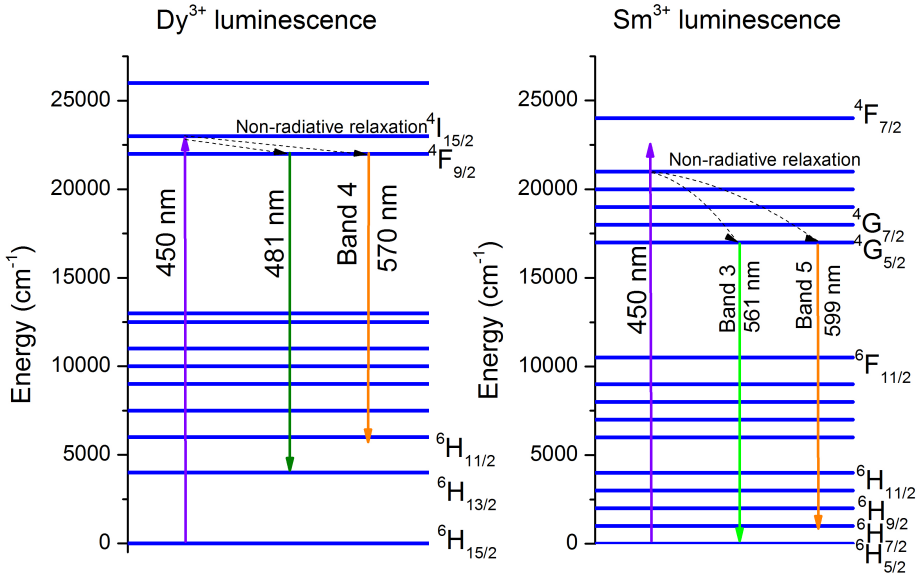

Figure 4.39: Emission process from Sm^{3+} and Dy^{3+} impurity ions present in 5% Yb:KGW matrix at an excitation wavelength 450 nm. The bands thus originated are shown in figure 4.38. The energy levels are only approximation of Sm^{3+} and Dy^{3+} in Yb:KGW matrix and are obtained from [153]–[155].

Band number	**Impurity ion**	**Transition**	Band energy cm^{-1}(nm)
Band 1	Er^{3+}	$^{2}H_{11/2} \rightarrow {}^{4}I_{15/2}$	18867 cm^{-1} (530 nm)
Band 2	Er^{3+}	$^{4}S_{3/2} \rightarrow {}^{4}I_{15/2}$	18115 cm^{-1} (552 nm)
Band 3	Sm^{3+}	$^{4}G_{5/2} \rightarrow {}^{6}H_{5/2}$	17825 cm^{-1} (561 nm)
Band 4	Dy^{3+}	$^{4}F_{9/2} \rightarrow {}^{6}H_{15/2}$	17523 cm^{-1} (570 nm)
Band 5	Sm^{3+}	$^{4}G_{5/2} \rightarrow {}^{6}H_{7/2}$	16658 cm^{-1} (599 nm)

Table 4.13: Source of impurity emission bands in Figure 4.38 and their assignment to different transitions. The bands are numbered according to decreasing energies.

Chapter 5

Conclusion

Radiative emission properties between states having same spin are studied for an organic fluorophore (Rhodamine 101) and a lanthanide ion (Yb^{3+}). The singlet state $S_1 \rightarrow S_0$ emission in Rhodamine 101 and $^2F_{5/2} \rightarrow {}^2F_{7/2}$ transitions in Yb^{3+} is targeted in this study. Both of these transitions are electronic, and they are well coupled with the phonons in the matrix enclosing them. Any change in electron-phonon interaction in both these systems can be monitored by investigating the changes in the absorption and emission spectra. The difference in the emission spectrum with the variation in the environment is studied for Rhodamine 101 molecule and Yb^{3+} ion.

Micro porous silica nanoparticles doped with Rhodamine 101 dye was prepared by a modified Stöber process. Monoclinic double tungstate (potassium-gadolinium tungstate ($KGd(WO_4)_2$) doped with Yb^{3+} (Yb:KGW) were prepared using two different methods: The Top-Seeded Solution Growth (TSSG) method was employed to create bulk single crystal of 5% Yb:KGW. A 3% Yb:KGW bulk Yb:KGW crystal prepared using the same technique was grind using ball milling to produce nanopowder of 3% Yb:KGW. Nanoparticles of 5% Yb:KGW were also grown chemically by a sol-gel technique (modified Pechini method) .

Deposits of Yb:KGW nanoparticles of average thickness 1-1.5 µm were made for studying the emission behaviour of Yb^{3+} in a crystal matrix. Laser ablation in liquid (Liquid Phase - Pulsed Laser Ablation- LP-PLA) was employed to create suspensions of YP1 glass nanoparticles from a 16% YP1 glass purchased. Particles of sizes 200-300 nm were generated

and photographed.
Size of the particles was estimated using the imaging techniques (SEM and TEM). The silica nanoparticles had an average diameter of 100±20 nm. Yb:KGW nanoparticles used in the study had an average diameter of 350±20 nm.
A fluorescence detection set-up was developed for recording emission spectra from solutions, suspensions and coatings. The used excitation wavelengths are in the visible and in the Infra-red with a resolution of 1 cm^{-1} in the near IR and 10 cm^{-1} in the visible. A monochromator (Oriel MS125) in conjunction with CCD detector (Andor 401 BV) was used to record fluorescence spectra in the visible. A Fourier transform spectrometer (Vertex 80, Bruker optics) was used to record emissions in the near infrared (800-1100 nm). The spectrometer used in the visible was calibrated using a Hg-Ar pen ray lamp, a diode laser at 532.8 nm, a He-Ne laser at 632.8 nm and a sodium vapour lamp. The emissions from Yb^{3+} doped nanoparticles were measured for an integration time of 3-4 hours. A double beam absorption spectrometer, Lamda 1050 UV/Vis/NIR spectrometer from Perkin-Elmer was used for recording all absorption spectra.

5.1 Emission properties of Rhodamine molecules in ethanol and silica nanoparticle surface

Solutions: The absorption spectrum of Rhodamine 101 is heavily dependent on the polarity of the solvent used. The maxima of the main absorption band and hence of the fluorescence are shifted to shorter wavelengths with increase in polarity of the solvent, and the extinction coefficient at the absorption maximum is slightly reduced. The shift in the absorption spectrum with change in solvent polarity was characterized. Shifts as high as 12-14 nm to the shorter wavelength can be observed in the absorption spectrum when the dipole moment of the solvent increases from 1.6 D to 1.8 D.

The $S_0 \rightarrow S_1$ absorption band of Rhodamine 101 solution in ethanol has an absorption maximum at 17391 cm^{-1} (λ_{max}= 575 nm). The absorption spectrum structure extends over ca. 4000 cm^{-1} with shoulders at 18800 cm^{-1} and 20300 cm^{-1}.

The emission spectra of Rhodamine 101 solution at different excitation wavelengths between 532 nm to 632 nm were studied. Wavelength dependent emission spectra show the independence of the quantum efficiency at different excitation wavelengths (Kasha's rule). A tunable wavelength source was made by modifying the output of a super continuum source for the purpose.

Properties of Rhodamine 101 dye molecule when excited at lower energy, 15802 cm^{-1} (632.8 nm) are discussed. The anti-Stokes emission spectrum of 10^{-4}M Rhodamine 101 in ethanol was obtained when excited at 632.8 nm using a He-Ne laser. A comparison of the normalized absorption and emission spectrum gives an estimate of the 0-0 vibronic band origin which is estimated to be at 17035 cm^{-1} (587 nm). The anti-Stokes emission in Rhodamine 101 ethanol solution depends on the concentration. The emission spectrum shifts to longer wavelengths with increase in concentration. The red shift in the emission spectra with increasing concentration is the result of the "inner filter effect" (both primary and secondary inner filter effect before the spectrometer records the spectrum).

Temperature dependent anti-Stokes spectra of the solution gave an estimate of the energy difference of the excitation energy and the 0-0 vibronic band origin (1233 cm^{-1}). This was estimated from the Arrhenius plot of inverse of temperature versus the intensity at a constant wavelength.

Modification in the dye emission spectrum upon attaching to a silica nanoparticle surface was investigated. The particles were of average size 100$\pm$20 nm. The absorption spectra of the molecules were obtained by removing the scattering of the silica nanoparticles through a base line correction. The extinction curves of the particles were found to drop non-linearly with time, leaving the absorption from the Rhodamine molecules dissolved in the solvent even after the particles were settled completely. This indicated that the molecules were not exactly attached to the particle surfaces. Luminescence from Rhodamine molecules attached to these hydrothermally prepared porous silica nanoparticles suspended

in ethanol was recorded. The emission and absorption spectrum showed little modifications when compared to those of the Rhodamine 101 solution of approximately same concentration. Thus the emission was dominated by the molecules which were detached from the silica nanoparticle surface.

5.2 Emission properties of Yb^{3+} in glassy and crystalline matrices

5.2.1 Ytterbium ion in phosphate glass

YP1 bulk: Spectroscopic properties of Yb^{3+} in a phosphate glass (YP1) were analysed. Eight bands were identified in the glass absorption spectrum and five bands to the emission spectrum. At room temperature, only one main band and a shoulder are resolved in the extinction spectrum of YP1 glass (Figure 4.4). The peak extinction was recorded at 10319 cm^{-1} (969 nm), unlike the usually reported absorption maxima of Ytterbium doped phosphate glasses (at 10265 cm^{-1} (975 nm) corresponding to band A for commercially available Kigres Qx/Yb glasses) [117]. A shoulder at higher energies appear at ≈10844 cm^{-1}(922 nm), a position matching the energies reported for the transition a→g.

Band positions and widths of the bands in the extinction spectrum were estimated by fitting Voigt profiles to the emission spectrum. The homogeneous widths of the bands were smallest for the transitions between the lowest Stark levels (a→e and e→a) . The inhomogeneous widths for the glass for all transitions are large (between ≈100-200 cm^{-1}). The considerably large inhomogeneous widths were attributed to the presence of OH^- ions present in the (hygroscopic) YP1 glass matrix. OH^- ions have rotational-vibrational absorption bands at 10301 cm^{-1} which is also the band center of band A (transition a→e). Hence the fits made for the bands in absorption spectrum should be influenced by the OH^- absorption band.

The emission spectrum of the Yb^{3+} in bulk YP1 glass was measured at two different excitation wavelengths, λ_{exc}= 981.8 nm and λ_{exc}= 1023

nm. Both spectra are similar. Only the transitions from the lowest Stark level 'e' of the $^2F_{5/2}$ is involved in the emission process since the levels f and g are short lived due to efficient non-radiative relaxation. In the emission spectrum, the absorption of OH^- ions is observed as a transmission loss, which had to be subtracted for further analysis of the spectrum. Voigt profiles corresponding to the transitions, **e**→a (band A'), **e**→b (band B'), **e**→c (band C'), **e**→d (band D') were fit to the spectrum to find homogeneous and inhomogeneous widths. An additional band, band E' was identified as a vibronic band. The vibronic transition was identified based on the fact that its energy is much lower than the lowest possible electronic transition between Stark level 'e' of the $^2F_{5/2}$ to any level of $^2F_{7/2}$. The only difference of the spectra at different excitation wavelength was that Gaussian widths increased $\approx$ 5% with the increase in excitation wavelength.
The Stark energy levels of the YP1 glass were estimated from the absorption and emission spectra. The Barycenter plot of the Stark energy levels corroborated the assignments of the band centers to the Stark level transitions stated above. The emission cross-sections of the glass were calculated using the reciprocity method and agreed with the normalized emission spectrum.

YP1 nanoparticles: The maximum of the absorption spectrum of YP1 nanoparticles was red shifted by 22 nm when compared to the absorption spectrum of bulk YP1 glass. A similar red shift with reduction in size was previously reported for Eu^{3+} in Yb_2O_3 [97] (mentioned in detail in section 4.2.2, page 96). The shift and increase in the width of the spectrum could be due to the increase in surface defects. The nanoparticles generated had irregular surfaces as is evident from the images of the nanoparticles. The inhomogeneous widths of the nanoparticle extinction spectrum increased by $\approx$ 28 % in comparison to the bulk.
The emission spectrum of the YP1 nanoparticles (at both excitation wavelengths) was similar to that of the bulk YP1 glass. The inhomogeneous FWHM of the transitions in nanoparticles increased by $\sim$ 10-20 % when compared to the bulk. This increase is due to the influence of surface defects. Energy level diagram of the nanoparticle was obtained from the absorption and emission spectrum of the nanoparticle. The en-

ergy barycenters of the Yb^{3+} states $^2F_{5/2}$ and $^2F_{7/2}$ of the nanoparticles showed little variation from the free ion barycenters, supporting the assignments made for the bands of the Voigt fits. No modifications were observed in the electronic energy levels of Yb^{3+} in YP1 nanoparticle. This is as expected since quantum confinement is not prominent among lanthanide ions in nano materials for sizes above 5 nm [168] (YP1 nanoparticles created using ablation had sizes ranging between 200-300 nm). But size reduction will definitely affect the phonon bands of the di-electric phosphate glass matrix in which Yb^{3+} is incorporated. Since the electronic energy levels of Yb^{3+} and phononic energy levels of the glass are strongly coupled, the transitions involved during absorption and emission can be influenced. This would have led to the red shift in absorption maxima in the extinction spectrum of the nanoparticle when compared to the bulk [137].

5.2.2 Yb^{3+} in KGW crystal

Yb:KGW Bulk crystal:

The emission spectrum of the uncut, unpolished 5% Yb:KGW was measured at two different excitation wavelengths, λ_{exc}= 981.8 nm and λ_{exc}= 1023 nm. Yb^{3+} ion in a crystal experiences a stronger crystal field, and the crystal field splitting is more pronounced. Hence the bands in the emission spectrum of Yb:KGW crystals are well resolved compared to YP1 glass. Voigt fits can be made for each of the transitions **e**→a (band A'), **e**→b (band B'), **e**→c (band C'), **e**→d (band D') and band E' (vibronic band). Homogeneous and inhomogeneous widths of these transitions were estimated from the Voigt fits for the bands.

The band center of band E' lies in the anti-Stokes emission region, and having energy equal to the transition f→a at 10472 cm^{-1}(954.92 nm). Since the level 'f' is short lived (refer analysis on YP1 glass, section 1.2) an emission from that level is highly unlikely to happen, hence it is possible that the band E' is phonon enabled. The line e→c (9673 cm^{-1}) after interaction with a phonon of energy 760 cm^{-1}can absorb its energy and result in the vibronic band E' at 10459 cm^{-1}. This conclusion is corroborated by Raman studies on KGW single crystals (see table 4.9).

Yb:KGW nanoparticle:

The emission spectra of 3% Yb:KGW HTSG nanoparticles and 5% Yb:KGW Pechini nanoparticles at λ_{exc} = 981.8 nm were recorded and compared. The only pronounced difference between the bulk and the 3%: Yb:KGW HTSG nanoparticle emission spectra is the change in emission intensity due to change in concentration. A pronounced difference from the emission spectrum of 5% Yb:KGW Pechini nanoparticles when compared to the 5% Yb:KGW bulk emission spectrum is that the band corresponding to the transition **e**$\rightarrow$d (band D') is not clearly resolved. The intensity at 9637 cm^{-1} where the origin of the transition band D' is placed is considerably decreased. For the HTSG nanoparticles, the maximum intensity of the band D' was 96% of band C', while for Pechini nanoparticles, this decreased to 46%. A reduction in the intensity of the band D' would indicate the quenching of the transition **e**$\rightarrow$d. No reasoning can be provided now for the origin of quenching or as to why only the transition **e**$\rightarrow$d is selectively quenched.

The inhomogeneous widths obtained from Voigt fits for the emission spectrum of the 3% Yb:KGW HTSG nanoparticles increased by $\approx$35% and that for 5% Yb:KGW Pechini nanoparticles increased by $\approx$40 % in comparison to the bulk. Hence the inhomogeneous widths are affected by the surface defects and impurities present in the nanoparticle matrix.

The excitation intensities and widths at 980 nm were compared to those formed at 1023 nm. The widths and the band positions remain the same for both the excitation wavelengths.

The luminescence from other rare earth impurity ions in bulk 5% Yb:KGW was also discussed. Er^{3+} was a dominant impurity present in all the samples. The energy overlap between the $^2F_{5/2}$ level in Yb^{3+} and $^4I_{11/2}$ level in Er^{3+} allows the efficient resonant energy transfer between both ions. Er^{3+} can absorb the excitation energies both at 10185 cm^{-1} (981.8 nm) and 9775 cm^{-1} (1023 nm) and populate the $^4F_{11/2}$ level ($^4I_{15/2}\rightarrow$ $^4F_{11/2}$). But the energy transfer process between $^2F_{7/2}$ in Yb^{3+} and $^4F_{11/2}$ in Er^{3+} is stronger, and will hence dominate. From the $^4F_{11/2}$ Er^{3+} level the energy can be transferred back to Yb^{3+} or relax within Er^{3+} ions. This relaxation produces luminescence centered at $\approx$10000 cm^{-1}(1000 nm) (associated with the $^4I_{11/2}\rightarrow$ $^4I_{15/2}$ transition). The metastable state $^4I_{13/2}$ can also be populated via non-radiative relaxation from

$^4I_{11/2}$. Relaxation from $^4I_{13/2}$ to the electronic ground state ($^4I_{13/2} \rightarrow$ $^4I_{15/2}$ transition) creates an emission band around 6666.67 cm^{-1} (1500 nm). Er^{3+} at $^4I_{13/2}$ can also absorb energy from another Yb^{3+} ion and get excited to $^2H_{11/2}$. The $^2H_{11/2} \rightarrow {}^4I_{15/2}$ and $^4S_{3/2} \rightarrow {}^4I_{15/2}$ transitions in Er^{3+} produce green luminescence.

An excitation at 21978 cm^{-1}(455 nm) of the 5% Yb:KGW bulk crystal provided luminescence bands at 18867 cm^{-1}(532 nm), 18115 cm^{-1} (552 nm), 17825 cm^{-1} (561 nm), 16658 cm^{-1}(599 nm), and 17523 cm^{-1} (570 nm). The first two bands originate from the impurity Er^{3+}, the second two bands from Sm^{3+}, and the last one from Dy^{3+}. The presence of these impurities would also influence the measured widths and intensities of the $^2F_{5/2} \rightarrow {}^2F_{7/2}$ transitions in Yb^{3+}.

5.3 Future aspects

The emission properties of individual particles can be rightly estimated only by taking smaller ensembles of the same. Anti-Stokes emission studies from smaller number of particles would also be the next move towards the idea of a 'micro-junction cooling' mentioned in the introduction. An optical trap [163]-[172], [174-179] would be a perfect tool for this, since any other methods of measurement will need physical contact with the sample, eventually heating up the sample. Study on aerosol traps are well advanced [176]-[179], and hence a combination of an optical trap set-up and a fluorescence detection set up is feasible. A single beam gradient force optical trap set-up was developed in this regard, so that the emission from fewer number of particles can be studied (details of this set-up is provided in the appendix C).

Chapter 6

Outlook

Improvements in the set-up design

One of the drawbacks of the fluorescence measurement during the study was that the emission properties observed could not be assigned to a single or finite number of nanoparticles, but to an ensemble average of millions of nanoparticles of sizes ranging from 100-200 nm. In order to achieve what can be called close to much smaller ensemble emission study a modified set-up was developed (Figure 6.1). The modified set-up consists of an optical trap set-up which can suspend liquid aerosol particles in air. The optical trap set up used was a single beam gradient force optical trap. The wavelength of the trap beam was in the near infrared (1064 nm). The suspended particles were then to be excited by a probe laser (632.8 nm or 980 nm). As a first step towards the development of the set-up, a gradient force optical trap was developed and liquid aerosols (36 wt % NaCl in H_2O) of sizes ranging 2-5µm were trapped.

The working principle, design, and the alignment procedures of the trap is described in Appendix C.

Anti-Stokes fluorescence from optically trapped Rhodamine doped/ Yb^{3+} doped liquid/solid aerosols

Dye solution droplets optically trapped had shown lasing properties before [163]–[169]. The anti- Stokes emission properties will be extremely interesting in this case since the anti-Stoke excitation can potentially remove the heat out of the micro drop let laser. Solid aerosols like Yb^{3+} doped glass or crystal nanoparticle can be very efficiently trapped op-

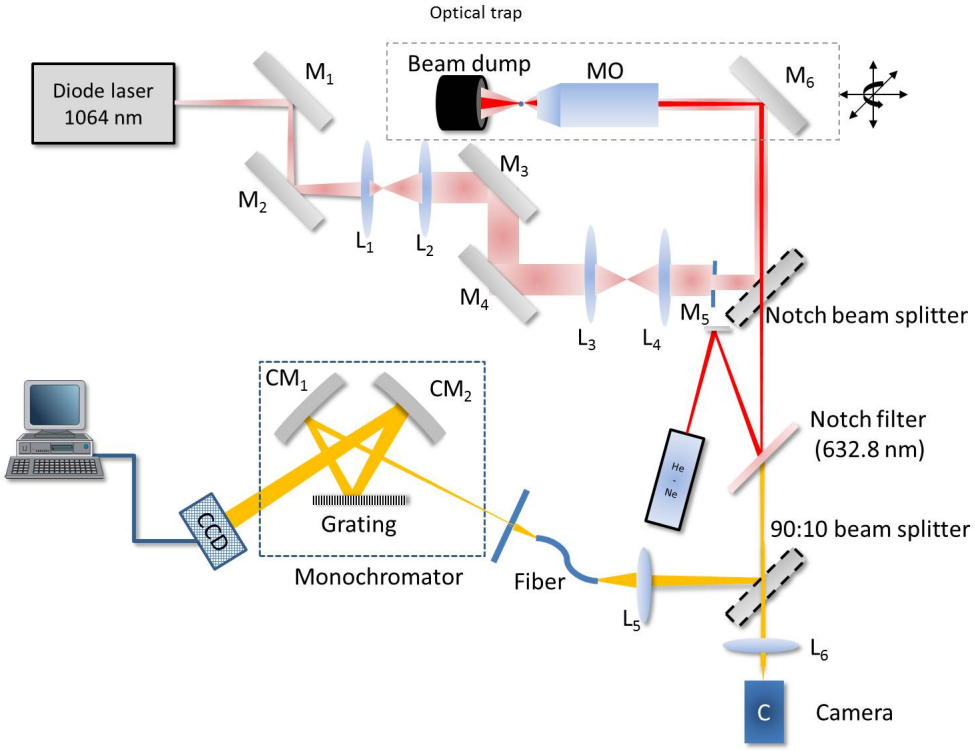

Figure 6.1: Optical trap set-up

tically by using Bessel beams instead of usual Gaussian beams used [170]–[172]. Bessel beam can be created using an axicon [171]. This also makes simultaneous trapping of multiple aerosols possible. An optical set-up which combines optical trapping and fluorescence detection satisfies all the criteria for what next to single nanoparticle detection and therefore has a potential to contribute in a meaningful way to areas of fluorescence spectroscopy.

Appendix A

Instrumentation & Sample preparation

Instrumentation curves

Calibration curve 1

$$\lambda = -0.0000000137101P^3 + 0.0000074380167P^2 + 0.1611639968075P + 391.7222965366360 \quad \text{(A.1)}$$

Standard deviation of the residual: 0.99 nm. The caliberation curve obtained is shown in Figure A.1.

Calibration curve 2

$$\lambda = -0.0000000321194P^3 + 0.0000233983208P^2 + 0.1494028786389P + 529.6759449293060 \quad \text{(A.2)}$$

Standard deviation of the residual: 0.99 nm. The caliberation curve obtained is shown in Figure A.2

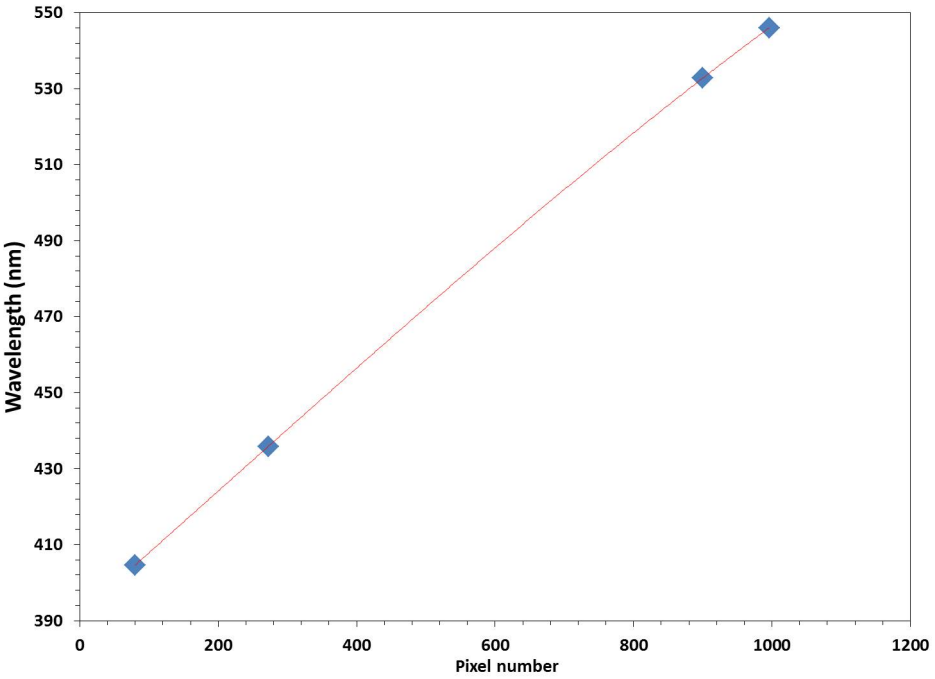

Figure A.1: Calibration curve 1: Caliberation curve for 100 µm entrance slit for MSR 4.5 VSR 23 (centre wavelength 478 nm)

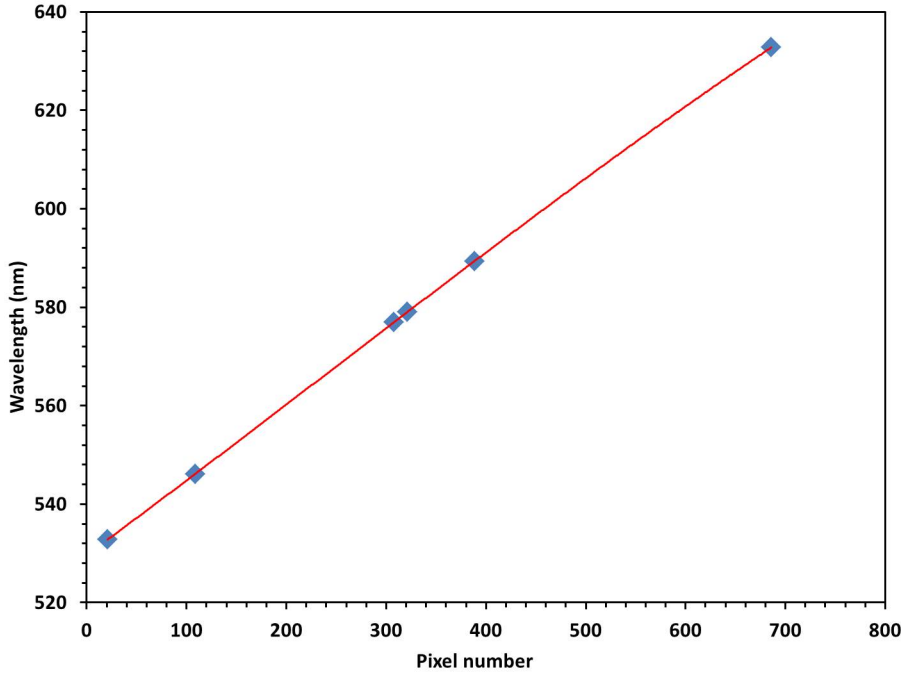

Figure A.2: Caliberation curve 2: Caliberation fit made for 100 µm entrance slit for MSR 6 PSR 10 (centre wavelength set at 610 nm)

Emission spectra of lasers used

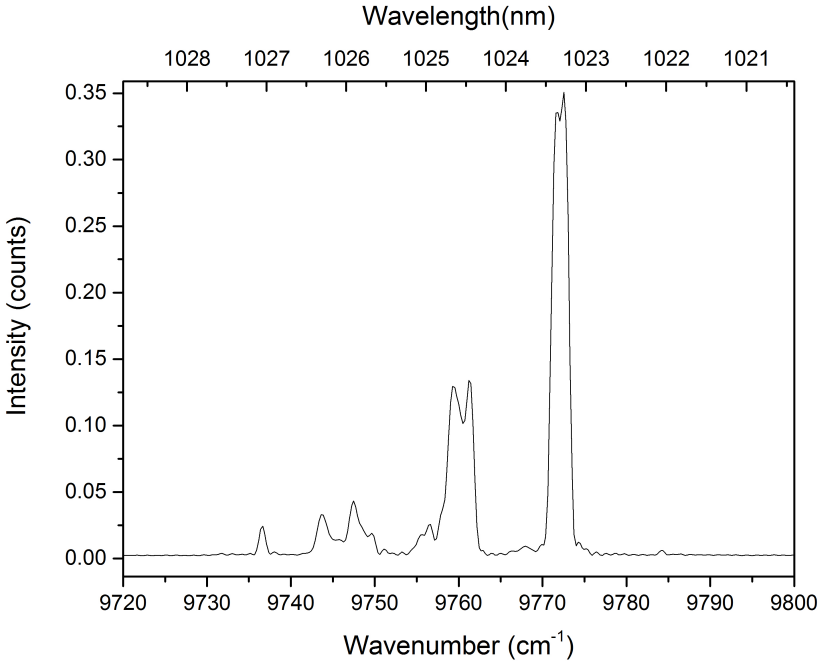

Figure A.3: Emission spectrum of CW diode laser with emission centered at wavelength 1024 nm

Sample preparation techniques

Preparation of silica nanoparticles using modified Stöber process

As a part of collaboration with Prof. Micheal Morris's group in UCC, micro porous silica NPs doped with dye molecules of random sizes ranging from 1to 100 nm were prepared by the Block Copolymer Group (BCPG) in chemistry department, UCC. 0.25 M Tetraethylorthosilicate (TEOS) was added to premixed solution of ethylene glycol and water (3:4) with magnetic stirring. The mixture was stirred for 10-15 min. 0.1 wt% of Rhodamine dyes added to the solution. After being stirred for 10-20 min, the mixture was then transferred to a Teflon-lined autoclave, and the hydrothermal reaction was carried at 160 °C for 12 h. The resulted sample was centrifuged and washed with water and ethanol for several

times. The sample was then vacuumed at room temperature, and grind to powder.

Preparation of Yb:KGW bulk and nano crystals

The experimental procedure followed in this work for growing bulk and nano single crystals by the TSSG-SC and Pechini technique is the result of previous works carried out at the Physics and Crystallography of Materials and Nanomaterials, FiCMA-FiCNA, group of the Universitat Rovira i Virgili, URV, in Tarragona.

Top-seeded solution growth technique

The Top-Seeded Solution Growth (TSSG) method is one of the methods included in the high temperature solution (HTS) techniques for the growth of bulk single crystals. The crystal growth process by high temperature TSSG– Slow Cooling (TSSG-SC) method is based on the concepts of solubility and supersaturation. At a given temperature, a limited amount of a substance dissolves in a particular solvent. The amount dissolved defines the solubility at that temperature.

Experimental set-up

Figure 2.1 shows the schematic representation and the picture of the system used to grow KTP and RTP single crystals by using the TSSG-SC method. It includes a single-thermal-zone vertical tubular furnace, the crystal seed attach, rotation, and pulling systems, the crucible and its support, and the temperature controller/programmer. The heat is produced by a Kanthal resistance heating wire which is rolled around an alumina tube. The whole system is thermally insulated from the environment by means of insulator refractory bricks of alumina and an external metallic steel cover that can also be seen in the cross-section of the furnace provided in the schematic representation. The temperature in the furnace is measured with an S-type thermocouple Pt/Pt-Rh 10%

(partially protected by covering it with an alumina tube) and placed near the resistances of the central zone of the furnace to guarantee a reliable and stable measurement. The temperature in the furnace is controlled by a Eurotherm 903 controller/programmer that allows controlling the temperature with a precision of 0.01 K. It is connected to a thyristor that controls the power of the furnace. The mechanical part of the growth device, which consists of a series of high precision mechanisms attached to two different stepper motors and a bell clamp, are placed above the furnace, and supports, vertically displaces, and rotates the crystal seed during the crystal growth process. It comprises a vertical metal structure that is extremely rigid and stable from which an alumina rod is hung. The speed of rotation and the speed of pulling can be modified according to the voltage provided by the power source. The seed is attached to a platinum holder, which is also attached to an alumina rod, both which are laced with thin platinum wire. The attach system can be moved up and down to locate the crystal seed precisely in contact with the surface of the solution. This movement can be monitored with a micro-metric comparer for better precision with an accuracy of 0.01 mm. To identify the best location for the crucible filled with the solution inside the furnace, an alumina rod, which can be manually handled upwards and downwards, was used to place the crucible at the right position. The temperature profile of the solution in the furnace is shown in Figure A.4. When the platinum crucible filled with the solution is located inside the furnace, the thermal gradient of the solution must be measured and optimized to assure a suitable thermal gradient in the solution while keeping the surface of the solution colder than the bottom of the crucible. This can be achieved by adjusting the height of the crucible support to place it in the right thermal zone of the furnace.

Experimental procedure

For the TSSG-SC growth process, it is very important to have an accurate knowledge of saturation temperature (T_s), the temperature below which the crystal starts to grow. The solution should be homogenized before starting to determine T_s. The saturation temperature can be defined as the highest temperature at which the seed crystal remains undissolved, and the lowest temperature at which no spontaneous nucleation occurs.

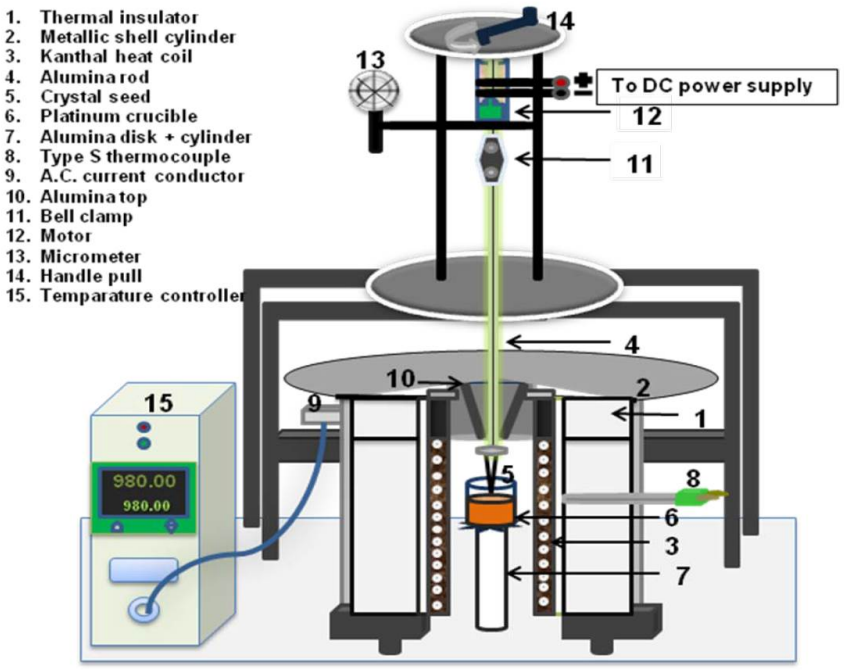

Figure A.4: Schematic view of the verticular tubular furnace used in the bulk singlecrystal growth experiments.

To have an estimation of T_s, nucleation on a Pt wire can be analyzed. To obtain the desired orientation of the crystal, the crystal seed has to be selected with the same structure of the material to be grown before introducing into the solution, so that the substance precipitating from the solution grows around the seed crystal to form a larger single crystal keeping the crystallographic orientation of the seed. The crystal seed should be placed at the coldest point of the solution on the surface of the solution just at the centre of the platinum crucible. The temperature profile of the solution inside the furnace is shown in Figure A.5. If the growth process is started at $T>T_s$, The crystal seed will dissolve and will lose contact with the solution. If the growth process is started at $T<T_s$, the spontaneous nucleation and growth will prevail over the top-seeded growth, resulting in numerous small crystals visible on the surface of the molten system. The saturation temperature T_s, can be determined precisely by placing the seed in contact with the surface of the solution and controlling the temperature at which neither growth nor dissolution of the seed is observed. The best way to do that is, by using a starting temperature T above T_s and then decrease the temperature until T_s is

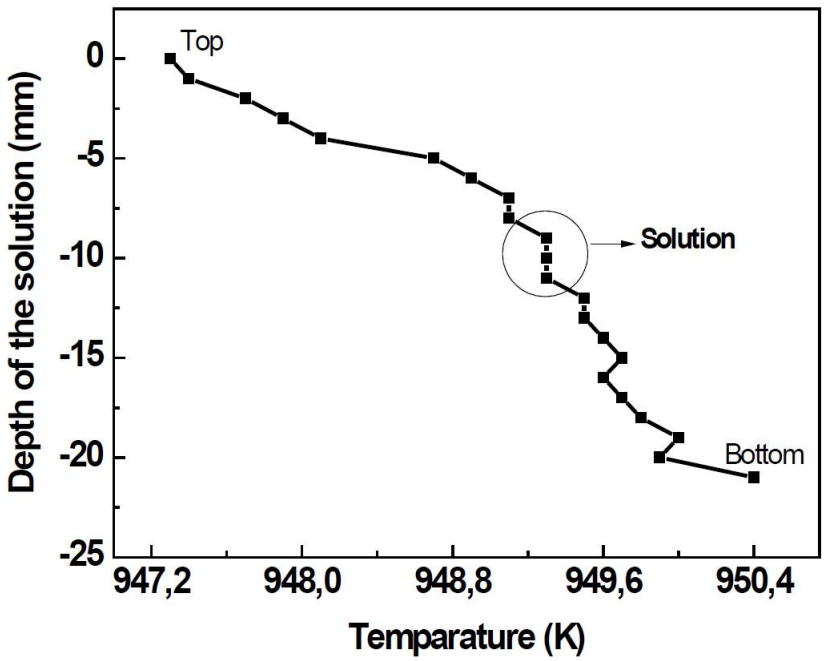

Figure A.5: Temperature profile of the solution inside the furnace

reached, in other words, only dissolution of the crystal seed should be observed before reaching T_s. In this way, it allows dissolving the outer layer of the crystal seed, thus the crystal growth process can proceed from a structure with less crystal defects. The growth/dissolution of the crystal seed is controlled with an accuracy of ~10 μm with a Mitutoyo micrometer comparer fixed at the mechanical structure of the furnace that allows vertical travelling of the rod, which supports the crystal seed (see in Figure A.5).

After determining the T_s, the seed is placed in contact with the surface of the solution and a rotation of the seed over its axis is applied. Later the slow cooling of the solution is applied to create supersaturation in the solution. From T_s, the temperature is decreased by 15 K typically at a rate of 0.1 Kh^{-1}. To obtain single crystals with larger sizes the interval of cooling can be increased and a pulling rate can also be applied during the crystal growth process. In the case of our growth experiments the crystals were pulled up of 0.5 mm after every 12 h from the surface of the solution during the crystal growth. The mixing of the solution must be good in order to maintain a good homogenisation of the solution and to obtain macroscopic defect free crystal. When the slow cooling programme is

finished, the grown crystal is extracted slowly from the solution, 1 mm every 5 min in our case, and placed slightly above the surface of the solution. Then, the furnace is cooled down to room temperature at 15 Kh^{-1}. As the typical growth period runs for a couple of weeks, the ability to observe the quality of the growing crystal can lead to substantial saving of system run time since it allows to decide to abort a growth run that has been spoiled by spontaneous nucleation.

The bulk crystals used in the fluorescence measurements were uncut and unpolished.

Sol-gel modified Pechini method

The modified Pechini method is used to synthesize potassium-rare earth tungstates ($KRE(WO_4)_2$ or KREW) nanoparticles. Stoichiometric amounts of the oxides of the elements contained in the nanoparticles were first converted to their nitrate forms by dissolution in concentrated HNO_3. Later the excess of HNO_3 was evaporated to obtain nitrate precipitates by slow heating. In the next step, the tungstates, and an aqueous solution of ethylene diamine tetra-acetic acid (EDTA), used as the chelating agent in a specific molar ratio (C_M) to prepare metal- EDTA complexes, were mixed and added to them to nitrate precipitates. The molar ratio C_M was defined as

$$C_M = \frac{[EDTA]}{[METAL]} \tag{A.3}$$

which describes the degree of the chelation process of the metal in the organic product. Afterwards, ethylene glycol (EG), the sterification agent was added in molar ratio (C_E), which describes the degree of sterification between the chelating agent and the ethylene glycol:

$$C_E = \frac{[EDTA]}{[EG]} \tag{A.4}$$

In this process, the molar ratios of CM and CE are used in the ratio of 2:1, respectively. The resulting solution was heated slowly to obtain the precursor resin, which is rigid polyster net that reduces any segregation

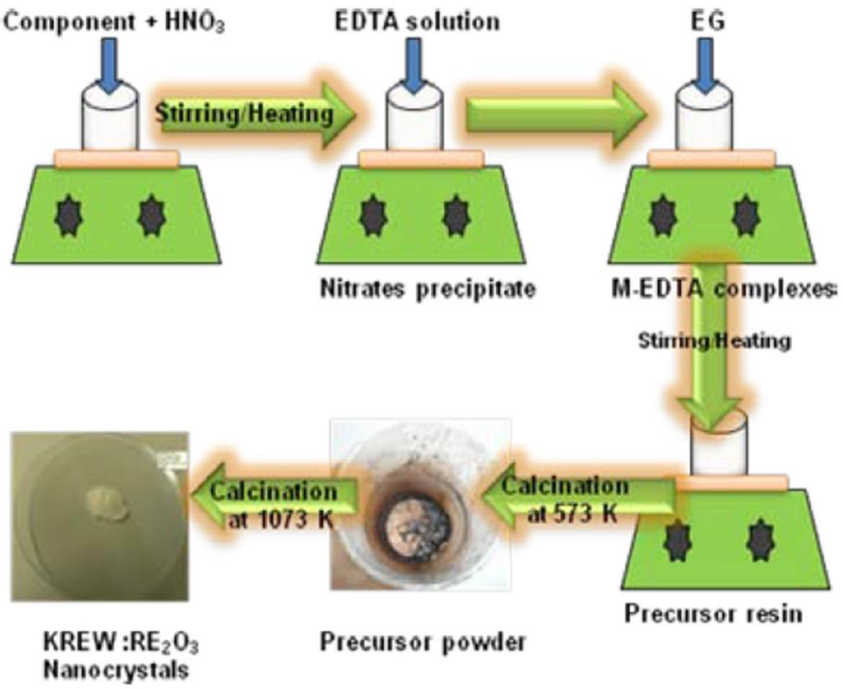

Figure A.6: Schematic diagram of the synthesis method used to obtain nanoparticles of luminescent by the sol-gel Pechini method [95]

of metals. The following stage is the two step calcinations procedure using furnace.

1. Calcination at 573 K for 3 hours, during which the precursor resin decomposes to provide the precursor powder.

2. The calcinations procedure depends on the nanocrystals. Each material was calcined at a certain temperature and for a particular length of time in accordance with the previous studies.

The schematic view of the synthesis of nanoparticles by modified sol-ge Pechini method is shown in Figure A.6.

XRD patterns of Yb:KGW samples

X-ray diffraction analysis was carried out for Yb^{3+} doped tungstate crystal samples to understand the doping effect on crystalline structure. The X-ray powder diffraction pattern for all three Yb:KGW are shown in Figure A.7. The X-ray diffraction results confirm the monoclinic structure of Yb^{3+} doped KGW crystals. There is no change in the crystalline

nature of Yb:KGW from the pure KGW. According to previous reports, the lattice parameters should slightly decrease for Yb doped KGW crystal compared to the pure KGW [173]. The reason for this small change may is due to the ionic radius of Gd^{3+} (1.06Å), which is larger than the Yb^{3+} ionic radius (0.86 Å) and Yb^{3+} in KGW occupies the same position as Gd^{3+} [173].

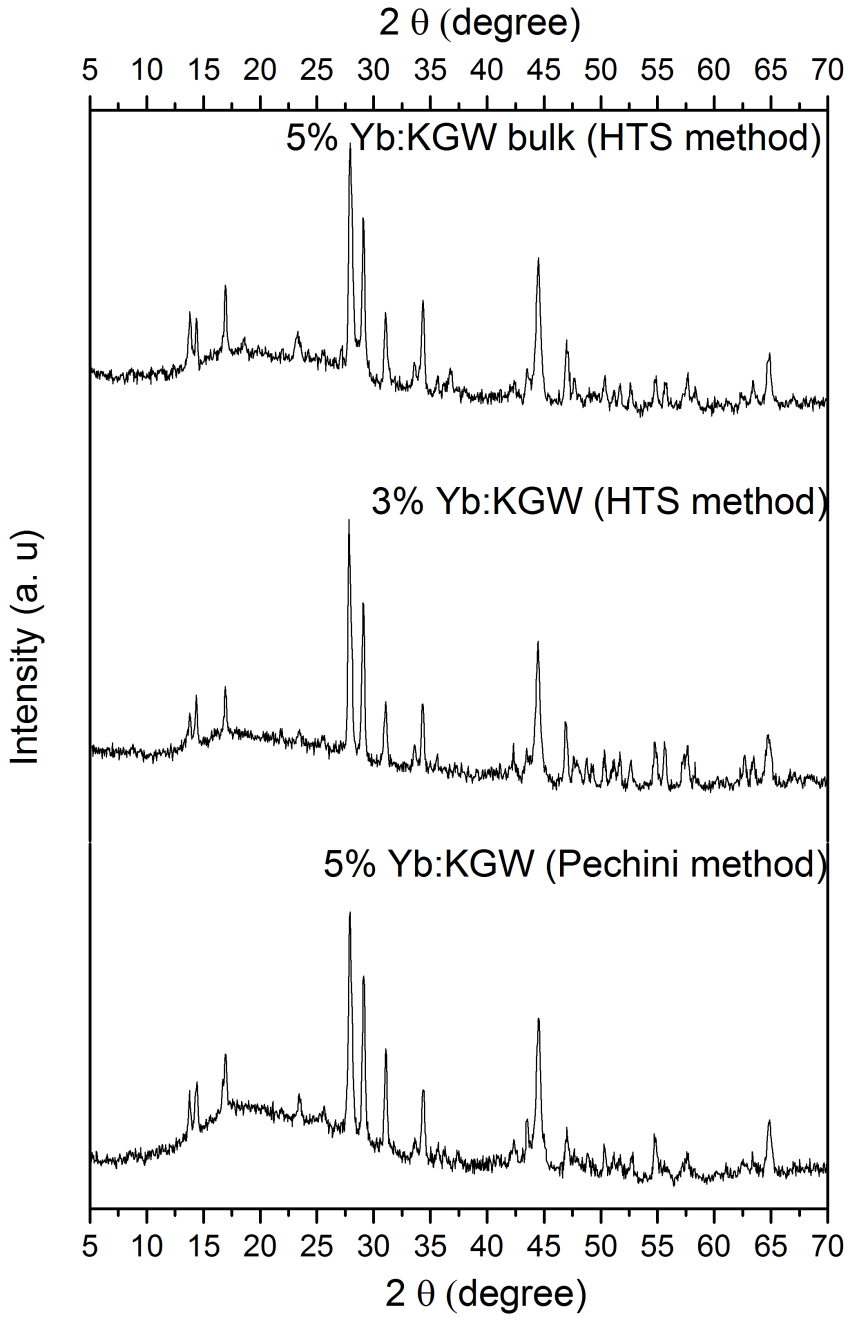

Figure A.7: XRD patterns of Yb:KGW nanocrystal samples compared to the bulk. Powder XRD spectra confirms that the grown crystals are monoclinic in structure and the doping incorporation slightly alter the lattice parameters.

Appendix B

Absorption and emission curves

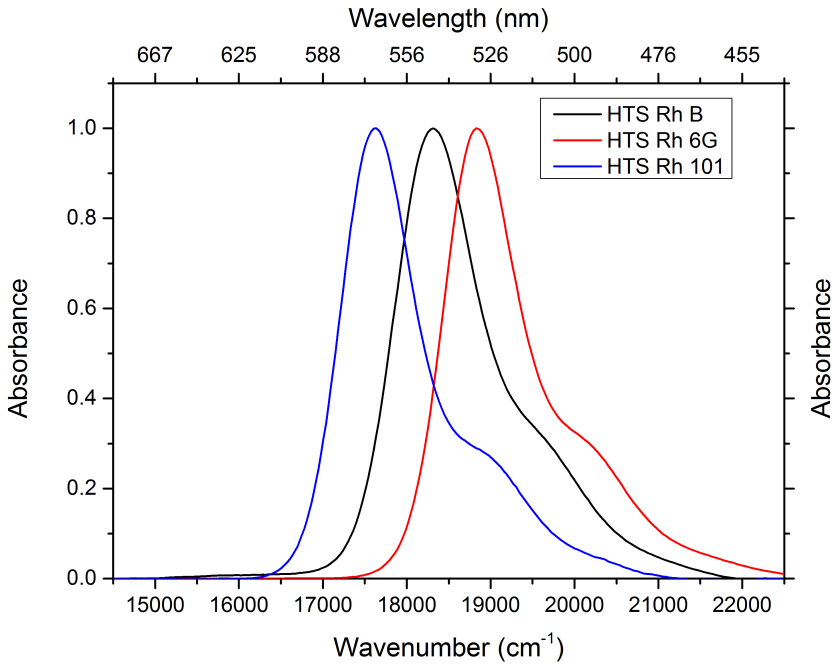

Figure B.1: Normalized absorption spectrum of all three Rhodamine doped silica nanoparticles

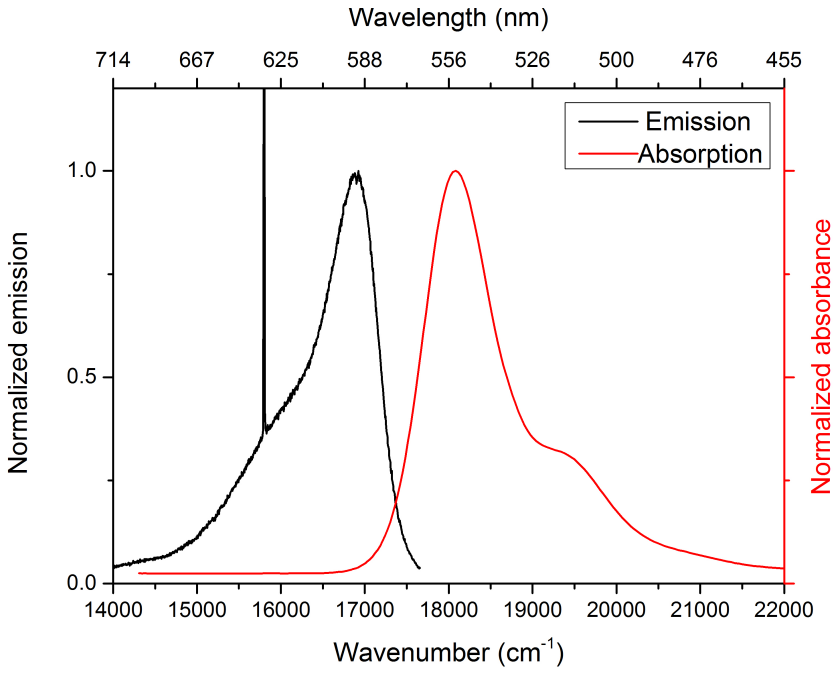

Figure B.2: Normalized absorption and emission spectrum for HTS Rh B suspension in ethanol (Approximate concentration of the suspension is 10^{-3} M)

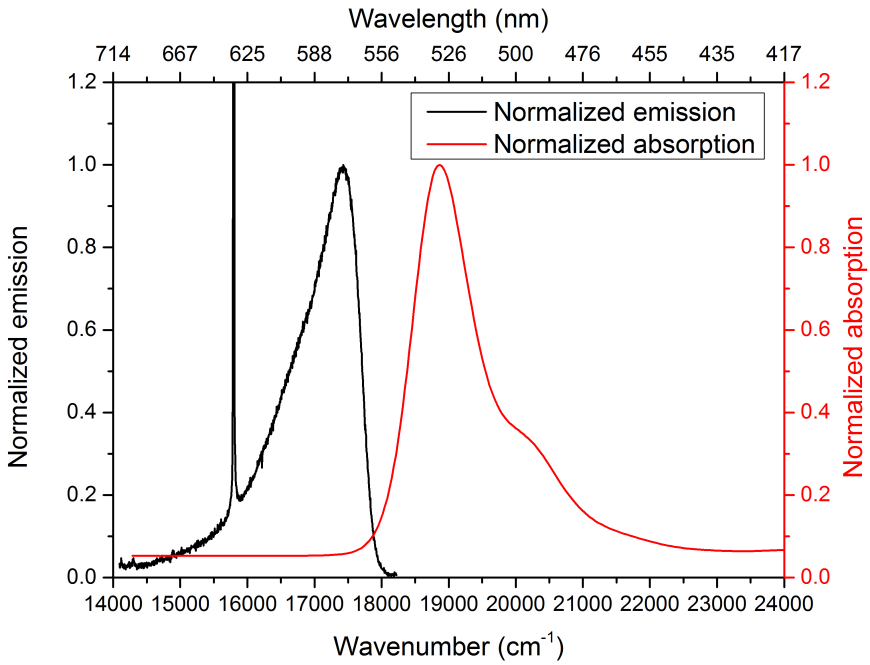

Figure B.3: Normalized absorption and emission spectrum for HTS Rh 6G suspension in ethanol (Approximate concentration of the suspension is 10^{-4} M)

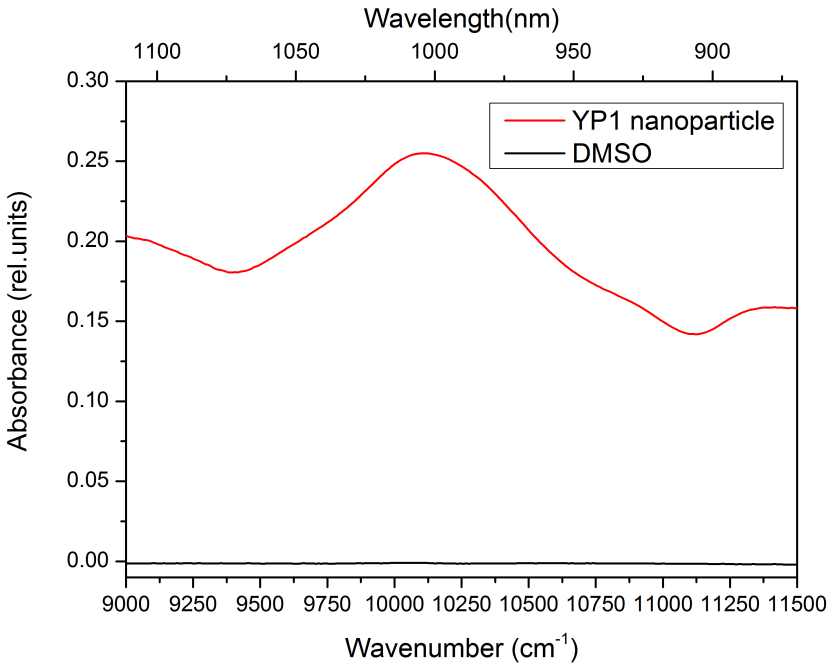

Figure B.4: Extinction spectrum of YP1 nanoparticles in DMSO (red line) synthesized via laser ablation. The black line shows the extinction spectrum of DMSO (both are measured with DMSO as reference sample).

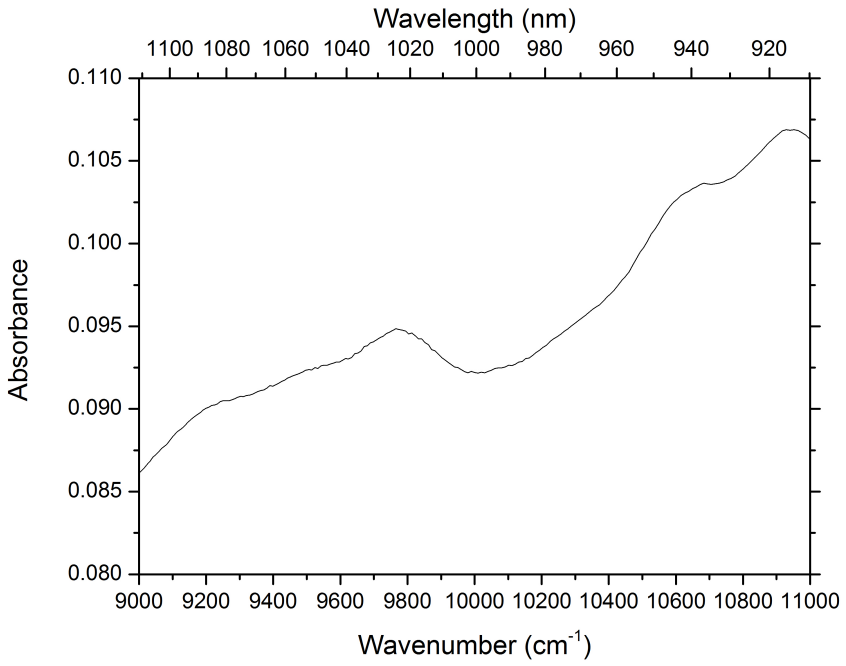

Figure B.5: Extinction spectrum of 5% Yb:KGW Pechini nanoparticles. Rayleigh scattering dominated in the extinction. The spectrum was measured in ethanol in a 5 cm cell.

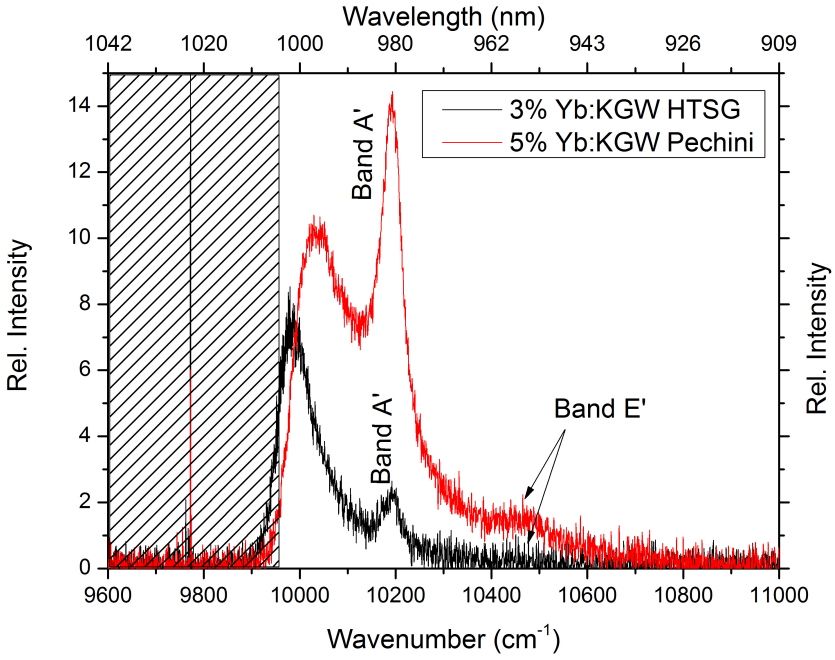

Figure B.6: Emission spectrum of 3% Yb:KGW HTSG and 5% Yb:KGW Pechini nanoparticle samples at excitation wavelength λ_{exc}= 1023 nm. The acquisition time is 3 hrs. All conditions for both the samples are maintained same except the concentration. The shaded region denotes the cut off region of the short pass filter at 1000 nm. Band A is centered at 10190 cm^{-1}(981.3 nm) and Band E' is centered at 10468 cm^{-1}.

Appendix C

Optical trapping of aerosols

The set-up and development of the single beam gradient force optical trap is described in this chapter.
For modelling of the set-up, alignment and troubleshooting of the trap was followed closely as in publication by Lee et al. [174]

Optical trapping of aerosols in air using a single beam gradient force optical trap

The principle behind single beam optical trapping of aerosols is the generation of a large intensity gradient in a very small volume. The intensity gradient produces a so called "gradient force" [175]–[178] which needs to be large enough to compensate the radiation pressure generated due to scattering of photons. The principle of optical trapping is explained for a micron sized silica bead in Figures C.1 and C.2.

Optical instrumentation
The set-up of the optical trap developed is shown in Figure 6.1. The heart of the trap is a laser microscopic objective with a high numerical aperture focussing the laser light. The large intensity gradient generated by the laser focused in a very small area drags the aerosols towards the focus of the beam. The inverted microscope arrangement is obtained using a camera-microscopic objective combination. The laser beam is

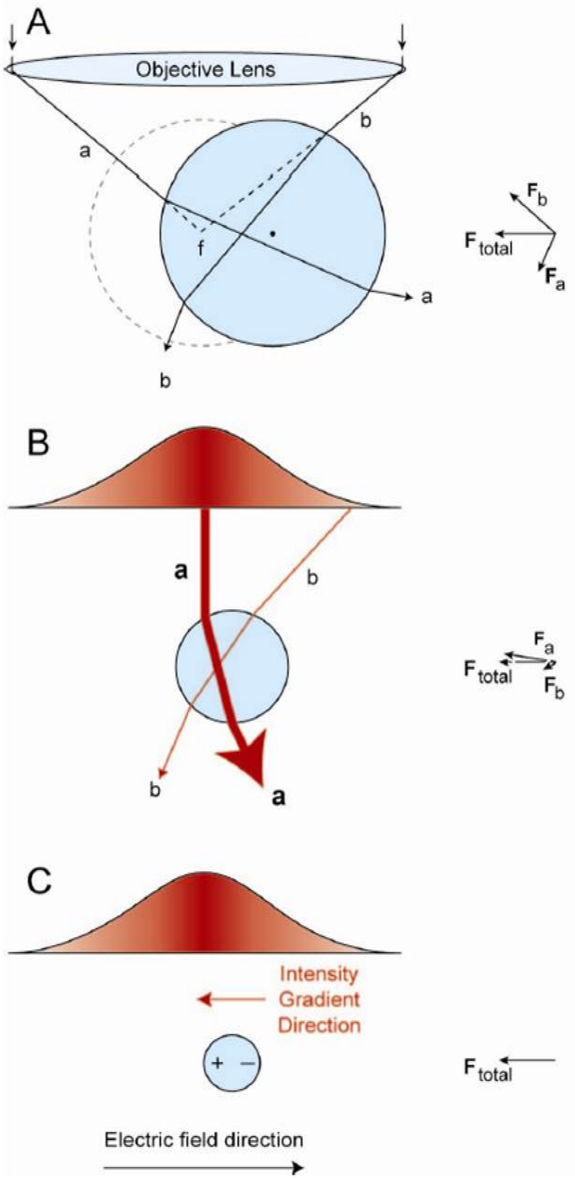

Figure C.1: Simplified illustrations of optical trapping. (A) The ray-optics diagram. In the absence of the bead, two rays (a and b) are focused through the objective lens to position f, the true laser focus (dashed line). Refraction through the bead, which is displaced to the right of the laser focus, causes the new focus to lie to the right of f. After exiting the bead, ray a and ray b are refracted as shown in Figure. F_a and F_b represent the forces exerted on the bead by rays a and b; F_{total} is the sum of these two vectors and points to the left. (B) The force from a single-beam gradient optical trap with Gaussian intensity profile; two rays are drawn. The central ray, a, is of higher intensity than the extreme ray, b. Again, the bead is displaced to the right of the true laser focus. The total force on the bead, F_{total}, again points to the left. (C) Dielectric particles much smaller than the wavelength of light can be considered to be perfect dipoles. The gradient in intensity, and hence electric field, produces a Lorentz force on the particle directed towards the laser focus (Figure obtained from Shaevitz *et al.* [179]).

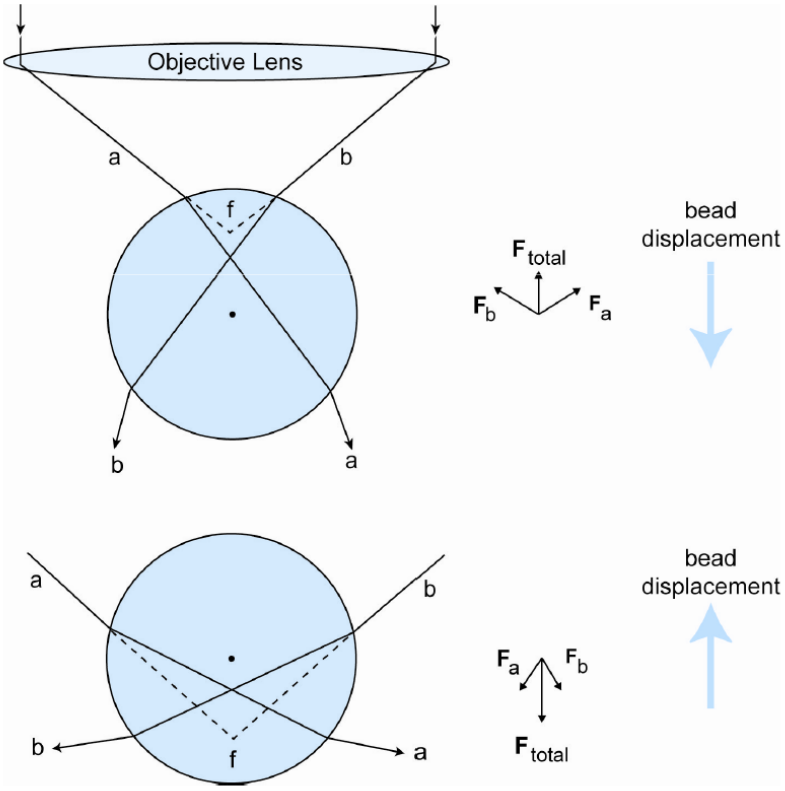

Figure C.2: Description of axial trapping forces. Axial displacements of a bead in an optical trap change the relative amount of divergence of the focused laser light. In the absence of the bead, two rays (a and b) are focused through the objective lens to position f, the true laser focus. (A) Refraction through the bead, which is displaced below the laser focus, causes the new focus to lie below f. Upon exiting the bead the two rays are more convergent; ray a is bent down and to the left, while ray b is deflected down and to the right. F_a and F_b represent the forces imparted to the bead by rays a and b; F_{total} is the sum of these two vectors and points to upwards. (B) When the bead is displaced above the laser focus, the deflected rays a and b are more divergent, and the resulting force points downward (Figure obtained from Shaevitz *et al.* [179]).

guided through a beam expander (L_1 and L_2) to a microscopic objective. The beam expander enlarges the beam larger than the diameter of the input aperture of the microscopic objective (MO). The beam coming out after the focus is terminated in a beam dump. M_3, M_4, L_3 and L_4 are mounted on XYZ translational stages and form the beam steering optics. All mirrors and lenses are anti-reflection coated to ensure minimum loss of laser power. The optics is held in a cage system. CAD drawings of the cage are shown in Figure C.11.

For the optical trap to work, an oil immersed 100× objective with a numerical aperture (NA) 1.25 is used. The beam expander generated a magnification of 5, thereby increasing the beam diameter to 12 mm. A 4f telescope arrangement (L_3 and L_4) is used to make the microscope imaging plane conjugate to the steering mirror M_6 (refer Figure 6.1). This means that a generated trap can be moved directly along the sample plane with minimal distortion using the mirror mount. The beam collimation and diameter at the back aperture can be controlled using a pair of lenses on a rail mount separated by distance equal to sum of their focal lengths.

Laser

The critical characteristics of the laser beam are the spatial beam profile, power and the wavelength. The first two determine the the focussing properties. In order to focus the beam to a smaller area, it has to be in single transverse mode. Power of the laser is the most fundamental characteristic to check performance. The selection of laser wavelength depends on the intended use of the trap. The wavelength used determines the absorption of energy by the object to be trapped. In order to focus the beam to a single small point, it has to be in single transverse mode.

We used the Ventus 1064 laser with single transverse mode, near diffraction limited, CW beam. The beam diameter is 2.4mm ± 0.2mm with spatial mode TEM_{00} (Gaussian profile) and band width 80GHz. Divergence observed was 0.6 mrad and M^2 factor <1.5. For the laser chosen, power stability is $< 0.2\%$ rms and noise less than 0.2% rms with pointing stability less than 5 µrad/°C. The output can be made symmetric and

non-astigmatic by spatial filtering using a pinhole-lens combination.

Optics

There are many sources of power loss in an optical trap set-up, mainly reflection losses in the collimation and steering optics. These can be reduced by ensuring optics are coated with anti-reflection dielectric coatings at the appropriate wavelengths. Secondly, the degree of overfilling at the back of the objective lens must be taken into account. A Olympus PLN 100X Oil Immersion Objective was purchased for the purpose. The lens had a magnification 100×, numerical Aperture of 1.25, with a working distance of 0.15 mm. A pair of steering mirrors is used (M_1 and M_2) to give control over both the angle and the displacement of the beam relative to subsequent optics. It is common practice to slightly overfill the back aperture of the objective since the rays focussed from the edge of the objective provide a larger gradient force because they are entering the focus at a larger angle with respect to the normal. The beam collimation and diameter at the back of the objective lens can be controlled using a pair of lenses mounted on an optical rail separated by a distance equal to sum of their focal lengths. Assuming that the output of the laser is collimated, the magnification, M, of the telescope should be given by the ratio of diameter of the input aperture of the objective lens (D_{obj}) to the diameter of the output of the laser. For a simple telescope composed of two convex lenses, L_1 and L_2 , with focal lengths f_1 and f_2, respectively, that are separated by $d_1 = f_1 + f_2$, and the lateral magnification, M, is given by $M = f_2 / f_1$. The beam expander generated a magnification of 5, thereby increasing beam diameter to 12 mm (diameter of the input aperture of the objective lens, $D_{obj} = 5$ mm) . The power loss between source and the objective lens was monitored using a power meter. Once the beam is perfectly aligned and collimated, airy rings can be observed in the camera (Figure C.3). If the beam is not going in the microscopic objective properly, the airy rings formed will be distorted.

A dichroic Notch beam splitter, (NFD-01 1064, Semrock) reflects the 1064 nm laser beam and allows the red laser (632.8 nm) to pass through. A Notch filter (NF 633-25, Thorlabs) was used to align the red laser with the IR laser beam. It reflects the light from the He-Ne and allows the emission from the sample to pass through. A second beam splitter (plate

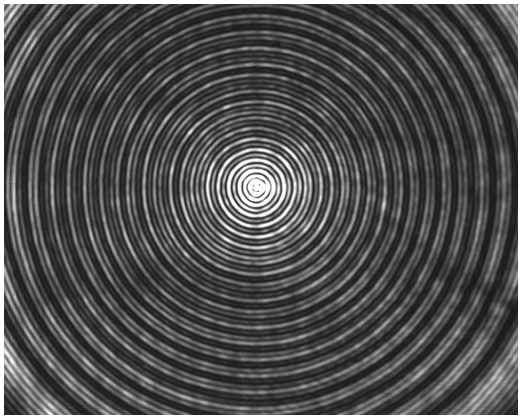

Figure C.3: Airy disk imaged in the camera after alignment.

beam splitter 90-10 BSX10, Thorlabs) was used to observe and record the trapping with a camera when simultaneously recording spectra with a CCD.
The sample chamber is illuminated by a blue LED for illuminating the trapped particles (Figure C.9).

Sample chamber and aerosol generator

A commercial medical nebuliser (Omron Microair U22) is used to generate and introduce aerosol droplets into the sample chamber for trapping. The average diameter of the droplets generated by the nebulizer is estimated to be 4.2µm (Figure C.7). A cuboidal head attachment with nozzle (Figure C.5, C.6) was designed and attached to the head of the nebuliser to control the number of particles generated. The narrow funnel shape of the head helped to release only those particles which move horizontally with respect to the length of the head. Particles with velocity components in other directions will get blocked out and condenses on the sides of the head.
The major design considerations for the sample chamber were reduction of air turbulence and initial velocity of the droplets. The chamber is made airtight to ensure minimum air turbulence (FigureC.8, Figure C.9). The bottom of the chamber is sealed by a microscopic glass coverslip of average thickness 125 μm. The droplets were allowed to enter the chamber through a narrow hole of diameter 1 mm on the side. The aerosols leaving the nebulizer will be having a velocity in the x-y direction perpendicular to the bottom of the sample chamber. Once the aerosols

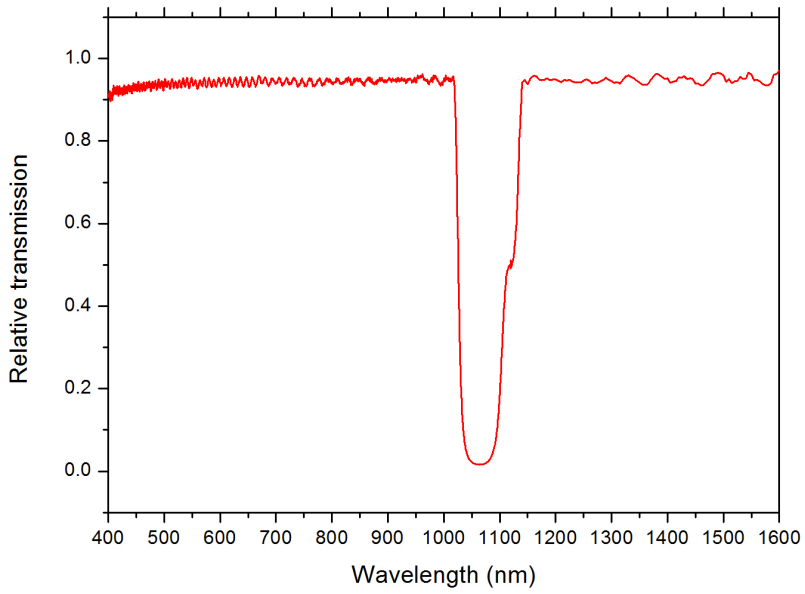

Figure C.4: Transmission of NFD-01 1064 at an angle of incidence 45.

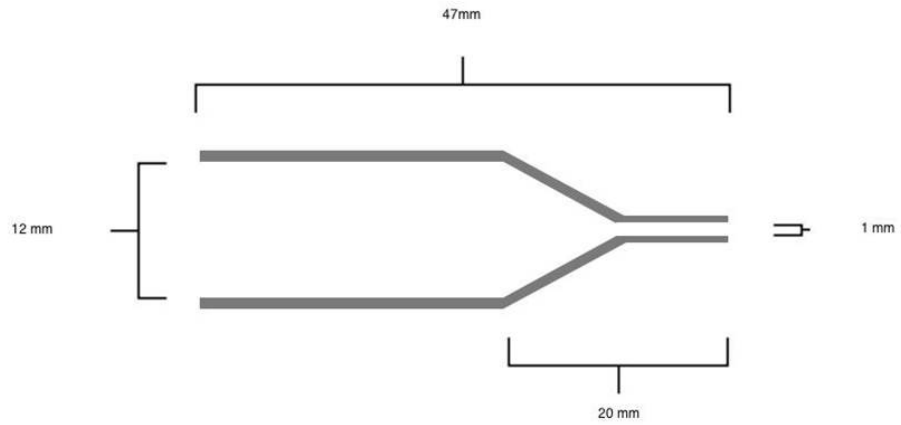

Figure C.5: Design of the nozzle for aerozol delivery at the head.

Figure C.6: Adapter and nozzle attached to the nebulizer (The material used was Acrylonitrile butadiene styrene (ABS) plastic).

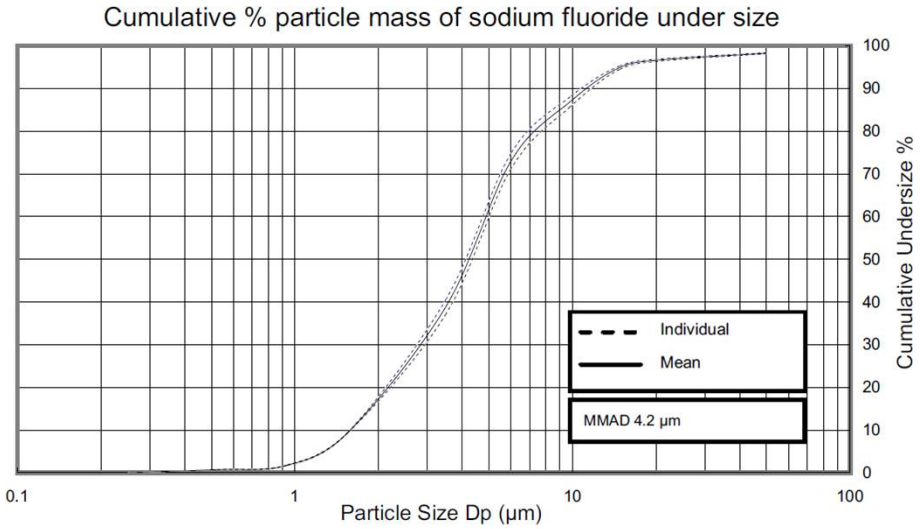

Figure C.7: Particle size distribution of Omron NE U22 nebulizer for sodium flouride solution (from manual of Omron NE U22).

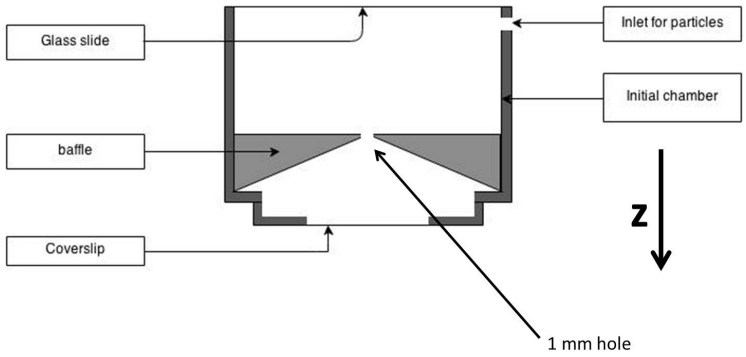

Figure C.8: Sample chamber design

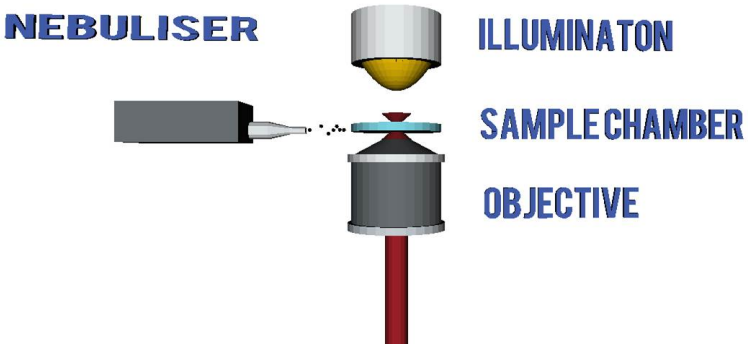

Figure C.9: 3D representation of sample chamber and inlet for aerosol droplets. The nebulizer is kept at a small distance away from the opening to control the number of particles entering the chamber.

come under the control of gravity, they fall down to the center of the chamber. The particles which are away from the center are filtered by a series of baffles made of plastic. The baffle used acts as a velocity filter to receive only those droplets which have velocity in the z- direction and pass through the centre. This design reduces the number of particles to a desirable amount. There will be refraction of the beam due to the glass slide and settling water droplets on the base. The chamber and the head of nebulizer were designed using Tinkercad and later 3D printed using Makerbot. The material used was Acrylonitrile butadiene styrene (ABS) plastic which suits all the design considerations. A translator with micron level precision is used to move the sample chamber in z-direction (i.e, vertical direction, refer Figure 6.1).

Imaging system

The microscope objective lens used for trapping is also used for imaging the trapped particle. The light for imaging is provided by a blue LED placed on top of the chamber(Figure C.9). Since the trapping light and the imaging light pass through the same objective, the trapped particle can be viewed with a CCD camera. A dichroic Notch filter is placed in front of the camera to prevent the backscattered IR radiation entering the camera. This is important to prevent damage to the CCD. The beam splitter allows the light from the blue LED to pass through while reflects the 1064 nm beam. This permits the two beams to follow the same path through the objective, but allows only the IR light to reach the camera. A high speed (90 fps) USB 3.0 vision camera (Ximea) was used for that purpose.

Optical trapping of water droplets

A solution of 38 wt % salt (NaCl) in water was prepared and inserted in the nebulizer. The modified nozzle was attached to the outlet of the nebulizer, and the was held it near the opening on the side of the sample chamber using a stand. The power of the laser was set to approximately 15 mW at the focus. The light back reflected from the microscopic objective-glass cover-slip interface was examined. The shape of the airy disc pattern was observed to check the alignment. The focus of the laser was adjusted such that the trap centre is approximately 1-2 mm from the bottom surface of the chamber. The defocused airy rings can be used to locate the lateral position of the single-beam optical trap. If a droplet falls close to the trap,

- the droplet will 'hop' toward the beam and become localized at the beam focus . This indicates that the laser is successfully trapping.
- the sphere is trapped in the beam but appears out of focus. This indicates that the trapping (tweezing) plane and the imaging plane are not coincident.
- water droplets are pushed out of the focus toward the top surface of the chamber.

Images of the trapped droplets are shown in Figure C.10. Trapped particles can be controlled in the lateral direction by moving the steering

mirror M_4 and observing the lateral motion. Trapped particles can be moved in the axial direction by moving the axial position of microscopic objective. At all times, the image of the droplet should stay in focus. If the trapped drop is out of focus, adjust the separation between lenses L_1 and L_2 so that the trapping plane and imaging plane become coincident. Avoid adjusting the positions of L_3 and L_4 as they are critical to the steering lens arrangements. The trapping event was viewed and recorded using the camera. The droplet was moved in the transverse direction and axial direction using the moving stages. In the future this set-up can be used to study fluorescence from trapped solid and liquid aerosols.

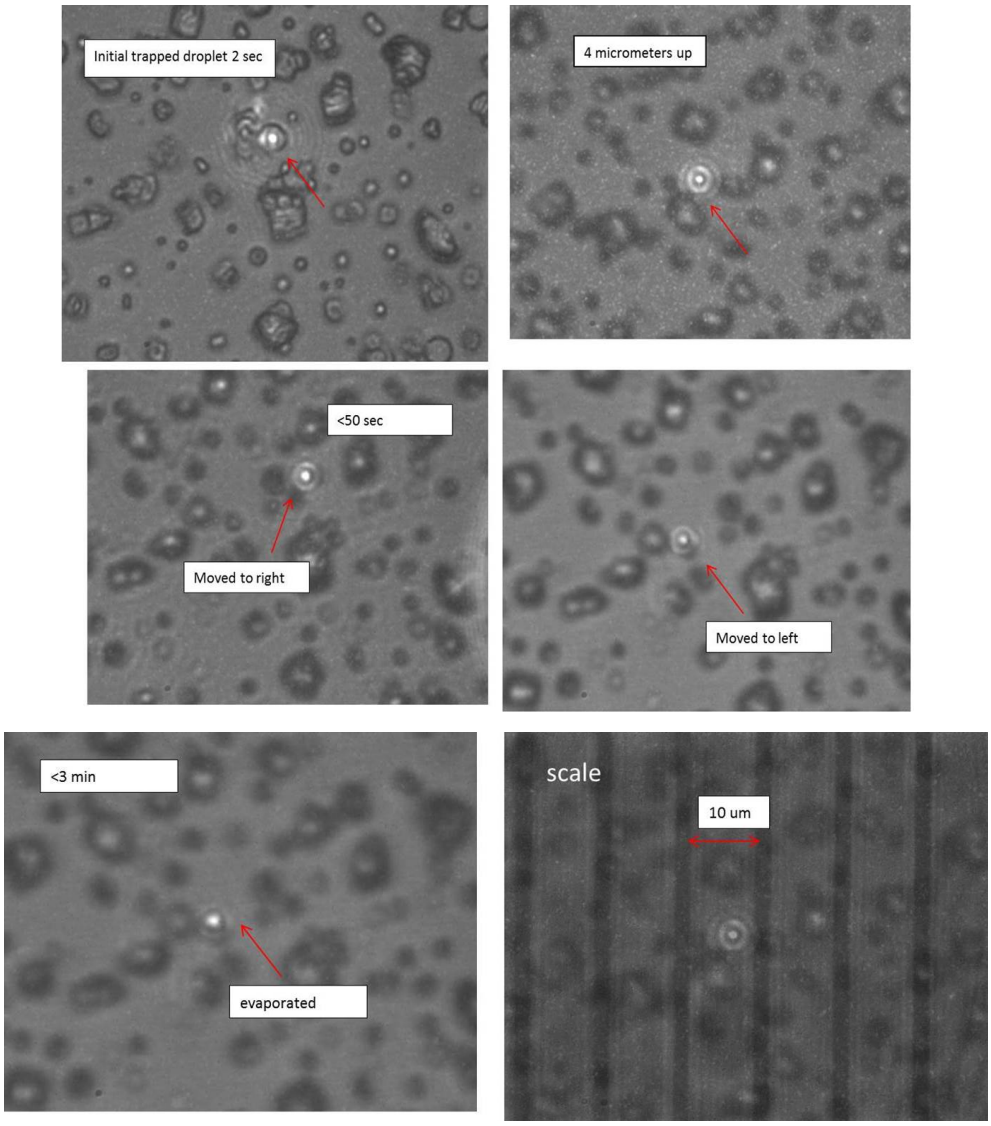

Figure C.10: Trapped droplets. First Figure from the top indicates the trapped droplet right after 2 seconds of the aerosol introduced into the trap. The second Figure in the right shows the particle moved $4\mu m$ up. Second row first Figure: 50 seconds after trapping, droplet moved to right. Second row second Figure: 50 seconds after trapping particle moved to right. Third row first Figure : 3 minutes after trapping, droplet is evaporated. Third row final Figure shows the trapped droplet with the scale. Each vertical line is seperated by 10 μm.

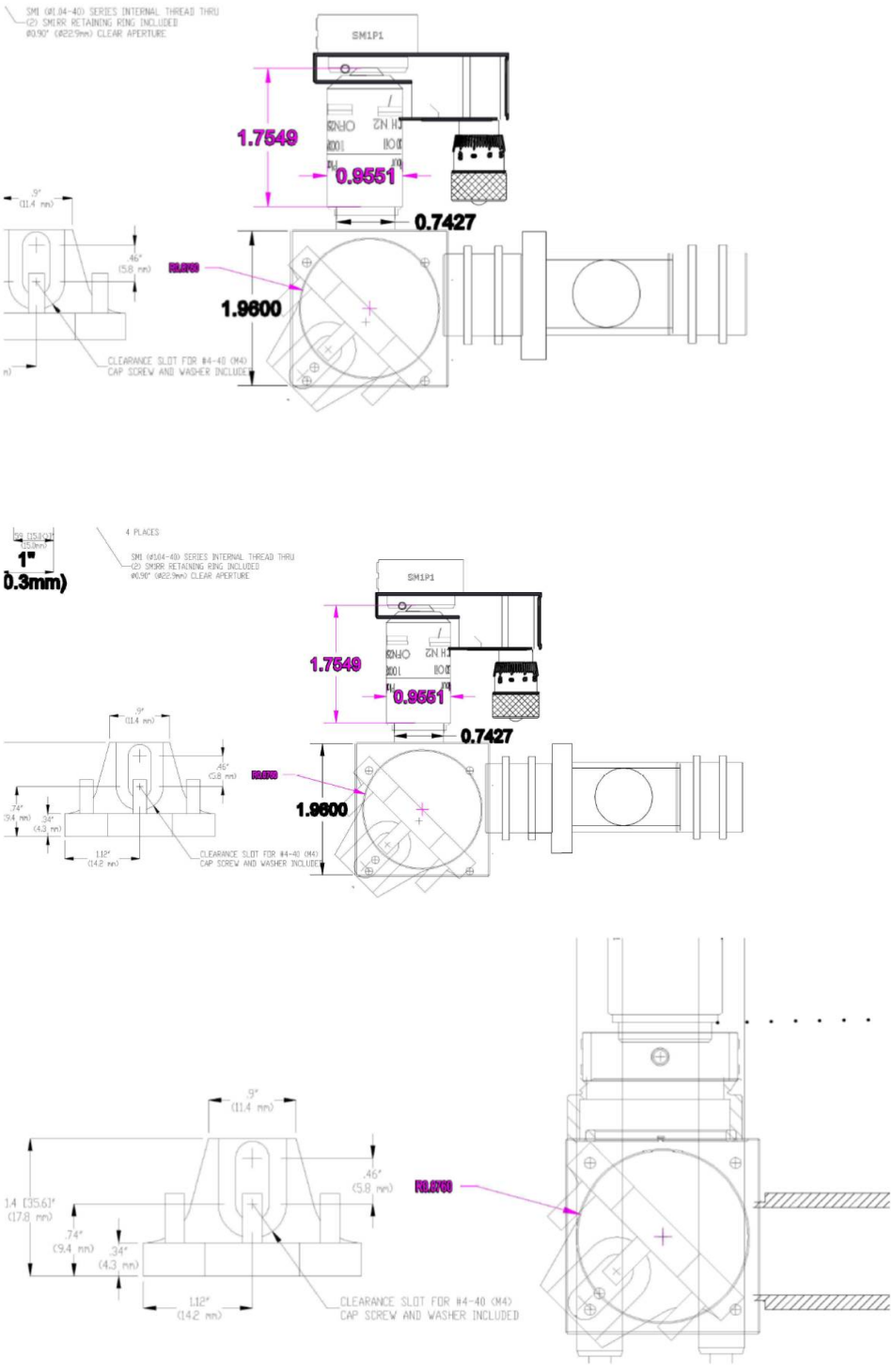

Figure C.11: CAD drawings of the cage set-up

Bibliography

[1] A. J. Kenyon, "Recent developments in rare-earth doped materials for optoelectronics," Progress in Quantum Electronics, vol. 26, no. 4–5. pp. 225–284, 2002.

[2] Z. Li, J. C. Barnes, A. Bosoy, J. F. Stoddart, and J. I. Zink, "Mesoporous silica nanoparticles in biomedical applications," Chem. Soc. Rev., vol. 41, no. 7, p. 2590, 2012.

[3] F. Wang, W. B. Tan, Y. Zhang, X. Fan, and M. Wang, "Luminescent nanomaterials for biological labelling," Nanotechnology, vol. 17, no. 1, pp. R1–R13, 2006.

[4] W. J. Parak, T. Pellegrino, and C. Plank, "Labelling of cells with quantum dots.," Nanotechnology, vol. 16, pp. R9–R25, 2005.

[5] J. B. Castor, S.B., Hendrick, "Rare Earth Elements," Ind. Miner. Rocks Commod. Mark. Uses, pp. 769–792, 2006.

[6] G. Charalampides, K. I. Vatalis, B. Apostoplos, and B. Ploutarch-Nikolas, "Rare Earth Elements: Industrial Applications and Economic Dependency of Europe," Procedia Econ. Financ., vol. 24, pp. 126–135, 2015.

[7] C. V. Shank, "Physics of dye lasers," Rev. Mod. Phys., vol. 47, no. 3, pp. 649–657, 1975.

[8] G. S. Shankarling and K. J. Jarag, "Laser dyes," Resonance, vol. 15, no. 9, pp. 804–818, 2010.

[9] C. M. Carbonaro, A. Anedda, S. Grandi, and A. Magistris, "Hybrid materials for solid-state dye laser applications.," J. Phys. Chem. B, vol. 110, no. 26, pp. 12932–12937, 2006.

[10] W. T. Silfvast, "Lasers," Cambridge University Press., vol. 11, 2011.

[11] F. P. Schafer, "Dye lasers and laser dyes in physical chemistry," in Dye Lasers: 25 Years, M. Stuke, Springer, pp. 19–36, vol 70, 1992.

[12] V. Ter-Mikirtychev, "Fundamentals of fiber lasers and fiber amplifi-

ers," Springer Series in Optical Sciences, vol. 181. pp. 1–253, 2014.
[13] M. Sheik-Bahae and R. I. Epstein, "Laser cooling of solids," Laser Photonics Rev., vol. 3, no. 1–2, pp. 67–84, 2009.
[14] M. P. Hehlen, M. Sheik-Bahae, R. I. Epstein, S. D. Melgaard, and D. V Seletskiy, "Laser cooling of solids to cryogenic temperatures," J. Mater. Chem. C, 2013.
[15] G. Nemova and R. Kashyap, "Laser cooling of solids," Reports Prog. Phys., vol. 73, no. 8, p. 86501, Aug. 2010
[16] S. V Petrushkin and V. V Samartsev, "Advances of laser refrigeration in solids," Laser Phys., vol. 20, no. 1, pp. 38–46, 2009.
[17] M. Sheik-Bahae and R. I. Epstein, "Laser cooling of solids," Laser Photonics Rev., vol. 3, no. 1–2, pp. 67–84, Feb. 2009.
[18] J. Kim, A. Kapoor, and M. Kaviany, "Material metrics for laser cooling of solids," Phys. Rev. B - Condens. Matter Mater. Phys., vol. 77, no. 11, 2008.
[19] J. L. Clark and G. Rumbles, "Laser Cooling in the Condensed Phase by Frequency Up-Conversion," pp. 2037–2040, 1996.
[20] G. Nemova and R. Kashyap, "Temperature distribution in laser-cooled rare-earth doped solid-state samples," J. Opt. Soc. Am. B 27(12), 2460–2464 (2010).
[21] D. V Seletskiy, S. D. Melgaard, S. Bigotta, A. Di Lieto, and M. Tonelli, "Laser cooling of solids to cryogenic temperatures," Nat. Photonics, no. January, pp. 1–4, 2010.
[22] J. L. Clark, P. F. Miller, and G. Rumbles, "Red Edge Photophysics of Ethanolic Rhodamine 101 and the Observation of Laser Cooling," vol. 5639, no. 98, pp. 4428–4437, 1998.
[23] Y. Wang, Z. H. Li, W. Y. Zhong, H. Li, D. K. Xu, and H. Y. Chen, "Rhodamine B doped silica nanoparticle labels for protein microarray detection," Sci. China Chem., vol. 53, no. 4, pp. 747–751, 2010.
[24] K. Saito, M. Tokunaga, a H. Iwane, and T. Yanagida, "Dual-colour microscopy of single fluorophores bound to myosin interacting with fluorescently labelled actin using anti-Stokes fluorescence.," J. Microsc., vol. 188, no. Pt 3, pp. 255–263, 1997.
[25] A. Sharma and S. G. Schulman, "Introduction to fluorescence spectroscopy," Tech. Anal. Chem. Ser., p. xiv, 173 , 1999.
[26] J. R. Lakowicz, "Principles of fluorescence spectroscopy", Springer

USA, vol. 26, pp. 1-25, 2006.
[27] G. Liu and B. Jacquier, "Spectroscopic Properties of Rare Earths in Optical Materials", Springer, vol. 83., 2005.
[28] K. H. Drexhage, "Structure and Properties of Laser Dyes," in Dye Lasers, F. P. Schäfer, Ed. Berlin, Heidelberg: Springer Berlin Heidelberg, 1973, pp. 144–193.
[29] M. L. Lesiecki and J. M. Drake, "Use of the thermal lens technique to measure the luminescent quantum yields of dyes in PMMA for luminescent solar concentrators.," Appl. Opt., vol. 21, no. 3, pp. 557–560, 1982.
[30] R. A. Ali and O. M. Abdul-munem, "Study the spectroscopic characteristics of Rhodamine B Dye in Ethanol and Methanol mixture and Calculation the Quantum Efficiency" J. Baghdad for Sci., vol. 9, no. 2, 2012.
[31] H. B. Rodríguez and E. S. Román, "Energy transfer from chemically attached rhodamine 101 to adsorbed methylene blue on microcrystalline cellulose particles.," Photochem. Photobiol., vol. 83, no. 3, pp. 547–55, 2007.
[32] T. Karstens and K. Kobs, "Rhodamine-B and Rhodamine-101 As Reference Substances for Fluorescence Quantum Yield Measurements," J. Phys. Chem., vol. 84, pp. 1871–1872, 1980.
[33] R. F. Kubin and A. N. Fletcher, "Fluorescence quantum yields of some rhodamine dyes," J. Lumin., vol. 27, no. 4, pp. 455–462, 1982.
[34] R. Menzel and E. Thiel, "Intersystem crossing rate constants of rhodamine dyes: influence of the amino-group substitution," Chem. Phys. Lett., vol. 291, no. July, pp. 237–243, 1998.
[35] V. E. Korobov and A. K. Chibisov, "Primary processes in the photochemistry of rhodamine dyes," J. Photochem., vol. 9, no. 4, pp. 411–424, 1978.
[36] P. C. Beaumont, D. G. Johnson, and B. J. Parsons, "Photophysical properties of laser dyes: picosecond laser flash photolysis studies of Rhodamine 6G, Rhodamine B and Rhodamine 101," J. Chem. Soc. Faraday Trans., vol. 89, no. 23, p. 4185, 1993.
[37] J. A. Verge, M. H. Bartl, and B. J. Scott, "Single-Photon Hot Band Absorption Induced Anti-Stokes Luminescence of Rhodamine 101 in Mesostructured Thin Films," no. 4, pp. 392–395, 2003.

[38] A.P. Demchenko "The red-edge effects: 30 years of exploration", Luminescence, vol. 17, pp.19-42, 2002.
[39] A. Arauzo, A. Lazarescu, S. Shova, E. Bartolomé, R. Cases, J. Luzón, J. Bartolomé, and C. Turta, "Structural and magnetic properties of some lanthanide (Ln = Eu(iii), Gd(iii) and Nd(iii)) cyano-acetate polymers: field-induced slow magnetic relaxation in the Gd and Nd substitutions.," Dalton Trans., pp. 12342–12356, 2014.
[40] H. M. Grosswhite and H. Crosswhite, "Parametric model for f-shell configurations. I. The effective-operator Hamiltonian," J. Opt. Soc. Am. B, vol. 1, no. 2, pp. 246–254, Apr. 1984.
[41] F. Auzel, "A fundamental self-generated quenching center for lanthanide-doped high-purity solids," J. Lumin., vol. 100, no. 1, pp. 125–130, 2002.
[42] N. Rösch, "Time-reversal symmetry, Kramers' degeneracy and the algebraic eigenvalue problem," Chem. Phys., vol. 80, no. 1–2, pp. 1–5, 1983.
[43] L. F. Chibotaru, A. Ceulemans, and H. Bolvin, "Unique definition of the Zeeman-splitting g tensor of a kramers doublet," Phys. Rev. Lett., vol. 101, no. 3, 2008.
[44] F. Auzel, "On the maximum splitting of the ($^2F_{7/2}$) ground state in Yb^{3+}doped solid state laser materials," J. Lumin., vol. 93, no. 2, pp. 129–135, Jun. 2001, and references there in.
[45] M. Ito, C. Goutaudier, Y. Guyot, K. Lebbou, T. Fukuda, and G. Boulon, "Crystal growth, Yb^{3+} spectroscopy, concentration quenching analysis and potentiality of laser emission in $Ca_{1-x}Yb_xF_{2+x}$," J. Physics-Condensed Matter, vol. 16, no. 8, pp. 1501–1521, 2004.
[46] M. C. Pujol, R. Sole, J. Massons, J. Gavald, X. Solans, C. Zaldo, F. Diaz, and M. Aguilo, "Structural study of monoclinic $KGd(WO_4)_2$ and effects of lanthanide substitution," J. Appl. Crystallogr., vol. 34, no. 1, pp. 1–6, 2001.
[47] Z. Luo and Y. Huang, "An empirical relationship between laser threshold and chemical composition of laser crystals," Opt. Commun., vol. 206, no. 1–3, pp. 159–164, 2002.
[48] M. P. Hehlen, "Crystal-field effects in fluoride crystals for optical refrigeration," Proc. SPIE, vol. 7614. pp. 761404–761412, 2010.
[49] A. Belafhal, "Shape of spectral lines: Widths and equivalent widths of the Voigt profile," Opt. Commun., vol. 177, no. 1, pp. 111–118, 2000.

[50] J. T. Fournier and R. H. Bartram, "Inhomogeneous broadening of the optical spectra of Yb^{3+} in phosphate glass," J. Phys. Chem. Solids, vol. 31, no. 12, pp. 2615–2624, Dec. 1970.
[51] L. Macalik, P. E. Tomaszewski, R. Lisiecki, and J. Hanuza, "The crystal structure, vibrational and luminescence properties of the nanocrystalline $KEu(WO_4)_2$ and $KGd(WO_4)_2$:Eu^{3+} obtained by the Pechini method," J. Solid State Chem., vol. 181, pp. 2591–2600, 2008.
[52] G. Lei, J. Anderson, M. Buchwald, B. Edwards, and R. Epstein, "Determination of spectral linewidths by Voigt profiles in Yb3+-doped fluorozirconate glasses," Phys. Rev. B, vol. 57, no. 13, pp. 7673–7678, 1998.
[53] L. D. Deloach, S. A. Payne, L. L. Chase, L. K. Smith, W. L. Kway, and W. F. Krupke, "Evaluation of Absorption and Emission Properties of Yb^{3+} Doped Crystals for Laser Applications," IEEE J. Quantum Electron., vol. 29, no. 4, pp. 1179-1191, 1993.
[54] R. K. Brow, "Review: the structure of simple phosphate glasses," J. Non. Cryst. Solids, vol. 263, pp. 1–28, 2000.
[55] B. E. Warren, "Summary of Work on Atomic Arrangement in Glass," J. Am. Ceram. Soc., vol. 24, no. 8, pp. 256–261, 1941.
[56] P. S. Salmon, "Amorphous materials - Order within disorder," Nat. Mater., vol. 1, no. 2, pp. 87–88, 2002.
[57] D. Thangaraju, P. Samuel, and S. Moorthy Babu, "Growth of two-dimensional $KGd(WO_4)_2$ nanorods by modified sol-gel Pechini method," in Optical Materials, 2010, vol. 32, no. 10, pp. 1321–1324.
[58] A. Z. Grasiuk, S. V. Kurbasov, and L. L. Losev, "Picosecond parametric Raman laser based on $KGd(WO_4)_2$ crystal," Opt. Commun., vol. 240, no. 4–6, pp. 239–244, 2004.
[59]M. C. Pujol, R. Solé, J. Gavaldá, J. Massons, M. Aguiló, F. Díaz, V. Nikolov, and C. Zaldo, "Growth and ultraviolet optical properties of $KGd_{1-x}RE_x(WO_4)_2$ single crystals," J. Mater. Res., vol. 14, no. 9, pp. 3739–3745, 1999.
[60] M. C. Pujol, C. Cascales, M. Aguilo, and F. Diaz, "Crystal growth, crystal field evaluation and spectroscopy for thulium in monoclinic $KGd(WO_4)_2$ and $KLu(WO_4)_2$ laser crystals," J. Physics-Condensed Matter, vol. 20, no. 34, p. 9, 2008.
[61] M. Pujol, M. Bursukova, F. Güell, X. Mateos, R. Solé, J. Gavaldà,

M. Aguiló, J. Massons, F. Díaz, P. Klopp, U. Griebner, and V. Petrov, "Growth, optical characterization, and laser operation of a stoichiometric crystal $KYb(WO_4)_2$," Phys. Rev. B, vol. 65, pp. 1–11, 2002.
[62] M. Galceran, M. C. Pujol, M. Aguilo, and F. Diaz, "Sol-gel modified Pechini method for obtaining nanocrystalline $KRE(WO_4)_2$ (RE = Gd and Yb)," J. Sol-Gel Sci. Technol., vol. 42, no. 1, pp. 79–88, 2007.
[63] D. Kasprowicz, M. Drozdowski, A. Majchrowski, and E. Michalski, "Spectroscopic properties of $KGd(WO_4)_2$: (Er, Yb) single crystals studied by Brillouin scattering method," Opt. Mater. (Amst)., vol. 30, no. 1, pp. 152–154, 2007.
[64] D. Kasprowicz, T. Runka, A. Majchrowski, E. Michalski, and M. Drozdowski, "Vibrational properties of Nd^{3+}, Eu^{3+}, Er^{3+} and Ho^{3+} doped $KGd(WO_4)_2$ single crystals studied by Raman scattering method," in Physics Procedia, 2009, vol. 2, no. 2, pp. 539–550.
[65] D. Kasprowicz, M. G. Brik, A. Majchrowski, E. Michalski, and A. Biadasz, "Spectroscopic studies of $KGd(WO_4)_2$:Ho^{3+} single crystals," J. Alloys Compd., vol. 509, no. 5, pp. 1430–1435, 2011.
[66] D. Kasprowicz, S. Mielcarek, A. Majchrowski, E. Michalski, and M. Drozdowski, "Optical properties of $KGd(WO_4)_2$ single crystals studied by Brillouin spectroscopy," Cryst. Res. Technol., vol. 41, no. 6, pp. 541–546, 2006.
[67]A. Senthil Kumaran, S. Moorthy Babu, S. Ganesamoorthy, I. Bhaumik, and A. K. Karnal, "Crystal growth and characterization of $KY(WO_4)_2$ and $KGd(WO_4)_2$ for laser applications," J. Cryst. Growth, vol. 292, no. 2, pp. 368–372, 2006.
[68] D. Rand, D. Miller, D. J. Ripin, and T. Y. Fan, "Cryogenic Yb^{3+} doped materials for pulsed solid- state laser applications," Opt. Mater Express, vol. 1, pp. 434–450, 2011.
[69] L. Tang, Z. Lin, L. Zhang, and G. Wang, "Phase diagram, growth and spectral characteristic of Yb^{3+}:$KY(WO_4)_2$ crystal," J. Cryst. Growth, vol. 282, no. 3–4, pp. 376–382, Sep. 2005.
[70] M. C. Pujol, M. Rico, C. Zaldo, R. Solé, V. Nikolov, X. Solans, M. Aguiló, and F. Diaz, "Crystalline structure and optical spectroscopy of Er^{3+}-doped $KGd(WO_4)_2$ single crystals," Appl. Phys. B, vol. 68, no. 2, pp. 187–197, 1999.
[71] B. C. Edwards, J. E. Anderson, R. I. Epstein, G. L. Mills, and A.

J. Mord, "Demonstration of a solid-state optical cooler : An approach to cryogenic refrigeration," vol. 6489, no. 1999, pp. 7–12, 2012.
[72] R. I. Epstein, M. Buchwald, B. Edwards, T. Gosnell, and C. Mungan, "Observation of laser-induced fluorescent cooling of a solid," Nature, vol. 377. pp. 500–503, 1995.
[73] R. Frey, F. Micheron, and J. P. Pocholle, "Comparison of Peltier and anti-Stokes optical coolings," J. Appl. Phys., vol. 87, no. 9, p. 4489, 2000.
[74] P. Pringsheim, "Zwei Bemerkungen {ü}ber den Unterschied von Lumineszenz- und Temperaturstrahlung," Zeitschrift f{ü}r Phys., vol. 57, no. 11, pp. 739–746.
[75] J. Fernandez, A. Garcia-Adeva, and R. Balda, "Anti-Stokes Laser Cooling in Bulk Erbium-Doped Materials," Phys. Rev. Lett., vol. 97, no. 3, p. 33001, Jul. 2006.
[76] D. V Seletskiy, S. D. Melgaard, R. I. Epstein, A. Di Lieto, M. Tonelli, and M. Sheik-Bahae, "Local laser cooling of Yb:YLF to 110 K.," Opt. Express, vol. 19, no. 19, pp. 18229–36, Sep. 2011.
[77] B. Heeg and G. Rumbles, "Influence of radiative transfer on optical cooling in the condensed phase," J. Appl. Phys., vol. 93, no. 4, p. 1966, 2003.
[78] W. Patterson, S. Bigotta, M. Sheik-Bahae, D. Parisi, M. Tonelli, and R. Epstein, "Anti-Stokes luminescence cooling of Tm^{3+} doped BaY_2F_8.," Opt. Express, vol. 16, no. 3, pp. 1704–10, Feb. 2008.
[79] C. V Bindhu, S. S. Harilal, G. K. Varier, R. C. Issac, V. P. N. Nampoori, and C. P. G. Vallabhan, "Measurement of the absolute fluorescence quantum yield of rhodamine B solution using a dual-beam thermal lens technique," J. Phys. D. Appl. Phys., vol. 29, no. 4, pp. 1074–1079, Apr. 1996.
[80] M. H. Bartl, B. J. Scott, G. Wirnsberger, A. Popitsch, and G. D. Stucky, "Single-photon hot band absorption induced anti-Stokes luminescence of rhodamine 101 in mesostructured thin films," ChemPhysChem, vol. 4, no. 4, pp. 392–395, 2003.
[81] D. Magde, R. Wong, and P. G. Seybold, "Fluorescence Quantum Yields and Their Relation to Lifetimes of Rhodamine 6G and Fluorescein in Nine Solvents: Improved Absolute Standards for Quantum Yields," Photo-chemistry and photobiology, vol. 75, no. 4, pp. 327–334, 2002.

[82] M. Sheik-bahae, B. Imangholi, M. P. Hasselbeck, R. I. Epstein, and S. Kurtz, "Advances in Laser Cooling of Semiconductors," Proc. SPIE 6115, Physics and Simulation of Optoelectronic Devices XIV, vol. 6115, 2006.
[83] S. D. Melgaard, A. R. Albrecht, M. P. Hehlen, and M. Sheik-Bahae, "Solid-state optical refrigeration to sub-100 Kelvin regime," Sci. Rep., vol. 6, p. 20380, Feb. 2016.
[84] G. Bunzli, "Rare Earth Luminescent Centers in Organic and Biochemical Compounds" in Spectroscopic Properties of Rare Earths in Optical Materials, Springer, vol. 83. pp 462-499, 2005.
[85] S. R. Bowman and C. E. Mungan, "New materials for optical cooling," , Appl. Phys. B, vol. 71, pp. 807–811, 2000.
[86] X. L. Ruan and M. Kaviany, "Enhanced laser cooling of rare-earth-ion-doped nanocrystalline powders," Phys. Rev. B, vol. 73, no. 15, p. 155422, Apr. 2006.
[87] V. Venkatramu, R. Vijaya, S. F. León-Luis, P. Babu, C. K. Jayasankar, V. Lavín, and L. J. Dhareshwar, "Optical properties of Yb^{3+}-doped phosphate laser glasses," J. Alloys Compd., vol. 509, no. 16, pp. 5084–5089, 2011.
[88] M. Galceran, M. C. Pujol, M. Aguilo, and F. Diaz, "Sol-gel modified Pechini method for obtaining nanocrystalline $KRE(WO_4)_2$ (RE = Gd and Yb)," J. Sol-Gel Sci. Technol., vol. 42, no. 1, pp. 79–88, 2007.
[89] F. Márquez, C. M. Zicovich-Wilson, A. Corma, E. Palomares, and H. García, "Naphthalene included within all-silica zeolites: Influence of the host on the naphthalene photophysics," J. Phys. Chem. B, vol. 105, no. 41, pp. 9973–9979, 2001.
[90] I. L. Li, Z. K. Tang, X. D. Xiao, C. L. Yang, and W. K. Ge, "Optical properties of organic dyes in nanoporous zeolite crystals," Appl. Phys. Lett., vol. 83, no. 12, p. 2438, 2003.
[91] G. Sastre and A. Corma, "The confinement effect in zeolites," J. Mol. Catal. A Chem., vol. 305, no. 1–2, pp. 3–7, 2009.
[92] F. Márquez and M. J. Sabater, "Emission frequency modulation by electronic confinement effect: Congo Red incorporated within a dendritic structure," J. Phys. Chem. B, vol. 109, no. 35, pp. 16593–16597, 2005.
[93] M. D. Shirk and P. A. Molian, "A review of ultrashort pulsed laser ablation of materials," J. Laser Appl., vol. 10, no. 1, p. 18, 1998.

[94] T. Nunokawa, Y. Onodera, M. Hara, Y. Kitamoto, O. Odawara, and H. Wada, "Preparation of Y_2O_3:Er,Yb nanoparticles by laser ablation in liquid," Appl. Surf. Sci., vol. 261, pp. 118–122, Nov. 2012.
[95] M. Galceran, M. C. Pujol, C. Méndez, A. García, P. Moreno, L. Roso, M. Aguiló, and F. Díaz, "Synthesis of monoclinic $KGd(WO_4)_2$ nanocrystals by two preparation methods," J. Nanoparticle Res., vol. 11, no. 3, pp. 717–724, 2009.
[96] G. W. Yang, "Laser ablation in liquids: Applications in the synthesis of nanocrystals," Progress in Materials Science, vol. 52, no. 4. pp. 648–698, 2007.
[97] H. S. Yang, K. S. Hong, S. P. Feofilov, B. M. Tissue, R. S. Meltzer, and W. M. Dennis, "Electron-phonon interaction in rare earth doped nanocrystals," J. Lumin., vol. 83–84, pp. 139–145, 1999.
[98] M. V Gryaznova, V. V Danilov, and V. A. Smirnov, "On the question of pulsed laser cooling: Collective luminescence and light quenching in high-concentration solutions of rhodamine 101," , J. Opt. Tech., pp. 351–353, 2005.
[99] W. Stöber, A. Fink, and E. Bohn, "Controlled growth of monodisperse silica spheres in the micron size range," J. Colloid Interface Sci., vol. 26, no. 1, pp. 62–69, Jan. 1968.
[100] Galceran, M., Pujol, M. C., Aguiló, M. & Díaz, F., "Synthesis and characterization of nanocrystalline Yb:Lu_2O_3 by modified Pechini method", Mater. Sci. Eng. B Solid-State Mater. Adv. Technol., 146, 7–15 (2008).
[101] A. Dragomir, J. G. McInerney, and D. N. Nikogosyan, "Femtosecond measurements of two-photon absorption coefficients at $\lambda = 264$ nm in glasses, crystals, and liquids: erratum," Appl. Opt., vol. 41, no. 27, p. 5655, 2002.
[102] A. A. Ruth, S. Dixneuf, and J. Orphal, "Laser-induced plasmas in ambient air for incoherent broadband cavity-enhanced absorption spectroscopy," Opt. Express, vol. 23, no. 5, pp. 6092–6101, Mar. 2015.
[103] K. H. H. Drexhage, "Fluorescence efficiency of laser dyes," J. Res. Natl. Bur. Stand. Sect. A Phys. Chem., vol. 80A, no. 3, p. 421, 1976.
[104] N. O. McHedlov-Petrosyan and Y. V. Kholin, "Aggregation of rhodamine B in water," Russ. J. Appl. Chem., vol. 77, no. 3, pp. 414–422, 2004.

[105] H. Tajalli, A. Ghanadzadeh Gilani, M. S. Zakerhamidi, and M. Moghadam, "Effects of surfactants on the molecular aggregation of rhodamine dyes in aqueous solutions," Spectrochim. Acta - Part A Mol. Biomol. Spectrosc., vol. 72, no. 4, pp. 697–702, 2009.
[106] F. L. Arbeloa, P. R. Ojeda, and I. L. Arbeloa, "On the aggregation of rhodamine B in ethanol," Chem. Phys. Lett., vol. 148, no. 2–3, pp. 253–258, 1988.
[107] I. López Arbeloa and P. Ruiz Ojeda, "Dimeric states of rhodamine B," Chem. Phys. Lett., vol. 87, no. 6, pp. 556–560, 1982.
[108] F. M. Zehentbauer, C. Moretto, R. Stephen, T. Thevar, J. R. Gilchrist, D. Pokrajac, K. L. Richard, and J. Kiefer, "Fluorescence spectroscopy of Rhodamine 6G: Concentration and solvent effects," Spectrochim. Acta - Part A Mol. Biomol. Spectrosc., vol. 121, pp. 147–151, 2014.
[109] B. Heeg, P. A. Debarber, and G. Rumbles, "Influence of fluorescence reabsorption and trapping on solid-state optical cooling," vol. 44, no. 15, pp. 3117–3124, 2005.
[110] M. W. Forbes and R. a Jockusch, "Gas-phase fluorescence excitation and emission spectroscopy of three xanthene dyes (rhodamine 575, rhodamine 590 and rhodamine 6G) in a quadrupole ion trap mass spectrometer.," J. Am. Soc. Mass Spectrom., vol. 22, no. 1, pp. 93–109, Jan. 2011.
[111] I. Miletto, A. Gilardino, P. Zamburlin, S. Dalmazzo, D. Lovisolo, G. Caputo, G. Viscardi, and G. Martra, "Dyes and Pigments Highly bright and photostable cyanine dye-doped silica nanoparticles for optical imaging : Photophysical characterization and cell tests," Dye. Pigment., vol. 84, no. 1, pp. 121–127, 2010.
[112] A. Van Blaaderen and A. Vrij, "Synthesis and Characterization of Colloidal Dispersions of Fluorescent , Monodisperse Silica Spheres," vol. 81, no. 2, pp. 2921–2931, 1992.
[113] A. Imhof, M. Megens, J. J. Engelberts, D. T. N. De Lang, R. Sprik, and W. L. Vos, "Spectroscopy of Fluorescein (FITC) Dyed Colloidal Silica Spheres," pp. 1408–1415, 1999.
[114] Y. L. Choi, J. H. Lee, J. Jaworski, and J. H. Jung, "Mesoporous silica nanoparticles functionalized with a thymidine derivative for controlled release," J. Mater. Chem., vol. 22, pp. 9455–9457, 2012.
[115] T. Fujii, A. Ishii, and M. Anpo, "Absorption and fluorescence spec-

tra of rhodamine B molecules encapsulated in silica gel networks and their thermal stability," J. Photochem. Photobiol. A Chem., vol. 54, no. 2, pp. 231–237, 1990.
[116] W. Stöber, A. Fink, and E. Bohn, "Controlled growth of monodisperse silica spheres in the micron size range," J. Colloid Interface Sci., vol. 26, no. 1, pp. 62–69, 1968.
[117] S. Dai, A. Sugiyama, L. Hu, Z. Liu, G. Huang, and Z. Jiang, "The spectrum and laser properties of ytterbium doped phosphate glass at low temperature," J. Non. Cryst. Solids, vol. 311, pp. 138–144, 2002.
[118] Y. Mao, P. Deng, F. Gan, H. Yang, and W. Shen, "Spectroscopic properties of ytterbium in phosphate glass," Mater. Lett., vol. 57, no. 2, pp. 439–443, Dec. 2002.
[119] B. Yang, X. Liu, X. Wang, J. Zhang, L. Hu, and L. Zhang, "Compositional dependence of room-temperature Stark splitting of Yb^{3+} in several popular glass systems," Opt. Lett., vol. 39, no. 7, pp. 1772–1774, Apr. 2014.
[120] L. Zhang, T. Xue, D. He, M. Guzik, and G. Boulon, "Influence of Stark splitting levels on the lasing performance of Yb^{3+} in phosphate and fluorophosphate glasses," Opt. Express, vol. 23, no. 2, pp. 1505–1511, Jan. 2015.
[121] W. Demtröder, Laser Spectroscopy: Basic Concepts and Instrumentation, Springer, vol. 1, no. 11, pp 7-219, 2003.
[122] R. T. Brundage and W. M. Yen, "Low-temperature homogeneous linewidths of Yb^{3+} in inorganic glasses," Phys. Rev. B, vol. 33, no. 6, pp. 4436–4438, Mar. 1986.
[123] L. B. Fletcher, J. J. Witcher, N. Troy, S. T. Reis, R. K. Brow, R. M. Vazquez, R. Osellame, and D. M. Krol, "Femtosecond laser writing of waveguides in zinc phosphate glasses," Opt. Mater. Express, vol. 1, no. 5, pp. 845–855, Sep. 2011.
[124] H. Büning-Pfaue, "Analysis of water in food by near infrared spectroscopy," Food Chem., vol. 82, no. 1, pp. 107–115, Jul. 2003.
[125] C. Jacinto, S. L. Oliveira, L. A. O. Nunes, T. Catunda, and M. J. V Bell, "Thermal lens study of the OH^- influence on the fluorescence efficiency of Yb^{3+} -doped phosphate glasses," Appl. Phys. Lett., vol. 86, no. 7, pp. 1–3, 2005.
[126] M. Kasha, "Characterization of electronic transitions in complex

molecules," Discussions of the Faraday Society, vol. 9. p. 14, 1950.
[127] R. Balda, J. Fernández, A. J. García, and G. F. Imbusch, "The influence of local coordination ions on the optical properties of Eu^{3+} in fluoro-chloride glasses," J. Lumin., vol. 76–77, pp. 551–554, Feb. 1998.
[128] E. Antic-Fidancev, "Simple way to test the validity of $^{2S+1}L_J$ barycenters of rare earth ions (e.g. $^4f_2$, $^4f_3$ and $^4f_6$ configurations)," J. Alloys Compd., vol. 300–301, pp. 2–10, Apr. 2000.
[129] P.-H. Haumesser, R. Gaumé, B. Viana, E. Antic-Fidancev, and D. Vivien, "Spectroscopic and crystal-field analysis of new Yb-doped laser materials," J. Phys. Condens. Matter, vol. 13, no. 23, pp. 5427–5447, 2001.
[130] E. Rukmini, A. Renuka Devi, and C. K. Jayasankar, "Crystal free-ion energy level analysis of Er^{3+} ($^4f_{11}$) in various crystal hosts-oxygen coordinated systems," Phys. B Condens. Matter, vol. 193, no. 2, pp. 166–176, Feb. 1994.
[131] N. V Kuleshov, A. A. Lagatsky, A. V Podlipensky, V. P. Mikhailov, and G. Huber, "Pulsed laser operation of Yb-doped $KY(WO_4)_2$ and $KGd(WO_4)_2$," Opt. Lett., vol. 22, no. 17, pp. 1317–1319, 1997.
[132] H. Zhou, W. Li, K. Yang, N. Lin, B. Jiang, Y. Pan, and H. Zeng, "Hybrid ultra-short Yb:YAG ceramic master-oscillator high-power fiber amplifier.," Opt. Express, vol. 20, Suppl 4, no. May, pp. A489-95, 2012.
[133] D. E. McCumber, "Einstein relations connecting broadband emission and absorption spectra," Phys. Rev., vol. 136, no. 4A, 1964.
[134] X. Zou and H. Toratani, "Evaluation of spectroscopic properties of Yb^{3+}-doped glasses.," Physical review. B, Condensed matter, vol. 52. pp. 15889–15897, 1995.
[135] H. S. Yang, K. S. Hong, S. P. Feofilov, B. M. Tissue, R. S. Meltzer, and W. M. Dennis, "Electron-phonon interaction in rare earth doped nanocrystals," J. Lumin., vol. 83–4, pp. 139–145, 1999.
[136] R. N. Bhargava, "Doped nanocrystalline materials - Physics and applications (Review)," J. Lumin., vol. 70, no. 1–6, pp. 85–94, 1996.
[137] R. N. Bhargava, "The role of impurity in doped nanocrystals," J. Lumin., vol. 72, pp. 46–48, 1997.
[138] Y. Zeng, S. Grandner, C. L. P. Oliveira, A. F. Thünemann, O. Paris, J. S. Pedersen, S. H. L. Klapp, and R. von Klitzing, "Effect of particle size and Debye length on order parameters of colloidal silica suspensions

under confinement," Soft Matter, vol. 7, no. 22, p. 10899, 2011.
[139] M. Carleer, A. Jenouvrier, A.-C. Vandaele, P. F. Bernath, M. F. Mérienne, R. Colin, N. F. Zobov, O. L. Polyansky, J. Tennyson, and V. A. Savin, "The near infrared, visible, and near ultraviolet overtone spectrum of water," J. Chem. Phys., vol. 111, no. 6, p. 2444, 1999.
[140] "Eksma optics." http://eksmaoptics.com/.
[141] N. V Kuleshov, A. A. Lagatsky, A. V Podlipensky, V. P. Mikhailov, and G. Huber, "Pulsed laser operation of Yb-doped KY(WO4)(2) and KGd(WO4)(2)," Opt. Lett., vol. 22, no. 17, pp. 1317–1319, 1997.
[142]D. Kasprowicz, T. Runka, M. Szybowicz, M. Drozdowski, A. Majchrowski, E. Michalski, and J. Zmija, "Spectroscopic properties of $KGd(WO_4)_2$ and $KGd(WO_4)_2$:Ho^{3+} single crystals studied by Brillouin and Raman scattering methods," J. Mol. Struct., vol. 792–793, pp. 139–145, 2006.
[143]D. Kasprowicz, T. Runka, A. Majchrowski, and E. Michalski, "Low-temperature vibrational properties of $KGd(WO_4)_2$: (Er, Yb) single crystals studied by Raman spectroscopy," J. Phys. Chem. Solids, vol. 70, no. 9, pp. 1242–1247, 2009.
[144] D. Kasprowicz, T. Runka, A. Majchrowski, E. Michalski, and M. Drozdowski, "Vibrational properties of Nd^{3+}, Eu^{3+}, Er^{3+} and Ho^{3+} doped $KGd(WO_4)_2$ single crystals studied by Raman scattering method," in Physics Procedia, 2009, vol. 2, no. 2, pp. 539–550.
[145] D. Zhang, D. Wang, J. Zhang, Q. Zhang, S. Wan, D. Sun, Y. Sun, and S. Yin, "In situ investigation of the microstructure of $KGd(WO_4)_2$ crystal growth boundary layer by confocal laser Raman microscopy," CrystEngComm, vol. 14, no. 24, p. 8722, 2012.
[146] W. F. Krupke, "Ytterbium solid-state lasers. The first decade," IEEE Journal of Selected Topics in Quantum Electronics, vol. 6, no. 6. pp. 1287–1296, 2000.
[147] R. N. Bhargava, D. Gallagher, and T. Welker, "Doped nanocrystals of semiconductors - a new class of luminescent materials," J. Lumin., vol. 60, pp. 275–280, 1994.
[148] E. Cantelar, R. Nevado, G. Lifante, and F. Cusso, "Modelling of optical amplification in Er/Yb co-doped $LiNbO_3$ waveguides," Opt. Quantum Electron., vol. 32, no. 6–8, pp. 819–827, 2000.
[149] J. Zhou, W. Zhang, T. Huang, L. Wang, J. Li, W. Liu, B. Jiang, Y. Pan, and J. Guo, "Optical properties of Er,Yb co-doped YAG transparent

ceramics," Ceram. Int., vol. 37, no. 2, pp. 513–519, 2011.
[150] E. Cantelar and F. Cussó, "Dynamics of the Yb^{3+} to Er^{3+} energy transfer in $LiNbO_3$," Appl. Phys. B, vol. 69, no. 1, pp. 29–33, 1999.
[151] T. Liu, Q. Meng, and W. Sun, "Luminescence properties of $NaY(WO_4)_2$:Sm^{3+}, Eu^{3+} phosphors prepared by molten salt method," J. Lumin., vol. 170, pp. 219–225, 2016.
[152] M. C. Pujol, C. Cascales, M. Rico, J. Massons, F. Diaz, P. Porcher, and C. Zaldo, "Measurement and crystal field analysis of energy levels of Ho^{3+} and Er^{3+} in $KGd(WO_4)_2$ single crystal," in Journal of Alloys and Compounds, 2001, vol. 323–324, pp. 321–325.
[153] S. K. Pillai, L. M. Sikhwivhilu, and T. K. Hillie, "Synthesis, characterization and photoluminescence properties of Dy^{3+}-doped nano-crystalline SnO_2," Mater. Chem. Phys., vol. 120, no. 2–3, pp. 619–624, 2010.
[154] F. Yang, C. Tu, H. Wang, Y. Wei, Z. You, G. Jia, J. Li, Z. Zhu, X. Lu, and Y. Wang, "Growth and spectroscopy of Dy^{3+} doped in ZnWO4 crystal," Opt. Mater. (Amst)., vol. 29, no. 12, pp. 1861–1865, 2007.
[155] A. Kumar, D. Rai, and S. . Rai, "Optical properties of Sm^{3+} ions doped in tellurite glass," Spectrochim. Acta Part A Mol. Biomol. Spectrosc., vol. 59, pp. 917–925, 2003.
[156] H. Wang, J. Li, G. Jia, Z. You, F. Yang, Y. Wei, Y. Wang, Z. Zhu, X. Lu, and C. Tu, "Optical properties of Dy^{3+} ions in sodium gadolinium tungstates crystal," J. Lumin., vol. 126, no. 2, pp. 452–458, 2007.
[157] K. Ning, X. He, L. Zhang, Y. Liu, J. Yin, P. Zhang, G. Chen, X. Wang, Z. Chen, C. Shi, J. Hong, and Y. Hang, "Spectroscopic characteristics of $GdVO_4$: Dy_{3+} crystal," Opt. Mater. (Amst)., vol. 37, pp. 745–749, 2014.
[158] G. Dominiak-Dzik, "Sm^{3+}-doped $LiNbO_3$ crystal, optical properties and emission cross-sections," J. Alloys Compd., vol. 391, no. 1–2, pp. 26–32, 2005.
[159] J. F. Martel, S. Jandl, B. Viana, and D. Vivien, "Crystal-field study of Sm^{3+} ions in Sm_2O_3, Sm^{3+}:Gd_2O_3 and Sm^{3+}:Y_2O_3," J. Phys. Chem. Solids, vol. 61, no. 9, pp. 1455–1463, 2000.
[160] L. Panayiotidou, M. Stylianou, N. Arabatzis, C. Drouza, P. Lianos, E. Stathatos, and A. D. Keramidas, "Synthesis, crystal structure and luminescence of novel Eu^{3+}, Sm^{3+} and Gd^{3+} complexes of 1,3,5- and 1,2,4-triazines," Polyhedron, vol. 52, pp. 856–865, 2013.

[161]G. Q. Wang, Y. F. Lin, X. H. Gong, Y. J. Chen, J. H. Huang, Z. D. Luo, and Y. D. Huang, "Polarized spectral properties of Sm^{3+}:$LiYF_4$ crystal," J. Lumin., vol. 147, pp. 23–26, 2014.
[162] H. Hu and W. Zhang, "Synthesis and properties of transition metals and rare-earth metals doped ZnS nanoparticles," Opt. Mater. (Amst)., vol. 28, no. 5, pp. 536–550, Apr. 2006.
[163] M. Aas, A. Jonáš, A. Kiraz, O. Brzobohatý, J. Ježek, Z. Pilát, and P. Zemánek, "Spectral tuning of lasing emission from optofluidic droplet microlasers using optical stretching.," Opt. Express, vol. 21, no. 18, pp. 21380–94, 2013.
[164] M. Aas, A. Jonáš, and A. Kiraz, "Lasing in optically manipulated, dye-doped emulsion microdroplets," Opt. Commun., vol. 290, pp. 183–187, Mar. 2013.
[165] H. Azzouz, L. Alkhafadiji, S. Balslev, J. Johansson, N. a Mortensen, S. Nilsson, and a Kristensen, "Levitated droplet dye laser.," Opt. Express, vol. 14, no. 10, pp. 4374–9, 2006.
[166] M. Guillon, K. Dholakia, and D. Mcgloin, "Optical trapping and spectral analysis of aerosols with a supercontiuum laser source Abstract :," vol. 16, no. 11, pp. 7655–7664, 2008.
[167] S. Ishizaka, Y. Suzuki, and N. Kitamura, "Laser trapping and picosecond time-resolved spectroscopy of water droplets in air: cavity-enhanced spontaneous emission of $Ru(bpy)_3Cl_2$," Phys. Chem. Chem. Phys., vol. 12, no. 33, pp. 9852–7, 2010.
[168] Y. Karadag, M. Aas, A. Jonáš, S. Anand, D. McGloin, and a. Kiraz, "Dye lasing in optically manipulated liquid aerosols," Opt. Lett., vol. 38, no. 10, pp. 1669–1671, 2013.
[169] K. C. Neuman and S. M. Block, "Optical trapping.," Rev. Sci. Instrum., vol. 75, no. 9, pp. 2787–809, Sep. 2004.
[170] T. Cizmar, V. Garces-Chavez, K. Dholakia, and P. Zemanek, "Optical trapping in counter-propagating Bessel beams," Opt. Trapp. counter-propagating Bessel beams, vol. 5514, pp. 643–651, 2004.
[171] J. Arlt and K. Dholakia, "Generation of high-order Bessel beams by use of an axicon," Opt. Commun., vol. 177, no. 1, pp. 297–301, 2000.
[172] M. D. Summers, J. P. Reid, and D. McGloin, "Optical guiding of aerosol droplets," Opt. Express, vol. 14, no. 14, pp. 6373–80, Jul. 2006.
[173] V. Kushawaha, A. Michael, and L. Major, "Effect of Nd concentra-

tion on the Nd:KGW laser," Appl. Phys. B Laser Opt., vol. 58, no. 6, pp. 533–535, 1994.
[174] W. M. Lee, P. J. Reece, R. F. Marchington, N. K. Metzger, and K. Dholakia, "Construction and calibration of an optical trap on a fluorescence optical microscope.," Nat. Protoc., vol. 2, no. 12, pp. 3226–38, 2007.
[175] A. Ashkin, "Optical trapping and manipulation of neutral particles using lasers.," Proc. Natl. Acad. Sci. U. S. A., vol. 94, pp. 4853–4860, 1997.
[176] D. R. Burnham and D. McGloin, "Modeling of optical traps for aerosols," J. Opt. Soc. Am. B, vol. 28, no. 12, p. 2856, Nov. 2011.
[177] D. G. Grier, "A revolution in optical manipulation," Nature, vol. 424, no. 6950, pp. 810–6, Aug. 2003.
[178] A. Ashkin, J. M. Dziedzic, J. E. Bjorkholm, and S. Chu, "Observation of a single-beam gradient force optical trap for dielectric particles," vol. 11, no. 5, pp. 288–290, 1986.
[179] J. W. Shaevitz, "A Practical Guide to Optical Trapping," University of Washington, pp. 1–19, 2006.

List of Figures

List of Tables